

University of Cambridge

**Department of Applied Mathematics
and Theoretical Physics**

**Stability of Fluid-Loaded
Structures**

**Sevag Arzoumanian
St. John's College**

A dissertation submitted for the degree of Doctor of Philosophy

February 2011

Preface and Acknowledgements

This dissertation is the result of my own work and includes nothing which is the outcome of work done in collaboration or as part of another degree or diploma. Parts of chapters 2 through 4 and chapter 9 have been published as an ASME paper (Arzoumanian & Peake, 2010). This research was funded by a Benefactor's Scholarship from St. John's College, Cambridge.

I gratefully express my thanks to my supervisor, Prof. Nigel Peake, for his continued encouragement, insight and immeasurable enthusiasm. During my time at the Center for Mathematical Studies, I have benefitted greatly from almost daily contact and many inspiring conversations with him and am glad to take this opportunity to express my gratitude.

I am indebted to my college, St. John's, for providing a warm and welcoming home during this dissertation's long journey towards submission.

This dissertation is dedicated to the memory of Prof. David G. Crighton (1942-2000) whose vision has inspired much of this work.

Summary

It is known theoretically that infinitely long fluid loaded plates in mean flow exhibit a range of unusual phenomena in the long time limit. These include convective instability, absolute instability and negative energy waves which are destabilized by dissipation. However, structures are necessarily of finite length and may have discontinuities. We have undertaken an analytical and computational study to investigate the response of finite plates, and of plates with local inhomogeneities, to ascertain if these unusual effects might be realized in practice. Analytically, we adopt Crighton & Oswell's (1991) structural acoustics approach and take a "wave scattering" --as opposed to a "modal superposition"-- view of the fluttering plate problem. First, we derive the energy balance relations for the extended plate (i.e., plate with two sided flow, spring foundation and plate pretension) and define a generalized wave impedance valid for both positive energy waves (PEW) and negative energy waves (NEW). Next, we solve for the scattering coefficients of localized plate discontinuities using a multipole source approach. Our solutions are exact and include the nearfields due to fluid-loading effects. We introduce the concept of power normalized scattering coefficients, and show that overall power is conserved during the scattering process if the sign of the wave energy is preserved. We argue that energy conservation, combined with the presence of NEWs on the plate, are responsible for the phenomenon of over-scattering, or of amplified reflection/transmission. These are scattering processes that draw energy from the mean flow into the plate. Next, we use the Wiener-Hopf technique to solve for the scattering coefficients of a variety of plate leading and trailing edge conditions --including the flag like configuration of a free trailing edge with wake. We find that the edges are over-reflective in the frequency range where NEWs are present. The exception is a free trailing edge with wake where, remarkably, the wake is found to absorb almost all of the incident wave energy. We use combinations of these upstream and downstream edge reflection matrices to solve for the complex resonance frequencies of long, finite plates immersed in mean flow. Finally, we construct the response of a finite plate by a superposition of infinite plate propagating waves continuously scattering off the plate ends. We solve for the unstable resonance frequencies and temporal growth rates for long plates. We derive upper and lower bounds on the unstable growth rates of finite plates with given edge conditions. We find that a flag-like configuration of a clamped leading edge and a free trailing edge with wake is destabilized for sub-critical flow speeds only for very long plate lengths and only in the presence of convectively unstable waves. We present a comparison between direct computational results and the infinite plate theory. In particular, the resonance response of a moderately sized plate is shown to be in excellent agreement with the long plate analytical predictions.

Contents

Preface and Acknowledgements	iii
Summary	v
1 Introduction	1
1.1 Immediate Precursors to Current Work	4
1.2 Remainder of Thesis	7
2 The Infinite Flow-Loaded Plate	9
2.1 Causal Solution and Location of Poles	11
2.1.1 General Solution	12
2.1.2 The Effect of Finite λ and T	13
2.2 Plate Response	15
2.2.1 Far Field Response	17
2.2.2 Drive Point Admittance & Power into Plate	17
2.3 Pinch Parameters and Absolute Instability	18
2.3.1 For $T = 0$	19
2.3.2 For $T \neq 0$	22
2.4 Convective Instability	23
3 Energy Balance	26
3.1 Energy Equations for Plate and Fluid	26
3.2 Wave Flux, Wave Energy and Wave Impedance	32
3.3 Existence of Negative Energy Waves	35
4 Scattering from Local Discontinuities	40
4.1 Plate Equation with Multipole Loads	40
4.2 Scattered Field: the Green's Function Matrix	42
4.2.1 Evaluating the Nearfield Integrals	44
4.3 Response to Multipole Loads	47
4.3.1 Far Field Response	47
4.3.2 Drive Point Admittance & Power into Plate	50
4.3.3 Pressure and Potential Response	53
4.4 Scattering from Representative Discontinuities	57
4.4.1 Break in Plate	60
4.4.2 Clamped Constraint	64

4.4.3	Free-Clamped Discontinuity	65
4.4.4	Free-Hinged Discontinuity	68
4.4.5	Rotational Crack	71
4.4.6	Translational Crack	74
4.4.7	Pinned Constraint	79
4.5	Power Balance	80
4.5.1	Example: Clamped Constraint	83
4.6	Summary	84
5	Resonance of Quasi Finite Plate Segments	85
5.1	Condition for Resonance	86
5.1.1	Propagating Waves Only: Large L Asymptotics	86
5.1.2	Including Nearfields: Exact Solution for all L	88
5.2	Structural Energy Balance for Resonant Segment	93
5.3	Finite Segment Configurations	94
5.3.1	Clamped Leading Edge, Clamped Trailing Edge	95
5.3.2	Free-Clamped Leading Edge, Free-Clamped Trailing Edge	103
5.3.3	Clamped Leading Edge, Free Trailing Edge	106
5.4	Summary	107
6	Scattering from Leading Edge	110
6.1	System Equations Using Half-Range Transforms	111
6.2	Wiener-Hopf Equation	115
6.3	Solution for Arbitrary Edge Conditions	117
6.4	Reflection Coefficients for Representative Edge Conditions	122
6.4.1	Free Edge	122
6.4.2	Clamped Edge	123
6.4.3	Constraint at Edge	125
6.4.4	Hinged Edge	129
6.5	Response for Leading Edge Drive	130
6.6	Summary	134
7	Scattering from Trailing Edge	135
7.1	System Equations Using Half-Range Transforms	135
7.2	Wiener-Hopf Equation	137
7.3	Upstream Solution	139
7.4	Downstream Solution	142
7.4.1	The Wake Impedance	143
7.5	Reflection Coefficients for Representative Edge Conditions	144
7.5.1	Free Edge with Wake	144
7.5.2	Free Edge without Wake	148
7.5.3	Constraint at Edge without Wake	148
7.5.4	Hinged Edge without Wake	150
7.6	Response for Trailing Edge Drive	153
7.6.1	Without Wake	153
7.6.2	With Wake	154

7.7	Summary	156
8	Global Modes of Long, Finite Plates	158
8.1	Global Modes for Large L	158
8.1.1	Estimates of Maximum Growth Rate	159
8.1.2	From Maximum Gain to Temporal Growth Rate	161
8.1.3	The Kulikovskii Condition	162
8.1.4	An Explicit Kulikovskii Condition?	163
8.2	Finite Flag Configurations	163
8.2.1	Clamped Leading Edge, Free Trailing Edge (No Wake)	163
8.2.2	Clamped Leading Edge, Free Trailing Edge (With Wake)	171
8.2.3	Free Leading Edge, Free Trailing Edge (With Wake)	176
8.3	Summary	179
9	Computational Results for Finite Plate	180
9.1	Computational Model	180
9.2	Results for a Baffled Plate Clamped at Both Edges	181
9.2.1	Spectral Content	183
9.2.2	Growth Rate	186
9.2.3	A Word on Convergence	186
9.3	Comparison with Analytical Predictions	189
9.3.1	Reflection Coefficients for a Clamped, Baffled Plate	190
9.3.2	Global Modes for Long Plate	191
9.4	Conclusion	193
10	Conclusions	196
10.1	Summary of Results	196
10.2	Outline for Future Work	198
10.2.1	Further Work on Local Scatterers	199
10.2.2	Refining the Edge Coefficients	199
10.2.3	A More Complete Wake Model	200
10.2.4	Improving the Finite Flag Analytical Model	200
10.2.5	Further Computational Studies	201
10.2.6	Validation with Other Published Results	202
11	References	204
A	Derivation of Jump Matrix $\partial^n G_+^{(m)} - \partial^n G_-^{(m)}$	208
B	Wiener-Hopf Solution Details	211
B.1	Exact Factorization of Kernel $K(k, \omega)$	211
B.2	Determining the Edge Potential $\varphi(+0)$	212
C	Computational Model of Baffled Plate	216
C.1	Computational model	216
C.2	Implementation Including Geometric Nonlinearities	218
C.3	Fully Linear Implementation	221

C.3.1	Singular Panels	223
C.3.2	Spatial Discretization	225
C.3.3	Evaluation of Spatial Integrals	226
C.3.4	Combined Plate Equation	228
C.3.5	Time Stepping	228
C.4	Addendum: Derivation of Non-Linear Influence Coefficients	229
C.4.1	Fundamental Solutions	229
C.4.2	Evaluation of Integrals	230

Chapter 1

Introduction

Heavy fluid loading on elastic structures can have a profound effect on the nature and properties of the structural waves that are present (Crighton, 1989). This effect is particularly pronounced at low frequencies and when the fluid is in bulk motion over the structure. Plates and membranes in contact with a uniformly flowing fluid are known to possess a range of parameters over which downstream travelling waves are so overwhelmed by the flow that they lose their character as structural waves and propagate at roughly the mean flow speed. This is accompanied by unusual effects such as convective instability and negative energy waves (Crighton & Oswell, 1991).

The unstable response of elastic structures in contact with a fluid in bulk motion is a fundamental problem in fluid-structure interactions. It is intimately involved in a range of phenomena, from panel flutter, to the flapping of flags, to the biomechanics of snoring and has preoccupied researchers in fluid-mechanics and aero/hydroelasticity since the early 1960s. The stability properties of large scale underwater engineering structures are also of considerable concern. Of particular interest are the effects of structural discontinuities such as ribs, rivets and gaps and their possible role in creating a strong coupling mechanism between the plate and the fluid, leading to significant radiation of sound into the water or to potentially catastrophic instabilities.

In this dissertation, we focus on the unstable response of fluid loaded plates in mean flow. Three distinct theoretical treatments of this linear, fluid-elastic problem can be found in the literature. (Here we generally follow the classification given in

Abrahams & Wickham (2001). A more comprehensive introduction to the general problem can be found in Paidoussis (2004)).

1) In traditional hydrodynamic stability theory (Benjamin 1960, Kramer 1960, Landahl 1962, Kornecki 1978), one is interested in the effects of wall compliance on the generation of instabilities (e.g., of the Tollmien–Schlichting type) at the fluid-structure interface. This approach is often based on the local properties of the dispersion equation, where one typically prescribes a travelling wave disturbance and solves for the ensuing evolution of wave trains. Commonly, the instabilities are a priori assumed to be spatial or temporal, since a simple analysis of the dispersion equation does not provide that information. This ‘fluid-centric’ approach, intended for solving initial boundary value type problems, is perhaps best suited for studying wave instabilities in infinite domains –spatially and temporally– where there are no physical discontinuities, external forcing agent or impulsive starts. It is only relatively recently that the hydrodynamic stability community has begun considering ‘receptivity’ problems where some localized source switched on at $t = 0$ drives the flow instability (e.g., Huerre & Monkewitz (1990) and Schmid & Henningson (2001) in contrast to Drazin & Reid (1981)).

2) Traditional Aero/Hydroelasticity theory takes a more ‘structure-centric’ approach to the study of panel flutter. In this approach, the Galerkin method (Ellen 1973, Kornecki 1974, Dowell 1975) is commonly used to express the vibrations of a necessarily finite fluid-loaded structure in terms of a modal expansion of the equivalent *in-vacuo* modes. These fluid-less modes are chosen as basis functions because they comprise a complete and orthogonal set that automatically satisfy the structural edge conditions. In this approach one fixes the panel length, prescribes the edge conditions and then solves for the critical flow velocity thresholds for the onset of temporal instability caused by the unsteady hydrodynamic forcing. There is no natural way of incorporating external sources or structural inhomogeneities. This approach is perhaps best suited for relatively short panels with moderate levels of fluid loading. It is not altogether clear if it can provide useful physical insights for problems where the flow entirely ‘disarms’ the structure, as in convective instability.

3) The theory of structural acoustics (Brazier-Smith & Scott 1984, Crighton & Oswell 1991) is specially equipped for dealing with scenarios where there is strong fluid-structure coupling and where localized structural discontinuities and inhomogeneities are present. In this theory, one is typically concerned with the response of the fluid-elastic system to localized forcing at a single frequency switched on at $t = 0$. Since it is possible to find more than one solution to this problem, the need to obtain the unique ‘causal’ solution requires one to carry out a global analysis of the dispersion relation in the entire complex ω - k plane. This involves allowing both ω and k to be simultaneously complex and evaluating the dispersion relation not only at the prescribed real frequency, but over a wide range of positive imaginary frequencies as well. This type of analysis is not only required to properly identify the convective and absolute instabilities present in the system but, just as crucially, to properly characterize the spatial location of the waves upstream or downstream of the driver, or of any structural discontinuity or edge. This approach is specially suited for studying the interaction of waves with structural discontinuities, including the exchange of energy between the fluid and the elastic structure. It is best characterized as a ‘wave-centric’ approach because it inherently captures the strong coupling between the fluid and the structure.

The aim of this dissertation is to use the wave-based theory of Crighton & Oswell (1991) to solve for the linear response and stability properties of finite, flow-loaded structures. We undertake a systematic study of the scattering properties of waves from local plate discontinuities and from the edges of long plates. We derive limits on the unstable growth rates of finite plates based on the scattering and propagation properties of these waves and solve for the complex eigenfrequencies as a function of plate length and edge conditions. Finally, as a means of validating our overall approach, we build a computational model for the direct integration of the fluid-plate equations to which we compare our wave based predictions.

1.1 Immediate Precursors to Current Work

The application of the *structural acoustics* approach to the basic problem of an infinite elastic plate in uniform flow can be traced back to Brazier-Smith & Scott (1984), who were the first to adapt the method of Briggs & Bers, initially developed in the context of spatial instabilities in plasma physics, for this fluid-elastic problem. Solving for the causal response, Brazier-Smith & Scott correctly identified the spatial location, with respect to an external driving force, of the propagating and convectively unstable waves and were the first to predict the existence of a critical velocity U_c for absolute instability as well the existence of a neutral wave with group velocity pointed towards the driver.

Crighton & Oswell (1991) provided an analytical framework for the results of Brazier-Smith & Scott (1984) and uncovered additional unusual phenomena. They undertook a systematic study of the ‘basic problem of structural acoustics,’ or the response to a single frequency line drive, for a plate in mean flow and found a range of frequencies over which the real part of the drive admittance was negative indicating that the driver was in fact absorbing energy from the system. They identified the presence of negative energy waves (NEW) and confirmed the existence of an anomalous neutral wave whose group velocity is directed towards the driver (in apparent violation of the Lighthill radiation condition). They provided asymptotic expressions for the convectively unstable, anomalous neutral and conventional propagating waves as well as for the turning point frequencies that delimit the stable and unstable regimes. Perhaps their greatest contribution, however, was their detailed study of the energy flow and power balance in the coupled fluid-plate system including their derivation of an exact expression for the wave energy flux. As we will see in later chapters of this thesis, Crighton & Oswell’s formulation for the wave flux will prove indispensable in our own understanding of the scattering process from plate discontinuities and edges.

Subsequent to the publication of these two pioneering works, many studies that consisted of variations of this basic problem have been published. Much of this work has involved adding complexity to the original configuration of a thin beam in ideal flow to see if the unusual phenomena observed in this simple system may be found in

more realistic configurations.

The effect of transverse plate curvature was examined by Peake (1997) who found that it acted to first order as an added spring foundation and that it had a generally stabilizing effect on the flow. One notable result was that the introduction of infinitesimally small transverse curvature pushed the absolute instability boundary so high that it entered into a parameter regime that was physically unrealizable. In contrast, convectively unstable waves and NEWs were found to be more robust under the effect of transverse plate curvature.

Lucey (1998) performed a direct numerical simulation of Crighton & Oswell's single frequency, line driven problem for a finite plate and found broad qualitative agreement with the infinite plate theory at early response times. Most notably, he observed a convectively unstable wave downstream of the driver accompanied by negative power injected into the plate at the driver over the range of frequencies predicted by the infinite theory. He observed that, a short time following startup, the finiteness of the plate played a major role in the subsequent evolution of the plate response. In particular, energy continuously scattered from the upstream and downstream edges was found to introduce disturbances at frequencies other than the drive frequency. The frequency-wavenumber content of these waves that appeared for large time were seen to fall on or near the dispersion curve of the infinite plate, but concentrated in the immediate vicinity of the pinch point (ω_p, k_p) . Lucey also observed the presence of absolute instability on the plate, in the form of a slowly travelling disturbance with frequency-wavenumber content at the expected (ω_p, k_p) , but at flow speeds well below the critical speed U_c . These disturbances did not appear to depend on the amount of structural damping/dissipation in the system and were quickly overwhelmed by the convectively unstable disturbances introduced by the plate edges.

The stability of fluid-loaded plates with inviscid shear layer profiles was considered by Lingwood & Peake (1999). They found that for a simple broken line profile, the absolute instability and anomalous mode results are qualitatively unchanged including in the limit of infinitesimally small shear layer thickness. For a more realistic Blasius profile, they found that the anomalous modes did likewise persist over a wide range of

shear layer thicknesses. The results for absolute instability, however, were significantly different from the mean flow case as the presence of the critical layer pushed the critical flow speed to unrealizably high values. More crucially, it was found that in the limit of a disappearing shear layer, the critical velocity for uniform flow is not regained leading the authors to conclude that the mean flow idealized problem was an ‘unattainable singular limit.’

Abrahams & Wickham (2001) considered the effects of finite plate thickness (Timoshenko-Midlin plate theory) and fluid compressibility. They found that, in the limit of small fluid-to-plate density ratio, these effects do not introduce qualitatively different behaviour. In contrast, the addition of structural dissipation was found to make the system absolutely unstable for all flow velocities. Green & Crighton (2000) examined the three dimensional problem of a point force on an infinite two dimensional plate in contact with a three dimensional fluid in mean flow. The boundary for absolute instability was found to be identical to that of a line driven plate. However, the parameter regimes for the existence of convectively unstable and negative energy waves were found to shrink with increased transverse wavenumber in a way that was qualitatively similar to the effect of increasing the foundation spring constant discovered by Peake (1997). This resulted in the convective growth being confined to within a wedge shaped region downstream of the driver. De Langre (2000) examined the effects of plate pre-tension and showed that it raised the critical speed for the onset of absolute instability. He also showed that in the limit of large plate tension, the results for a membrane in mean flow are recovered.

Peake (2001) considered the nonlinear evolution, in a plate of infinite extent, of the marginally convectively unstable waves and showed that they can exhibit solitary-wave solutions with the potential to achieve large deflection amplitudes. He also considered the evolution of NEWs destabilized by structural damping and found that they become saturated at weakly nonlinear amplitudes and, in the most realistic case in which nonlinear tension is the controlling force, the fluid-loaded plate system approaches a state of static deflection. Metcalfe (2005) studied the problem of a ribbed membrane in mean flow and observed behavior that was comparable to that found for quiescent fluid

loaded plates. For regularly spaced point discontinuities he observed the expected pass and stop band structure and for disordered structures he observed the phenomenon of Anderson localization.

Finally, Peake (2004) used the Wiener-Hopf technique to solve for the reflection matrices at the leading and trailing edges of an asymptotically long baffled plate clamped at both ends. These reflection coefficients were then used to solve for the complex eigenfrequencies (including the unstable temporal growth rates) of a finite baffled plate. He found that the plate is temporally unstable both for parameter values where the infinite plate is convectively unstable and for values where it is stable but supports NEWs. When non-linear tension effects are added, the finite plate system was shown to possess points of minimum action at non-zero frequencies suggesting the possibility of nonlinear dynamic flutter.

1.2 Remainder of Thesis

The problem of the fluid-loaded plate in an infinite domain studied by Crighton & Oswell (1991) is introduced in chapter 2 where we extend some of their analytical results to include double sided flow and the effects of plate pre-tension. These include an approximate expression for the onset of absolute instability as a function of plate tension. In chapter 3 we derive the energy balance relations for a fluid-loaded plate with two sided flow, spring foundation and plate pretension. We introduce the ‘wave impedance’ and generalize its definition to include negative energy waves. This will prove to be instrumental in later chapters where energy arguments are used to demonstrate the key role of negative energy waves in the amplification of waves as they interact with plate discontinuities and edges.

In chapter 4 we undertake a rigorous study of the scattering problem from local discontinuities using the ‘multipole source’ approach developed by Howe (1994). We solve for the reflection and transmission coefficients of a large number of local scatterers and discuss the physics behind each. We apply the concept of a generalized ‘wave impedance’ to solve for the power normalized scattering coefficients, and show that overall power is indeed conserved during the scattering process if the sign of the wave

energy is maintained. We argue that the presence of negative energy waves alone is responsible for the phenomenon of over-scattering or amplified reflection and transmission. These are scattering processes that draw energy from the mean flow into the plate. In chapter 5 we develop a framework for analyzing the response of plate segments formed by two local scatterers on an otherwise infinite fluid-loaded plate. We solve for the complex eigenfrequencies of these quasi-finite segments exactly, thanks to our ability to include all the scattered nearfields associated with fluid loading.

In chapters 6 and 7 we use the Weiner Hopf technique to solve for the scattered field from the upstream and downstream edges of semi-infinite plates immersed in mean flow. We find that, with the exception of a free trailing edge with wake, the edges are ‘over-reflective’ in the frequency range where negative energy waves are present. In chapter 8, we combine pairs of upstream and downstream reflection coefficients obtained in chapters 6 and 7, to solve for the resonant response of very long plates. We derive bounds on the unstable growth rates of these plates based on the edge conditions and plate parameters.

In chapter 9 we introduce a computational model of a finite plate in an infinitely long rigid baffle. We solve for the response to an impulsive load and compare the spectral content of disturbances to the dispersion equation of the corresponding infinite plate and find that there’s a great deal of overlap. For large time, we find that the plate response is dominated by a single frequency and temporal growth rate and show that this coincides exactly with the dominant complex eigenfrequency identified by the method of chapter 8.

Chapter 2

The Infinite Flow-Loaded Plate

The linearized equations for a line driven fluid-loaded plate, shown in figure 2.1 with pre-tension and spring foundation in mean (inviscid, irrotational, incompressible) flow are (Crighton and Oswell 1991, Peake 2004)

$$\left[\tilde{B} \frac{\partial^4}{\partial \tilde{x}^4} - \tilde{T} \frac{\partial^2}{\partial \tilde{x}^2} + \tilde{\lambda} + \tilde{m} \frac{\partial^2}{\partial \tilde{t}^2} \right] \tilde{\eta}(\tilde{x}, \tilde{t}) = -\alpha \tilde{p}(\tilde{x}, 0, \tilde{t}) + \tilde{F}_0 \delta(\tilde{x} - \tilde{x}_s), \quad (2.1a)$$

$$\frac{\partial}{\partial \tilde{y}} \tilde{\varphi}(\tilde{x}, 0, \tilde{t}) = \left[\frac{\partial}{\partial \tilde{t}} + \tilde{U} \frac{\partial}{\partial \tilde{x}} \right] \tilde{\eta}(\tilde{x}, \tilde{t}), \quad (2.1b)$$

$$\tilde{p}(\tilde{x}, \tilde{y}, \tilde{t}) = -\tilde{\rho}_f \left[\frac{\partial}{\partial \tilde{t}} + \tilde{U} \frac{\partial}{\partial \tilde{x}} \right] \tilde{\varphi}(\tilde{x}, \tilde{y}, \tilde{t}), \quad (2.1c)$$

$$\left[\frac{\partial^2}{\partial \tilde{x}^2} + \frac{\partial^2}{\partial \tilde{y}^2} \right] \tilde{p}(\tilde{x}, \tilde{y}, \tilde{t}) = 0. \quad (2.1d)$$

Here, $\tilde{\eta}$ is the plate displacement, \tilde{p} the fluid pressure, $\tilde{\varphi}$ the fluid potential. A tilda is used throughout this thesis to denote dimensional quantities. Additionally, $\tilde{\rho}_f$ is the fluid density, $\tilde{m} = \tilde{\rho}_s \tilde{h}$ is the linear density of the plate (with $\tilde{\rho}_s$ the plate bulk density and \tilde{h} the plate thickness), $\tilde{B} = \tilde{E} \tilde{h}^3 / (12(1 - \nu^2))$ is the plate bending stiffness (where

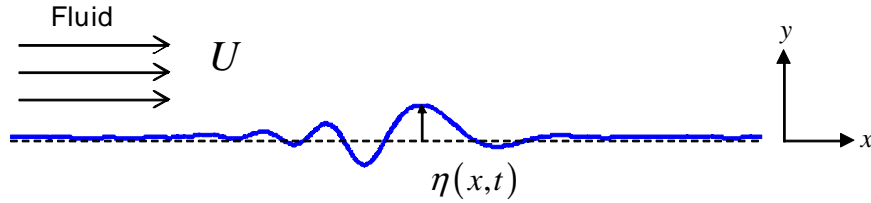


Figure 2.1: Infinite fluid loaded plate configuration.

\tilde{E} is the plate's Young's modulus and ν its Poisson's ratio), \tilde{T} is the plate pre-tension, $\tilde{\lambda}$ is the foundation spring constant, \tilde{x}_s is the location of the applied drive and \tilde{F}_0 is the amplitude of the load. The parameter α equals 1 or 2 for one-sided or two-sided fluid loading, respectively.

We follow Crighton & Oswell (1991) and non-dimensionalize lengths by $\tilde{m}/\tilde{\rho}_f$ and time by $\tilde{m}^{5/2}/\tilde{\rho}_f^2\tilde{B}^{1/2}$ to obtain the following scalings

$$\begin{aligned}\eta &= \frac{\tilde{\rho}_f}{\tilde{m}}\tilde{\eta}, & p &= \frac{\tilde{m}^3}{\tilde{\rho}_f^3\tilde{B}}\tilde{p}, & \varphi &= \frac{\tilde{m}^{1/2}}{\tilde{B}^{1/2}}\tilde{\varphi}, \\ U &= \frac{\tilde{m}^{3/2}}{\tilde{\rho}_f\tilde{B}^{1/2}}\tilde{U}, & T &= \frac{\tilde{m}^2}{\tilde{\rho}_f^2\tilde{B}}\tilde{T}, & \lambda &= \frac{\tilde{m}^4}{\tilde{\rho}_f^4\tilde{B}}\tilde{\lambda}, \\ F_0 &= \frac{\tilde{m}^2}{\tilde{\rho}_f^2\tilde{B}}\tilde{F}_0, & \delta(x) &= \frac{\tilde{m}}{\tilde{\rho}_f}\delta(\tilde{x}).\end{aligned}\tag{2.2}$$

With this choice of a non-dimensionalization scheme, the flow-loaded plate equations (2.1) become

$$\left[\frac{\partial^4}{\partial x^4} - T\frac{\partial^2}{\partial x^2} + \lambda + \frac{\partial^2}{\partial t^2}\right]\eta(x, t) = -\alpha p(x, 0, t) + F_0\delta(x - x_s),\tag{2.3a}$$

$$\frac{\partial}{\partial y}\varphi(x, 0, t) = \left[\frac{\partial}{\partial t} + U\frac{\partial}{\partial x}\right]\eta(x, t),\tag{2.3b}$$

$$p(x, y, t) = -\left[\frac{\partial}{\partial t} + U\frac{\partial}{\partial x}\right]\varphi(x, y, t),\tag{2.3c}$$

$$\left[\frac{\partial^2}{\partial x^2} + \frac{\partial^2}{\partial y^2}\right]p(x, y, t) = 0.\tag{2.3d}$$

For the case where $T = \lambda = 0$ and the bending stiffness is the only restoring force in the plate, the non-dimensional speed U is the sole parameter governing this system of equations. We note here that the re-dimensionalization of U (or any other velocity of the system) is independent of the plate thickness, i.e.,

$$\tilde{U} = \frac{\tilde{E}^{1/2}}{\sqrt{12(1-\nu^2)}}\frac{\tilde{\rho}_f}{\tilde{\rho}_s^{3/2}}U.$$

This set of coupled fluid-plate equations are transformed in time and space, solved in the frequency-wavenumber (ω - k) domain, and transformed back to yield

$$\eta(x, t) = \frac{1}{4\pi^2} \int_{-\infty+i\omega_i}^{+\infty+i\omega_i} \Psi(x, \omega) F(\omega) e^{-i\omega t} d\omega,\tag{2.4}$$

$$\Psi(x, \omega) = \int_{\Gamma_k} \frac{e^{ikx}}{D(k, \omega)} dk,\tag{2.5}$$

where

$$D(k, \omega) = [k^4 + Tk^2 + \lambda - \omega^2] - \frac{\alpha(\omega - Uk)^2}{\gamma(k)} \quad (2.6)$$

is the dispersion function and $\gamma(k) \equiv \sqrt{k^2}$ is defined as positive on the real k axis. The quantity $\omega_i \geq 0$ is chosen such that the inverse frequency transform is convergent and the choice of Γ_k is described in the next section. The dimensional counterparts for the radian frequency and wavenumber are

$$\begin{aligned} \tilde{\omega} &= \frac{\tilde{E}^{1/2}}{\sqrt{12(1-\nu^2)}} \frac{\tilde{\rho}_f^2}{\tilde{\rho}_s^2} \tilde{h}^2 \omega, \\ \tilde{k} &= \frac{\tilde{\rho}_f}{\tilde{\rho}_s} \tilde{h} k. \end{aligned}$$

By defining a pair of branch cuts up the imaginary k axis, from $\pm i0$ to $\pm i\infty$, we can re-express (Crighton & Oswell 1991) the dispersion equation in terms a pair of quintic polynomials each valid in either the left or the right half of the complex k plane for $k \neq 0$

$$P_{\pm}(k, \omega) \equiv kD(k, \omega) = k^5 + Tk^3 \mp \alpha U^2 k^2 - (\omega^2 \mp 2\alpha U\omega + \lambda) k \mp \alpha \omega^2, \quad \text{Re}\{k\} \gtrless 0. \quad (2.7)$$

2.1 Causal Solution and Location of Poles

The causal behaviour of a line driven infinite plate in the long time ($t \rightarrow \infty$) limit is determined using what has become known as the Briggs-Bers technique (Briggs 1964; Bers 1983). For a full description of this method as it is applied to fluid-structure interaction problems the reader is referred to the comprehensive treatments in Brazier-Smith & Scott (1984) and in Crighton & Oswell (1991). Only a brief description of the method will be provided here.

Initially, the temporal contour in (2.4) is defined with the imaginary part of the frequency, $\omega_i = \text{Im}(\omega)$, very large such that the contour lies above all singularities in the complex ω plane. This guarantees convergence in the limit of $t \rightarrow \infty$, even in the presence of instabilities. As the temporal contour is decreased towards the real ω axis, or as ω_i is gradually reduced to zero, the k -plane poles (2.5) –which correspond to the roots of the dispersion function (2.6) $D(k, \omega) = 0$ – move towards the real k axis. In

order to retain a causal solution, the k -contour Γ_k , initially positioned along the real k axis, must be deformed to avoid any pole crossings. If ω_i can be brought to zero without any such pole crossing, then the system is at worst convectively unstable. The spatial location of a response associated with a pole is determined by the half-plane from which the pole originated. Poles originating in the upper half plane ($\text{Im}(k) > 0$), are found downstream from the drive point, and poles originating in the lower half plane ($\text{Im}(k) < 0$) exist upstream from the drive point.

‘Neutral’ modes are those that come to rest on the real k axis for $\omega_i = 0$. These are the conventional ‘free’ waves of structural acoustics that propagate unattenuated to the far field. Poles that do not reach the real k axis for $\omega_i = 0$ are conventional ‘evanescent’ waves that are exponentially attenuated away from the drive point. Finally, ‘convectively unstable’ modes are those that cross the real k axis and come to rest for $\omega_i = 0$ outside the half-plane from which they originated. These modes grow exponentially away from the drive point, upstream or downstream from the driver as determined by the half plane from which they originated.

If two k -plane poles originating from different half planes collide for $\omega_i > 0$, the descent of the temporal contour towards $\text{Im}(\omega) = 0$ must be halted at the given finite, positive value of ω_i , leading to unstable temporal growth everywhere on the plate. The response is said to be ‘absolutely unstable’ and Crighton & Oswell (1991) show that this happens for flow speeds exceeding a critical value, $U > U_c$. Unless otherwise noted, we will assume in this thesis that U does not exceed this absolute instability threshold and that we can therefore plot spatial dispersion plots of complex k vs. real ω as shown in figure 2.2.

2.1.1 General Solution

For $U < U_c$ and $T = \lambda = 0$, Crighton & Oswell (1991) show that the causal response can have three distinct frequency regimes (figure 2.2):

1) $\omega > \omega_p$: Absolute stability. Two conventional propagating waves (k_1^+ and k_1^-), and two conventional evanescent waves, (k_2^+ and k_2^-), as shown in figure 2.3d. In this thesis, the superfixes $+$ and $-$ refer to waves found downstream and upstream,

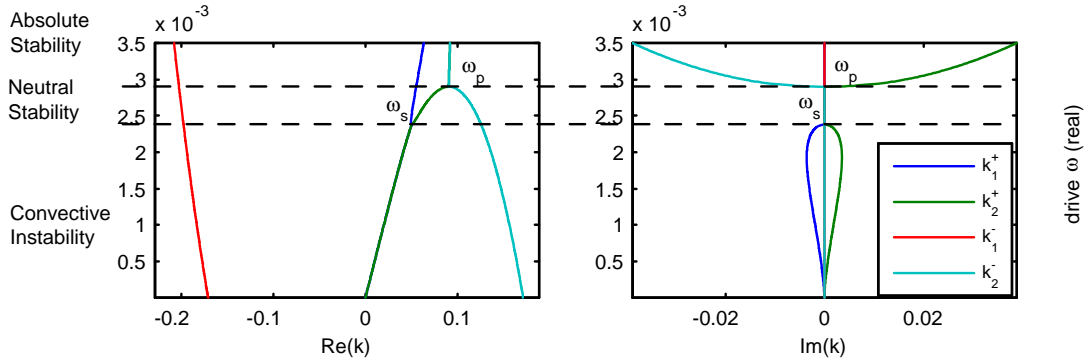


Figure 2.2: Dispersion diagram for prescribed (real) frequency for the following non-dimensional fluid/plate parameters: $U = 0.05$, $\alpha = 2$ & $T = \lambda = 0$.

respectively, of a point scatterer or drive point.

2) $\omega_s < \omega < \omega_p$: Neutral stability. Four propagating waves, two of which are positive energy waves (PEWs: k_1^+ and k_1^-) and two are negative energy waves (NEWs: k_2^+ and k_2^-), as shown in figure 2.3c. Wave energy, which will be defined more formally in the next chapter, is the amount of work done to build up a wave from rest. Positive energy waves (PEWs) have positive ‘activation energy’ and behave conventionally. Negative energy waves (NEWs) have negative ‘activation energy’ and are destabilized by damping. NEWs are responsible for the phenomenon of ‘over-scattering.’

3) $\omega < \omega_s$: Convective instability. One exponentially increasing wave (k_1^+) and one exponentially decaying wave (k_2^+), and two propagating waves, one of which is a PEW (k_1^-) and one, a NEW (k_2^-), as shown in figure 2.3b (where $\omega_a = 0$ for $\lambda = 0$). The two downstream travelling wavenumbers are complex conjugate pairs with an associated phase speed of U to leading order in ω .

2.1.2 The Effect of Finite λ and T

Positive spring foundation and tension have a generally stabilizing effect. Increasing λ and T reduces, or in some instances entirely eliminates, the regimes over which the various types of instabilities occur. Quantitative details of the influence of non-zero λ and T will be provided in later sections of this chapter and in chapter 3. Therefore, only a brief qualitative sketch will be provided here. Peake (1997) has investigated

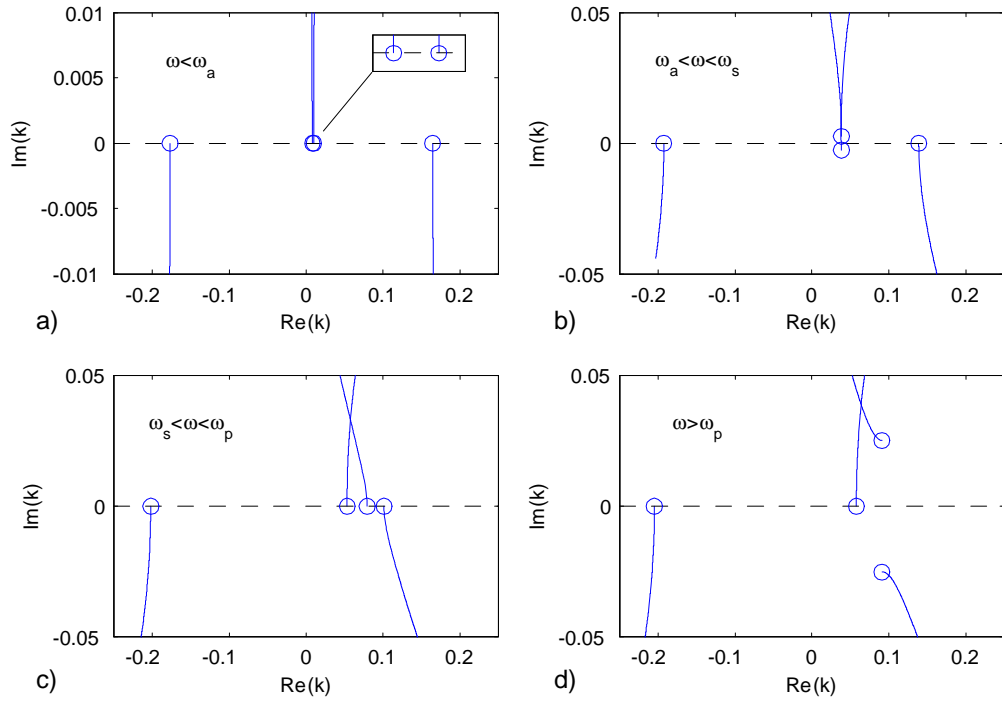


Figure 2.3: k -plane poles and their trajectories for four representative frequency regimes, as indicated on the figures. For $U = 0.05$, $\alpha = 2$, $\lambda = 2U^5$ & $T = 0$.

the effect of non-zero λ whereas de Langre (2002) and subsequently Peake (2004) have examined the effect of non-zero T .

1) Increasing λ or T increases the boundary for absolute instability. De Langre (2002) has shown that in the limit of large T , one recovers the result for a membrane in mean flow given in Kelbert & Sazanov (1996).

2) Increasing λ or T shrinks and eventually eliminates the ω - k range over which convective instability occurs. However, there are qualitative differences between the two. For λ small, two distinct looping branches of neutral waves appear as shown in figure 2.4a. The turning point (ω_s, k_s) moves lower and a third turning point (ω_a, k_a) grows out of the origin, limiting the frequency range of convective instability to $\omega_a < \omega < \omega_s$. The k -plane pole for $\omega_a \neq 0$ are plotted in figure 2.3a. As λ is increased, ω_a and ω_s approach each other (roughly) along the $\omega = Uk$ line and eventually fuse with each other thereby eliminating the convective regime. In contrast, increasing T only generates the loopy branch associated with (ω_s, k_s) as shown in figure 2.4b. As T is increased, ω_s approaches and eventually fuses with the origin again (roughly) along the $\omega = Uk$ line (figure 2.4c).

3) For a sufficiently large value of λ , the pinch point (ω_p, k_p) crosses the k -axis, eliminating the second branch of the dispersion equation from the first quadrant together with the existence of NEWs. Increasing T likewise shrinks the range over which NEWs may exist but there is no finite value of T that eliminates them entirely. Details are given in chapter 3.

2.2 Plate Response

The Greens function of the fluid loaded plate is

$$G_{\pm}(x - x_s) = \pm \frac{ie^{ik_1^{\pm}(x-x_s)}}{D_k(k_1^{\pm})} \pm \frac{ie^{ik_2^{\pm}(x-x_s)}}{D_k(k_2^{\pm})} + \frac{1}{2\pi} \int_0^{+\infty} \frac{e^{\mp v(x-x_s)}}{D(\pm iv)} dv + \frac{1}{2\pi} \int_0^{+\infty} \frac{e^{\mp v(x-x_s)}}{D(\mp iv)} dv, \quad (2.8)$$

where

$$D_k(k) \equiv \partial D(k) / \partial k = 4k^3 + 2Tk + \frac{\alpha(\omega^2 - U^2k^2)}{k\gamma(k)}, \quad (2.9)$$

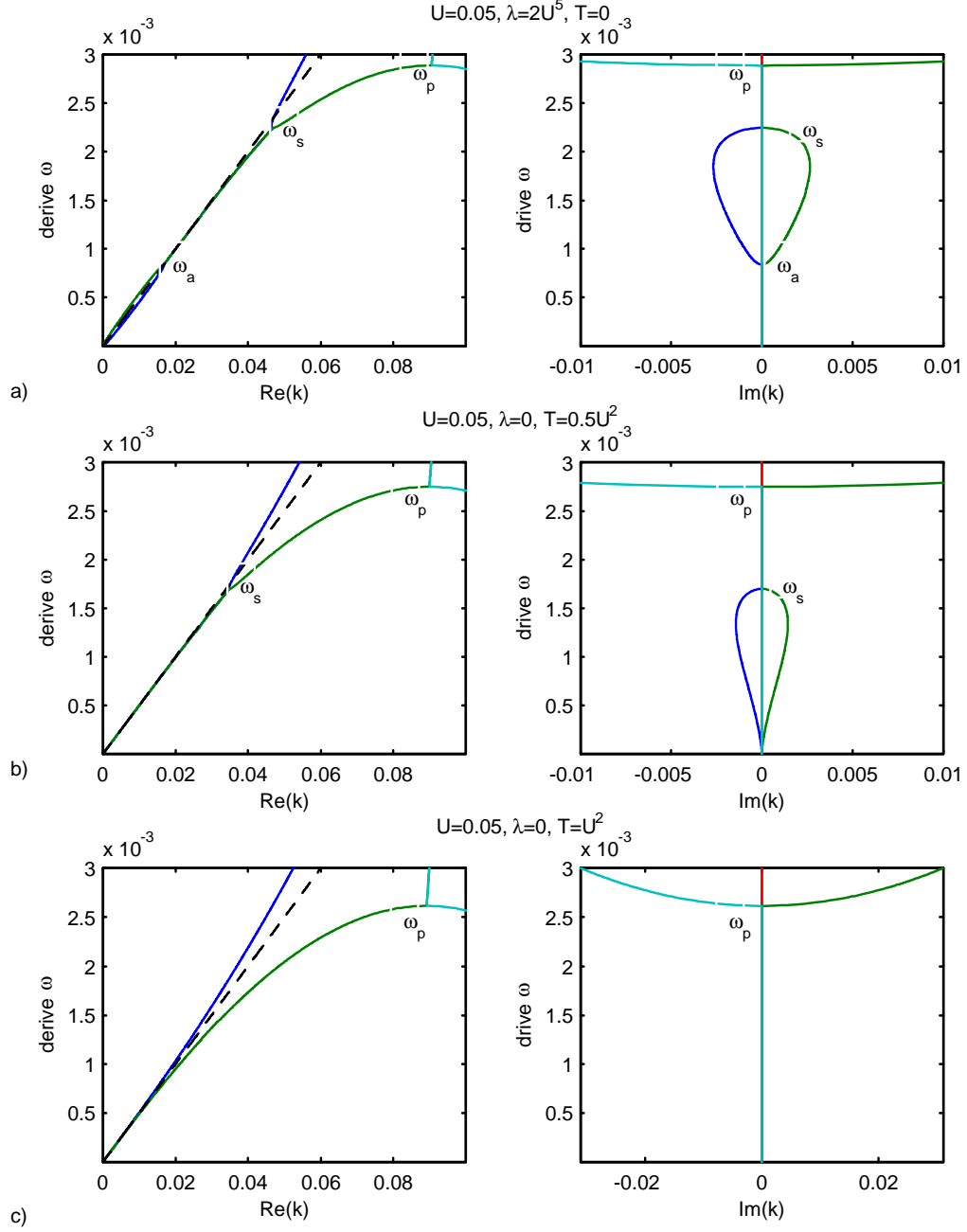


Figure 2.4: Detail of dispersion diagram showing the influence of non-zero λ and T on the roots of an infinite plate for $U = 0.05$, $\alpha = 2$. a) $\lambda = 2U^5$ & $T = 0$, b) $\lambda = 0$ & $T = \frac{1}{2}U^2$, c) $\lambda = 0$ & $T = U^2$.

and $D(k)$ is the dispersion function given in (2.6). The \pm signs correspond to response to the right or left, respectively, of the drive. The Green's function is composed of far field propagation terms generated by the system poles which are zeros of the dispersion equation and of near-field terms generated by the branch line integrals which decay algebraically away from the drive.

The plate response is simply the Green's function multiplied by the load amplitude

$$\eta(x \gtrless x_s) = F_0 G_{\pm}(x - x_s). \quad (2.10)$$

2.2.1 Far Field Response

In the far field, the causal solution consists of two upstream and two downstream waves and can be written in terms of the 'far field' Green's function,

$$\eta(|x| \gg |x_s|) = F_0 G_{\pm}(\infty),$$

where,

$$G_{\pm\infty}(x) \equiv \sum_{j=1}^2 \frac{\pm i e^{ik_n^{\pm}(x-x_s)}}{D_k(k_j^{\pm})} \quad (2.11)$$

is defined as the Green's function composed of only the pole contributions to (2.8).

The far field amplitude for the individual waves $\pm j$ is given by

$$A_{\pm j} = \frac{\pm i F_0}{D_k(k_j^{\pm})}, \quad (2.12)$$

where the \pm signs correspond to the propagation direction of the ' j ' wave.

2.2.2 Drive Point Admittance & Power into Plate

The drive point admittance is the time rate of change of the response at the drive location $x = x_s$ per unit force. In terms of the Green's function it is

$$Y_{dp} = -i\omega G(0). \quad (2.13)$$

The real part of Y_{dp} represents power per unit force injected into the plate by the drive.

Given that the Greens function is continuous at the source, either $G_+(0)$ or $G_-(0)$ can be used to evaluate Y_{dp} . However it is advantageous to use the averaged quantity $-i\omega(G_+(0) + G_-(0))/2$ because the real part of the drive point admittance can then be expressed in terms of the pole contributions alone, the contributions from the branch line integrals averaging out to zero.

To see this, expand and combine the terms under the integral in (2.8) (evaluated at $x - x_s = 0$) to find the following expression for the branch line integral (BLI)

$$BLI^\pm(0) = \frac{1}{2\pi} \int_0^{+\infty} 2v [v^4 - Tv^2 + \lambda] \frac{\mp i P_r - P_i}{P_r^2 + P_i^2} dv, \quad (2.14)$$

where $P_r = v^2 [v^4 - Tv^2 + \lambda]^2 + \alpha^2 [\omega^4 - 2\omega^2 U^2 v^2 + 2U^4 v^4]$ and $P_i = \alpha^2 [4\omega U^3 v^3 - 4\omega^3 U v]$ are real quantities that do not contain any \pm factors. Taking the average $-i\omega(BLI^+(0) + BLI^-(0))/2$ results in the cancellation of the term involving the \pm factor and yields

$$\frac{i\omega}{\pi} \int_0^{+\infty} v [v^4 - Tv^2 + \lambda] \frac{P_i}{(P_r^2 + P_i^2)} dv$$

which is pure imaginary.

The time averaged power injected into the plate at the drive is therefore given by $1/2 \operatorname{Re} \{-i\omega\eta(0) \bar{F}_0\}$:

$$\Pi = \frac{1}{4} \operatorname{Re} \left\{ \sum_{n=1}^4 \frac{\pm \omega}{D_k(k_n^\pm)} \right\} |F_0|^2, \quad (2.15)$$

where n represents the four waves in sequential order with the right going waves as $n = 1, 2$ accompanied by the upper (+) sign followed by the two left going waves as $n = 3, 4$ accompanied by the lower (-) sign.

2.3 Pinch Parameters and Absolute Instability

Crighton & Oswell (1991) show that the pinch point (k_p, ω_p) , which corresponds to the merging between the two $\operatorname{Re}\{k\} > 0$ roots k_1^+ and k_2^- that originate in opposite half planes, is a saddle point of the dispersion equation (2.6), i.e.

$$\left. \frac{\partial P_+(k)}{\partial k} \right|_{k=k_p} = 0.$$

The pinch can occur for real ω_p or for complex ω_p . If $\text{Im}\{\omega_p\} > 0$, then Absolute Instability exists. There is a critical flow velocity U_c below which $\text{Im}\{\omega_p\} = 0$, and given that one of the pinching roots, k_1^+ , always occurs with its complex conjugate pair k_2^+ , it follows that the transition between $U < U_c$ and $U > U_c$ must correspond to a triple root of the dispersion function $P_+(k)$

$$P_+(k) = k^5 + Tk^3 - \alpha U^2 k^2 - (\omega^2 - 2\alpha U\omega + \lambda)k - \alpha\omega^2 = 0, \quad (2.16a)$$

$$P'_+(k) = 5k^4 + 3Tk^2 - 2\alpha U^2 k - (\omega^2 - 2\alpha U\omega + \lambda) = 0, \quad (2.16b)$$

$$P''_+(k) = 20k^3 + 6Tk - 2\alpha U^2 = 0. \quad (2.16c)$$

Our aim is to solve this system of equations for the critical velocity $U_c(T, \lambda)$.

First, we combine (2.16a) with (2.16b) and eliminate the ωU terms to obtain an equation for the pinch point as a function of U that does not include the parameter λ

$$4k_p^5 + 2Tk_p^3 - \alpha U^2 k_p^2 + \alpha\omega_p^2 = 0. \quad (2.17)$$

Next, we solve (2.16c) for the critical velocity

$$\alpha U_c^2 = 10k_c^3 + 3Tk_c, \quad (2.18)$$

and combine this with (2.17) to obtain an equation relating the frequency and wavenumber at the critical point

$$6k_c^5 + Tk_c^3 - \alpha\omega_c^2 = 0. \quad (2.19)$$

2.3.1 For $T = 0$

For the case where the pre-tension is zero, it is possible to obtain an exact expression for the critical velocity as a function of λ . Simply set $T = 0$ in (2.18) and solve for the critical wavenumber (choosing the real, positive root) as a function of U_c

$$k_c = \left(\frac{\alpha U_c^2}{10} \right)^{\frac{1}{3}}. \quad (2.20)$$

Use this, together with (2.19), to eliminate k and ω from (2.17) and obtain an equation for U_c as a function of the plate parameters alone

$$\beta U_c^{8/3} \left[U_c^{2/3} - U_0^{2/3} \right] - \lambda = 0, \quad (2.21)$$

where

$$\beta \equiv \frac{3\alpha^{2/3}}{5^{5/3}2^{2/3}} \approx 0.129\alpha^{2/3}, \quad (2.22)$$

and

$$U_0 = \alpha \frac{2^{1/2}5^{5/4}}{3^{3/4}} \left[2 - \frac{15^{1/2}}{2} \right]^{3/2} \approx 0.074\alpha \quad (2.23)$$

is the critical velocity for $T = \lambda = 0$ derived previously in Crighton & Oswell (1991) for the case of one-sided loading, $\alpha = 1$. It is clear from the form of the equation that a non-zero, positive spring constant increases the threshold of absolute instability, U_c , and therefore has a stabilizing effect.

By making the change of variable $u = U^{2/3}$, (2.21) is transformed into a 5th order polynomial equation in the velocity variable

$$\beta u_c^5 - \beta u_c^4 u_0 - \lambda = 0. \quad (2.24)$$

Here, $u_0 = U_0^{2/3}$. No known closed form solutions exist for this type of quintic. However, a numerical solution is easy to obtain using standard polynomial root finding routines, and the results are plotted in figure (2.5b). In addition, approximate solutions for u_c can be obtained in the asymptotic limit of small and large λ .

For small λ , the first order term is $u_c - u_0 \approx \lambda / (\beta u_0^4)$. We therefore seek an expansion of the form $u_c \approx u_0 + \lambda u_1 + \lambda^2 u_2 + \dots$ and find to second order in λ

$$\begin{aligned} u_c &\approx u_0 + \frac{\lambda}{\beta u_0^4} + \frac{4\lambda^2}{\beta^2 u_0^9} + O(\lambda^3), \\ \Rightarrow U_c &\approx \left[u_0 + \frac{\lambda}{\beta U_0^{10/3}} + \frac{4\lambda^2}{\beta^2 U_0^6} + \dots \right]^{\frac{3}{2}}, \quad \lambda \ll \beta U_0^{10/3}. \end{aligned} \quad (2.25)$$

For large λ , the leading order term is $u_c \approx (\lambda/\beta)^{1/5}$. We seek solutions of the form $u_c \approx u_1 \lambda^{1/5} + u_2 + u_3 \lambda^{-1/5} + \dots$ and obtain to second order

$$\begin{aligned} u_c &\approx \frac{\lambda^{1/5}}{\beta^{1/5}} + \frac{u_0}{5} + O(\lambda^{-1/5}) \\ \Rightarrow U_c &\approx \left[\frac{\lambda^{1/5}}{\beta^{1/5}} + \frac{U_0^{2/3}}{5} + \dots \right]^{\frac{3}{2}}, \quad \lambda \gg \frac{\beta U_0^{10/3}}{5^5}. \end{aligned} \quad (2.26)$$

These asymptotic solutions are overlaid on the exact numerical result in figure (2.5b).

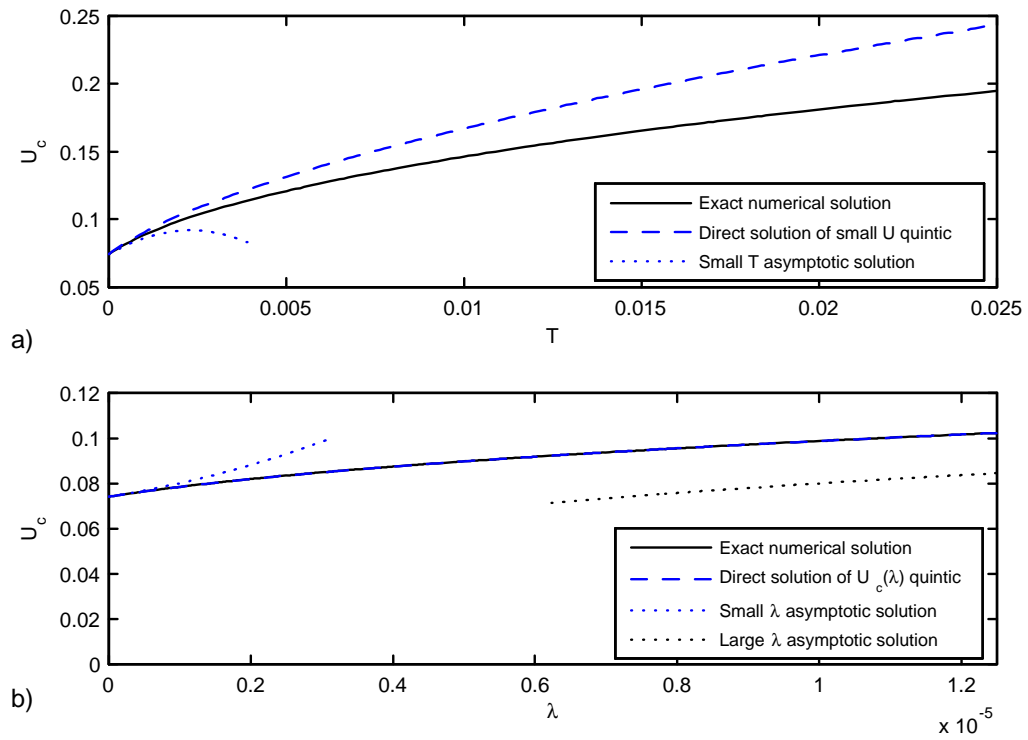


Figure 2.5: Critical velocity for Absolute Instability as a function of plate parameters for $\alpha = 1$. a) U_c as a function of non-dimensional plate tension T , b) U_c as a function of non-dimensional plate spring foundation constant λ .

2.3.2 For $T \neq 0$

For non-zero tension, it has not proved possible to obtain the equivalent of (2.21), an exact equation for U_c as a function of the plate parameters alone. The stumbling block is our inability to obtain a compact enough expression for the critical wavenumber $k_c(U_c, T)$ from the cubic equation (2.18). We therefore attempt an approximate solution for small U .

We expand k_c in powers of $U^{2/3}$ and choose the distinguished scaling $T \sim U^2$ to obtain

$$k_c \approx \left(\frac{\alpha}{10}\right)^{1/3} U_c^{2/3} + \frac{1}{10^{2/3} \alpha^{1/3}} \frac{T}{U_c^{2/3}} + O\left(U_c^{10/3}\right). \quad (2.27)$$

We substitute (2.27) into (2.19) and retain the leading order terms in T to obtain

$$\omega_c^2 \approx \frac{3\alpha^{2/3}}{10^{2/3} 5} U_c^{10/3} - \frac{1}{5} T U_c^2 + O\left(U_c^{14/3}\right), \quad (2.28a)$$

$$\omega_c \approx \frac{3^{1/2} \alpha^{1/3}}{5^{1/2} 10^{1/3}} U_c^{5/3} - \frac{10^{1/3}}{5^{1/2} 3^{1/2} 2 \alpha^{1/3}} T U_c^{1/3} + O\left(U_c^{9/3}\right). \quad (2.28b)$$

Substituting these first order accurate expressions for k_c , ω_c^2 and ω_c into $P'_+(k)$ (i.e., (2.27) and (2.28) into (2.16b)) we obtain an order $O(U_c^4)$ accurate equation for $U_c(T, \lambda)$

$$\beta U_c^{8/3} \left[U_c^{2/3} - U_0^{2/3} \right] - T \gamma U_c^{4/3} - \frac{T}{5} U_c^2 - \lambda \approx 0, \quad (2.29)$$

where

$$\gamma \equiv \alpha^{2/3} \frac{3^{3/2} 5^{1/2} - 10}{3^{1/2} 5^{1/2} 10^{2/3}} \approx 0.0901 \alpha^{2/3}, \quad (2.30)$$

and β is as given in (2.22). We note that the approximation in (2.29) only involves the tension terms. This equation is exact as far as the spring support is concerned and in fact reduces to (2.21) for $T = 0$. It is also clear from the form of (2.29) (including the sign of the T terms) that positive plate pre-tension increases the critical velocity U_c for the onset of absolute instability and therefore has a stabilizing effect.

By making the change of variable $u = U^{2/3}$ as before, (2.29) reduces to a quintic in $u(T, \lambda)$. For the special case of $\lambda = 0$, (2.29) reduces to a cubic in $u(T)$

$$\beta u_c^3 - \beta u_c^2 u_0 - \frac{T}{5} u_c - T \gamma \approx 0. \quad (2.31)$$

This small U solution for $U_c(T)$ is compared with the exact solution obtained by direct numerical solution of equations (2.16) in figure (2.5a).

Although closed form solutions for the cubic in (2.31) are available, the resulting expressions are too unwieldy to be of any practical use. Instead, a small T solution for (2.31) is obtained. We expand u_c in full powers of T and find, to first order,

$$\begin{aligned} u_c &\approx u_0 + \left(\frac{\gamma}{\beta u_0^2} + \frac{1}{5u_0} \right) T + O(T^2), \\ \Rightarrow U_c &\approx \left[U_0^{2/3} + \left(\frac{\gamma}{\beta U_0^{4/3}} + \frac{1}{5U_0^{2/3}} \right) T + \dots \right]^{\frac{3}{2}}, \quad T \ll 1. \end{aligned} \quad (2.32)$$

Figure (2.5a) compares this asymptotic solution with the direct numerical solution of the approximate cubic of (2.31) as well as with the exact solution of equations (2.16).

2.4 Convective Instability

With k assumed real and positive, we solve $P_+(k) = 0$ for the ω roots and obtain the following two branches of the ‘temporal’ dispersion equation

$$\omega(k) = \frac{\alpha U k \pm [(\alpha + k)(k^5 + T k^3 + \lambda k) - \alpha U^2 k^3]^{\frac{1}{2}}}{\alpha + k}. \quad (2.33)$$

The branch points are given by the zeros of the radical in (2.33) and consist of the real, positive k roots of

$$k_b^5 + \alpha k_b^4 + T k_b^3 + \alpha(T - U^2)k_b^2 + \lambda k_b + \lambda \alpha = 0. \quad (2.34)$$

We note that, in addition to the k_b roots given above, the origin is also a branch point for all values of U , T , and λ .

Peake (1997) has examined the effect of a spring foundation (or equivalently, adding a small amount of transverse curvature to a flat plate) in the absence of plate pre-tension ($T = 0$ & $\lambda \neq 0$) and shown that a positive spring constant limits/reduces the regime for convective instability and therefore has a stabilizing effect. He shows that for values of the spring constant smaller than

$$\lambda_1 = \frac{U^4}{4}, \quad (2.35)$$

there are two branch points k_a and k_b which bound the ω - k range over which convective instability can occur. Increasing λ causes k_a and k_b to approach each other until their

merger at precisely $\lambda = \lambda_1$ eliminates the convective range. Equation (2.35) was obtained from equation (4.5) in Peake (1997) after making the transformation

$$\lambda \rightarrow \frac{12(1 - \nu^2)}{\rho^2 a^2}, \quad (2.36)$$

where a is the plate transverse radius (assumed large), ρ is the density ratio between the plate and fluid and ν is Poisson's ratio.

In this section, we focus on the case $\lambda = 0$ and $T \neq 0$. Without a spring foundation, the branch point equation (2.34) reduces to $k_b^3 + \alpha k_b^2 + T k_b + \alpha(T - U^2) = 0$ and can be factored as

$$(k_b + \alpha)(k_b^2 + T) - \alpha U^2 = 0. \quad (2.37)$$

For small U , we follow Crighton & Oswell (1991) and use the scaling $k \sim U$ for $k \leq k_b$ to approximate the term in the first parentheses as $k_b + \alpha \approx \alpha$ (this is equivalent to ignoring the plate inertia w.r.t. to the fluid inertia) and obtain an approximate expression for the branch point as a function of plate tension

$$k_b \approx (U^2 - T)^{\frac{1}{2}}, \quad \omega_b \approx U(U^2 - T)^{\frac{1}{2}}, \quad U \ll 1. \quad (2.38)$$

We note that, unlike for the case of non-zero spring foundation, there is only one non-zero branch point for $T \neq 0$. Equation (2.38) does show, however, that plate tension has a comparable stabilizing effect; increasing T reduces k_b and shrinks the range $0 < k < k_b$ over which convective instability may exist. It also follows from (2.38) that values of plate tension greater than $T > T_1$, where $T_1 \approx U^2$ to leading order, lead to the merger of k_b with the branch point at the origin and hence to the disappearance of the convectively unstable range.

More rigorously, we expand k_b in powers of U and choose the distinguished scaling $T \sim U^2$ to obtain the asymptotic expansion

$$k_b \approx (U^2 - T)^{\frac{1}{2}} - \frac{U^2}{2\alpha} + O(U^3), \quad U \ll 1. \quad (2.39)$$

We set $k_b = 0$ and solve for T to obtain a second order accurate expression for the cut-off tension

$$T_1 \approx U^2 - \frac{U^4}{4\alpha^2}, \quad U \ll 1. \quad (2.40)$$

Now that we have an expression for k_b , we can write the radical in (2.33) in the vicinity of the branch point (with $\lambda = 0$) as

$$[(k + \alpha)(k^2 + T) - \alpha U^2]^{1/2} \approx \alpha^{1/2} k^{3/2} [(k + k_b)(k - k_b)]^{1/2}.$$

The only approximation involved in this step and in what follows is $k + \alpha \approx \alpha$. The two branches of the dispersion equation become $\omega(k) \approx Uk \pm k^{3/2} \alpha^{-1/2} [(k + k_b)(k - k_b)]^{1/2}$, which, in terms of the separation variable from the branch point $\delta k \equiv k - k_b$ can be rewritten as

$$\omega(k) \approx Uk \pm \frac{2^{1/2} k^2}{\alpha^{1/2}} \left(1 - \frac{\delta k}{2k}\right)^{1/2} (\delta k)^{1/2}, \quad k \ll \alpha.$$

In the immediate vicinity of the branch point, this simplifies further to

$$\omega(k) \approx Uk \pm \frac{2^{1/2} k^2}{\alpha^{1/2}} (\delta k)^{1/2}, \quad k \ll \alpha, \quad \delta k/k \ll 1, \quad (2.41)$$

and reveals that the branches of the dispersion equation are split evenly about Uk by $\sim \pm \sqrt{\delta k}$. For points lying above the branch point (i.e., $k > k_b$), this split is between the pair of purely real branches that define k_1^+ and k_1^- . For points within the convectively unstable range (i.e., $k < k_b$), this split manifests itself in the imaginary parts of k_1^+ and k_1^- . This can be observed in figures 2.4b and 2.4c.

Finally, if we combine the expression for λ_1 in (2.35) with the leading order term for T_1 in (2.40) we can write down the condition, valid for small U , for the elimination of the convective range

$$T + 2\sqrt{\lambda} > U^2. \quad (2.42)$$

This condition is identical to equation (3.2) of Peake (2004).

Chapter 3

Energy Balance

In this chapter, we derive the energy balance equation for the line driven plate. The derivation parallels that given by Crighton and Oswell (1991) and is extended to include the augmented plate equation and two sided flow.

3.1 Energy Equations for Plate and Fluid

Multiplying both sides of the plate equation (2.3a) by the plate velocity $\partial\eta/\partial t$ and integrating over an interval X_1 to X_2 containing the line drive gives an energy equation for the plate. The individual terms on the left hand side can be manipulated (by repeated use of the chain rule) to yield

$$\begin{aligned}\int_{X_1}^{X_2} \frac{\partial^4 \eta}{\partial x^2} \frac{\partial \eta}{\partial t} dx &= \left. \frac{\partial^3 \eta}{\partial x^3} \frac{\partial \eta}{\partial t} \right|_{X_1}^{X_2} - \left. \frac{\partial^2 \eta}{\partial x^2} \frac{\partial^2 \eta}{\partial x \partial t} \right|_{X_1}^{X_2} + \frac{1}{2} \frac{\partial}{\partial t} \int_{X_1}^{X_2} \left(\frac{\partial^2 \eta}{\partial x^2} \right)^2 dx, \\ - \int_{X_1}^{X_2} T \frac{\partial^2 \eta}{\partial x^2} \frac{\partial \eta}{\partial t} dx &= - \left. T \frac{\partial \eta}{\partial x} \frac{\partial \eta}{\partial t} \right|_{X_1}^{X_2} + \frac{1}{2} \frac{\partial}{\partial t} \int_{X_1}^{X_2} T \left(\frac{\partial \eta}{\partial x} \right)^2 dx, \\ + \int_{X_1}^{X_2} \lambda \eta \frac{\partial \eta}{\partial t} dx &= + \frac{1}{2} \frac{\partial}{\partial t} \int_{X_1}^{X_2} \lambda \eta^2 dx, \\ + \int_{X_1}^{X_2} \frac{\partial^2 \eta}{\partial t^2} \frac{\partial \eta}{\partial t} dx &= + \frac{1}{2} \frac{\partial}{\partial t} \int_{X_1}^{X_2} \left(\frac{\partial \eta}{\partial t} \right)^2 dx.\end{aligned}$$

Collecting these terms back into the equation, the plate energy equation can be expressed as

$$\frac{d}{dt} [T_p + V_p] + J_p (X_2) - J_p (X_1) = \frac{1}{2} |F_0|^2 \operatorname{Re} \{Y_{dp}\} + \Pi_{pv}, \quad (3.1)$$

where

$$T_p = \frac{1}{2} \int_{X_1}^{X_2} \left(\frac{\partial \eta}{\partial t} \right)^2 dx \quad (3.2)$$

is the structural kinetic energy,

$$V_p = \frac{1}{2} \int_{X_1}^{X_2} \left\{ \left(\frac{\partial^2 \eta}{\partial x^2} \right)^2 + T \left(\frac{\partial \eta}{\partial t} \right)^2 + \lambda \eta^2 \right\} dx \quad (3.3)$$

is the structural potential energy,

$$J_p = \eta_{xxx} \eta_t - \eta_{xx} \eta_{xt} - T \eta_x \eta_t \quad (3.4)$$

is the structural energy flux,

$$\frac{1}{2} |F|^2 \operatorname{Re} \{Y_{dp}\} = \int_{X_1}^{X_2} F \delta(x) \frac{\partial \eta}{\partial t} dx \quad (3.5)$$

is the power injected into the plate at the drive expressed in terms of the drive point admittance Y_{dp} (2.13) and

$$\Pi_{pv} = - \int_{X_1}^{X_2} \alpha p \frac{\partial \eta}{\partial t} dx \quad (3.6)$$

is the rate of working of the fluid on the plate.

The gradient of the momentum equation (2.3c) multiplied by the fluid fluctuating velocity $\nabla \varphi$ can be manipulated in the following ‘conservation’ form

$$\frac{\partial}{\partial t} \left[\frac{1}{2} (\nabla \varphi)^2 \right] + \nabla \cdot \left[\left(p + U \frac{\partial \varphi}{\partial x} \right) \nabla \varphi \right] = 0, \quad (3.7)$$

where the first term represents the rate of change of fluid kinetic energy and the second is the divergence of the fluid flux. Integrating (3.7) over a control volume $V = V^+ + V^-$ spanning the plate segment as shown in figure 3.1 and applying the divergence theorem, we obtain

$$\frac{d}{dt} \int_V \frac{1}{2} (\nabla \varphi)^2 dV = - \int_S \left(p + U \frac{\partial \varphi}{\partial x} \right) \nabla \varphi \cdot \hat{n} dS, \quad (3.8)$$

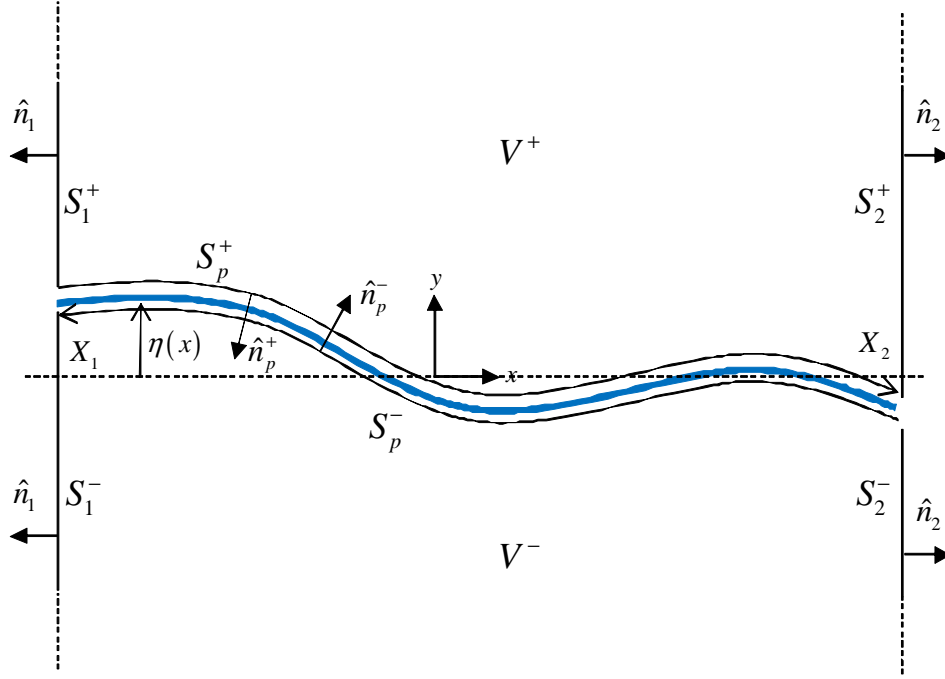


Figure 3.1: Control volume and integration surfaces for evaluation of energy balance equation.

where \hat{n} is the unit outward normal to the surface $S = S_1^+ + S_1^- + S_2^+ + S_2^-$ bounding the control volume. Equation (3.8) represents a balance between the time rate of change of kinetic energy in the control volume and the fluid fluxes into the volume.

The integral along the upstream vertical control surfaces S_1^\pm at X_1 , where the suffixes $+/-$ connote ‘above’/‘below’ plate, is (taking $\hat{x} \cdot \hat{n}_1 = -1$)

$$\begin{aligned}
 - \int_{S_1^+ + S_1^-} \left(p + U \frac{\partial \varphi}{\partial x} \right) \frac{\partial \varphi}{\partial x} dS = \\
 - \left\{ \int_{\eta(X_1)}^{+\infty} \left(p \frac{\partial \varphi}{\partial x} + U \left(\frac{\partial \varphi}{\partial x} \right)^2 \right) \Big|_{X_1} dy + \int_{\eta(X_1)}^{-\infty} \left(p \frac{\partial \varphi}{\partial x} + U \left(\frac{\partial \varphi}{\partial x} \right)^2 \right) \Big|_{X_1} (-dy) \right\} \\
 \approx -\alpha \int_0^{+\infty} \left(p \frac{\partial \varphi}{\partial x} + U \left(\frac{\partial \varphi}{\partial x} \right)^2 \right) \Big|_{X_1} dy
 \end{aligned}$$

for η small. Similarly, the vertical surface integral at X_2 yields (with $\hat{x} \cdot \hat{n}_2 = +1$)

$$\int_{S_2^+ + S_2^-} \left(p + U \frac{\partial \varphi}{\partial x} \right) \frac{\partial \varphi}{\partial x} dS \approx \alpha \int_0^{+\infty} \left(p \frac{\partial \varphi}{\partial x} + U \left(\frac{\partial \varphi}{\partial x} \right)^2 \right) \Big|_{X_2} dy. \quad (3.9)$$

If, in addition to the anti-symmetry properties of the pressure and tangential velocity, we invoke (through the continuity condition) the symmetry property of the normal velocity given by

$$\frac{\partial \varphi}{\partial y} \Big|_{y=\eta+\epsilon} = \frac{\partial \eta}{\partial t} + U \frac{\partial \eta}{\partial x} = \frac{\partial \varphi}{\partial y} \Big|_{y=\eta-\epsilon}, \quad \epsilon \rightarrow 0,$$

the integrals along the top and bottom surface of the plate (with $\hat{y} \cdot \hat{n}_p^+ = -1$ and $\hat{y} \cdot \hat{n}_p^- = +1$ respectively) can be expressed in terms of the integral along the top surface only to yield

$$\begin{aligned} \int_{S_p^+} \left(p + U \frac{\partial \varphi}{\partial x} \right) \left(-\frac{\partial \varphi}{\partial y} \right) \Big|_{y=\eta+\epsilon} dS + \int_{S_p^-} \left(p + U \frac{\partial \varphi}{\partial x} \right) \left(+\frac{\partial \varphi}{\partial y} \right) \Big|_{y=\eta-\epsilon} dS \\ \approx -\alpha \int_{X_1}^{X_2} \left(p + U \frac{\partial \varphi}{\partial x} \right) \frac{\partial \varphi}{\partial y} \Big|_{y=+0} dx, \quad \eta \ll 1. \end{aligned}$$

The quantities p and φ and their derivatives decay exponentially with y , so there is no contribution from the integrals along the surfaces at infinity. Finally, summing all the surface integral contributions, the right hand side of (3.8) becomes

$$\begin{aligned} \int_S \left(p + U \frac{\partial \varphi}{\partial x} \right) \nabla \varphi \cdot \hat{n} dS \approx -\alpha \int_0^{+\infty} \left(p \frac{\partial \varphi}{\partial x} + U \left(\frac{\partial \varphi}{\partial x} \right)^2 \right) \Big|_{X_1} dy \\ + \alpha \int_0^{+\infty} \left(p \frac{\partial \varphi}{\partial x} + U \left(\frac{\partial \varphi}{\partial x} \right)^2 \right) \Big|_{X_2} dy - \alpha \int_{X_1}^{X_2} \left(p + U \frac{\partial \varphi}{\partial x} \right) \frac{\partial \varphi}{\partial y} \Big|_{y=+0} dx. \end{aligned} \quad (3.10)$$

We turn next to evaluating the volume integral of the fluid kinetic energy in (3.8). If we take φ to be the full potential and subtract off any terms not contributing to the fluctuating kinetic energy (i.e., terms involving the mean flow alone that will cause the fluid energy integral to diverge), we obtain

$$\begin{aligned} T_f &= \frac{1}{2} \int_{V^+ + V^-} \left[(U + \varphi_x)^2 + \varphi_y^2 - U^2 \right] dV \\ &= \frac{1}{2} \int_{V^+ + V^-} \left[\varphi_x^2 + \varphi_y^2 + 2U\varphi_x \right] dV. \end{aligned}$$

First, we rewrite the integral involving the volume V^+ above the physical plate at $y = \eta$ by taking $y = +0$ as the lower limit, being careful to subtract off the surplus volume spanning $0 < y < \eta$ not contained in V^+ . This gives

$$\begin{aligned} T_f(y > \eta) &= \frac{1}{2} \int_{\eta(x)}^{+\infty} dy \int_{X_1}^{X_2} [\varphi_x^2 + \varphi_y^2 + 2U\varphi_x] dx \\ &\approx \frac{1}{2} \int_0^{+\infty} dy \int_{X_1}^{X_2} [\varphi_x^2 + \varphi_y^2 + 2U\varphi_x] dx - \int_0^{\eta(x)} dy \int_{X_1}^{X_2} U\varphi_x dx, \end{aligned} \quad (3.11)$$

where the approximation in the final step consists of retaining only quadratic terms in the fluctuating variables, consistent with our linear approximation. Expanding φ_x in a Taylor series about $y = +0$, we evaluate the $\int_0^{\eta(x)} dy$ integral in (3.11) to find

$$\int_0^{\eta} U\varphi_x(y) dy \approx U\eta\varphi_x(+0) + \frac{1}{2}\eta^2 \frac{\partial \varphi_x}{\partial y} (+0) + \dots$$

Retaining the quadratic terms only, (3.11) becomes

$$T_f(y > \eta) \approx \int_0^{+\infty} dy \int_{X_1}^{X_2} \left[\frac{1}{2} (\nabla \varphi)^2 + U\varphi_x \right] dx - \int_{X_1}^{X_2} U\eta\varphi_x(+0) dx. \quad (3.12)$$

A similar set of arguments yields the following expression for the energy integral *below* the plate surface

$$T_f(y < \eta) \approx \int_{-\infty}^0 dy \int_{X_1}^{X_2} \left[\frac{1}{2} (\nabla \varphi)^2 + U\varphi_x \right] dx + \int_{X_1}^{X_2} U\eta\varphi_x(-0) dx.$$

This can be re-expressed in terms of the fluctuating quantities *above* the plate by making use of the anti-symmetry properties of the potential about the plate surface, $\varphi_x(-0) = -\varphi_x(+0)$, to give

$$T_f(y < \eta) \approx \int_0^{+\infty} dy \int_{X_1}^{X_2} \left\{ \frac{1}{2} (\nabla \varphi)^2 - U\varphi_x \right\} dx - \int_{X_1}^{X_2} U\eta\varphi_x(+0) dx. \quad (3.13)$$

Summing the upper and lower contributions, (3.12) and (3.13), to the energy integral and expressing the result in terms of upper variables only as in

$$T_f = T_f(y > \eta) + T_f(y < \eta) \approx \alpha \int_0^{+\infty} dy \int_{X_1}^{X_2} \frac{1}{2} (\nabla \varphi)^2 dx - \alpha U \int_{X_1}^{X_2} \eta\varphi_x(+0) dx,$$

allows us to write the linear approximation to the left hand side of (3.8) as

$$\frac{d}{dt} \int_V \frac{1}{2} (\nabla \varphi)^2 dV = \frac{d}{dt} [T_f] + \alpha U \int_{X_1}^{X_2} \left[\frac{\partial \eta}{\partial t} \varphi_x (+0) + \eta \frac{\partial \varphi_x (+0)}{\partial t} \right] dx. \quad (3.14)$$

We are now ready to combine (3.14) with (3.10) to form the conservation equation (3.7) for the fluid

$$\begin{aligned} \frac{d}{dt} [T_f] = & +\alpha \int_0^{+\infty} (p\varphi_x + U\varphi_x^2)|_{X_1} dy - \alpha \int_0^{+\infty} (p\varphi_x + U\varphi_x^2)|_{X_2} \\ & +\alpha \int_{X_1}^{X_2} (p + U\varphi_x) \varphi_y|_{y=+0} dx - \alpha U \int_{X_1}^{X_2} (\varphi_x \eta_t + \varphi_{xt} \eta)|_{y=+0} dx. \end{aligned} \quad (3.15)$$

The first two terms on the right of (3.15) are already flux-like quantities that do not involve integrals along the plate segment. The last two terms, both integrals over x , can be combined to yield an integrand that is a full differential with respect to x . This is accomplished by using the continuity equation (2.3b) to express the fluid velocity normal to the plate in terms of the plate deflection, leading to the cancellation of terms involving $\eta_t \varphi_x$, and yielding the intermediate result

$$+\alpha \int_{X_1}^{X_2} p \eta_t dx + \alpha \int_{X_1}^{X_2} [U^2 \varphi_x \eta_x + U p \eta_x - U \varphi_{xt} \eta] dx.$$

We then use the momentum equation (2.3c) to express p inside the brackets (i.e., the p multiplying η_x) in terms of φ and obtain the cancellation of the U^2 term. The expression inside the brackets is now a full differential in x , and can be evaluated to reveal a flux-like term as follows:

$$\begin{aligned} & +\alpha \int_{X_1}^{X_2} p \eta_t dx - \alpha U \int_{X_1}^{X_2} [\varphi_t \eta_x + \varphi_{xt} \eta] dx \\ = & +\alpha \int_{X_1}^{X_2} p \eta_t dx - \alpha U \int_{X_1}^{X_2} \frac{\partial}{\partial x} [\varphi_t \eta] dx \\ = & +\alpha \int_{X_1}^{X_2} p \eta_t dx - \alpha U [\varphi_t \eta]_{X_1}^{X_2}. \end{aligned}$$

Substituting these results back into (3.15), we obtain the power conservation equation for the fluid

$$\begin{aligned} \frac{d}{dt} [T_f] = & +\alpha \int_0^{+\infty} (p\varphi_x + U\varphi_x^2)|_{X_1} dy - \alpha \int_0^{+\infty} (p\varphi_x + U\varphi_x^2)|_{X_2} \\ & -\alpha U [\varphi_t \eta]_{X_1}^{X_2} + \alpha \int_{X_1}^{X_2} p\eta_t dx. \end{aligned} \quad (3.16)$$

The fluid and plate conservation equations (3.1 and 3.16) have a common term consisting of the integral of the pressure and plate velocity over the plate surface. Eliminating this term between the two gives a single power conservation equation for the fluid-plate system

$$\frac{d}{dt} [T_f + T_p + V_p] = \frac{1}{2} |F_0|^2 \operatorname{Re} \{Y_{dp}\} - [J_f + J_p + J_{pf}]_{X_1}^{X_2}, \quad (3.17)$$

where

$$T_f = \alpha \int_0^{+\infty} dy \int_{X_1}^{X_2} \frac{1}{2} (\nabla \varphi)^2 dx - \alpha U \int_{X_1}^{X_2} \eta \varphi_x (+0) dx \quad (3.18)$$

is the kinetic energy of the fluid,

$$J_f(X) = \alpha \int_0^{+\infty} (p\varphi_x + U\varphi_x^2)|_X dy \quad (3.19)$$

is the fluid flux, and

$$J_i = \alpha U \varphi_t \eta \quad (3.20)$$

is the plate-fluid ‘interface’ flux that only arises in the presence of non-zero U . Crighton and Oswell (1991) name this last term the ‘plate-fluid’ or ‘coupling’ flux. We prefer the label ‘interface’ because this quantity does not pre-suppose the presence of an elastic plate. It only requires a finite jump in potential across an interface with non-zero deflection from the horizontal. The interface flux also appears in the context of a trailing edge wake as we will see in chapter 7.

3.2 Wave Flux, Wave Energy and Wave Impedance

In this section we evaluate the fluxes for propagating waves in the far field of any source and identify a wave impedance associated with each travelling wave. Far from any

sources or plate boundaries and discontinuities, the time harmonic response variables are

$$\begin{aligned}\eta(x, t) &= Ae^{ikx-i\omega t}, \\ p(x, y, t) &= -A \frac{(\omega - Uk)^2}{\gamma(k)} e^{-\gamma(k)|y|} e^{ikx-i\omega t}, \\ \varphi(x, y, t) &= A \frac{(\omega - Uk)}{\gamma(k)} e^{-\gamma(k)|y|} e^{ikx-i\omega t},\end{aligned}$$

where A is the far field wave amplitude defined in (2.12). Substituting these into the expressions for the fluxes derived in section 3 and evaluating the x and t differentials and the y integrals, and taking the time average over a period, we find

$$J_p(x) = \frac{1}{2} \operatorname{Re} \left\{ \omega k \left(k^2 + |k|^2 + T \right) e^{i(k-\bar{k})x} \right\} |A|^2, \quad (3.21a)$$

$$J_f(x) = \frac{1}{2} \operatorname{Re} \left\{ \frac{\alpha \omega (\omega - Uk) (\omega - U\bar{k})}{k (\gamma(k) + \gamma(\bar{k}))} e^{i(k-\bar{k})x} \right\} |A|^2, \quad (3.21b)$$

$$J_i(x) = \frac{1}{2} \operatorname{Re} \left\{ \frac{\alpha \omega U (\omega - Uk)}{\gamma(k)} e^{i(k-\bar{k})x} \right\} |A|^2. \quad (3.21c)$$

The total wave flux is obtained by summing the individual fluxes, $J = J_p + J_f + J_i$. After some simplification, including enforcing of the identity

$$k\gamma(\bar{k}) - \bar{k}\gamma(k) = \pm |k|^2 \mp |k|^2 = 0, \quad \operatorname{Re}\{k\} \geq 0,$$

we find

$$J(x) = \frac{1}{2} \operatorname{Re} \left\{ \left[\frac{\alpha \omega (\omega^2 - U^2 k^2)}{k (\gamma(k) + \gamma(\bar{k}))} + \omega k (k^2 + |k|^2 + T) \right] e^{i(k-\bar{k})x} \right\} |A|^2. \quad (3.22)$$

These expressions hold for all wave types, including evanescent and convectively unstable waves. For neutral waves, $\bar{k} = k$, and the expression for the total flux reduces to

$$J(x) = \frac{\omega}{2} \left[\frac{\alpha (\omega^2 - U^2 k^2)}{2k\gamma(k)} + 2k^3 + Tk \right] |A|^2, \quad x \rightarrow \infty. \quad (3.23)$$

We identify the expression in the brackets as D_k from (2.9) and rewrite the wave flux as

$$J = \frac{1}{4} \omega D_k |A|^2. \quad (3.24)$$

Using the expression for the far field wave amplitude A given in (2.12), we find another way of expressing the wave flux,

$$J = \frac{1}{4} \frac{\omega}{D_k} |F_0|^2, \quad (3.25)$$

as a function of the driving force that sustains the steady state wave.

By writing $\partial D / \partial k = \partial D / \partial \omega \times \partial \omega / \partial k$ we obtain a further variant of the total wave flux,

$$J = \frac{1}{4} \omega D_\omega v_g |A|^2, \quad (3.26)$$

now expressed in terms of the group velocity v_g given by

$$v_g \equiv \frac{\partial \omega}{\partial k} = \frac{5k^4 + 3Tk^2 + \lambda - \omega^2 \pm 2\alpha U (\omega - Uk)}{2k \pm 2\alpha (\omega - Uk)}, \quad \text{Re}\{k\} \geq 0, \quad (3.27)$$

and in terms of the ω differential of the dispersion function

$$D_\omega = \frac{\partial D(k, \omega)}{\partial \omega} = - \left[2\omega + \frac{2\alpha (\omega - Uk)}{\gamma(k)} \right]. \quad (3.28)$$

We identify the terms multiplying v_g in (3.26) as the wave energy (up to a sign difference) as defined by Cairns (1979)

$$\begin{aligned} \mathcal{E} &= -\frac{\omega}{4} \frac{\partial D}{\partial \omega} |A|^2, \\ &= \frac{\omega^2}{4} \left[1 + \frac{\alpha (\omega - Uk)}{\gamma(k)} \right] |A|^2, \end{aligned} \quad (3.29)$$

where the dispersion function $D(k, \omega)$ is as defined in (2.6). Our equation for the wave energy (3.29) differs from the one given in Cairns (1979) by a minus sign. This is due entirely to a sign difference in our respective definitions of the dispersion function. Cairns defines his $D(k, \omega)$ so that the term corresponding to the plate inertial forces is positive.

The wave energy, first defined by Landahl (1962) and Benjamin (1963) in the context of fluid loaded plates, is the amount of work done to build up a wave from rest. Positive energy waves (PEWs) have positive ‘activation energy’ (i.e., net energy required from an external agency to create a steady state wave from rest) and behave conventionally. Negative energy waves (NEWs) have negative ‘activation energy’ and their generation results in a net decrease in the energy of the fluid loaded plate

system. NEWs are destabilized by damping and, more crucially, are responsible for the phenomenon of ‘over-scattering’ from plate discontinuities discussed in the next chapter.

From (3.28) it is easy to see that all neutral waves with phase speeds opposite in direction to the flow speed (in our case, negative phase speeds corresponding to $k < 0$) are POWs. We also observe that all waves with phase speeds exceeding the flow speed and that satisfy $\omega > Uk$ are also POWs. Solving the dispersion equation for the two ω roots (with k assumed real and positive), we obtain equation (2.33) and can proceed to show that all waves lying on the lower branch of the dispersion curve, and for which $\omega > 0$, are NEWs. Crighton & Oswell (1991) prove this for $T = \lambda = 0$. Numerically, one can show that this also holds true for all T , λ and U .

We note that, in line with the conventional understanding of the flux as the wave energy carried at the group velocity, the expression for the wave flux given in (3.26) can be rewritten as

$$J = \mathcal{E}v_g \quad (3.30)$$

using (3.27) and (3.29). The wave flux is a vector quantity and carries information about the direction of power flow given by the relative signs of \mathcal{E} and v_g .

The generalized wave impedance, defined as the ‘power per unit velocity amplitude carried by a neutral wave,’ is in contrast a scalar quantity. The wave impedance does not carry information regarding the direction of propagation but instead carries the sign of the wave energy.

The expression for wave impedance follows directly from the expression for the wave flux given in (3.30) with v_g replaced by its modulus and is given by

$$\begin{aligned} Z &= \frac{\mathcal{E}|v_g|}{\omega^2|A|^2}, \\ &= \frac{1}{4} \left[1 + \frac{\alpha(\omega - Uk)}{\gamma(k)} \right] |v_g|. \end{aligned} \quad (3.31)$$

3.3 Existence of Negative Energy Waves

As we’ve just seen, the existence of NEWs is bound up with the presence of the lower branch of the dispersion equation in the first quadrant of the real ω - k plane. These

consist of the solutions to the dispersion equation which correspond to the lower sign in (2.33) for ω and k real and positive. Peake (1997) has shown that increasing the spring constant λ (or, equivalently, adding some transverse curvature) limits the presence of this branch in the first quadrant and reduces the range of frequencies and wavenumber over which NEWs can exist. Peake (1997) also finds that for spring constants above a threshold value, $\lambda = \lambda_2$ (see (3.33) below), the lower branch disappears entirely from the first quadrant. He finds this threshold by solving for the value of λ that causes the pinch frequency to go negative. We will solve for this same threshold in a somewhat different but entirely equivalent way.

First, we identify the crossing point k_{cr} of the lower branch into the fourth quadrant by setting the numerator of (2.33) with the lower $(-)$ sign to zero, squaring the radical and dividing through by the common factors k and $(\alpha + k)$ to find

$$k_{cr}^4 + Tk_{cr}^2 - \alpha U^2 k_{cr} + \lambda = 0. \quad (3.32)$$

We note that for $\lambda = T = 0$, the crossing point is given exactly by

$$k_{cr}|_{\lambda=T=0} = (\alpha U^2)^{\frac{1}{3}}.$$

Next, we solve for the value of $\lambda = \lambda_2$ which causes the merging of k_{cr} and the pinch point k_p by combining (3.32) and the pinch equation (2.17) with $\omega_p = 0$ while setting $T = 0$ in both and find

$$\lambda_2 = \frac{3\alpha^{4/3}U^{8/3}}{2^{8/3}}. \quad (3.33)$$

This is an exact solution and is identical to equation (4.10) in Peake (1997) after one makes the transformation given in (2.36).

To determine the effect of plate pre-tension T on the presence of NEWs, we first undertake a purely numerical study. We set $\lambda = 0$ and find that increasing T uniformly from zero reduces the range of frequencies and wavenumbers over which the lower branch of the temporal dispersion equation (2.33) remains in the first quadrant but does not succeed in eliminating this range entirely as seen in figure 3.2. We find that both the pinch point (k_p, ω_p) and the crossing point $(k_{cr}, 0)$ approach the origin as T is increased but never reach it.

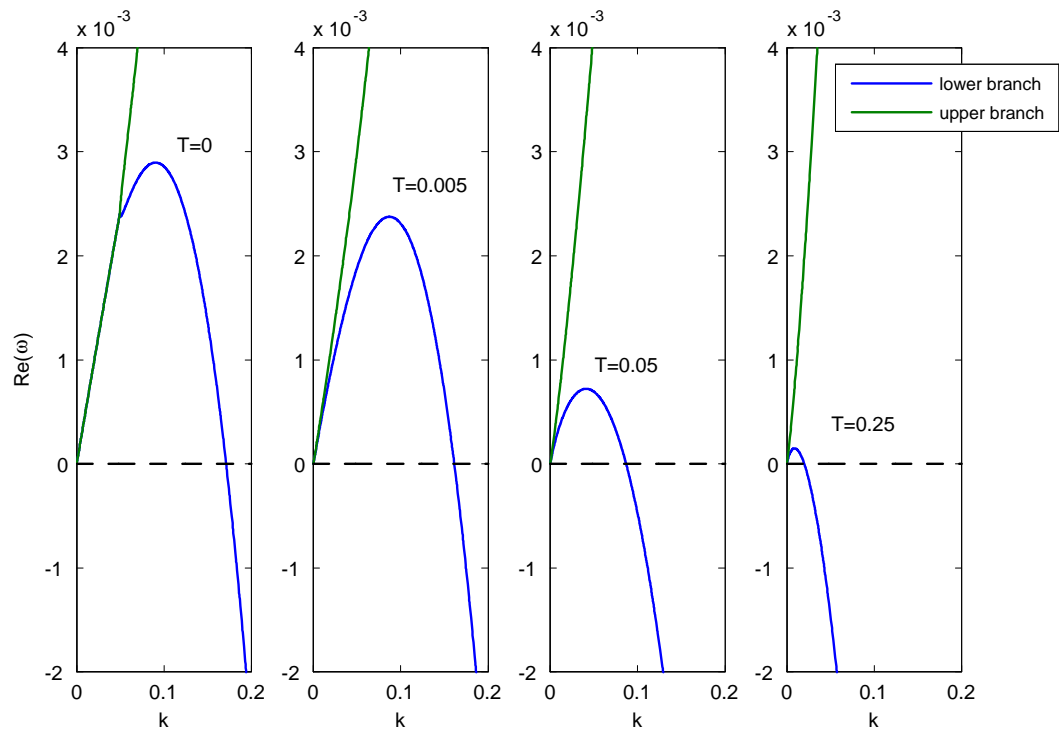


Figure 3.2: Temporal dispersion diagrams for four representative values of T for $U = 0.05$, $\lambda = 0$, $\alpha = 2$.

To confirm this analytically, we focus on the equation for the crossing point (3.32) and determine the trajectory of the relevant positive, real root as a function of T . Setting $\lambda = 0$ in (3.32), we obtain the reduced cubic

$$k_{cr}^3 + Tk_{cr} - \alpha U^2 = 0, \quad \lambda = 0. \quad (3.34)$$

The existence of a real and positive root indicates that a crossing point, and hence a range over which NEWs are present, exists. Equation (3.34) is of the form $x^3 + ax + b = 0$ and its radical is given by

$$\Delta \equiv \frac{b^2}{4} + \frac{a^3}{27} = \frac{\alpha^2 U^4}{4} + \frac{T^3}{27}, \quad (3.35)$$

which is clearly positive for all $T > 0$. This implies that there will always be one real root (and two complex conjugate roots) for all T . The real root is given by the exact expression

$$k_{cr} = \left(\frac{\alpha U^2}{2} + \Delta^{\frac{1}{2}} \right)^{\frac{1}{3}} + \left(\frac{\alpha U^2}{2} - \Delta^{\frac{1}{2}} \right)^{\frac{1}{3}}, \quad (3.36)$$

which can be re-written as $(\alpha U^2/2)^{1/3} \left\{ (\gamma + 1)^{1/3} - (\gamma - 1)^{1/3} \right\}$ where $\gamma \equiv (1 + 4T^3/(27\alpha^2 U^4))^{1/2} > 0$, and is clearly positive for all possible values of γ , i.e., $1 < \gamma < \infty$.

To evaluate k_{cr} in the limit $T \rightarrow \infty$, we perform large T asymptotics on (3.34) and find that to second order, the crossing point behaves as

$$k_{cr} \approx \frac{\alpha U^2}{T} - \frac{\alpha^3 U^6}{T^4} + \dots, \quad T \gg U^{3/4}. \quad (3.37)$$

This asymptotic result is overlaid on top of the exact solution of (3.36) in figure 3.3.

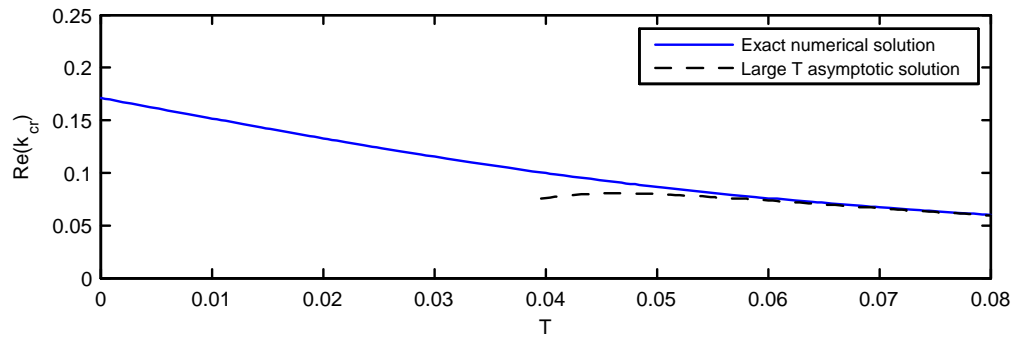


Figure 3.3: Crossing point of the lower branch of the temporal dispersion curve from the first into the fourth quadrant of the $\text{Re}(\omega-k)$ plane as a function of T for $U = 0.05$ and $\alpha = 2$.

Chapter 4

Scattering from Local Discontinuities

In this chapter we investigate the reflection and transmission of plate waves from point or ‘local’ discontinuities and inhomogeneities on an otherwise uniform, infinite, flow-loaded plate. Our approach is based on the technique described by M.S. Howe (Howe, 1994) for Euler plates in a quiescent fluid, adapted here to fluid loaded plates in mean flow with pre-tension and spring foundation. The method is extended to fluid-loaded plates for which the symmetry between left and right going waves is broken, and to plates that can sustain negative energy waves and support convectively unstable waves. Another key difference with quiescent fluid loading includes the possibility of a net exchange of energy between the plate and incompressible fluid at a discontinuity and the closely related phenomenon of ‘over-scattering,’ whereby individual scattered waves carry more power to the far field than that brought in by the incident wave.

4.1 Plate Equation with Multipole Loads

Consider an infinitely long fluid-loaded plate with pre-tension T , spring foundation constant λ and mean flow speed U that is uniform everywhere except for a structural discontinuity at $x = x_s$ (figure 4.1). A variety of structural conditions may be imposed at the abutting edges, from free to clamped to constrained by a combination of lumped

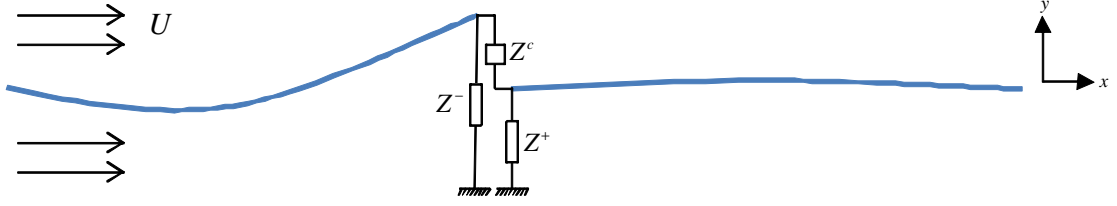


Figure 4.1: Scattering by local plate discontinuities. Z^\mp are the lumped parameter impedances constraining the edges. Z^c is a coupling impedance connecting the edges.

parameter springs, masses and dashpots with transverse and/or rotational degrees of freedom, attached to each edge independently or coupling one edge to the other, etc...

The fluid loaded plate equation (4.1) is valid everywhere except at the structural inhomogeneity where one of more derivatives of η may be discontinuous

$$\frac{\partial^4}{\partial x^4} \eta - T \frac{\partial^2}{\partial x^2} \eta + \lambda \eta + \frac{\partial^2}{\partial t^2} \eta = -\alpha p. \quad (4.1)$$

The pressure and potential obey the linearized Bernoulli equation (2.3c) and the continuity equation (2.3b) as before. In order to extend the domain of validity of the plate equation to include the discontinuity at $x = 0$, we introduce the infinitesimally small parameter ϵ , following Howe (1994) and write

$$\eta(x) = \eta(x) H(|x| - \epsilon), \quad \epsilon \rightarrow 0.$$

By repeated application of the chain rule, one can express the derivatives of a discontinuous function in terms of the delta function and the ‘one-sided’ derivatives of the function at a discontinuity as follows

$$\begin{aligned} \frac{\partial}{\partial x} [\eta(x) H(|x| - \epsilon)] &= H(|x| - \epsilon) \frac{\partial}{\partial x} \eta(x) + \eta(x) \frac{\partial}{\partial x} H(|x| - \epsilon) \\ &= H(|x| - \epsilon) \frac{\partial}{\partial x} \eta(x) + [\eta(+|\epsilon|) - \eta(-|\epsilon|)] \delta(x), \\ \frac{\partial^2}{\partial x^2} [\eta(x) H(|x| - \epsilon)] &= H(|x| - \epsilon) \frac{\partial^2}{\partial x^2} \eta(x) + \left[\frac{\partial}{\partial x} \eta(+|\epsilon|) - \frac{\partial}{\partial x} \eta(-|\epsilon|) \right] \delta(x) \\ &\quad + [\eta(+|\epsilon|) - \eta(-|\epsilon|)] \delta^{(1)}(x), \\ &\vdots \\ \frac{\partial^n}{\partial x^n} [\eta(x) H(|x| - \epsilon)] &= H(|x| - \epsilon) \frac{\partial^n}{\partial x^n} \eta(x) + \sum_{m=1}^n \Delta \left[\frac{\partial^{(n-m)}}{\partial x^{(n-m)}} \eta(0) \right] \delta^{(m-1)}(x), \\ \epsilon &\rightarrow 0, \end{aligned}$$

where $\Delta[f(x_s)] \equiv f(x_s + |\epsilon|) - f(x_s - |\epsilon|)$ is the ‘jump’ in the value of f at $x = x_s$.

For a discontinuity located at $x = x_s$, we proceed by multiplying the plate equation by $H(|x - x_s| - \epsilon)$, applying the identity

$$H(|x - x_s| - \epsilon) \frac{\partial^n}{\partial x^n} \eta(x) = \frac{\partial^n}{\partial x^n} [\eta(x) H(|x - x_s| - \epsilon)] - \sum_{m=0}^n \Delta \left[\frac{\partial^{(n-m)}}{\partial x^{(n-m)}} \eta(x_s) \right] \delta^{(m-1)}(x - x_s), \quad \epsilon \rightarrow 0,$$

and moving all the jump quantities to the r.h.s. to obtain

$$\frac{\partial^4}{\partial x^4} \eta - T \frac{\partial^2}{\partial x^2} \eta + \lambda \eta + \frac{\partial^2}{\partial t^2} \eta = -\alpha p + \sum_{m=0}^4 \Delta f_m \delta^{(m)}(x - x_s), \quad -\infty < x < +\infty, \quad (4.2)$$

where the jump functions Δf_m are

$$\begin{aligned} \Delta f_0 &= \Delta \left[\frac{\partial^3 \eta(x_s)}{\partial x^3} \right] - T \Delta \left[\frac{\partial \eta(x_s)}{\partial x} \right], & \Delta f_1 &= \Delta \left[\frac{\partial^2 \eta(x_s)}{\partial x^2} \right] - T \Delta [\eta(x_s)], \\ \Delta f_2 &= \Delta \left[\frac{\partial \eta(x_s)}{\partial x} \right], & \Delta f_3 &= \Delta [\eta(x_s)]. \end{aligned} \quad (4.3)$$

Local discontinuities in the plate are therefore equivalent to applying multipole loads to the structure (at the point of discontinuity). The multi-pole strengths are determined by enforcing the structural edge conditions at the discontinuity. As a result, the amplitude of a monopole source is given by the jump in the transverse (shear) force Δf_0 , a jump in the bending moment Δf_1 constitutes a dipole load, the strength of a quadrupole load Δf_2 is given by the jump in slope, and the jump in displacement Δf_3 constitutes the strength of an octupole source.

Four structural conditions (two per edge) are required for a unique solution. Equivalently, four multipole strengths are needed to fully characterize the discontinuity. This is all a consequence of the highest spatial derivative in the plate equation being of fourth order.

4.2 Scattered Field: the Green’s Function Matrix

The plate equation driven by multipole loads applied at a single location ‘begs’ for a Green’s function approach. The scattered field is thereby expressed as a sum over the

multi-pole Green's functions of the fluid loaded plate

$$\eta_{scat}^{\pm}(x) = \Delta f_0 G_{\pm}(x - x_s) + \Delta f_1 G_{\pm}^{(1)}(x - x_s) + \Delta f_2 G_{\pm}^{(2)}(x - x_s) + \Delta f_3 G_{\pm}^{(3)}(x - x_s) \quad (4.4)$$

where the one sided Green's functions are

$$G_{\pm}(x - x_s) = \pm \frac{ie^{ik_1^{\pm}(x-x_s)}}{D_k(k_1^{\pm})} \pm \frac{ie^{ik_2^{\pm}(x-x_s)}}{D_k(k_2^{\pm})} + \frac{1}{2\pi} \int_0^{+\infty} \frac{e^{\mp v(x-x_s)}}{D(\pm iv)} dv + \frac{1}{2\pi} \int_0^{+\infty} \frac{e^{\mp v(x-x_s)}}{D(\mp iv)} dv, \quad (4.5a)$$

$$G_{\pm}^{(m)}(x - x_s) = \frac{\partial^m}{\partial x_s^m} G_{\pm}(x - x_s). \quad (4.5b)$$

Here, $D_k(k) = \partial D(k) / \partial k$ where $D(k)$ is the dispersion function given in (2.6). In our notation for the one-sided Green's functions, $G_{\pm}^{(m)}$ signifies the m^{th} differential with respect to the source variable x_s for response locations to the right of the discontinuity, i.e., for positive (+) $x - x_s$. The one-sided Green's functions are composed of both far field propagation terms generated by the roots of the dispersion equation and by near-field terms generated by the branch line integrals representing fluid loading.

To solve for the unknown multipole amplitudes corresponding to a given discontinuity, (4.4) is substituted into the relevant structural edge conditions. In general, we will need to evaluate derivatives of response up to the third order. This suggests that we will require the elements of a 4×4 Green's function matrix whose (n, m) components are given by

$$\begin{aligned} \partial^n G_{\pm}^{(m)}(x - x_s) &\equiv \frac{\partial^n \partial^m}{\partial x^n \partial x_s^m} G_{\pm}(x - x_s) = \\ &\pm i \frac{(ik_1^{\pm})^n (-ik_1^{\pm})^m e^{ik_1^{\pm}(x-x_s)}}{D_k(k_1^{\pm})} \pm i \frac{(ik_2^{\pm})^n (-ik_2^{\pm})^m e^{ik_2^{\pm}(x-x_s)}}{D_k(k_2^{\pm})} \\ &+ \frac{1}{2\pi} \int_0^{+\infty} \frac{(\mp v)^n (\pm v)^m e^{\mp v(x-x_s)}}{D(\pm iv)} dv + \frac{1}{2\pi} \int_0^{+\infty} \frac{(\mp v)^n (\pm v)^m e^{\mp v(x-x_s)}}{D(\mp iv)} dv, \quad n + m \leq 3. \end{aligned} \quad (4.6)$$

We note that the denominator of the branch line integrals in (4.6) is of order $D(\pm iv) \sim v^4$ as $v \rightarrow \infty$. As a result, the near field integrals will be non-convergent at $x = x_s$ for $n + m > 3$. We overcome this difficulty by implementing a 'denominator augmentation' procedure inspired by a comparable technique described in Howe (1994), but different in its implementation here.

4.2.1 Evaluating the Nearfield Integrals

Our aim is to find an expression for the inverse transform of the Green's function, $G(x - x_s) = \int_{-\infty}^{+\infty} e^{ik(x-x_s)} / D(k, \omega) dk$, that converges at $x = x_s$ for all required orders of the derivative w.r.t. the source and receiver variables, or up to third order w.r.t. x and x_s combined. The denominator 'augmentation procedure' consists of using the identity

$$\gamma(k) = \frac{\gamma(k) D(k, \omega) + \alpha(\omega - Uk)^2}{k^4 + Tk^2 + \lambda - \omega^2} \quad (4.7)$$

to rewrite

$$\begin{aligned} \frac{1}{D(k, \omega)} &= \frac{1}{\gamma(k) D(k, \omega)} [\gamma(k)] \\ &= \frac{1}{\gamma(k) D(k, \omega)} \left[\frac{\gamma(k) D(k, \omega) + \alpha(\omega - Uk)^2}{k^4 + Tk^2 + \lambda - \omega^2} \right] \\ &= \frac{\alpha(\omega - Uk)^2}{\gamma(k) D(k, \omega) [k^4 + Tk^2 + \lambda - \omega^2]} + \frac{1}{[k^4 + Tk^2 + \lambda - \omega^2]}. \end{aligned} \quad (4.8)$$

The transform integral can now be divided into two parts, $G(x - x_s) = I_1 + I_2$, consisting of

$$I_1 = \frac{1}{2\pi} \int_{\Gamma} \frac{\alpha(\omega - Uk)^2}{\gamma(k) D(k, \omega) [k^4 + Tk^2 + \lambda - \omega^2]} e^{ik(x-x_s)} dk, \quad (4.9a)$$

$$I_2 = \frac{1}{2\pi} \int_{\Gamma} \frac{1}{[k^4 + Tk^2 + \lambda - \omega^2]} e^{ik(x-x_s)} dk. \quad (4.9b)$$

The advantage of recasting the Green's function transform in this form is that the integral I_1 containing the branch cut has now been augmented by $o(k^3)$ in the denominator. This gives an integrand that behaves like $1/k^7$ for $k \rightarrow \infty$, allowing differentiation under the integral sign up to six times, as required. The denominator of the second integral, I_2 , has the same order in k as the original integral. However, it does not contain a branch cut and can be easily evaluated using a residue approach, then differentiated as many times as required.

In addition to the branch cut contributions, I_1 has residue contributions from four poles per each half plane. These consist of the roots of the dispersion equation $D(k, \omega) = 0$, the two system poles per half plane k_1^{\pm} and k_2^{\pm} as before, and additionally, the zeros of the plate operator, $[k^4 + Tk^2 + \lambda - \omega^2] = 0$, i.e., the two *in-vacuo* poles

per half plane $\pm k_p$ and $\pm i k_m$ given in (6.12). It turns out that the residue contributions from the latter cancel out exactly by the *in-vacuo* pole contributions to the second integral I_2 . This is because, at the *in-vacuo* roots, the dispersion function reduces to $D(k_p, \omega) = -\alpha(\omega - Uk_p)^2 / \gamma(k_p)$ and the residue contribution for I_1 is simply $+i [4k_p^3 + 2Tk_p]^{-1}$, which is clearly $-1 \times$ the residue contribution from I_2 . This was to be expected because the *in-vacuo* roots are spurious roots introduced by our procedure and are not physical system roots that can be expected to propagate to the far field.

We now turn to evaluating the branch cut integral in I_1 . Given that the two evanescent *in-vacuo* roots sit on or near the imaginary axis, it would appear that our branch cut integral along this same axis would have to contend with these poles. It turns out that these poles are removed by zeros in the numerator when the contributions from the up and down legs of the branch cut integral are combined. To see this, we express the term $\gamma(k) D(k, \omega)$ in I_1 containing the branch cuts in terms of the quintic polynomials $P_{\pm}(k)$ introduced by Crighton and Oswell (1991) (defined here with a sign difference)

$$\gamma(k) D(k, \omega) \equiv P_{\pm}(k) = \pm k [k^4 + Tk^2 + \lambda - \omega^2] - \alpha(\omega - Uk)^2 \quad \text{Re}\{k\} \gtrless 0. \quad (4.10)$$

Setting $k = \pm iv$ for the branch line evaluations in the upper and lower half planes respectively, the sum of the up and down legs of the branch line integrals can be written as

$$BLI_{\pm} = \frac{1}{2\pi} \int_0^{+\infty} \left\{ \frac{1}{P_+(\pm iv)} - \frac{1}{P_-(\pm iv)} \right\} \frac{\alpha(\omega \mp iUv)^2}{[v^4 - Tv^2 + \lambda - \omega^2]} e^{\mp v(x-x_s)} dv, \quad (4.11)$$

where the \pm here refer to the sign of $(x - x_s)$. The term in the curly brackets simplifies to

$$\frac{1}{P_+(\pm iv)} - \frac{1}{P_-(\pm iv)} = \frac{-2(\pm v)(\omega \mp iUv)^2 [v^4 - Tv^2 + \lambda - \omega^2]}{v^2 [v^4 - Tv^2 + \lambda - \omega^2]^2 + \alpha^2 (\omega \mp iUv)^4} \quad (4.12)$$

and reveals the plate operator (in square brackets) in the numerator, which cancels out with an identical term in the denominator of the branch line integral (4.11), thereby removing the spurious *in-vacuo* poles.

Having implemented the above mentioned simplifications, the branch line integral in (4.11) is subtracted from the residue contributions to yield an expression for the

Green's function with greatly improved convergence properties

$$G_{\pm}(x - x_s) = \pm \frac{ie^{ik_1^{\pm}(x-x_s)}}{D_k(k_1^{\pm})} \pm \frac{ie^{ik_2^{\pm}(x-x_s)}}{D_k(k_2^{\pm})} + \pm \frac{i}{\pi} \int_0^{+\infty} \frac{v\alpha(\omega \mp iUv)^2}{v^2[v^4 - Tv^2 + \lambda - \omega^2]^2 + \alpha^2(\omega \mp iUv)^4} e^{\mp v(x-x_s)} dv. \quad (4.13)$$

The above equation can now be differentiated under the integral sign as many times as required for all x in order to fully populate the 4×4 Green's function matrix. The fully and rapidly convergent (n, m) terms of the Greens function matrix are therefore given by

$$\begin{aligned} \partial^n G_{\pm}^{(m)}(x - x_s) &\equiv \frac{\partial^n \partial^m}{\partial x^n \partial x_s^m} G_{\pm}(x - x_s) \\ &= \pm i \frac{(ik_1^{\pm})^n (-ik_1^{\pm})^m e^{ik_1^{\pm}(x-x_s)}}{D_k(k_1^{\pm})} \pm i \frac{(ik_2^{\pm})^n (-ik_2^{\pm})^m e^{ik_2^{\pm}(x-x_s)}}{D_k(k_2^{\pm})} \\ &\quad \pm \frac{i}{\pi} \int_0^{+\infty} \frac{\alpha v (\omega \mp iUv)^2 (\mp v)^n (\pm v)^m}{v^2[v^4 - Tv^2 + \lambda - \omega^2]^2 + \alpha^2(\omega \mp iUv)^4} e^{\mp v(x-x_s)} dv, \quad n + m \leq 6. \end{aligned} \quad (4.14)$$

Properties of the Green's Function Matrix

All Green's functions have the expected reciprocity properties that result from interchanging source and receiver

$$\partial^n G_{\pm}^{(m)}(x - x_s) = (-1)^{(n+m)} \partial^m G_{\pm}^{(n)}(x - x_s). \quad (4.15)$$

The Green's function matrices are therefore symmetric for $n + m$ even and skew symmetric for $n + m$ odd. The terms along the diagonal (which correspond to even $n + m$ and are therefore non-zero) represent drive and response pairs possessing the same degree of freedom and their imaginary parts represent the work done by the applied load on the plate.

The 'jump' in the Green's function, or the difference between the positive and negative one-sided Green's functions at the discontinuity $x - x_s = 0$, also has some

special properties. It can be shown that the ‘jump’ matrix is given by

$$\partial^n G_+^{(m)}(0) - \partial^n G_-^{(m)}(0) = \begin{bmatrix} 0 & 0 & 0 & -1 \\ 0 & 0 & +1 & 0 \\ 0 & -1 & 0 & -T \\ +1 & 0 & +T & 0 \end{bmatrix}. \quad (4.16)$$

The derivation is provided in Appendix A.

4.3 Response to Multipole Loads

Prior to deriving the scattering coefficients for specific types of discontinuities, we briefly analyze the response of the flow-loaded plate to excitation by multipole loads. The analysis parallels that given for a monopole load in chapter 2.

The solution to

$$\frac{\partial^4}{\partial x^4} \eta - T \frac{\partial^2}{\partial x^2} \eta + \lambda \eta + \frac{\partial^2}{\partial t^2} \eta = -\alpha p + F_m \delta^{(m)}(x - x_s), \quad (4.17)$$

or equivalently the deflection response to the m^{th} order load of amplitude F_m , is given by the m^{th} order Green’s function given in (4.14) with $n = 0$. The spatial response for unit load $F_m = 1$ and drive frequency $\omega = 0.002$ is plotted in figure 4.2 for a representative set of plate parameters.

4.3.1 Far Field Response

In the far field, the causal solution consists of two upstream and two downstream waves and can be written in terms of the far field Green’s function,

$$\eta(|x| \gg |x_s|) = F_m G_{\pm}^{(m)}(\infty),$$

where

$$G_{\pm\infty}^{(m)}(x) \equiv \sum_{j=1}^2 \frac{\pm i \left(-ik_j^{\pm}\right)^m e^{ik_n^{\pm}(x-x_s)}}{D_k(k_j^{\pm})} \quad (4.18)$$

is defined as the pole contributions alone of (4.14). The far field amplitude for an individual wave $\pm j$ is given by

$$A_{\pm j}^{(m)} = \pm i \frac{\left(-ik_j^{\pm}\right)^m}{D_k(k_j^{\pm})} F_m. \quad (4.19)$$

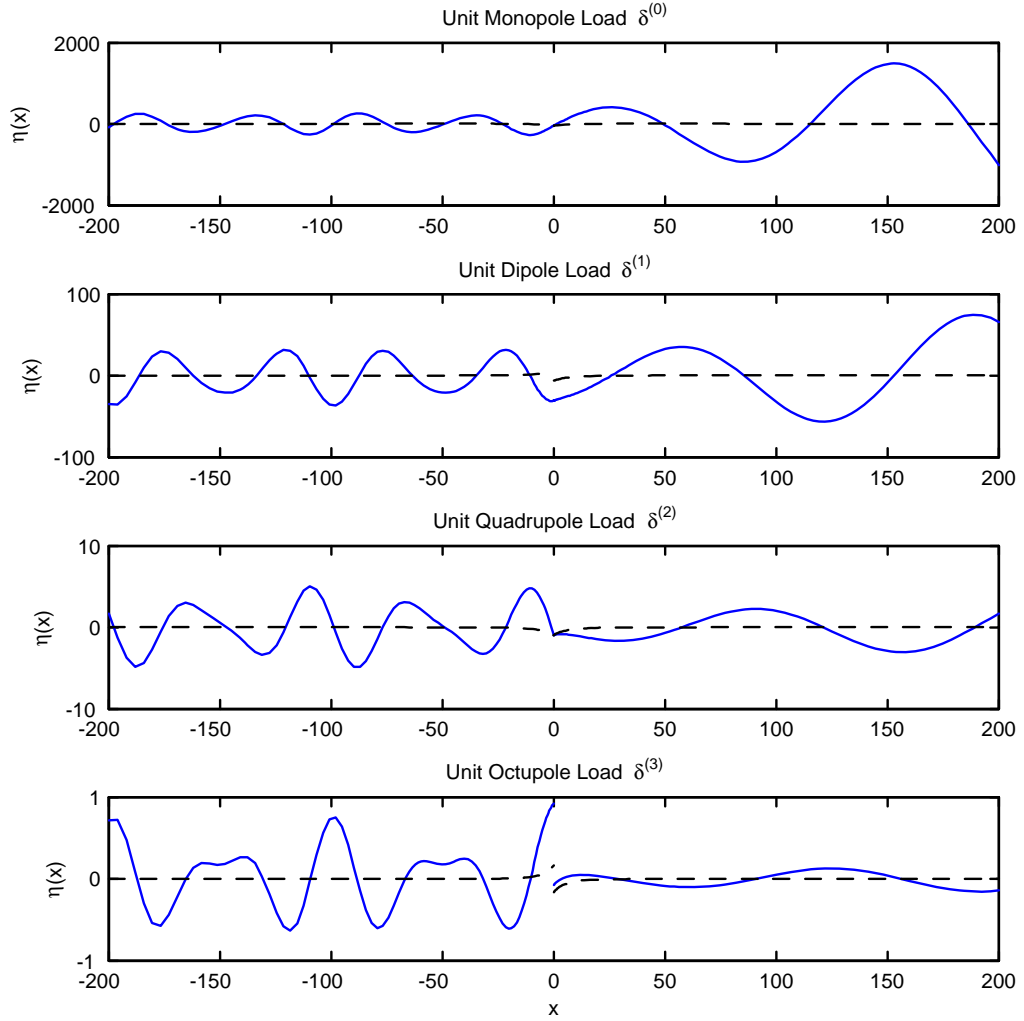


Figure 4.2: Spatial deflection response (pole and branch cut contributions) for unit multipole loads applied at $x = 0$, for $\omega = 0.002$ and $U = 0.05$, $T = U^2$, $\lambda = 0$. Dashed lines represent the near-field response alone.

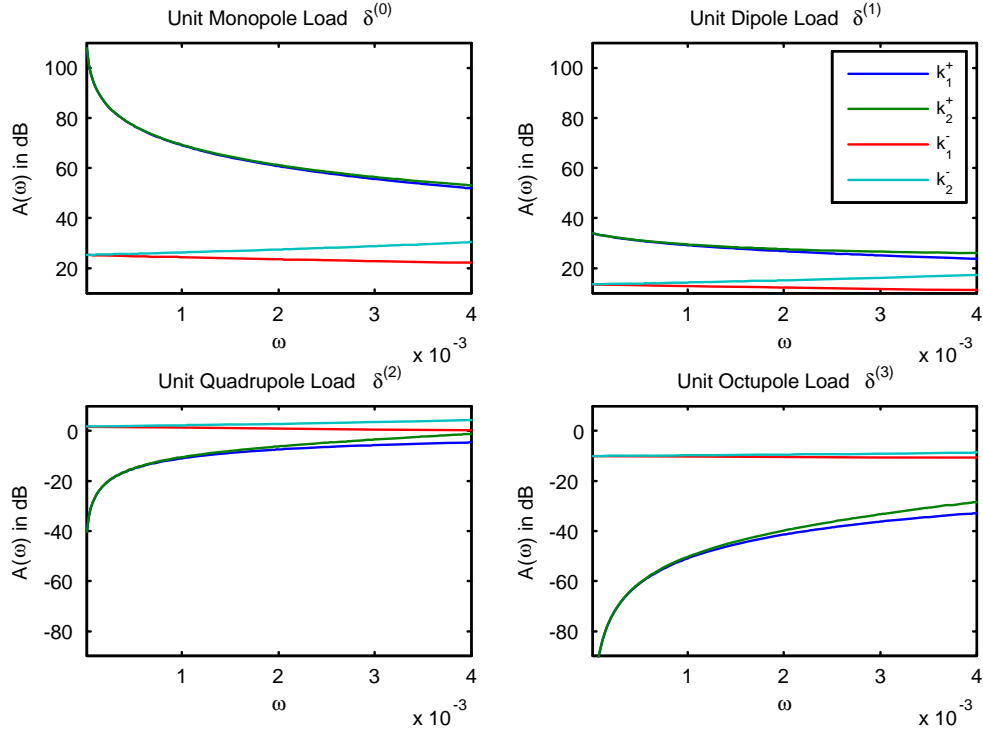


Figure 4.3: Far field wave amplitudes per unit multipole load as a function of drive frequency for $U = 0.05$, $T = U^2$, $\lambda = 0$ and $\alpha = 2$. The corresponding dispersion plot is given in figure 2.4c.

The amplitudes given in (4.19) are plotted as a function of drive frequency in figure 4.3, per unit load.

We can proceed to write down expressions for the wave energy fluxes generated by these multipole loads. In terms of far field amplitude, the expression is of course identical to that given for a monopole source (or indeed any type of compact source as long as we are in its far-field) and is given by

$$J_{\pm j}^{(m)} = \frac{1}{4} \operatorname{Re} \left\{ \omega D_k \left(k_j^{\pm} \right) \right\} \left| A_{\pm j}^{(m)} \right|^2. \quad (4.20)$$

The difference, in the form of a factor $\left| k_j^{\pm} \right|^{2m}$, arises when we express the far-field wave flux (using (4.19)) as a function of applied load amplitudes

$$J_{\pm j}^{(m)} = \frac{1}{4} \operatorname{Re} \left\{ \frac{\omega}{D_k \left(k_j^{\pm} \right)} \right\} \left| k_j^{\pm} \right|^{2m} |F_m|^2. \quad (4.21)$$

A feature that stands out from figures 4.2 and 4.3 is that higher order multipoles appear to impart more power to the upstream than to the downstream travelling waves. This is a direct consequence of the $\left(-ik_j^\pm\right)^m$ factor in the far-field amplitude of equation (4.19) and the fact that upstream travelling waves (or waves travelling against the flow) have relatively larger wavenumbers. This is the mathematical explanation for why discontinuities that can be modelled as higher order multipoles scatter relatively more energy into the upstream travelling waves irrespective of the direction and type of the incident wave. These types of discontinuities allow the downstream travelling waves to be transmitted relatively unimpeded, whereas upstream travelling waves are more likely to experience over-scattering.

4.3.2 Drive Point Admittance & Power into Plate

The drive point admittance is the ratio of the time rate of change of plate response to applied load at the drive location $x = x_s$. In our Green's function notation, it is given by

$$Y_{dp} = -i\omega \partial^n \widehat{G}^{(m)}(0), \quad (4.22)$$

where the over-hat denotes the arithmetic mean between the $+$ and $-$ components, or $\partial^n \widehat{G}^{(m)} \equiv \left(\partial^n G_+^{(m)} + \partial^n G_-^{(m)}\right)/2$. The elements of the 4×4 matrix of drive point admittances are plotted in figure 4.4 as a function of frequency. The diagonal terms represent ratios of response to load for the same mechanical degree of freedom (i.e., translational velocity and vertical force, rotational velocity and moment, etc...), and therefore have particular significance in terms of power exchange between the driver and the plate. In particular, the real part of a diagonal term represents power per unit drive injected into, or extracted from, the plate for a given drive type.

Negative values of the real part indicate that the drive is absorbing power from the plate to maintain the prescribed motion and is one indicator of the existence of instability. Crighton & Oswell (1991) discuss this phenomenon in great detail for the case of a monopole load (i.e., the term $Y_{dp}[1, 1]$ in our admittance matrix) and show that $\text{Re}\{Y_{dp}\} < 0$ is not limited to the convectively unstable range but extends all the way up to the pinch frequency ω_p , and coincides with the range over which

Negative Energy Waves (NEWs) exist. At $\omega = \omega_p$, $\text{Re}\{Y_{dp}\}$ jumps from $-\infty$ to a finite positive value. This singularity in Y_{dp} is due to the ω_p zero at of the D_k term in the denominator of the Green's function.

Examining the diagonal terms in figure 4.4, we note that negative values of $\text{Re}\{Y_{dp}\}$ are also present over the range $\omega < \omega_p$ for a dipole as well as a quadrupole load but not so for an octupole load. In fact, closer analysis reveals that the octupole Y_{dp} [4, 4] also descends to $-\infty$ in the immediate vicinity of ω_p just like all the other multipoles and that, for the parameters chosen in figure 4.4, the quadrupole Y_{dp} [3, 3] possesses a range of frequencies less than ω_p over which its real part ventures into positive territory. Therefore, one cannot in general associate the phenomenon of $\text{Re}\{Y_{dp}\} < 0$ too firmly with one multipole load over another. The sign of $\text{Re}\{Y_{dp}\}$ at a given frequency is an expression of the balance of total negative energy vs. the total positive energy imparted to the plate by a given multipole and as a results also depends on the plate parameters. It is, however, possible to make one generalization: the higher the order of the source, the more positive (or less negative) the value of $\text{Re}\{Y_{dp}\}$ for a given set of plate parameters. This property is, once again, a direct consequence of the $\left(-ik_j^\pm\right)^m$ factor discussed above.

As discussed in chapter 3, energy balance dictates that the power injected into (or extracted from) the plate at the drive is equal to the sum of the wave powers in the far field. A negative $\text{Re}\{Y_{dp}\}$ is simply an indication that more power was injected into the negative rather than the positive energy waves. Given that the wave with the largest wavenumber, k_1^- , is always a PEW ensures that $\text{Re}\{Y_{dp}\}$ becomes progressively more positive with multipole source order m through the $\left(-ik_j^\pm\right)^m$ weighting term in the far field wave amplitude equation (4.19).

Given that all Green's functions along the diagonal are continuous at the source, either $\partial^m G_+^{(m)}(0)$ or $\partial^m G_-^{(m)}(0)$ can be used to evaluate $Y_{dp}[m, m]$. The advantage of using the averaged quantity $-i\omega \left(\partial^m G_+^{(m)}(0) + \partial^m G_-^{(m)}(0)\right)/2$ was illustrated for a monopole load in section 2.2.2: the contributions from the branch line integrals average out to zero and the real part of the drive admittance can be expressed in terms of the pole contributions alone. The power into the plate per multipole order m is therefore

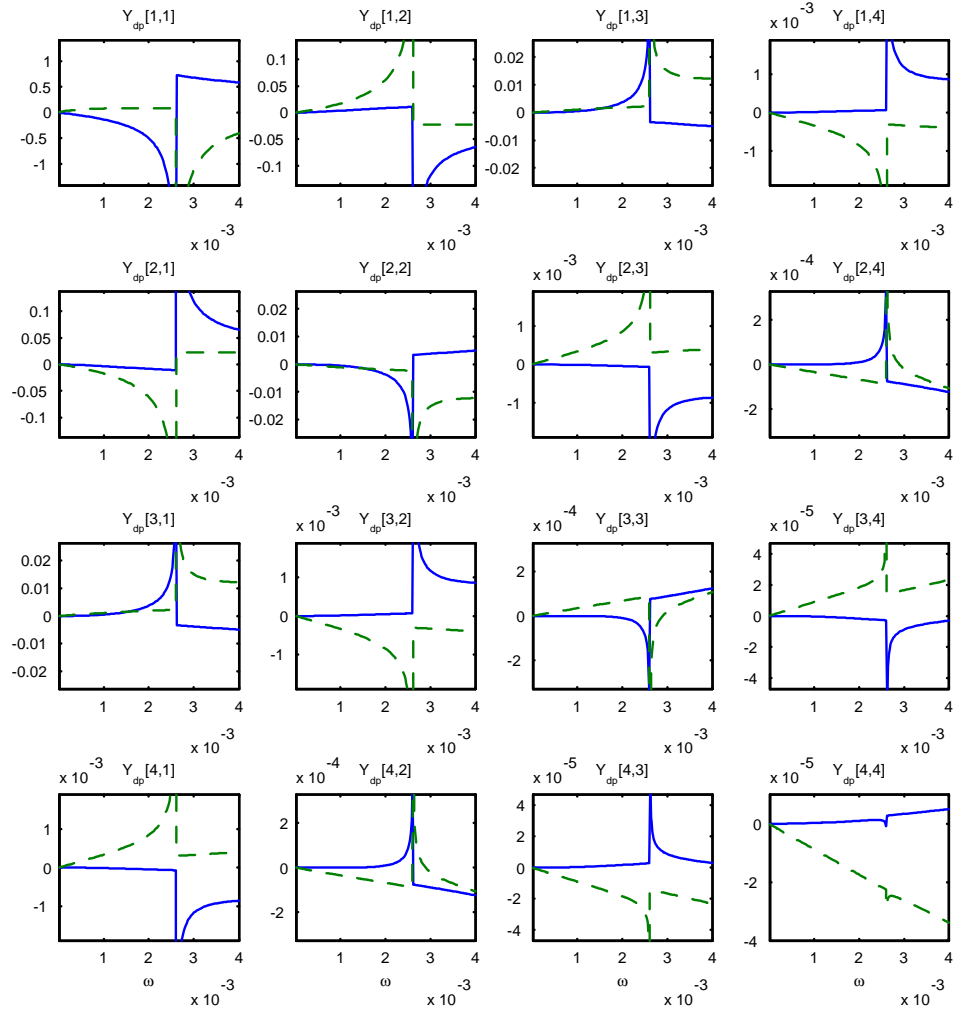


Figure 4.4: Real (solid) and imaginary (dashed) parts of the multi-pole drive point admittance matrix for $U = 0.05, T = U^2, \lambda = 0$ & $\alpha = 2$ (dispersion plot of figure 2.4c).

given by

$$\Pi^{(m)} = \frac{1}{4} \operatorname{Re} \left\{ \sum_{j=1}^2 \frac{\omega \left(k_j^+ \overline{k_j^+} \right)^m}{D_k \left(k_j^+ \right)} + \sum_{j=1}^2 \frac{\omega \left(k_j^- \overline{k_j^-} \right)^m}{D_k \left(k_j^- \right)} \right\} |F_m|^2. \quad (4.23)$$

Using the equation for the wave flux as a function of far field wave amplitude given in (4.20) and substituting in the multipole far-field amplitudes from (4.19), it is easy to show that the one dimensional power balance equation is satisfied for all orders m :

$$\begin{aligned} \sum_{j=1}^2 J_{+j} + \sum_{j=1}^2 J_{-j} &= \frac{1}{4} \sum_{j=1}^2 \operatorname{Re} \left\{ \omega D_k \left(k_j^+ \right) \right\} \left| \frac{i \left(-ik_j^+ \right)^m F_m}{D_k \left(k_j^+ \right)} \right|^2 \\ &\quad + \frac{1}{4} \sum_{j=1}^2 \operatorname{Re} \left\{ \omega D_k \left(k_j^- \right) \right\} \left| \frac{-i \left(-ik_j^- \right)^m F_m}{D_k \left(k_j^- \right)} \right|^2 \\ &= \frac{1}{4} \operatorname{Re} \left\{ \sum_{j=1}^2 \frac{\omega \left| k_j^+ \right|^{2m} |F_m|^2}{D_k \left(k_j^+ \right)} + \sum_{j=1}^2 \frac{\omega \left| k_j^- \right|^{2m} |F_m|^2}{D_k \left(k_j^- \right)} \right\} \\ &= \Pi^{(m)}. \end{aligned}$$

4.3.3 Pressure and Potential Response

The pressure response to a multipole load F_m is obtained through the inverse transform of $\tilde{p}(k, y) = -\tilde{\eta}(k) (\omega - Uk)^2 / \gamma(k) e^{-\gamma(k)|y|}$ and its higher order derivatives w.r.t. to the source variable

$$\frac{\partial^m}{\partial x_s^m} p(x, y) \equiv p^{(m)}(x, y) = \frac{1}{2\pi} \int_{\Gamma_k} \frac{-(\omega - Uk)^2 (-ik)^m F_m}{\gamma(k) D(k, \omega)} e^{ik(x-x_s)} e^{-\gamma(k)|y|} dk, \quad 0 \leq m \leq 2, \quad (4.24)$$

where Γ_k is the causal integral contour introduced in chapter 2. We note that $m = 2$ is the highest order multipole source that can be evaluated by taking the differential under the integral sign at $x = x_s$ due to the fact that the denominator is of order $\gamma(k) D(k, \omega) \sim k^5$ and the entire integrand is $\sim k^{m-3}$ for $k \rightarrow \infty$. We proceed as

before and separate the contour integral into pole and branch line contributions,

$$\begin{aligned}
p_{\pm}^{(m)}(x, y) = & \sum_{j=1}^2 \frac{\mp i \left(\omega - U k_j^{\pm} \right)^2 \left(-i k_j^{\pm} \right)^m F_m e^{i k_j^{\pm} (x - x_s)}}{\gamma \left(k_j^{\pm} \right) D_k \left(k_j^{\pm} \right)} e^{-\gamma \left(k_j^{\pm} \right) |y|} \\
& + \frac{1}{2\pi} \int_0^{+\infty} \frac{i (\omega \mp i v U)^2 (\pm v)^{m-1} F_m e^{\mp v (x - x_s)} e^{\pm i v |y|}}{D(\pm i v)} dv \\
& + \frac{1}{2\pi} \int_0^{+\infty} \frac{i (\omega \pm i v U)^2 (\mp v)^{m-1} F_m e^{\mp v (x - x_s)} e^{\mp i v |y|}}{D(\mp i v)} dv, \quad 0 \leq m \leq 2, \quad (4.25)
\end{aligned}$$

where the upper and lower signs \pm again refer to the upper and lower inequalities $x \gtrless x_s$, or to the response upstream or downstream of the drive point, respectively. The branch line integrals are only fully convergent for $m < 3$ and, in contrast to the inverse deflection transform, the additional branch cut term $\gamma(k)$ prevents the denominator augmentation technique from working in this instance. And for good reason! The pressure is in fact discontinuous for $m = 3$ at the source, as can be seen from figure 4.5, in which a finite difference based approach (see below) has been used to evaluate the $m = 3$ pressures close to the source.

In figure 4.5, we use the integral expression in (4.25) to evaluate $p_{\pm}^{(3)}(x)$ for response points sufficiently far from the drive point. In practice, we have found that $|x - x_s| > 1$ provides sufficient decay in the $e^{-v|x-x_s|}$ term for fast convergence as $v \rightarrow \infty$. For points closer to the source, or for $|x - x_s| \leq 1$ including $x = x_s$, we use the second order accurate one-sided finite difference formula

$$\begin{aligned}
\frac{\partial^{\pm 3} I_p(x)}{\partial x^3} \approx & \pm (-1)^3 (-5 I_p(x) + 18 (I_p(x) + \Delta x) - 24 (I_p(x) + 2\Delta x) \\
& + 14 (I_p(x) + 3\Delta x) - 3 (I_p(x) + 4\Delta x)) / (2\Delta x^3),
\end{aligned}$$

where

$$\begin{aligned}
I_p(x) \equiv & + \frac{1}{2\pi} \int_0^{+\infty} \frac{i (\omega \mp i v U)^2 F_m e^{\mp v (x - x_s)} e^{\pm i v |y|}}{(\pm v) D(\pm i v)} dv \\
& + \frac{1}{2\pi} \int_0^{+\infty} \frac{i (\omega \pm i v U)^2 F_m e^{\mp v (x - x_s)} e^{\mp i v |y|}}{(\mp v) D(\mp i v)} dv,
\end{aligned}$$

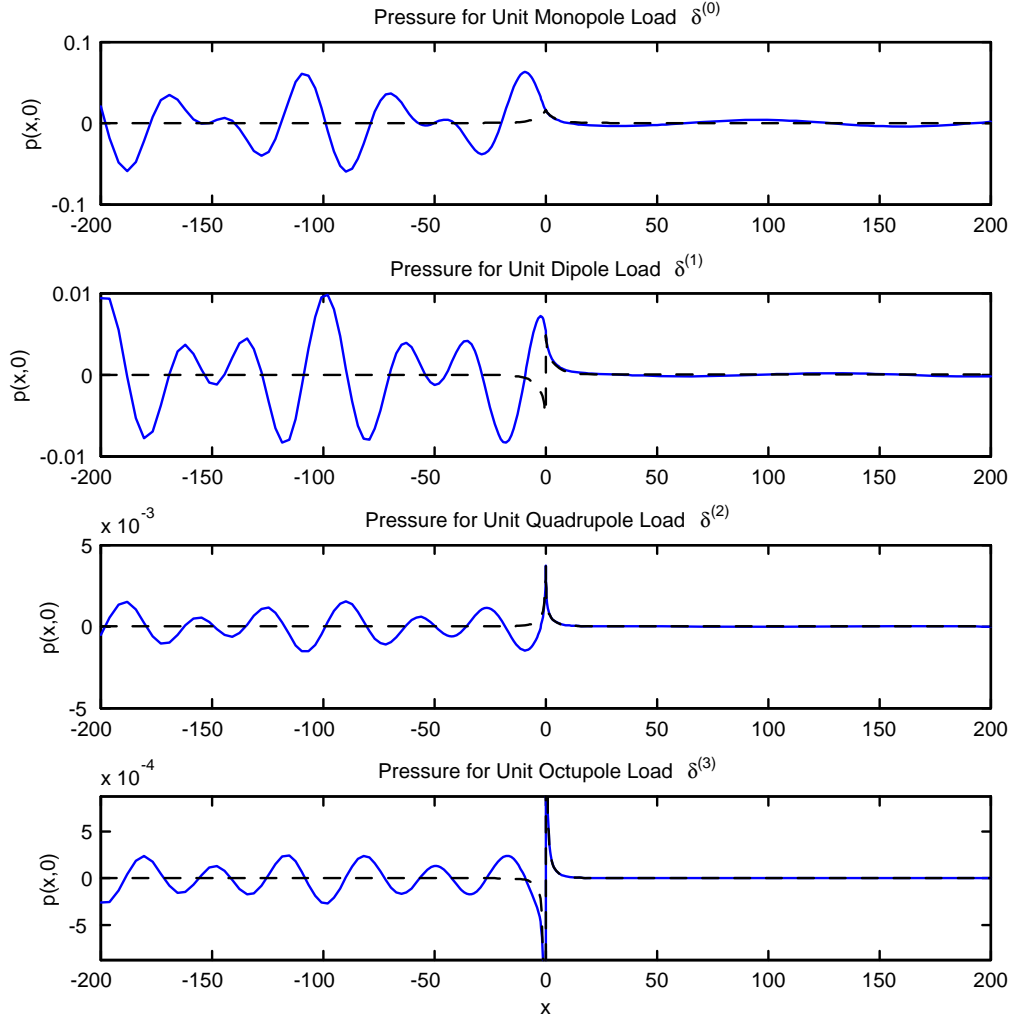


Figure 4.5: Spatial pressure response (pole and branch cut contributions) at $y = 0$ for unit multipole loads applied at $x = 0$, for $\omega = 0.002$ and $U = 0.05, T = U^2, \lambda = 0$. Dashed lines represent the pressure near-field (branch cut contributions) alone.

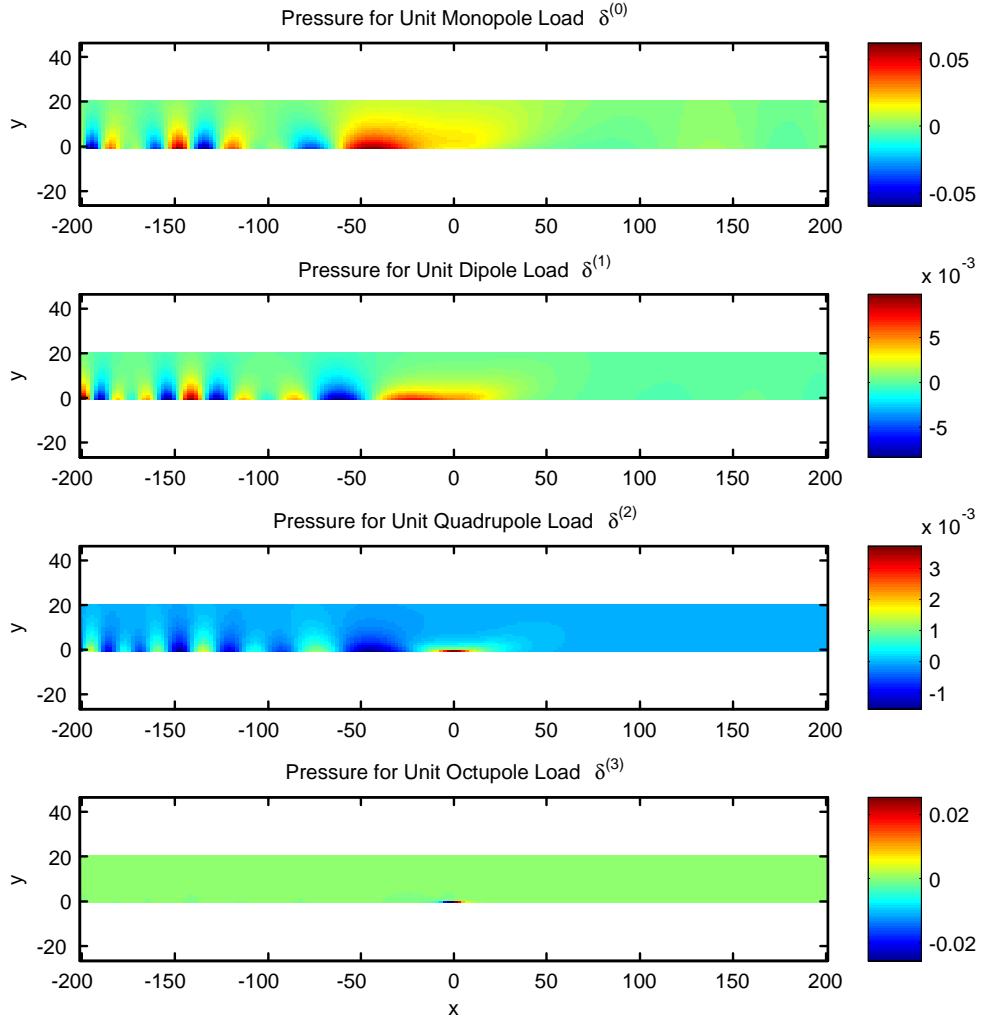


Figure 4.6: Two dimensional pressure response (pole and branch cut contributions) for unit multipole loads applied at $x = 0$, for $\omega = 0.002$ and $U = 0.05$, $T = U^2$, $\lambda = 0$.

to evaluate the third order derivative of the branch line contribution, having used (4.25) to evaluate the ‘zero’ order integrals in $I_p(x)$ above.

Figure 4.6 has the two dimensional pressure response for the same response parameters and shows the decay away from the plate surface into the fluid. Figures 4.5 and 4.6 highlight a very important property of the pressure response: the downstream travelling waves carry significantly less pressure than the upstream travelling waves. This is due entirely to the fact that in the frequency range of interest, downstream travelling disturbances are convected at nearly the flow speed U and therefore represent a pressure release boundary for the fluid. Mathematically, this is embodied in the $(\omega - Uk)^2$ factor in the pressure equation (4.25) which is exceedingly small for all downstream propagating waves whose phase velocities are U to leading order.

In similar fashion, the potential response to a multipole load F_m is obtained through the inverse transform of $\tilde{\varphi}(k, y) = i\tilde{\eta}(k)(\omega - Uk)/\gamma(k)e^{-\gamma(k)|y|}$ and its higher order derivatives. However, the numerator is now of lower order in k and the entire integrand varies as $\sim k^{m-4}$ for $k \rightarrow \infty$. Separating the contour integral into pole and branch line contributions, we obtain an expression that converges for all multipole orders of interest:

$$\begin{aligned} \varphi_{\pm}^{(m)}(x, y) = & \sum_{j=1}^2 \frac{\mp (\omega - Uk_j^{\pm}) (-ik_j^{\pm})^m F_m e^{ik_j^{\pm}(x-x_s)}}{\gamma(k_j^{\pm}) D_k(k_j^{\pm})} e^{-\gamma(k_j^{\pm})|y|} \\ & + \frac{1}{2\pi} \int_0^{+\infty} \frac{(\omega \mp ivU)(\pm v)^{m-1} F_m e^{\mp v(x-x_s)} e^{\pm iv|y|}}{D(\pm iv)} dv \\ & + \frac{1}{2\pi} \int_0^{+\infty} \frac{(\omega \pm ivU)(\mp v)^{m-1} F_m e^{\mp v(x-x_s)} e^{\mp iv|y|}}{D(\mp iv)} dv, \quad 0 \leq m \leq 3. \end{aligned}$$

4.4 Scattering from Representative Discontinuities

A scattering coefficient is defined as the ratio of the scattered far-field wave amplitude to the incident wave amplitude. A scattering matrix \mathbf{S} operates on a vector of incident

wave amplitudes to produce a vector of transmitted and reflected wave amplitudes, or

$$\begin{bmatrix} A_{+1}^{scat} \\ A_{+2}^{scat} \\ A_{-1}^{scat} \\ A_{-2}^{scat} \end{bmatrix} = \begin{bmatrix} S_{11} & S_{12} & \cdots & S_{14} \\ S_{21} & \ddots & & \\ \vdots & & & \\ S_{41} & & & S_{44} \end{bmatrix} \begin{bmatrix} A_{+1}^{inc} \\ A_{+2}^{inc} \\ A_{-1}^{inc} \\ A_{-2}^{inc} \end{bmatrix}, \quad (4.26)$$

where the suffixes on the wave amplitudes refer to the type of wave, characterized by its wavenumber, that is incident or scattered. For instance, the scattering coefficient $S_{12} = A_{+1}^{scat}/A_{+2}^{inc}$ represents the ratio of wave amplitudes for a scattered wave k_1^+ due to an incident wave k_2^+ . Since both waves are downstream travelling, S_{12} is a transmission coefficient. The scattering matrix can therefore be divided into transmission and reflection sub-matrices as follows

$$\mathbf{S} = \begin{bmatrix} T^T & R^L \\ R^T & T^L \end{bmatrix}, \quad (4.27)$$

where, T^T is a 2×2 ‘trailing edge’ transmission matrix that operates on a vector of wave amplitudes incident from the upstream to produce a vector of the same waves transmitted downstream, R^L is a 2×2 ‘leading edge’ reflection matrix that operates on a vector of upstream travelling waves to generate a vector of downstream travelling waves, etc...

We will present our results in terms of the power-normalized scattering coefficients P_{ij} instead of the raw scattering coefficients defined in (4.27). The raw coefficients represent ratios of plate deflection amplitude for waves that may have widely differing wavenumbers and as a result carry significantly differing amounts of wave power per unit amplitude at a given frequency. The power normalized coefficients, on the other hand, represent ratios of scattered to incident wave-powers (Stokes, et al. 2004). The two sets of coefficients are connected by means of the wave impedances defined in equation (3.31) through the following relation

$$P_{ij} = \frac{Z_i}{Z_j} |S_{ij}|^2, \quad (4.28)$$

where, Z_j and Z_i are the wave impedances of the incident and scattered waves respectively. We note that the transformation (4.28) reduces to just the ‘magnitude squared’

for the diagonal terms of \mathbf{S} . These coefficient represent scattering between the same wave-type and are already in power normalized form.

There are several advantages to working with a power normalized scattering matrix (4.28).

1) It provides a means of determining if over-scattering is taking place. Raw scattering coefficients that are greater than unity do not necessarily indicate over-scattering, but power-normalized coefficients that exceed unity indicate that the scattered power exceeds the incident power since incident and total scattered power must balance.

2) It provides the ultimate ‘check on algebra,’ whether in the derivation of expressions for the scattering coefficients or in their numerical evaluation. As shown in section 4.5 below, conservation of energy requires that the net power scattered is equal to the incident power. This in turn requires that the sum of all power normalized coefficients down each column of the matrix \mathbf{P} given in (4.28) is unity. This must hold at all frequencies for neutral waves, as long as the proper sign of the wave energy is retained in the wave impedance while normalizing the scattering coefficients. Any deviation from unity indicates that something is amiss.

Of course, the phenomenon of over-scattering is closely related to the property of energy conservation and follows from the existence of negative energy waves (Acheson 1979). An incident positive energy wave may ‘over-scatter’ into another positive energy wave with more power if one or more negative energy waves are also generated during the scattering process.

There is a three step process for obtaining scattering coefficients for a given plate discontinuity:

1) Apply the structural boundary conditions at the discontinuity to the total displacement $\eta = \eta_{inc} + \eta_{scat}$ via (4.4) and solve for the unknown multipole strengths in terms of the incident wave amplitudes.

2) Combine the multipole load amplitudes to obtain the far field scattered response through (4.19).

3) Assemble the scattering matrix by dividing each scattered wave amplitude by the incident wave amplitude and adding ‘1’ to each self scattering term, i.e., to the

transmitted terms along the diagonal of (4.28) because transmission is defined as the sum of the scattered and incident waves.

In what follows we will present results for a series of different plate discontinuities.

4.4.1 Break in Plate

A break or a ‘closed crack’ in the plate at $x = 0$ is produced by imposing a zero moment and zero transverse force condition at both edges, or

$$\frac{\partial^2}{\partial x^2} \eta = 0, \quad x = \pm 0, \quad (4.29a)$$

$$\frac{\partial^3}{\partial x^3} \eta - T \frac{\partial}{\partial x} \eta = 0, \quad x = \pm 0 \quad (4.29b)$$

respectively. We note that the tension does not contribute linear terms to the moment.

The transverse forces at both edges are zero, and so is the ‘jump’ in the transverse force across the edge. Therefore the coefficient of the monopole load in (4.4) is zero. For $T = 0$, the moment edge condition (4.29a) would have implied that the dipole source strength in (4.4) is also zero. However, with non-zero tension, the dipole strength is finite and given by $T \Delta [\eta(0)]$, as shown below .

We set $\Delta f_1 = 0$ in (4.4) and write the scattered field as a superposition of responses due to dipole, quadrupole and octupole sources on the equivalent infinite plate

$$\eta_{scat}^{\pm}(x) = \Delta f_1 G_{\pm}^{(1)}(x) + \Delta f_2 G_{\pm}^{(2)}(x) + \Delta f_3 G_{\pm}^{(3)}(x). \quad (4.30)$$

Assuming an incident displacement field of the form $\eta_{inc} = I e^{ik_j x}$ and writing the ‘total’ displacement field as $\eta = \eta_{inc} + \eta_{scat}$, the edge conditions yield the following pair of equations per edge

$$\begin{aligned} \Delta f_1 \partial^3 G_{\pm}^{(1)}(0) + \Delta f_2 \partial^3 G_{\pm}^{(2)}(0) + \Delta f_3 \partial^3 G_{\pm}^{(3)}(0) &= I k_j^2 \\ \Delta f_1 \left[\partial^3 G_{\pm}^{(1)}(0) - T \partial G_{\pm}^{(1)}(0) \right] + \Delta f_2 \left[\partial^3 G_{\pm}^{(2)}(0) - T \partial G_{\pm}^{(2)}(0) \right] \\ + \Delta f_3 \left[\partial^3 G_{\pm}^{(3)}(0) - T \partial G_{\pm}^{(3)}(0) \right] &= i I k_j (k_j^2 + T). \end{aligned}$$

These constitute four equations, but only three are linearly independent due to the special relationships between the one-sided Green’s functions given in (4.15) and (4.16).

The three independent equations are

$$\begin{aligned}\Delta f_1 + T\Delta f_3 &= 0, \\ \Delta f_1 \partial^2 G_-^{(1)}(0) + \Delta f_2 \partial^2 \widehat{G}^{(2)}(0) + \Delta f_3 \partial^2 G_-^{(3)}(0) &= Ik_j^2, \\ \Delta f_1 \left[\partial^3 \widehat{G}^{(1)}(0) - T\partial \widehat{G}^{(1)}(0) \right] + \Delta f_2 \left[\partial^3 G_-^{(2)}(0) - T\partial G_-^{(2)}(0) \right] \\ + \Delta f_3 \left[\partial^3 \widehat{G}^{(3)}(0) - T\partial \widehat{G}^{(3)}(0) \right] &= iIk_j (k_j^2 + T).\end{aligned}$$

As noted earlier, the dipole source Δf_1 only exists for non-zero tension T and its strength is proportional to the octupole source Δf_3 . Eliminating Δf_1 from the other two equations, we can solve for the quadrupole and octupole source strengths. After some simplifications, we find the following expressions for the multipole strengths due to a break in the plate:

$$\begin{aligned}\Delta f_3 &= \frac{-\left[\partial^3 G_-^{(2)} - T\partial G_-^{(2)}\right] Ik_j^2 + \partial^2 \widehat{G}^{(2)} iIk_j (k_j^2 + T)}{Det}, \\ \Delta f_2 &= \frac{\left[\partial^3 \widehat{G}^{(3)} - 2T\partial^2 \widehat{G}^{(3)} + T^2\partial \widehat{G}^{(1)}\right] Ik_j^2 + \left[\partial^3 G_-^{(2)} - T\partial G_-^{(2)}\right] iIk_j (k_j^2 + T)}{Det}, \\ \Delta f_1 &= -T\Delta f_3, \quad \Delta f_0 = 0,\end{aligned}\tag{4.31}$$

where

$$Det = \partial^2 \widehat{G}^{(2)} \left[\partial^3 \widehat{G}^{(3)} - 2T\partial^2 \widehat{G}^{(3)} + T^2\partial \widehat{G}^{(1)} \right] + \left[\partial^3 G_-^{(2)} - T\partial G_-^{(2)} \right],$$

and all Green's functions are understood to be evaluated at $x = 0$.

The reflection and transmission coefficients are obtained by substituting the multipole strengths solved in (4.31) back into the equivalent of (4.30) with the Green's functions replaced by their corresponding multipole far-field amplitude functions given in (4.19). The power normalized scattering coefficients as a function of frequency are plotted in figure (4.7) for all four incident waves. The spatial response upstream and downstream of the scatterer is plotted in figure (4.8) for a fixed frequency of $\omega = 0.002$.

As can be seen in figures 4.7a and 4.7c, this type of discontinuity is highly transmissive for waves incident from the upstream; the power-normalized transmission coefficient for k_1^+ and k_2^+ are very close to unity, while those for the other waves are at least 10 dB lower. This can also be seen directly in the spatial response of figure

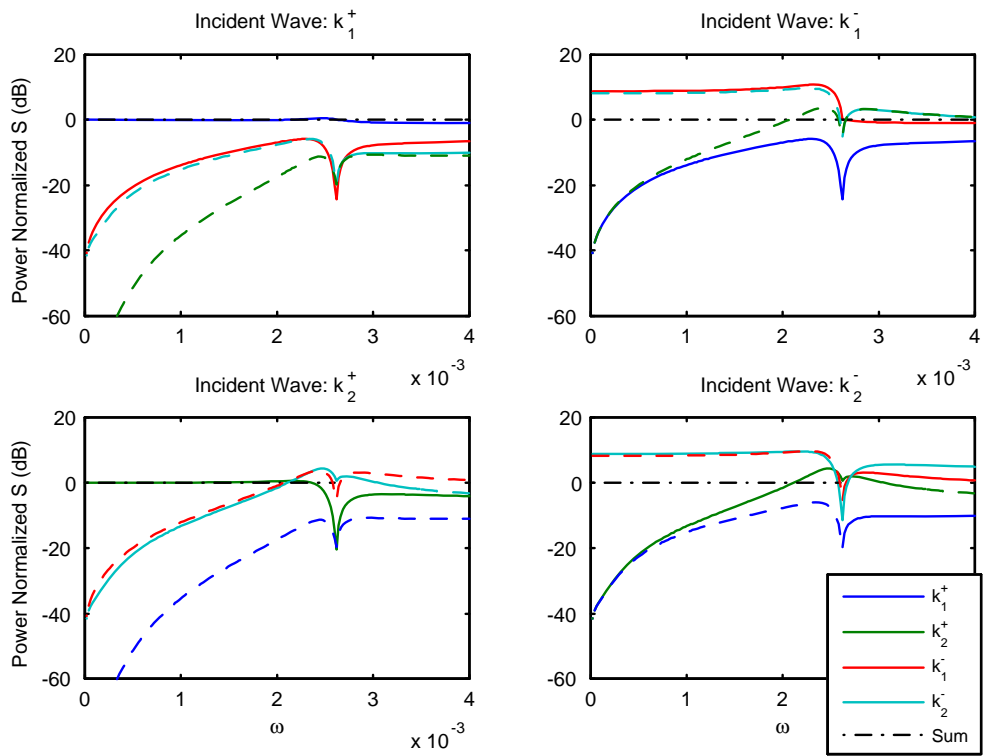


Figure 4.7: Power normalized scattering coefficients for a 'free-free' joint for $U = 0.05, T = U^2, \lambda = 0$ (dispersion plot of figure 2.4c). Dashed lines represent power scattered between incident and scattered waves of different energy sign.

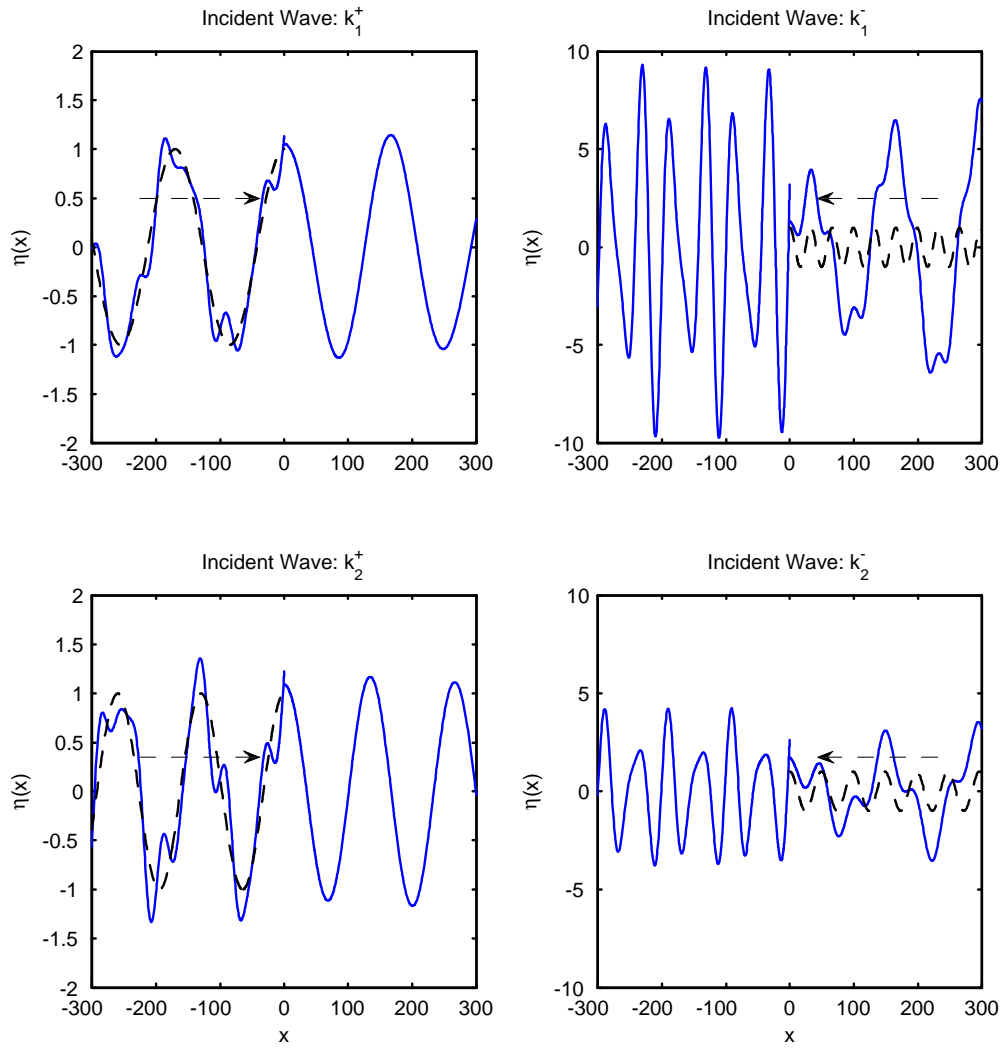


Figure 4.8: Spatial response for scattering by a 'free-free' joint at $\omega = 0.002$ and for $U = 0.05, T = U^2, \lambda = 0$. Dashed line represents a wave of unit amplitude incident from upstream or downstream.

4.8a where the incident wave (dashed, black) is transmitted across the discontinuity virtually unaltered, while the total deflection in $x < 0$ is only slightly distorted by the small-amplitude reflected waves. The wave impedance of a downstream propagating wave is dominated by the fluid based fluxes in the frequency range under consideration. As a result, the structural break in the plate does not present a significant impedance change and the incident wave is transmitted virtually intact.

In contrast, waves incident from downstream are over-transmitted and propagate upstream (e.g. wavenumber k_1^-) at significantly amplified levels over the range of frequencies that support negative energy waves ($\omega < \omega_p$). This can be seen by the significantly larger wave amplitudes in the transmitted region $x < 0$ (figure 4.8b). This corresponds to the power-normalized reflection and transmission coefficients in the corresponding figure 4.7b; for the frequency considered ($\omega = 0.002$) the transmitted waves k_1^- and k_2^- have amplitudes greater than unity. A similarly set of observations hold for figures 4.7d and 4.8d.

The power sum of all the waves scattered is represented by the dashed line in the figure 4.7 and is identically equal to 1 (0 dB). The generation of negative energy waves during the scattering process has therefore resulted in ‘over-scattering.’

4.4.2 Clamped Constraint

A clamped joint constrains the plate translationally and rotationally. The structural conditions at both edges are

$$\begin{aligned} \eta &= 0 & x = \pm 0, \\ \frac{\partial}{\partial x} \eta &= 0 & x = \pm 0. \end{aligned}$$

This type of constraint is therefore equivalent to applying monopole and dipole loads with the following strengths

$$\begin{aligned} \Delta f_0 &= \frac{-I \partial \widehat{G}^{(1)} + i k_j I \widehat{G}^{(1)}}{\left[\partial \widehat{G} \right]^2 + \widehat{G} \partial \widehat{G}^{(1)}}, \\ \Delta f_1 &= \frac{I \partial \widehat{G} + i k_j I \widehat{G}}{\left[\partial \widehat{G} \right]^2 + \widehat{G} \partial \widehat{G}^{(1)}}. \end{aligned} \tag{4.32}$$

The power normalized scattering coefficients are given in figure 4.9 and the spatial response for a fixed frequency is plotted in figure 4.10. As can be clearly seen from these figures, a clamped constraint is highly reflective for both upstream and downstream incident waves. Reflections are amplified (i.e., over-reflection) for both upstream (figures 4.9-4.10 a & c) and downstream (figures 4.9-4.10 b & d) incident waves for frequencies over which negative energy waves exist ($\omega < \omega_p$). Travelling waves incident from upstream are over-transmitted through the junction and propagate downstream at significantly amplified levels (figures 4.9-4.10 a & c). The power sum of all the waves scattered is represented by the dashed line in the figure and is once again identically equal to 1 (0 dB). The generation of waves with relatively large amplitudes and with opposite sign of the wave energy during the scattering process has resulted in both significant ‘over-reflection’ and ‘over-transmission.’

4.4.3 Free-Clamped Discontinuity

A discontinuity in the plate that is free at the upstream edge $x = -0$ and clamped at the downstream edge $x = +0$ obeys the structural edge conditions

$$\frac{\partial^2}{\partial x^2} \eta = 0, \quad x = -0, \quad (4.33a)$$

$$\frac{\partial^3}{\partial x^3} \eta - T \frac{\partial}{\partial x} \eta = 0, \quad x = -0, \quad (4.33b)$$

$$\eta = 0, \quad x = +0, \quad (4.33c)$$

$$\frac{\partial}{\partial x} \eta = 0, \quad x = +0. \quad (4.33d)$$

The scattered field in this case must be written in terms of all four multipole loads in (4.4), yielding four equations in four unknowns, most conveniently expressed in matrix form as

$$\begin{bmatrix} G_+ & G_+^{(1)} & G_+^{(2)} & G_+^{(3)} \\ \partial G_+ & \partial G_+^{(1)} & \partial G_+^{(2)} & \partial G_+^{(3)} \\ \partial^2 G_- & \partial^2 G_-^{(1)} & \partial^2 G_-^{(2)} & \partial^2 G_-^{(3)} \\ \partial^2 G_- & \partial^2 G_-^{(1)} & \partial^2 G_-^{(2)} & \partial^2 G_-^{(3)} \\ -T \partial G_- & -T \partial^{(1)} G_- & -T \partial^{(2)} G_- & -T \partial^{(3)} G_- \end{bmatrix} \begin{bmatrix} \Delta f_0 \\ \Delta f_1 \\ \Delta f_2 \\ \Delta f_3 \end{bmatrix} = \begin{bmatrix} -I \\ -iIk_j \\ Ik_j^2 \\ iIk_j (k_j^2 + T) \end{bmatrix}. \quad (4.34)$$

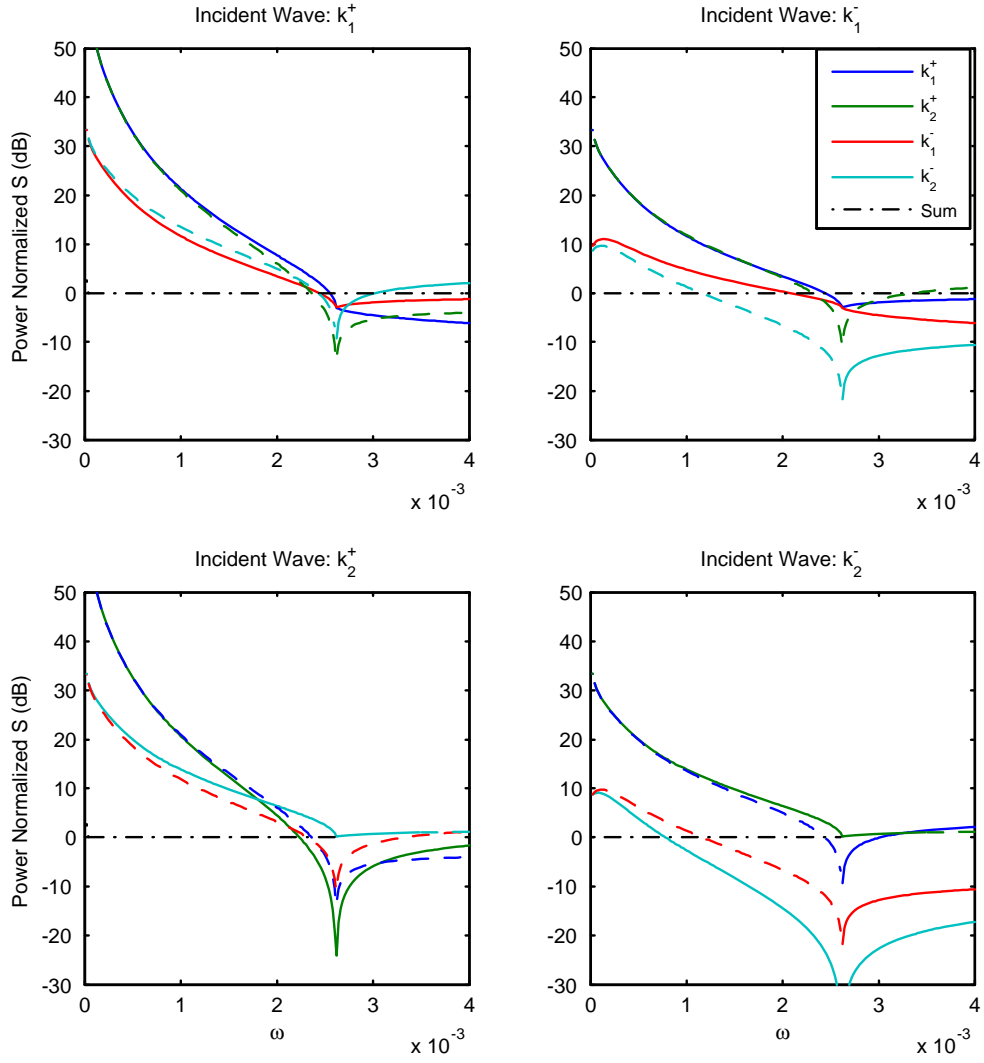


Figure 4.9: Power normalized scattering coefficients for a ‘clamped’ constraint for $U = 0.05, T = U^2, \lambda = 0$ (dispersion plot of figure 2.4c). Dashed lines represent power scattered between incident and scattered waves of different energy sign.

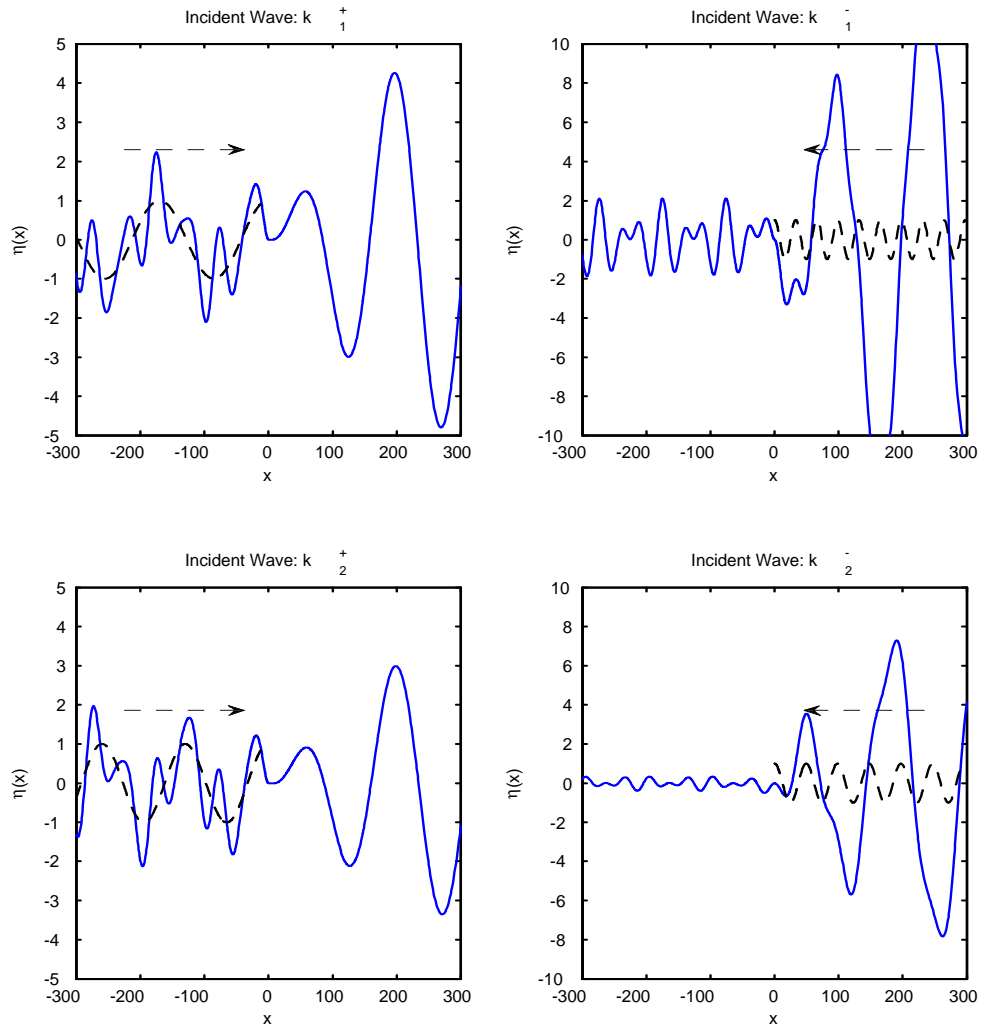


Figure 4.10: Spatial response for scattering by a 'clamped' constraint at $\omega = 0.002$ and for $U = 0.05, T = U^2, \lambda = 0$. Dashed line represents a wave of unit amplitude incident from upstream or downstream.

The power normalized scattering coefficients are given in figure (4.11) and the spatial response for a fixed frequency is plotted in figure (4.12). The scattering properties for this type of discontinuity are similar to those for the ‘clamped-clamped’ constraint. The levels of over-transmission experienced by upstream and downstream incident waves are almost identical for both. The amount of over-reflection, however, exceeds that for a clamped-clamped constraint.

4.4.4 Free-Hinged Discontinuity

If, instead of a clamped edge, the downstream plate has a hinged edge while the upstream edge remains free, the structural edge conditions become

$$\frac{\partial^2}{\partial x^2}\eta = 0 \quad x = -0 \quad (4.35a)$$

$$\frac{\partial^3}{\partial x^3}\eta - T\frac{\partial}{\partial x}\eta = 0 \quad x = -0 \quad (4.35b)$$

$$\eta = 0 \quad x = +0 \quad (4.35c)$$

$$\frac{\partial^2}{\partial x^2}\eta = 0 \quad x = +0. \quad (4.35d)$$

We consider this particular configuration because it may represent a good idealization for flags in tandem.

For the general case of non-zero tension, the scattered field must still be written in terms of all four multipole loads on the corresponding infinite plate (4.4). However, for $T = 0$ the coefficient of the quadrupole load reduces to the jump in the bending moment at the edge, which is identically zero. For the more general case $T \neq 0$, the multipole strengths in terms of the incident wave amplitude and wavenumber are obtained by solving the following 4×4 matrix equation

$$\begin{bmatrix} G_+ & G_+^{(1)} & G_+^{(2)} & G_+^{(3)} \\ \partial^2 G_+ & \partial^2 G_+^{(1)} & \partial^2 G_+^{(2)} & \partial^2 G_+^{(3)} \\ \partial^2 G_- & \partial^2 G_-^{(1)} & \partial^2 G_-^{(2)} & \partial^2 G_-^{(3)} \\ \partial^2 G_- & \partial^2 G_-^{(1)} & \partial^2 G_-^{(2)} & \partial^2 G_-^{(3)} \\ -T\partial G_- & -T\partial^{(1)}G_- & -T\partial^{(2)}G_- & -T\partial^{(3)}G_- \end{bmatrix} \begin{bmatrix} \Delta f_0 \\ \Delta f_1 \\ \Delta f_2 \\ \Delta f_3 \end{bmatrix} = \begin{bmatrix} -I \\ -iIk_j \\ Ik_j^2 \\ iIk_j(k_j^2 + T) \end{bmatrix}. \quad (4.36)$$

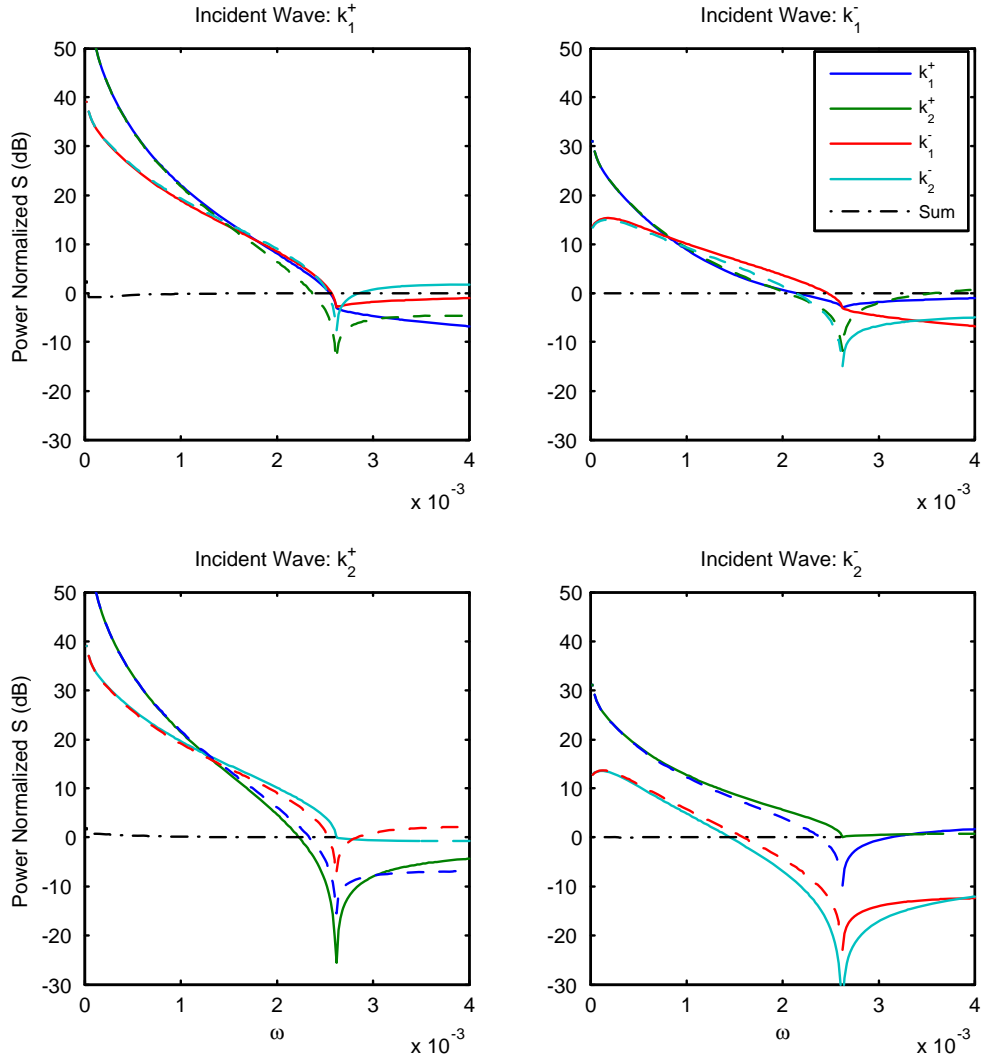


Figure 4.11: Power normalized scattering coefficients for a 'free-clamped' joint for $U = 0.05, T = U^2, \lambda = 0$ (dispersion plot of figure 2.4c). Dashed lines represent power scattered between incident and scattered waves of different energy sign.

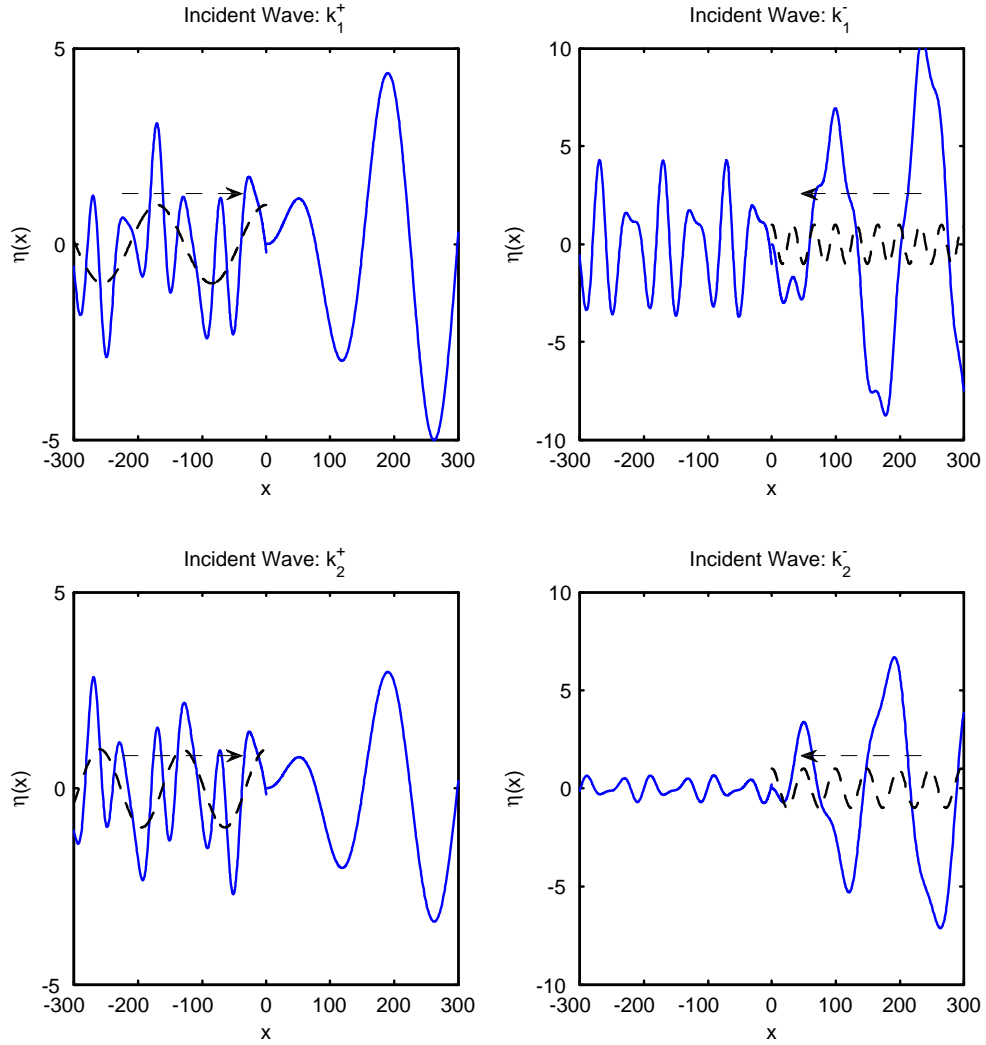


Figure 4.12: Spatial response for scattering by a 'free-clamped' joint at $\omega = 0.002$ and for $U = 0.05, T = U^2, \lambda = 0$. Dashed line represents a wave of unit amplitude incident from upstream or downstream.

The scattering coefficients and spatial response are documented in figures 4.13 and 4.14.

A ‘free-hinged’ discontinuity is in almost all respects qualitatively equivalent to a ‘free-clamped’ constraint. The ‘free-hinged’ constraint appears to be only slightly more over-reflective and over-transmissive than the ‘free-clamped’ constraint and these differences, on the order of 1-2 dB, are only manifest above $\omega = 0.001$.

4.4.5 Rotational Crack

A ‘rotational crack’ is idealized as a massless rotational spring with dimensionless spring constant K_r connecting the plate edges. The joint is assumed to have zero translational compliance (i.e., it is assumed to be infinitely rigid for transverse motions) and as a result there is continuity of displacement at the interface. The rotational spring does not carry any inertia, as a result there is continuity of transverse force and moment across $x = \pm 0$ (although the *local value* of the moment changes with the rotational stiffness). It follows that only the slope $\partial\eta/\partial x$ is discontinuous at $x = 0$. In summary, the structural conditions at the joint are

$$\eta(-0) = \eta(+0), \quad (4.37a)$$

$$K_r \left[\frac{\partial}{\partial x} \eta(+0) - \frac{\partial}{\partial x} \eta(-0) \right] = \frac{\partial^2}{\partial x^2} \eta(0), \quad (4.37b)$$

$$\frac{\partial^2}{\partial x^2} \eta(-0) = \frac{\partial^2}{\partial x^2} \eta(+0), \quad (4.37c)$$

$$\frac{\partial^3}{\partial x^3} \eta(-0) - T \frac{\partial}{\partial x} \eta(-0) = \frac{\partial^3}{\partial x^3} \eta(+0) - T \frac{\partial}{\partial x} \eta(+0). \quad (4.37d)$$

Conditions (4.37d) and (4.37a) eliminate the monopole and octupole sources, respectively ($\Delta f_0 = \Delta f_3 = 0$). Condition (4.37c) combined with (4.37a) gives $\Delta f_1 = \Delta [\partial^2 \eta(x_s) / \partial x^2] - T \Delta [\eta(x_s)] = 0$, eliminating the dipole component for all T . We therefore solve for a quadrupole load alone and find (after invoking the identity $\partial G_+^{(2)} - \partial G_-^{(2)} = 1$)

$$\Delta f_2 = - \frac{I k_j^2}{K_r - \partial^2 \widehat{G}^{(2)}}.$$

In the limit $K_r \rightarrow \infty$, $\Delta f_2 = 0$ and there is no discontinuity. In the limit $K_r \rightarrow 0$, $\Delta f_2 = I k_j^2 / \partial^2 \widehat{G}^{(2)}$ and the two edges are fully decoupled rotationally. The scattering

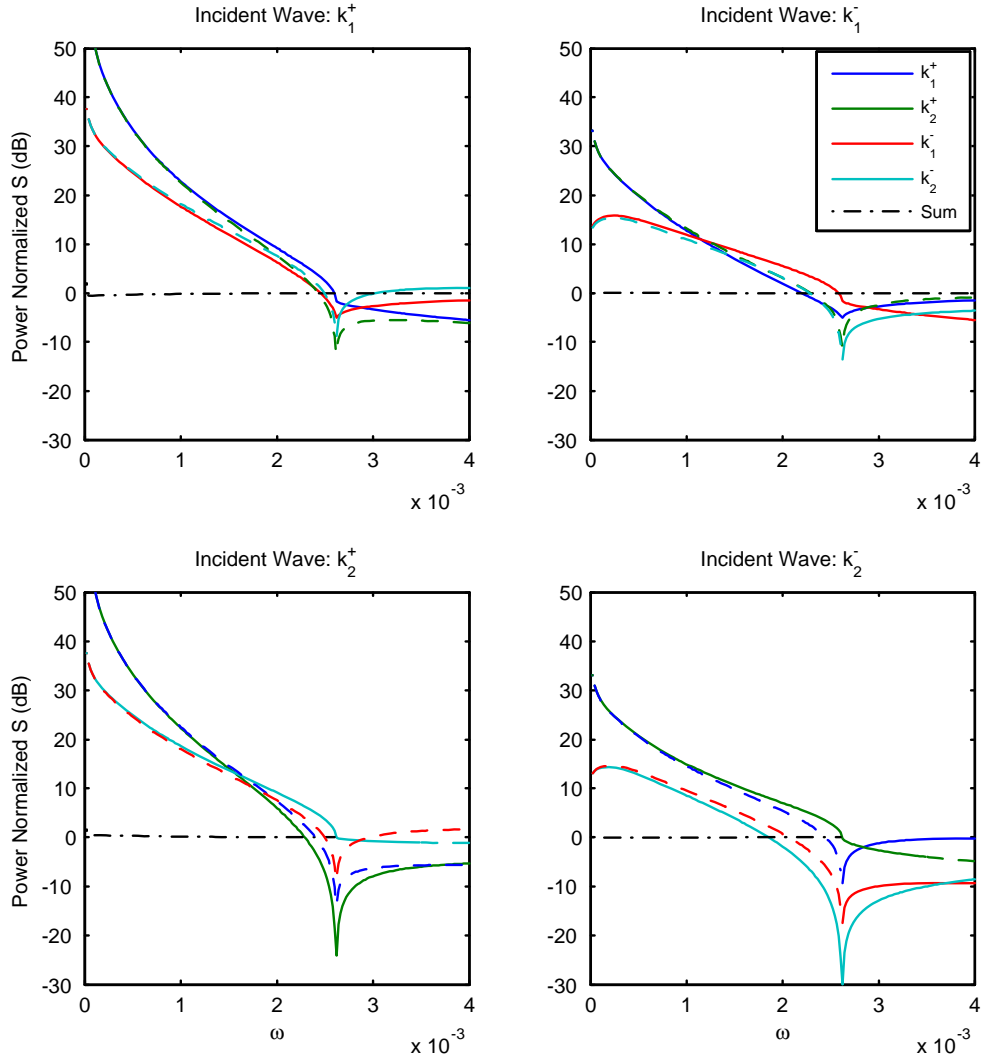


Figure 4.13: Power normalized scattering coefficients for a ‘free-hinged’ joint for $U = 0.05, T = U^2, \lambda = 0$ (dispersion plot of figure 2.4c). Dashed lines represent power scattered between incident and scattered waves of different energy sign.

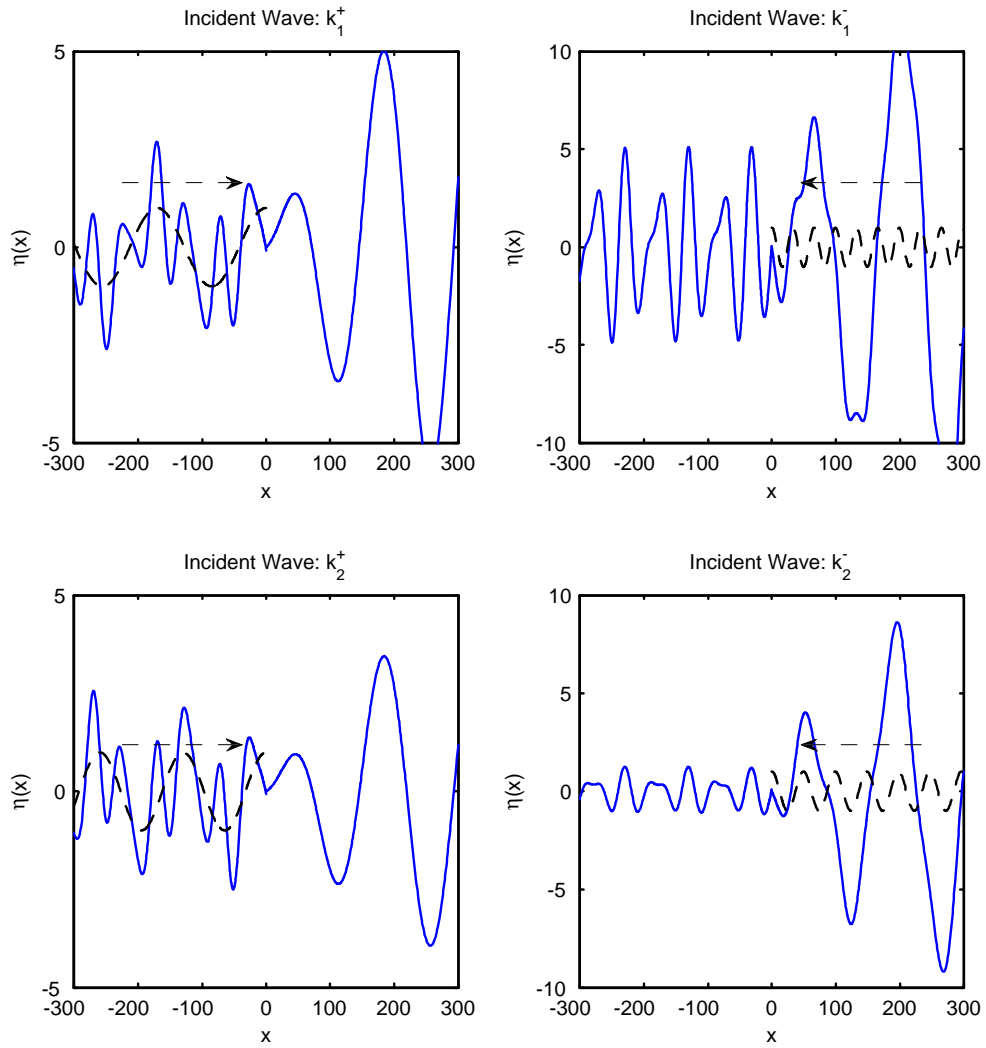


Figure 4.14: Spatial response for scattering by a 'free-hinged' joint at $\omega = 0.002$ and for $U = 0.05, T = U^2, \lambda = 0$. Dashed line represents a wave of unit amplitude incident from upstream or downstream.

coefficients and spatial response for the case $K_r = 0$ are plotted in figures 4.15 and 4.16.

This type of discontinuity is highly transmissive for upstream incident waves (figures 4.15- 4.16 a & b) and is reflective for waves incident from the downstream (figures 4.15- 4.16 c & d). It over-transmits waves incident from downstream in the frequency range over which negative energy waves are present.

4.4.6 Translational Crack

A ‘translational crack’ consists of a massless translational spring with non-dimensional stiffness K_t . It is infinitely rigid rotationally. Similar to the case of the rotational crack, there is continuity of transverse force and moment. However, instead of a discontinuity in slope, a translational crack introduces a discontinuity in deflection. The structural conditions at the joint are

$$-K_t [\eta(+0) - \eta(-0)] = \frac{\partial^3}{\partial x^3} \eta(0) - T \frac{\partial}{\partial x} \eta(0) \quad (4.38a)$$

$$\frac{\partial}{\partial x} \eta(-0) = \frac{\partial}{\partial x} \eta(+0) \quad (4.38b)$$

$$\frac{\partial^2}{\partial x^2} \eta(-0) = \frac{\partial^2}{\partial x^2} \eta(+0) \quad (4.38c)$$

$$\frac{\partial^3}{\partial x^3} \eta(-0) - T \frac{\partial}{\partial x} \eta(-0) = \frac{\partial^3}{\partial x^3} \eta(+0) - T \frac{\partial}{\partial x} \eta(+0). \quad (4.38d)$$

Conditions (4.38d) and (4.38b) eliminate the monopole and quadrupole sources, respectively ($\Delta f_0 = \Delta f_2 = 0$). Condition (4.38c) eliminates the dipole source $\Delta f_1 = \Delta [\partial^2 \eta(0) / \partial x^2] - T \Delta [\eta(0)]$ for the special case where the pre-tension is zero. For the more general case where $T \neq 0$, we solve for both a dipole and quadrupole source and find

$$\Delta f_1 = -T \Delta f_3 \quad (4.39a)$$

$$\Delta f_3 = \frac{ik_j (k_j^2 + T)}{K_t + [\partial^3 \widehat{G}^{(3)} + T^2 \partial \widehat{G}^{(1)}]} \quad (4.39b)$$

Note that as $K_t \rightarrow \infty$, $\Delta f_1 = \Delta f_3 = 0$ as expected.

This type of discontinuity is the most transmissive of all the ones tested for upstream incident waves even in the limit $K_r = 0$, as shown in figures 4.17 and 4.18.

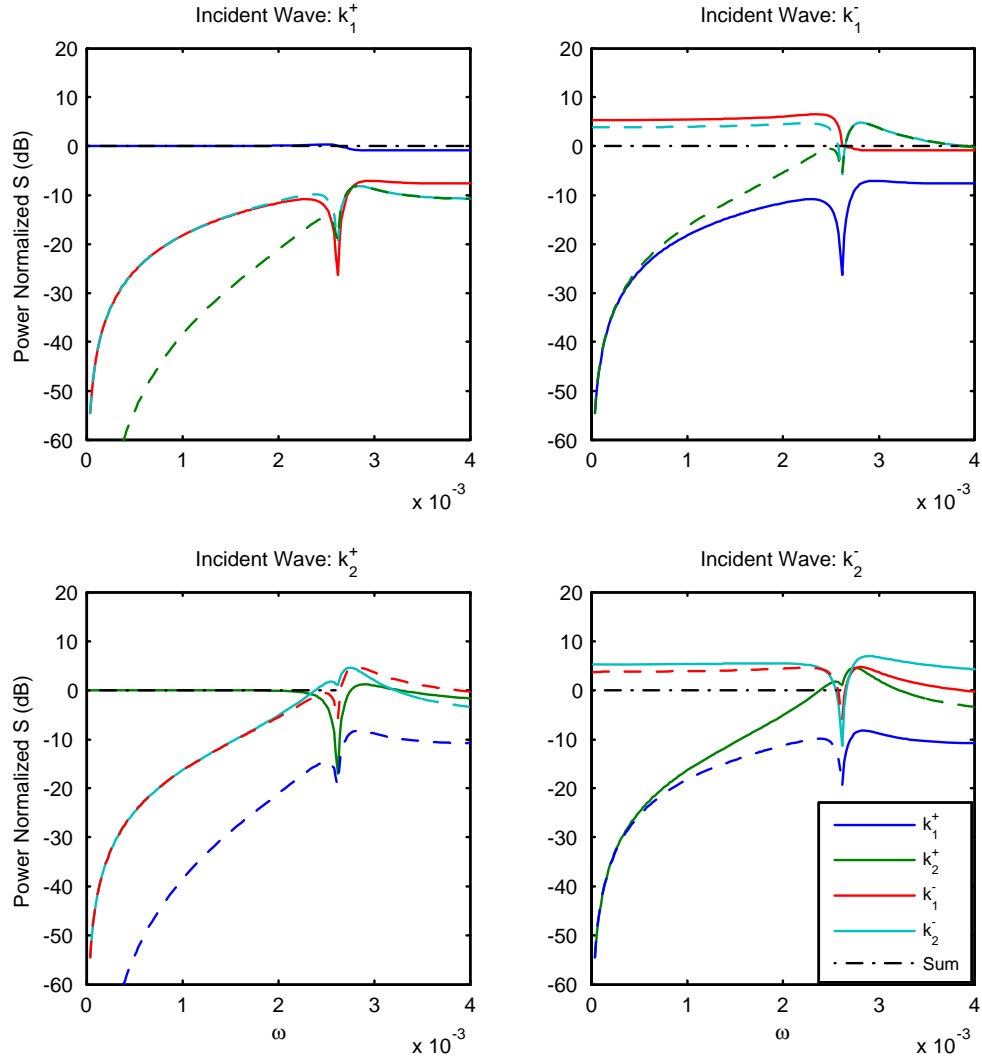


Figure 4.15: Power normalized scattering coefficients for a ‘rotational crack’ of infinite rotational compliance ($K_r = 0$) for $U = 0.05, T = U^2, \lambda = 0$ (dispersion plot of figure 2.4c). Dashed lines represent power scattered between incident and scattered waves of different energy sign.

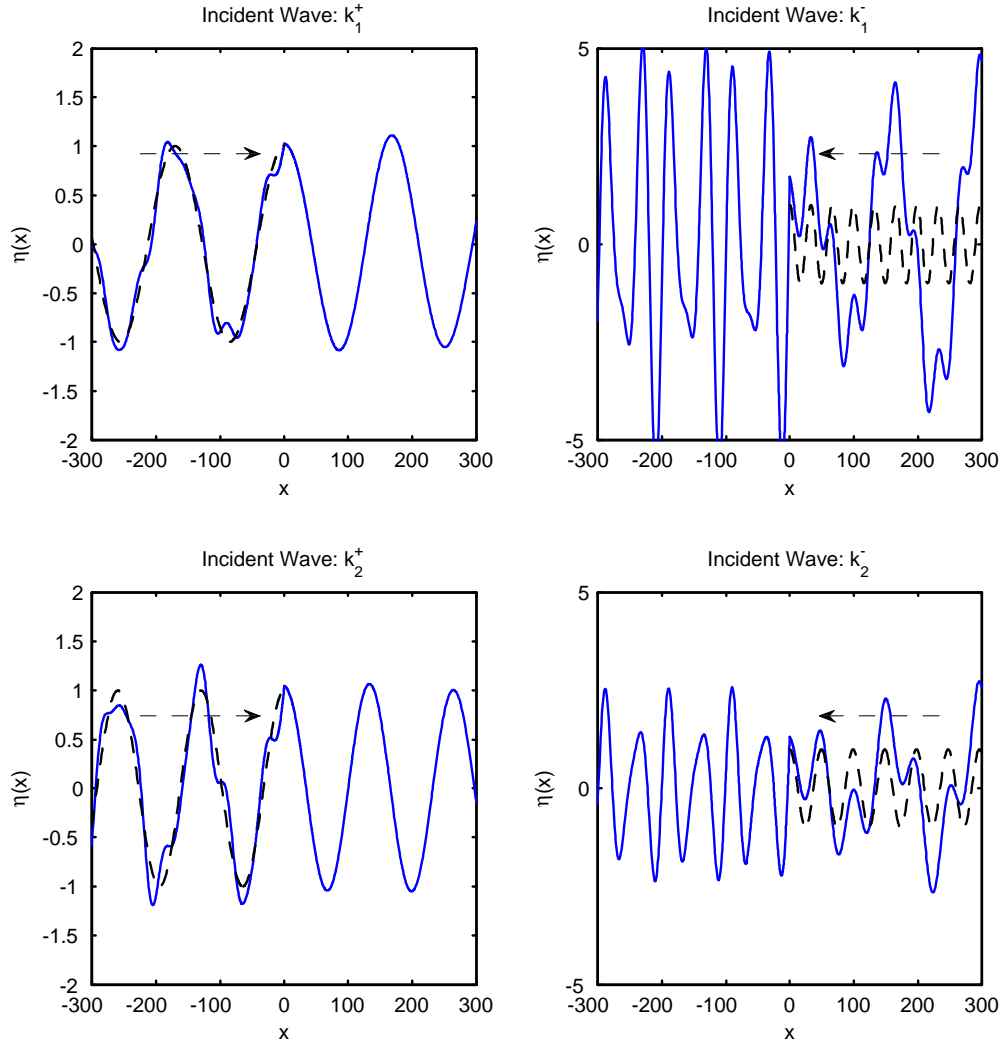


Figure 4.16: Spatial response for scattering by a 'rotational crack' of infinite rotational compliance ($K_r = 0$) at $\omega = 0.002$ and for $U = 0.05, T = U^2, \lambda = 0$. Dashed line represents a wave of unit amplitude incident from upstream or downstream.

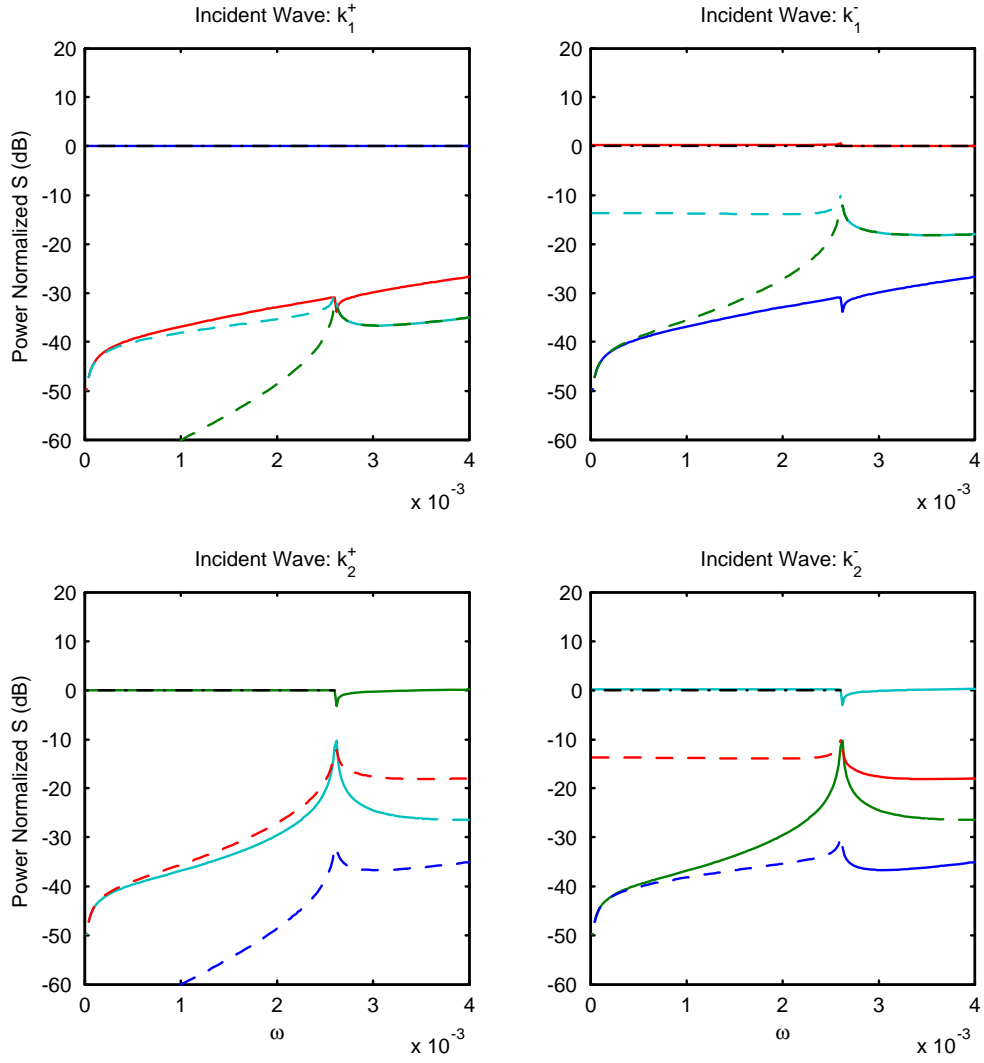


Figure 4.17: Power normalized scattering coefficients for a ‘translational crack’ of infinite translational compliance ($K_t = 0$) for $U = 0.05$, $T = U^2$, $\lambda = 0$ (dispersion plot of figure 2.4c). Dashed lines represent power scattered between incident and scattered waves of different energy sign.

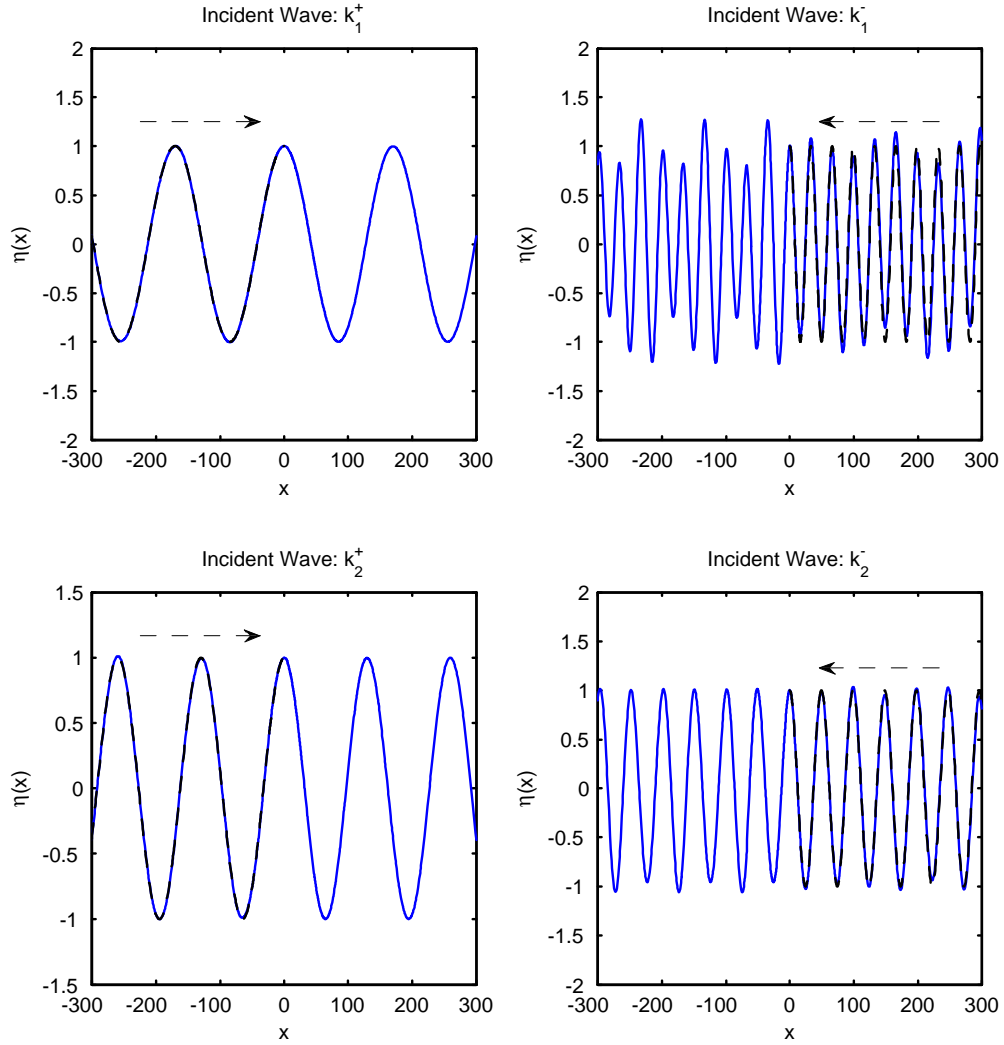


Figure 4.18: Spatial response for scattering by a 'translational crack' of infinite translational compliance ($K_t = 0$) at $\omega = 0.002$ and for $U = 0.05, T = U^2, \lambda = 0$. Dashed line represents a wave of unit amplitude incident from upstream or downstream.

4.4.7 Pinned Constraint

A pinned or hinged joint constrains the plate only translationally. The structural boundary conditions at both edges are zero displacement, zero bending moment and continuity of slope (since we don't permit buckling of the plate at the constraint)

$$\eta = 0 \quad x = \pm 0, \quad (4.40a)$$

$$\frac{\partial}{\partial x}\eta(-0) = \frac{\partial}{\partial x}\eta(+0), \quad (4.40b)$$

$$\frac{\partial^2}{\partial x^2}\eta = 0 \quad x = \pm 0. \quad (4.40c)$$

Conditions (4.40a) and (4.40b) ensure that the octupole and quadrupole source strengths are zero. Condition (4.40c) combined with (4.40a) ensures that the dipole strength $\Delta f_1 = \Delta [\partial^2 \eta(0) / \partial x^2] - T \Delta [\eta(0)]$ is zero. We therefore seek a solution involving a monopole load only and find

$$\Delta f_0 = \frac{-I}{\widehat{G}}. \quad (4.41)$$

We note that the load strength is independent of the incident wavenumber k_j . The results are plotted in figures 4.19 and 4.20.

It is worth comparing the scattering properties of a hinged constraint with that of a clamped constraint given earlier in figures 4.9-4.10. Although a sweeping generalization that is valid over all frequencies and wavetypes is hard to make, we can say that a hinged support is generally less over-reflective and over-transmissive than a clamped support. The differences are on the order of 10 dB at low frequencies and less so around $\omega = \omega_p$. This could have been expected. A hinged support constrains the plate only translationally whereas a clamped support constrains it both translationally and rotationally thereby providing a larger impedance discontinuity to an incident wave resulting in a more powerful scattering process.

What may have been less obvious is that a hinged constraint generally scatters relatively more wave power downstream compared with a clamped constraint. This can be explained as follows. A hinged constraint is a pure monopole scatterer whereas a clamped constraint is a combination of a monopole and a dipole. Given that higher order multipoles scatter comparatively more power into upstream waves (see section 4.3.1 above), the dipole component of the clamped support provides it with relatively

more scattered power into upstream travelling waves compared with the pure monopole of a hinged constraint.

4.5 Power Balance

Power balance or energy conservation during the scattering process requires that the total wave power scattered is equal to the power carried by the incident wave minus any mechanical energy injected into, or removed from, the plate-fluid system at the discontinuity. This may be due to dissipation at the joint or power loss to an attached dashpot. For a lossless or ‘conservative’ scattering process, the total power scattered, including the total transmitted wave-field, must equal the incident wave power.

For an incident wave $\eta_{inc} = I_j e^{ik_j x}$, the total power including the incident power can be written in terms of the far-field wave amplitudes (using (4.20)) as

$$J_{total} = \sum_{n=1}^4 \frac{1}{4} \operatorname{Re} \{ \omega D_k(k_n) \} |A_n|^2 + \frac{1}{4} \operatorname{Re} \{ \omega D_k(k_j) \} |I_j|^2 + \frac{1}{4} \operatorname{Re} \{ \omega D_k(k_j) \} \operatorname{Re} \{ 2A_j \bar{I}_j \}. \quad (4.42)$$

The final term arises from the interaction (i.e., amplitude sum) between the incident wave and the scattered wave having the same wavenumber $n = j$ on the transmitted side of the discontinuity. In terms of the applied multipole loads, the total wave flux can be written as (using (4.21))

$$J_{total} = \frac{1}{4} \sum_{n=1}^4 \sum_{m=0}^3 \operatorname{Re} \left\{ \frac{\omega}{D_k(k_n)} \right\} |k_n|^{2m} |\Delta f_m|^2 + \frac{1}{4} \operatorname{Re} \{ \omega D_k(k_j) \} |I_j|^2 + \frac{1}{4} \sum_{m=0}^3 \operatorname{Re} \{ i\omega (-ik_j)^m 2\Delta f_m \bar{I}_j \}. \quad (4.43)$$

Interchanging the order of summation in the leading term, and observing that the summation over the four scattered waves involved can be written in terms of the real part of the drive point admittance as

$$\sum_{n=1}^4 \frac{1}{2} \operatorname{Re} \left\{ \frac{\omega}{D_k(k_n)} \right\} |k_n|^{2m} = -\operatorname{Re} \left\{ -i\omega \partial^m \widehat{G}^{(m)} \right\}, \quad (4.44)$$

the power balance equation, $J_{total} - J_{incident} = 0$, that must hold for a conservative

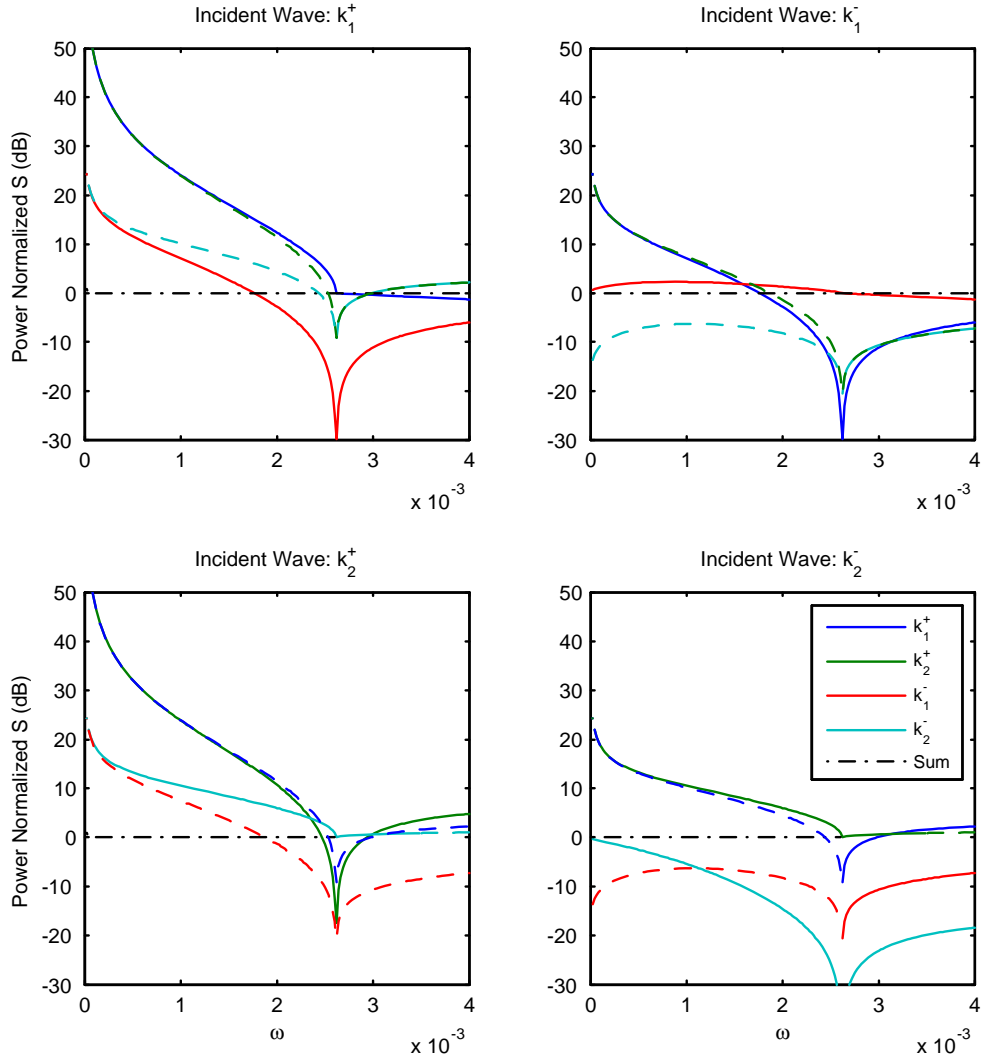


Figure 4.19: Power normalized scattering coefficients for a 'hinged' joint for $U = 0.05, T = U^2, \lambda = 0$ (dispersion plot of figure 2.4c). Dashed lines represent power scattered between incident and scattered waves of different energy sign.

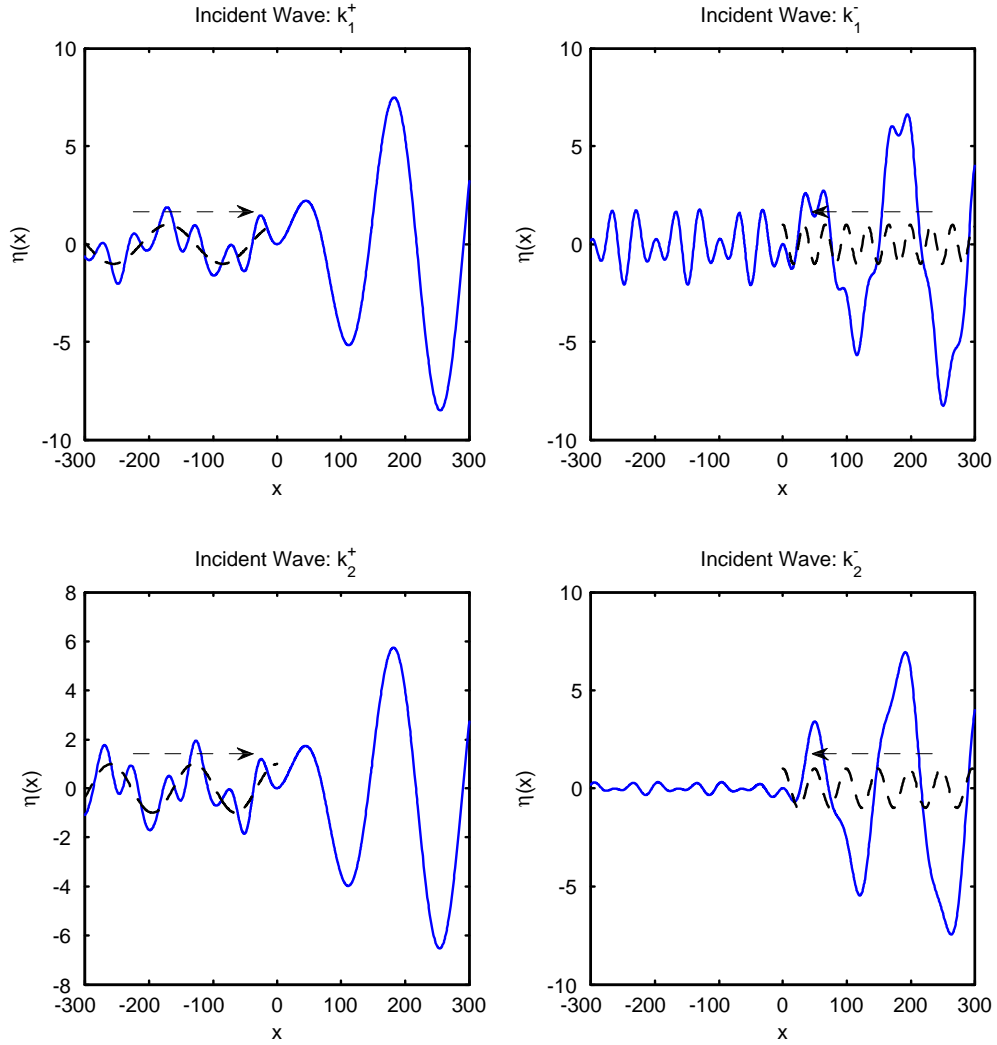


Figure 4.20: Spatial response for scattering by a 'hinged' constraint at $\omega = 0.002$ and for $U = 0.05, T = U^2, \lambda = 0$. Dashed line represents a wave of unit amplitude incident from upstream or downstream.

scattering process becomes

$$\sum_{m=0}^3 \operatorname{Re} \left\{ -i\omega \partial^m \widehat{G}^{(m)} \right\} |\Delta f_m|^2 + \sum_{m=0}^3 \operatorname{Re} \left\{ i\omega (-ik_j)^m \Delta f_m \overline{I_j} \right\} = 0. \quad (4.45)$$

For a dissipative scattering process, the 0 on the right hand side of (4.45) must be replaced by the power flowing out of the system. This could consist of power absorbed into a dashpot or power lost into shed vorticity at the discontinuity.

We note that the power balance identity of (4.45) holds for the sum over all relevant multipoles orders m , and *does not* in general hold for each order m taken individually. This is because the structural boundary conditions are satisfied for a very specific *combination* of multipole loads and not for the loads taken individually.

4.5.1 Example: Clamped Constraint

Substituting the monopole and dipole loads given in (4.32) into (4.45), we have for $m = 0$

$$\operatorname{Re} \left\{ -iG \right\} \frac{|\partial G^{(1)}|^2 + |k_j|^2 |G^{(1)}|^2}{|\partial G|^4 + |G|^2 |\partial G^{(1)}|^2} |I_j|^2 + \operatorname{Re} \left\{ \frac{i(-\partial G^{(1)} + ik_j G^{(1)}) \left((\overline{\partial G})^2 + \overline{G} \partial G^{(1)} \right)}{|\partial G|^4 + |G|^2 |\partial G^{(1)}|^2} \right\} |I_j|^2,$$

and for $m = 1$

$$\operatorname{Re} \left\{ -i\partial G^{(1)} \right\} \frac{|\partial G|^2 + |k_j|^2 |G|^2}{|\partial G|^4 + |G|^2 |\partial G^{(1)}|^2} |I_j|^2 + \operatorname{Re} \left\{ \frac{(k_j \partial G^{(1)} + ik_j^2 G^{(1)}) \left((\overline{\partial G})^2 + \overline{G} \partial G^{(1)} \right)}{|\partial G|^4 + |G|^2 |\partial G^{(1)}|^2} \right\} |I_j|^2.$$

Clearly, the individual equations do not equal zero. But their addition, together with the manipulation of terms using the reciprocal properties of the Green's function (4.15) yields

$$\begin{aligned} \operatorname{Re} \left\{ -iG \right\} \left(|\partial G^{(1)}|^2 + |k_j|^2 |G^{(1)}|^2 \right) + \operatorname{Re} \left\{ -i\partial G^{(1)} \right\} \left(|\partial G|^2 + |k_j|^2 |G|^2 \right) \\ + \operatorname{Re} \left\{ -i|\partial G|^2 \left(\overline{\partial G^{(1)}} - k_j^2 G \right) - i|\partial G^{(1)}|^2 \overline{G} + i|G|^2 k_j^2 \partial G^{(1)} \right\} = 0, \end{aligned}$$

which is identically zero for real k_j , or for an incident neutral wave.

For complex k_j , or for an incident convectively unstable wave that carries zero power, one can show that the self transmission and wave interaction terms carry zero power. The power balance in this case results from both the incident and total scattered powers being nil.

4.6 Summary

In this chapter we solved the problem of scattering from local discontinuities using a multipole source approach. We obtained the reflection and transmission coefficients of a large number of local scatterers and discussed the physical significance of each. Our solutions are exact and include the deflection, pressure and potential nearfields due to fluid-loading effects. We introduced the concept of power normalized scattering coefficients, and showed that overall power is conserved during the scattering process if the sign of the wave energy is preserved. We have argued that this property, combined with the presence of NEWs on the plate, is responsible for the phenomenon of over-scattering.

Chapter 5

Resonance of Quasi Finite Plate Segments

In this chapter we study the resonant growth of segments of plates bounded by two local scatterers on an otherwise uniform, infinite plate with one or two sided flow. We will make use of the reflection coefficients of the scatterers at the upstream and downstream ends of these segments together with the propagation properties of waves on the infinite plate to solve for the response within the finite segment. We will generally not consider the transmission coefficients of the scatterers as well as the response of the plate outside the boundaries of the segment. (Although it will not be explicitly solved for, the response of the plate outside these boundaries is, of course, implicitly included in our solution through the reflection coefficients.)

There are two major motivations for undertaking this type of study. Local resonance of panels formed by compact scatterers such as ribs, stiffeners or bulkheads on much larger structures such as ship or submarine hulls are of interest in themselves. These local scatterers provide mechanisms by which energy becomes trapped, leading to local amplification of response. In addition to being worthy of study in their own right, these types of quasi-finite systems are easier to study than the response of fully finite systems such as plates in a baffle or flags immersed in fluid and may provide insights into the latter. Not only are the reflection coefficients easier to obtain (the others require use of the Wiener-Hopf technique, as will be described in later chap-

ters) but, more crucially, the fluid nearfields are available in closed form and the entire system can be solved exactly.

One of the key lines of inquiry in this chapter will be the influence of the fluid nearfields on the eigenmodes of these quasi-finite systems. Since we can easily turn the nearfields on or off at will, we can gain insight into the limits of accuracy of the long plate asymptotic (i.e., far-field) theories applied in the context of a finite flag later in this thesis.

5.1 Condition for Resonance

Since we will be comparing the resonance frequencies obtained with and without the acoustic nearfields, we will introduce the eigenvalue equation for the simpler, approximate case for which all nearfields effects have been excluded. We will then generalize our approach to the exact case where all nearfield effects are included. We will refer to the former as including propagating waves only. By ‘propagating’ we understand waves corresponding to the four distinct poles of the dispersion equation, or waves whose propagation properties can be described by a simple spatial exponential function with real, complex or pure imaginary wavenumber. Our definition of a ‘propagating wave’ therefore includes evanescent waves associated with the structural nearfields, exponentially growing and decaying waves associated with the convectively unstable ranges as well as travelling or neutral waves (POW and NEW). By ‘nearfield,’ we understand the branch cut contributions only to the response.

5.1.1 Propagating Waves Only: Large L Asymptotics

Consider a plate segment of length L bounded by two scatterers described in terms of the leading and trailing edge reflection matrices R^L and R^T , respectively. Further, assume that the separation between the scatterers is large compared with the longest wavelength at the frequency of interest such that all nearfields can be neglected, i.e., that the scatterers are ‘in each other’s far-field.’

Define the two-dimensional right and left going wave amplitude vectors A^+ and A^- such that they are phased at the leading and trailing edges respectively. Invoking

the definition of the reflection coefficient, we can write down the (scalar) relationship between an incident and a reflected wave at the trailing edge $A_i^- = R_{ij}^T e^{ik_j^+ L} A_j^+$. The exponential term is a propagation phase factor that ‘adjusts’ the phase (or propagation growth) of the incident waves so that it is ‘referenced’ at the trailing edge. In matrix form, this relationship between two incident and two reflected waves can be written as

$$\begin{bmatrix} A_1^- \\ A_2^- \end{bmatrix} = \begin{bmatrix} R_{11}^T & R_{12}^T \\ R_{21}^T & R_{22}^T \end{bmatrix} \begin{bmatrix} e^{ik_1^+ L} & 0 \\ 0 & e^{ik_2^+ L} \end{bmatrix} \begin{bmatrix} A_1^+ \\ A_2^+ \end{bmatrix}, \quad (5.1)$$

or in abbreviated form

$$A^- = [R^T] [\Phi^+] A^+, \quad (5.2)$$

where $[\Phi^+]$ is a 2×2 diagonal right-going propagation matrix. At the leading edge, we can write

$$A^+ = [R^L] [\Phi^-] A^- \quad (5.3)$$

where

$$\Phi^- \equiv \begin{bmatrix} e^{ik_1^- L} & 0 \\ 0 & e^{ik_2^- L} \end{bmatrix}$$

is the 2×2 diagonal left-going propagation matrix.

The ‘gain’ in wave amplitude at the leading edge after one round trip $n \rightarrow n+1$ is obtained by substituting the equation for A^- (5.2) into (5.3)

$$\begin{aligned} A^+(n+1) &= [R^L] [\Phi^-] [R^T] [\Phi^+] A^+(n) \\ &= [\mathcal{G}^+] A^+(n), \end{aligned} \quad (5.4)$$

where $[\mathcal{G}^+] \equiv [R^L] [\Phi^-] [R^T] [\Phi^+]$ is defined as the gain matrix that operates on right (+) going waves. We can similarly derive a gain matrix that operates on left going waves: $[\mathcal{G}^-] \equiv [R^T] [\Phi^+] [R^L] [\Phi^-]$. \mathcal{G}^+ and \mathcal{G}^- are in general not equal, except when the condition for resonance is satisfied.

For real ω , the eigenvalues of \mathcal{G}^\pm determine the stability of the system. If all eigenvalues are inside the unit circle, the system is stable or damped. If one or more eigenvalues lie outside the unit circle, then the system is susceptible to unstable growth. If we now allow complex frequencies so that the temporal growth or decay rate is

captured in the sign and size of the imaginary part of frequency, we can state the most universal condition for resonance

$$A^\pm(n+1) = A^\pm(n), \quad (5.5)$$

i.e., that round trip performing wave vectors are equal in magnitude and phase at any fixed location on the finite plate. This is the same as stating that A^\pm is an eigenvector of \mathcal{G}^\pm , $[\lambda^\pm] A^\pm = [\mathcal{G}^\pm] A^\pm$, with eigenvalue $\lambda^\pm = 1$. This condition can be written as the system of homogeneous equations

$$[I - \mathcal{G}^\pm] A^\pm = 0 \quad (5.6)$$

where I is the identity matrix. The eigenvectors A^\pm are non-trivial solutions of this equation only for

$$\det(I - \mathcal{G}^\pm) = 0. \quad (5.7)$$

For this simple case where propagating waves only are included, one can multiply through the 2×2 matrices and solve for the individual terms of the gain matrix

$$\mathcal{G}^\pm = \begin{bmatrix} R^L \\ R^T \end{bmatrix} [\Phi^\mp] \begin{bmatrix} R^L \\ R^T \end{bmatrix} [\Phi^\pm] \quad (5.8)$$

to obtain, say for the right-going matrix,

$$\mathcal{G}^+ = \begin{bmatrix} R_{11}^T R_{11}^L e^{i(k_1^+ + k_1^-)L} + R_{12}^T R_{21}^L e^{i(k_2^+ + k_1^-)L} & R_{11}^T R_{12}^L e^{i(k_1^+ + k_2^-)L} + R_{12}^T R_{22}^L e^{i(k_2^+ + k_2^-)L} \\ R_{21}^T R_{11}^L e^{i(k_1^+ + k_2^-)L} + R_{22}^T R_{21}^L e^{i(k_2^+ + k_1^-)L} & R_{21}^T R_{12}^L e^{i(k_1^+ + k_2^-)L} + R_{22}^T R_{22}^L e^{i(k_2^+ + k_2^-)L} \end{bmatrix}. \quad (5.9)$$

A key property is that the $R^T R^L$ terms along the diagonal (products of reflection coefficients) are in fact power normalized quantities, whereas the off-diagonal terms are not. More on this in chapter 8.

5.1.2 Including Nearfields: Exact Solution for all L

In this section, we expand the approach of section 5.1.1 to include all nearfield contributions to the response of the finite segment. The formulation is exact and makes no assumptions about the separation distance between scatterers and is therefore valid for any arbitrary segment length and frequency, including the limiting cases of $L \rightarrow 0$

and $\omega \rightarrow 0$. Our derivation will entail generalizing the definitions of the reflection and propagation matrices to fully incorporate the nearfields.

Unlike propagating waves, whose propagation properties are captured by their complex wavenumbers alone, the nearfields are disturbances that are unique to each type of scatterer given that they are a function of the individual combination of multipole strengths that define the scatterer. This suggests that a truly universal propagation matrix that is independent of the edge conditions must have a separate entry for each multipole order. Essentially, we must treat the nearfield emanating from each of the four multipole loads as a separate, individual ‘wave-type,’ with its own unique propagation properties.

The propagation factor for a multipole of order m , located at $x = x_s$ and normalized by its amplitude at the source is

$$N_{\pm}^{(m)}(x - x_s) = \frac{G_{N\pm}^{(m)}(x - x_s)}{G_{N\pm}^{(m)}(0)}, \quad (5.10)$$

where

$$G_{N\pm}^{(m)}(x - x_s) = \pm \frac{1}{\pi} \int_0^{+\infty} \frac{\alpha v (\omega \mp iUv)^2 (\pm v)^m}{v^2 [v^4 - Tv^2 + \lambda - \omega^2]^2 + \alpha^2 (\omega \mp iUv)^4} e^{\mp v(x-x_s)} dv \quad (5.11)$$

are the branch cut contributions to the multipole Greens function given in (4.14). Normalization by $G_{N\pm}^{(m)}(0)$ is required in (5.10) because the propagation matrix operates on wave amplitudes defined in terms of plate deflection whereas the expression given in (4.14) is per unit applied load. The expanded propagation matrix now has four additional terms on its diagonal and is given by

$$\Phi^{\pm} \equiv \begin{bmatrix} e^{ik_1^{\pm}L} & 0 & 0 & 0 & 0 & 0 \\ 0 & e^{ik_2^{\pm}L} & 0 & 0 & 0 & 0 \\ 0 & 0 & N_{\pm}^{(0)}(L) & 0 & 0 & 0 \\ 0 & 0 & 0 & N_{\pm}^{(1)}(L) & 0 & 0 \\ 0 & 0 & 0 & 0 & N_{\pm}^{(2)}(L) & 0 \\ 0 & 0 & 0 & 0 & 0 & N_{\pm}^{(3)}(L) \end{bmatrix}. \quad (5.12)$$

The expanded reflection matrices must reflect the structure of the propagation matrix we’ve just defined in (5.12) above. We therefore require 6×6 reflection matrices

with three types of new terms: reflection coefficients for 1) nearfields generated by incident propagating waves, 2) propagating waves generated by incident nearfields and 3) nearfields generated by incident nearfields.

The *propagating to nearfield* reflection coefficient is

$$R^L_{\tau} [2 + i, j] = \Delta f_i \left(k_j^{\mp} \right) G_{N\pm}^{(i-1)}(0) \quad 1 \leq i \leq 4, \quad 1 \leq j \leq 2, \quad (5.13)$$

where $\Delta f_i \left(k_j^{\mp} \right)$ are the multipole source strengths of order i due to a unit incident propagating wave of wavenumber k_j computed by imposing the structural boundary conditions as described in chapter 4, and $G_{N\pm}^{(i)}(0)$ is the nearfield component of the Green's function of order i evaluated at the source $x - x_s = 0$ given in (5.11).

The *nearfield to propagating* reflection coefficient requires knowledge of the source (location, type) of the incident nearfield, and is given by

$$R^L_{\tau} [i, 2 + j] = \sum_{m=0}^3 \Delta f_m \left(N_{\mp}^{(j-1)}, L \right) G_{\pm\infty}^{(m)}(k_i^{\pm}) \quad 1 \leq i \leq 2, \quad 1 \leq j \leq 4, \quad (5.14)$$

where $\Delta f_m \left(N_{\mp}^{(j)}, L \right)$ are the multipole strengths corresponding to the structural conditions at the reflecting end due to a unit incident nearfield of order j generated at the other end of the segment, and

$$G_{\pm\infty}^{(m)}(k_i^{\pm}) \equiv \pm i \frac{(-ik_i^{\pm})^m}{D_k(k_i^{\pm})}$$

is the ‘farfield Green’s function’ of order m for the reflected wave k_i^{\pm} . To compute the $\Delta f_m \left(N_{\mp}^{(j)}, L \right)$ one has to, in general, solve a system of equations that satisfy the structural boundary conditions for a given incident nearfield. The procedure is comparable to that described in the chapter 4, with the sole difference arising in the evaluation of the incident wave terms. If we take as an example the matrix equation for a clamped-free discontinuity given in (4.34), only the right hand side vector – which carries information about the deflection, slope, and so forth of the incident disturbance – has to be altered to display the equivalent quantities for the incident

nearfield. Equation (4.34) therefore becomes

$$\begin{bmatrix} G_+ & G_+^{(1)} & G_+^{(2)} & G_+^{(3)} \\ \partial G_+ & \partial G_+^{(1)} & \partial G_+^{(2)} & \partial G_+^{(3)} \\ \partial^2 G_- & \partial^2 G_-^{(1)} & \partial^2 G_-^{(2)} & \partial^2 G_-^{(3)} \\ \partial^2 G_- & \partial^2 G_-^{(1)} & \partial^2 G_-^{(2)} & \partial^2 G_-^{(3)} \\ -T\partial G_- & -T\partial^{(1)} G_- & -T\partial^{(2)} G_- & -T\partial^{(3)} G_- \end{bmatrix} \begin{bmatrix} \Delta f_0 \\ \Delta f_1 \\ \Delta f_2 \\ \Delta f_3 \end{bmatrix} = \frac{1}{G_{N\mp}^{(m)}(L)} \begin{bmatrix} -G_{N\mp}^{(m)}(L) \\ -\partial G_{N\mp}^{(m)}(L) \\ -\partial^2 G_{N\mp}^{(m)}(L) \\ -\partial^3 G_{N\mp}^{(m)}(L) + T\partial G_{N\mp}^{(m)}(L) \end{bmatrix}, \quad (5.15)$$

where

$$\partial^n G_{N\pm}^{(m)}(L) = \pm \frac{i}{\pi} \int_0^{+\infty} \frac{\alpha v (\omega \mp iUv)^2 (\pm v)^m (\mp v)^n}{v^2 [v^4 - Tv^2 + \lambda - \omega^2]^2 + \alpha^2 (\omega \mp iUv)^4} e^{-v|L|} dv \quad (5.16)$$

are the various spatial derivatives (w.r.t. response location) of the nearfield Green's function (5.11).

The *nearfield to nearfield* reflection coefficient also requires solving for the multipole load strength $\Delta f_m(N_{\mp}^{(j)}, L)$ as above, but instead of summing over all multipole orders to generate a far field response, each individual load is combined with the corresponding nearfield Green's function of a given order to produce a separate coefficient

$$R_x^L [2 + i, 2 + j] = \Delta f_j(N_{\mp}^{(j-1)}, L) G_{N\pm}^{(i-1)}(0) \quad 1 \leq i \leq 4, \quad 1 \leq j \leq 4. \quad (5.17)$$

The Augmented Reflection and Gain Matrices

The augmented 6×6 reflection matrix operates on a vector of six incident wave amplitudes, two propagating and four nearfield, to produce a reflected vector of the same dimension and type. All wave amplitudes are referenced, in terms of magnitude and phase, at the scattering discontinuity. The reflection matrix is composed of four submatrices

$$R[6 \times 6] = \begin{bmatrix} R_{PP}[2 \times 2] & R_{PN}[2 \times 4] \\ R_{NP}[4 \times 2] & R_{NN}[4 \times 4] \end{bmatrix}, \quad (5.18)$$

where R_{PP} is the conventional propagating to propagating reflection matrix discussed in chapter 4, R_{NP} is the incident propagating to reflected nearfield submatrix defined in (5.13), R_{PN} is the incident nearfield to reflected propagating submatrix defined in (5.14) and R_{NN} is the incident nearfield to reflected nearfield submatrix defined in (5.17).

The reflection matrices at the upstream and downstream boundaries can be combined with the augmented propagation matrices (5.12) as in (5.8) to give an augmented gain matrix that now operates on a vector of six wave amplitudes instead of just two. The condition for resonance is given once again by (5.7) and solution of this equation now yields the exact eigenfrequencies of the system. These are the discrete set of complex resonance frequencies at which it is possible to combine the six upstream travelling and six downstream travelling disturbances (2 propagating waves & 4 nearfields) that satisfy the structural edge conditions at both ends. That unique combination of wave amplitudes is given by the eigenvector of the gain matrix corresponding to the unit eigenvalue $\lambda = 1$

$$\begin{aligned}\mathcal{G}^+ A^+ &= \lambda A^+, \quad \lambda = 1, \\ \mathcal{G}^- A^- &= \lambda A^-, \quad \lambda = 1.\end{aligned}$$

Once the right and left going eigenvectors have been solved for, the displacement mode shapes can be obtained by building the weighted sum of propagation factors, also evaluated at the complex eigenfrequency, as follows

$$\psi_{disp}(x) = \left[e^{ik_1^+ x}, \dots, N_+^{(3)}(x) \right] A^+ + \left[e^{ik_1^- x}, \dots, N_-^{(3)}(x) \right] A^-, \quad (5.19)$$

where the row vectors are simply the diagonals of the propagation matrix (5.12).

Pressure Mode Shapes

We can define propagation factors for the pressure that act on the same eigenvectors to give us the pressure mode shapes corresponding to the deflection mode shapes given above. Given that the eigenvectors are in terms of plate deflection, the six pressure propagation factors must have the following form

$$\phi_{pres}^\pm(x, y) = \left[(\omega - Uk_1^\pm)^2 e^{ik_1^\pm x} e^{-\gamma(k_1^\pm)|y|} / \gamma(k_1^\pm), \dots, N_{pres\pm}^{(3)}(x, y) \right], \quad (5.20)$$

where,

$$N_{pres\pm}^{(m)}(x, y) = \frac{1}{2\pi N_{\pm}^{(m)}(0)} \left\{ \int_0^{+\infty} \frac{i(\omega \mp ivU)^2 (\pm v)^{m-1} e^{\mp vx} e^{\pm iv|y|}}{D(\pm iv)} dv + \int_0^{+\infty} \frac{i(\omega \pm ivU)^2 (\mp v)^{m-1} e^{\mp vx} e^{\mp iv|y|}}{D(\mp iv)} dv \right\}, \quad 0 \leq m \leq 2$$

is the pressure nearfield from (4.25), normalized by the displacement nearfield at the boundary. For $m = 3$, the above expression can still be used except in the immediate vicinity of $x = 0$, where a finite difference based solution, such as the one described in section 4.3.3 may be employed. In terms of these propagation factors, the pressure mode shapes are

$$\begin{aligned} \psi_{pres}(x, y) &= [\phi_{pres}^+(x, y)] A^+ + [\phi_{pres}^-(x, y)] A^- \\ &= \left[(\omega - Uk_1^+)^2 e^{ik_1^+ x} e^{-\gamma(k_1^+)|y|} / \gamma(k_1^+), \dots, N_{pres+}^{(3)}(x, y) \right] A^+ \\ &\quad + \left[(\omega - Uk_1^-)^2 e^{ik_1^- x} e^{-\gamma(k_1^-)|y|} / \gamma(k_1^\pm), \dots, N_{pres-}^{(3)}(x, y) \right] A^-. \end{aligned} \quad (5.21)$$

5.2 Structural Energy Balance for Resonant Segment

We are now in a position to write down the structural balance equation, given in (3.1), for the finite segment at resonance using the displacement and pressure eigenmodes of the previous section. The time averaged power exchange between the flow and the structure (at the plate-fluid interface) is

$$\langle \Pi_{pv} \rangle = -\frac{i\omega\alpha}{2} \int_0^L \text{Re} \left\{ \psi_{pres}(x, y=0) \overline{\psi(x)} \right\} dx. \quad (5.22)$$

The time averaged structural flux out of the segment at the edges is

$$\langle J_p(L) - J_p(0) \rangle = \frac{i\omega}{2} \text{Re} \left\{ \partial^3 \psi(x) \overline{\psi(x)} - \partial^2 \psi(x) \overline{\partial \psi(x)} - T \partial \psi(x) \overline{\psi(x)} \right\} \Big|_0^L, \quad (5.23)$$

where 0 and L are just inside the finite region. The structural energy balance equation states that the time rate of change of structural kinetic and potential energy, T_p and V_p , is equal to power injected into the plate by the fluid minus the structural flux

exiting the plate at the edges, or

$$\left\langle \frac{d}{dt} [T_p + V_p] \right\rangle = \langle \Pi_{pv} \rangle - \langle J_p(L) - J_p(0) \rangle. \quad (5.24)$$

Hence, if the quantity on the right hand side of (5.24) is positive, the segment will experience unstable resonant growth, otherwise the resonance will be neutrally stable or damped. For upstream and downstream edge conditions that give a net outward structural flux of zero, $\langle J_p(L) - J_p(0) \rangle = 0$, the stability of the system is determined entirely by the sign and magnitude of $\langle \Pi_{pv} \rangle$.

The structural flux at the edge is identically zero for two canonical edge conditions: free and clamped. As a result, the stability of finite segments made up of any combination of free or clamped edge conditions, such as all three examples considered below, is determined solely by the sign and magnitude of the power exchange between the structure and the fluid. We note, however, that $\langle \Pi_{pv} \rangle > 0$ is neither a necessary nor a sufficient condition for instability.

There are two general scenarios that can lead to unstable resonance:

1) $\langle J_p(L) - J_p(0) \rangle \geq 0$ and $\langle \Pi_{pv} \rangle > 0$, with $\langle \Pi_{pv} \rangle > \langle J_p(L) - J_p(0) \rangle$. The outward structural flux is either zero or positive but less than the power injected by the fluid into the plate, leading to unstable growth. This includes the special case of $\langle J_p(L) - J_p(0) \rangle = 0$ corresponding to clamped or free edge conditions discussed above.

2) $\langle J_p(L) - J_p(0) \rangle < 0$ and $\langle \Pi_{pv} \rangle > \langle J_p(L) - J_p(0) \rangle$. The fluid may be absorbing power from the plate but the net structural flux *into* the segment is positive and greater than this loss, resulting in unstable growth.

5.3 Finite Segment Configurations

In this section we present results for the complex eigenfrequencies and mode shapes for a number of finite segment configurations. The examples offered here are by no means an exhaustive set. They are chosen simply to illustrate some of the recurring features of response that were observed from studying a larger set of finite segments constructed by pairing a large number of local scatterers described in chapter 4. We

limit our analysis to a set of relatively short plates with the primary aim of examining the effects of turning the nearfields ‘on’ and ‘off.’

We shall see that the nearfields do have an effect on the complex eigenvalues of finite segments, but that this effect is limited to short segment lengths and to low frequencies. They provide an adjustment to the eigenfrequencies, but do not alter the modal structure or introduce new resonances. In addition, their effect on the stability of the system is not consistent. Although we’ve observed that the inclusion of nearfield effects often reduces the imaginary parts of the eigenfrequencies (as shown in all the examples below), this is not universally true for all finite segment configurations.

5.3.1 Clamped Leading Edge, Clamped Trailing Edge

L = 140

The power normalized leading and trailing edge reflection coefficients for a clamped-clamped finite segment are plotted in figure 5.1. The infinite plate supporting this pair of scatterers has one-sided fluid flow ($\alpha = 1$) and enough tension ($T = U^2$) to eliminate local convective instability.

We note that, although the combined reflection and transmission processes at each edge do conserve power as discussed in chapter 4, the total power reflected is not necessarily equal to the incident wave power. This can be seen in the dashed-dotted lines of figure 5.1 which deviate substantially from 0dB. However, this quantity (the total reflected power) has very little significance in terms of the stability of a finite segment. For $\omega < \omega_p$ it is the amount of over-reflection of the individual coefficients that matters. For instance, a total reflected power of zero (corresponding to a descent to $-\infty$ dB in the figures below) simply indicates that the pair of positive and negative energy waves that are reflected have the exact same magnitude (but opposite sign of the wave energy). However, in the range $\omega > \omega_p$, where only positive energy waves exist, a power sum curve that dips below 0 dB indicates that the edge is effectively dissipative (through transmission to infinity) and will cause the neutral resonances falling within that frequency range to be damped. We will observe this phenomenon in this and in one other example configuration considered later in this section.

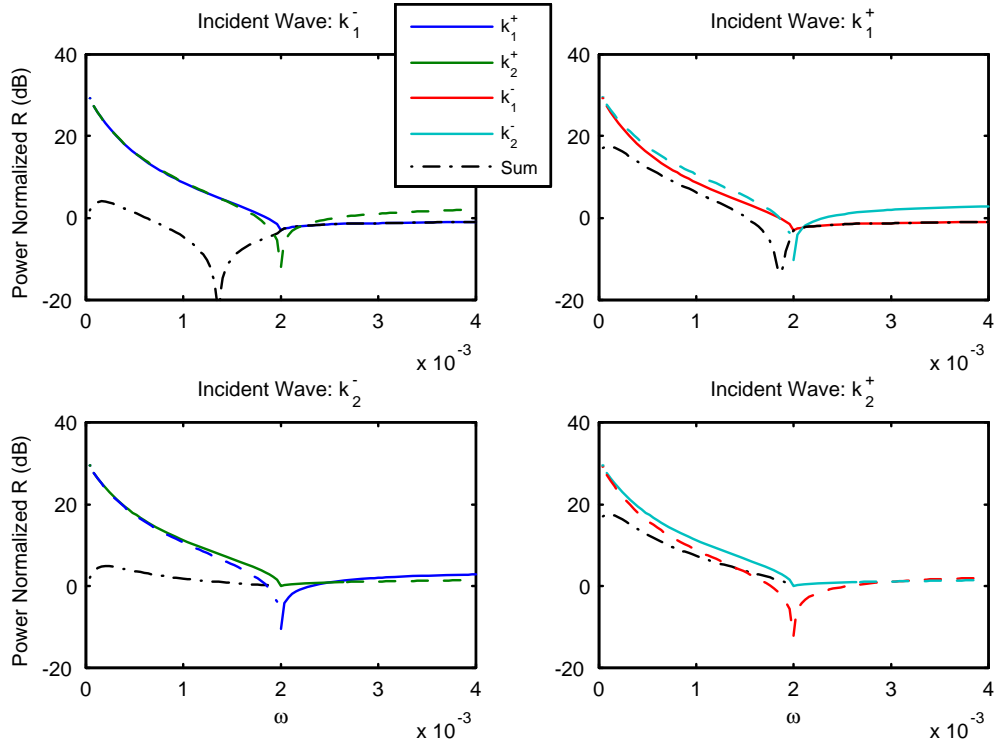


Figure 5.1: Power normalized reflection coefficients for a clamped-clamped upstream edge (figures in left column) and a clamped-clamped trailing edge (figures in right column) with one sided flow, $\alpha = 1$, and for plate parameters $U = 0.05$, $T = U^2$ and $\lambda = 0$.

We consider a segment with separation distance L between scatterers of 140 and form the two gain matrices defined in section 5.1: the 6×6 ‘full’ gain matrix which contains all nearfield and propagating terms, and the 2×2 ‘propagating only’ matrix. The eigenvalues for both sets of matrices, evaluated for real frequency, are plotted in figure 5.2. The solid lines are the real part of the eigenvalues and the dashed lines, the imaginary parts. The figure for the ‘full’ gain matrix has six eigenvalues but only one, the ‘maximum eigenvalue,’ is of order unity and shows up in the plot. The other eigenvalues are significantly smaller in magnitude and do not show up in the figure. The same holds for the two eigenvalues of the ‘propagation only’ gain matrix. The presence of one dominant eigenvalue was a common feature of all finite segment configurations we examined. The exception is in the immediate vicinity of $\omega = \omega_p$, where more than one eigenvalue may become comparable to unity.

A consequence of all this is that the trace of the gain matrix (i.e., the sum of all the eigenvalues) and the maximum eigenvalue are often equivalent and can be used interchangeably to estimate the relevant eigenfrequencies of a finite system. We note that the maximum eigenvalues for both sets of matrices, as shown in figure 5.2, are nearly identical except at very low frequencies where the nearfields introduce a very slight perturbation in both the real and imaginary parts.

We obtain initial guesses for the complex eigenvalues by looking for the zero crossings of the imaginary parts of the maximum eigenvalue. We chose the zero crossings that coincide approximately with the local maxima of the real part of the eigenvalue, as shown by the circles in figure 5.2. A gain rate per resonance frequency is obtained based on this local maximum of the real part and converted to an approximate temporal growth rate using an expression for the round trip time across the plate derived in section 8.1.2. An initial estimate for the complex eigenfrequency is thus formed and fed into a solver for the exact roots of the system determinant given in (5.7).

The results for the first three complex eigenfrequencies for a clamped-clamped segment of length $L = 140$ are given in figure 5.3, for both sets of gain matrices. We observe that the slight difference in the initial estimate of the first eigenfrequency between the two cases is also reflected in the exact solutions which are off by 1.2% and

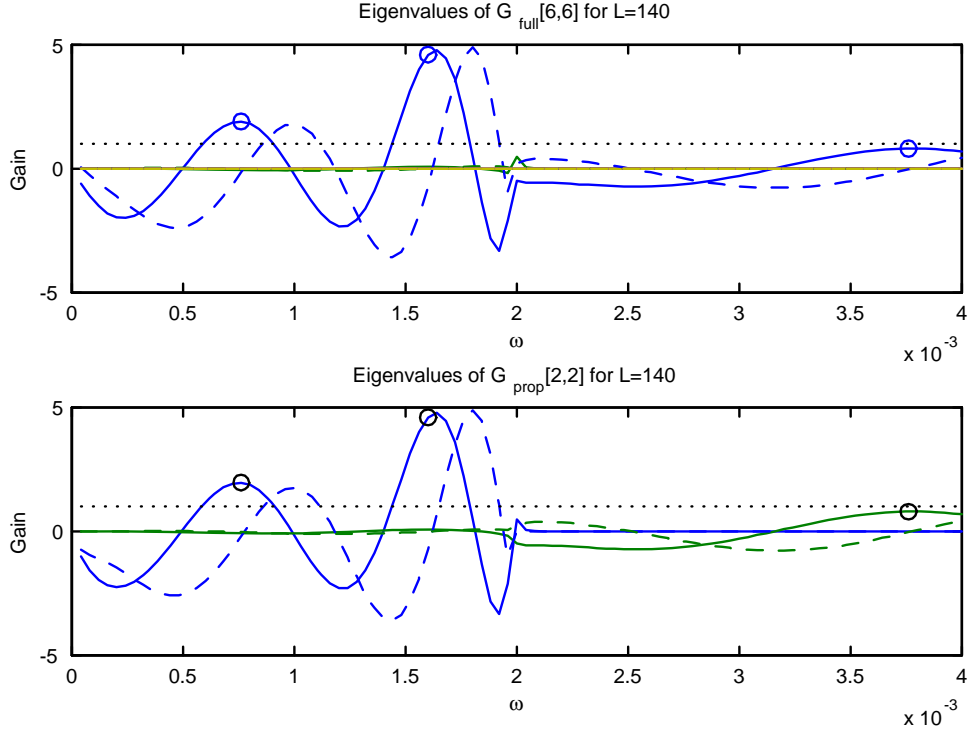


Figure 5.2: Real (solid) and imaginary (dashed) parts of eigenvalues of the ‘full’ and ‘propagating only’ gain matrices, for a finite segment clamped-clamped at the upstream edge and clamped-clamped at the downstream edge. Plate parameters: $U = 0.05$, $T = U^2$, $\lambda = 0$ and $\alpha = 1$.

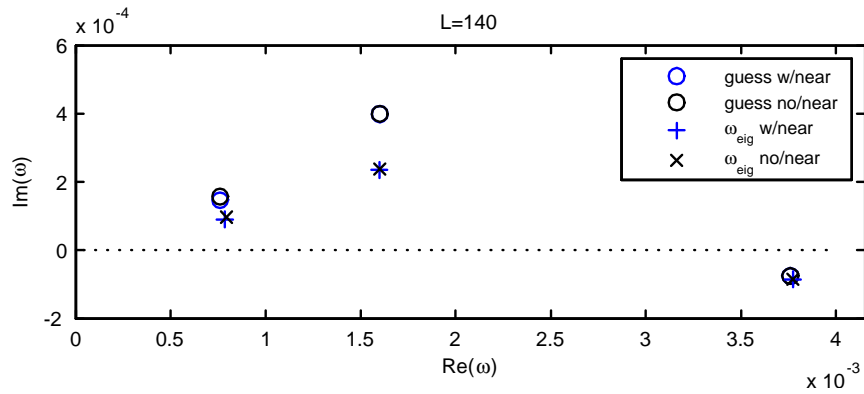


Figure 5.3: Complex eigenfrequencies for a finite segment clamped-clamped at the upstream edge and clamped-clamped at the downstream edge. Plate parameters: $U = 0.05$, $T = U^2$, $\lambda = 0$ and $\alpha = 1$.

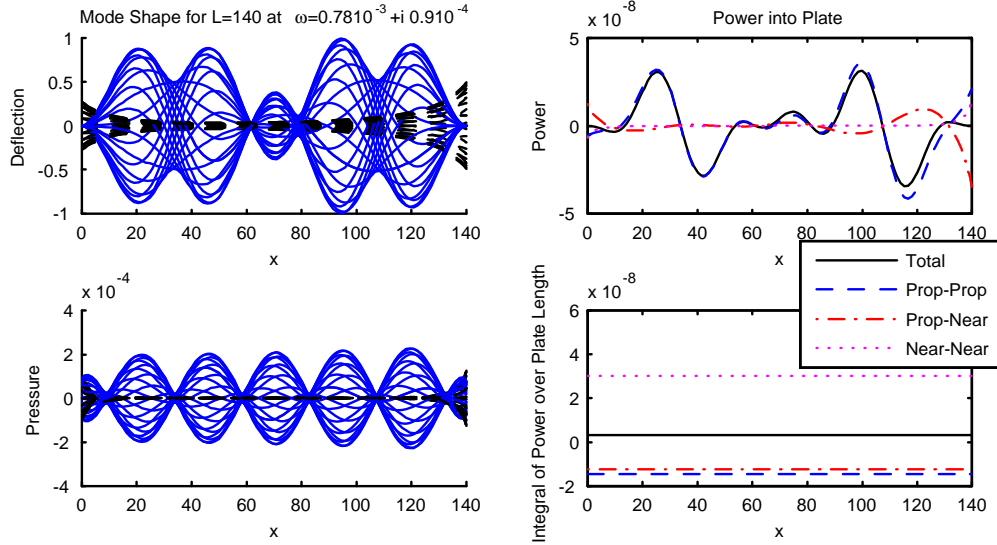


Figure 5.4: Modeshapes and power exchange between plate and fluid for lowest frequency eigenmode of a finite segment clamped-clamped at the upstream edge and clamped-clamped at the downstream edge. Plate parameters: $U = 0.05$, $T = U^2$, $\lambda = 0$ and $\alpha = 1$.

7.4% in their real and imaginary parts respectively. The higher order eigenfrequencies are off by less than 1%.

We also note that the initial guesses appear to overestimate the temporal growth rate for the unstable eigenfrequencies. This was a consistent feature across all finite segment configurations examined, and indeed of many finite flag configurations discussed in chapter 8. (However, we have made no effort to ascertain if this is a general rule or simply a trend.) For a detailed discussion of why there is a discrepancy between the initial estimates based on the gain matrix evaluated at real frequencies and the actual complex eigenfrequency roots of (5.7), the reader is encouraged to read ahead to section 8.1. In a nutshell, it has to do with the reflection coefficients and propagation paths in the gain matrix being evaluated at real frequencies instead of at the complex frequencies that capture the temporal growth rates of the incident, reflected and propagating waves on the resonant segment.

Figures 5.4 through 5.6 plot the mode shapes associated with the three lowest eigenfrequencies in figure 5.3. They consist of snapshots for ten equally spaced time

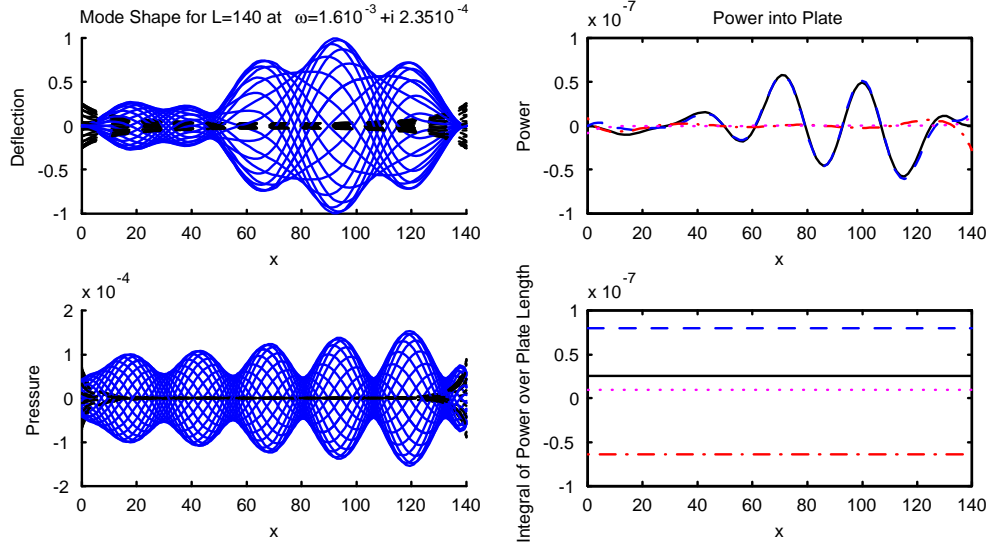


Figure 5.5: Modeshapes and power from the fluid into the plate for second lowest eigenmode of a finite segment clamped-clamped at the upstream edge and clamped-clamped at the downstream edge. Plate parameters: $U = 0.05$, $T = U^2$, $\lambda = 0$ and $\alpha = 1$. Legend same as in figure 5.4.

intervals per half cycle. The pressure mode shapes represent the pressure field associated with the normalized deflection mode shapes shown in the same figure. The solid lines represent the total response field, which include all propagating and nearfield components, and the dashed lines represent the nearfield contribution alone. They are provided to illustrate the relative importance of the nearfield for a given eigenmode.

Each figure also contains plots of the power injected by the fluid into the finite segment for that eigenmode. The relevant expression for the power from the fluid into the plate was derived in (5.22) and is presented in two forms: the integrand as a function of space (top right hand sub-figure), and the integral evaluated over the segment length and displayed as a constant line over the plate length (bottom right-hand sub-figure). As discussed in section 5.2, finite segment configurations, such as clamped-clamped, that result in zero net structural flux at the edges have the special property that the sign of this power quantity, i.e., the rate of working of the fluid on the finite plate, uniquely determines the stability properties of the segment. This is confirmed by the positive sign of the net power into the plate for the first two unstable

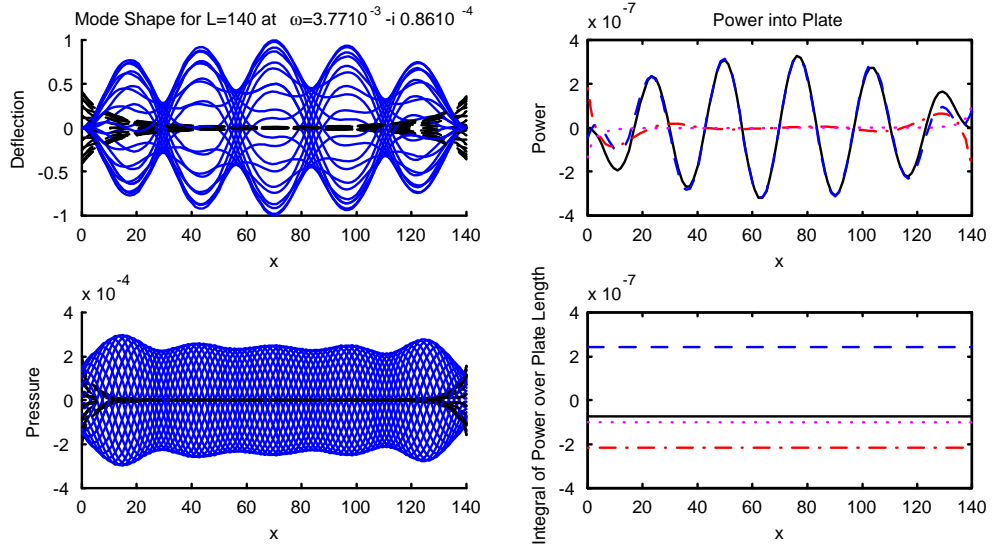


Figure 5.6: Modeshapes and power from the fluid into the plate for third lowest eigenmode of a finite segment clamped-clamped at the upstream edge and clamped-clamped at the downstream edge. Plate parameters: $U = 0.05$, $T = U^2$, $\lambda = 0$ and $\alpha = 1$. Legend same as in figure 5.4.

modes (figures 5.4 & 5.5) and the negative sign for the third mode which was earlier determined (from figure 5.6) to be stable and damped.

The power into the plate is further subdivided into three constitutive components, each representing the pairing between a deflection mode shape and a pressure mode shape. The solid line represents the actual power when the full field deflection and pressure mode shapes are used and is equal to the sum of the three individual components. This subdivision is necessary for determining the relative significance of the nearfields in evaluating the power exchanged between the fluid and the plate.

The lowest eigenmode (figure 5.4) shows a prominent presence of the nearfields which explains the 7.4% shift in $\text{Im}\{\omega_{eig}\}$ observed in figure 5.3. The prominence of the nearfield should be determined not only by its relative magnitude at the edges – for a clamped edge, this is bound to be a good percentage of the maximum propagating amplitude at any frequency – but in terms of how quickly it decays away from the edge (or how far it travels within the span of the plate). This prominence is reflected in the contribution of the nearfields to the net power into the plate. This can be

seen from the critical role played by the ‘nearfield and nearfield’ and ‘propagating and nearfield’ components in determining not only the magnitude, but more crucially, the proper sign of the net power. Using the propagating only mode shapes we would have erroneously concluded that this eigenmode was stable and damped instead of unstable (doesn’t change conclusion based on the sign of $\text{Im}\{\omega_{\text{eig}}\}$, though). Also, note how the net power differs from the propagating only power everywhere on the plate, not just in the immediate vicinity of the edges.

The second unstable eigenmode occurs at twice the frequency of the first and therefore shows a less prominent, but nevertheless important, role for the nearfields. Although the nearfields are evidently not needed for determining the real and imaginary parts of the eigenfrequencies to within 1% accuracy, they are still required for accounting for the power exchange between the fluid and the plate as can be seen from the right hand side plots of figure 5.5 which show that their contribution to the total power is of the same order as that of the propagating field alone. One noticeable difference with the lower frequency eigenmode is that the effect of the nearfield is limited to the immediate area around the edges which none the less still contribute the bulk of the net power, the spatially varying field due to the propagating waves alone having integrated out, through cancellations between positive and negative regions, to a comparable value.

The net power into the plate is negative for the third mode (figure 5.6), confirming that it is stable and damped. We note that the effect of the nearfield is at least as pronounced as it was for the second mode, even though this third eigenmode occurs at a much higher frequency. It is worth saying a few words about the node-less shape of the pressure eigenmode in figure 5.6. This resonance occurs above the pinch frequency ($\omega_{\text{eig}} > \omega_p$), so there are only two conventional propagating waves, one travelling downstream at a phase speeds 19% faster than the flow speed U , and the other travelling upstream. The phase speed of the downstream going wave is still close enough to the convective speed U that it entrains relatively little pressure (as a consequence of the $(\omega - Uk)^2$ factor in the term relating deflection and pressure). Therefore the contribution to the pressure field comes almost entirely from the upstream travelling

wave and with little interference from the downstream going pressure, looks much like a pressure disturbance that is propagating to the left. The deflection amplitudes for the upstream and downstream going waves are still comparable, hence the substantial nodal structure in the deflection mode shape.

The upstream travelling waves dominate the pressure response even more dramatically for mode shapes corresponding to eigenfrequencies lower than the pinch frequency, $\omega_{eig} < \omega_p$. The phase speeds of the downstream propagating waves are even closer to the convective speed U at these frequencies. However, the interference pattern created by the presence of two neutral waves propagating upstream generates a much more pronounced nodal structure – at the shorter wavelengths corresponding to these same waves – as seen in figures 5.4 & 5.5.

5.3.2 Free-Clamped Leading Edge, Free-Clamped Trailing Edge

$L = 60$

The power normalized reflection coefficients for identical ‘free-clamped’ conditions at the leading and trailing edge are plotted in figure 5.7. The infinite plate has two-sided fluid flow ($\alpha = 2$) and enough pre-tension ($T = U^2$) to eliminate convectively unstable waves. This configuration may serve as a suitable model for flags in tandem.

The first two eigenfrequency solutions for a segment of length $L = 60$ are plotted in figure 5.8. It turns out that the higher frequency solution – an apparently neutral eigenfrequency at precisely $\omega = \omega_p$ – is in fact a spurious root of the system determinant. The ‘eigenmode’ associated with this root does not satisfy the structural edge conditions, and the entire solution must therefore be discarded. The spurious ‘eigenmode’ that corresponds to this root is plotted for reference in figure 5.9 and clearly shows the violation of the ‘clamped’ condition at the leading edge.

The lower frequency root, by contrast, is genuine as evinced by the mode shapes of figure 5.10. We observe the significant influence of the nearfields in the mode shapes and the power balance plots. This is reflected in the sizeable shift (by about 16% for $\text{Re}\{\omega_{eig}\}$) in the complex eigenfrequency seen in 5.8.

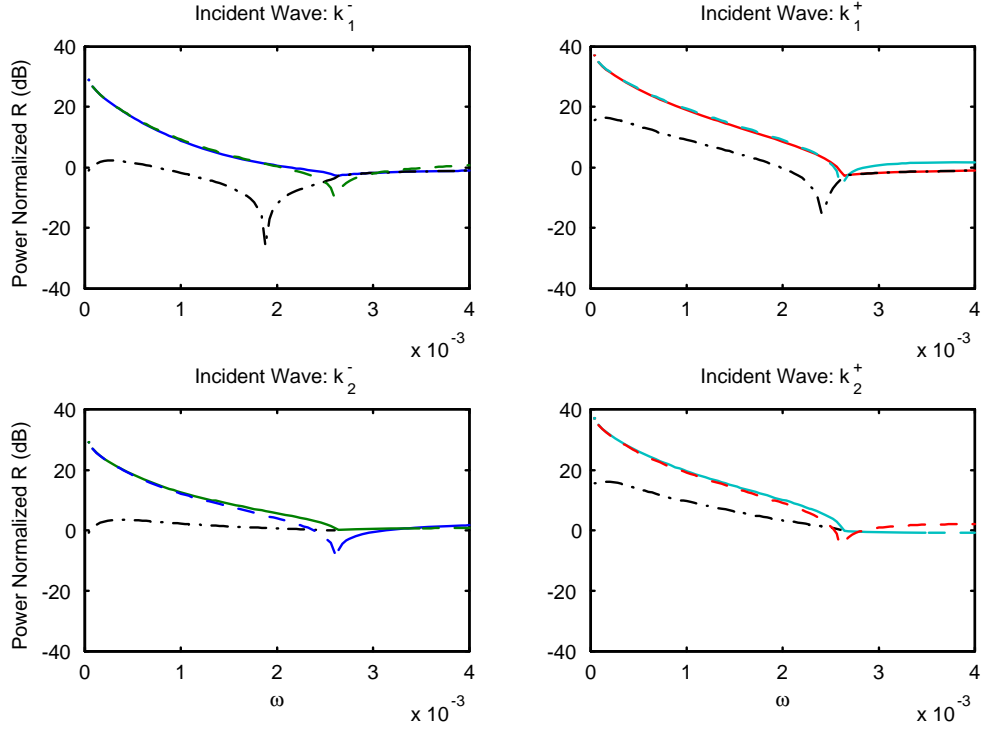


Figure 5.7: Power normalized reflection coefficients for a free-clamped upstream edge and a free-clamped trailing edge for plate with two sided flow and parameters: $U = 0.05$, $T = U^2$, $\lambda = 0$, and $\alpha = 2$. Legend same as for figure 5.1.

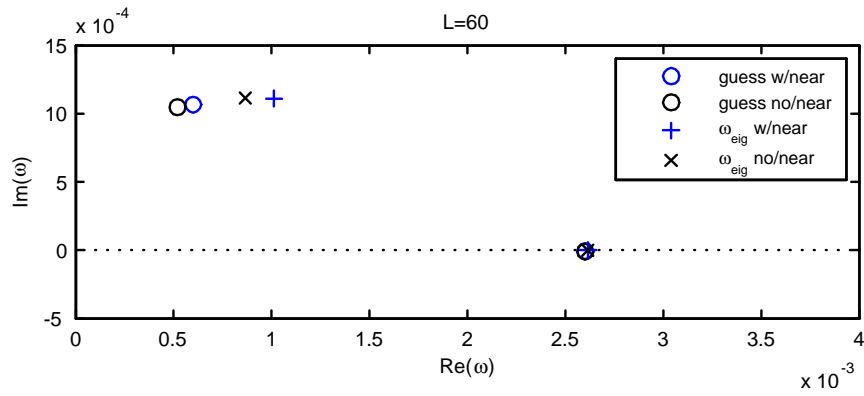


Figure 5.8: Complex eigenfrequencies for a finite segment of length $L = 60$ with free-clamped conditions at the upstream edge and free-clamped conditions at the downstream edge. Plate parameters: $U = 0.05$, $T = U^2$, $\lambda = 0$ and $\alpha = 2$.

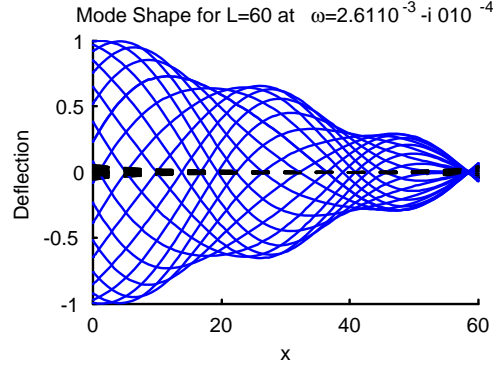


Figure 5.9: Erroneous modeshape for spurious eigenfrequency at $\omega = \omega_p$.

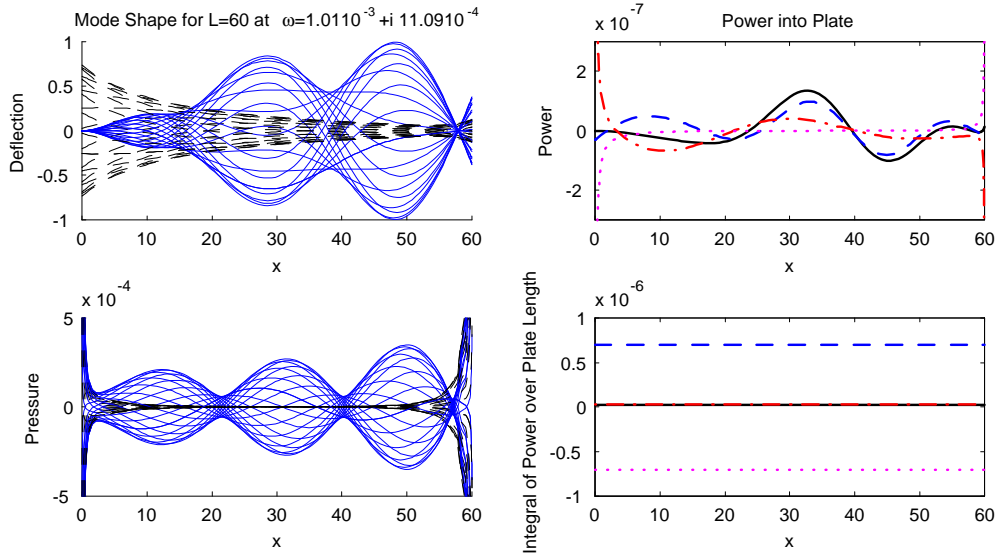


Figure 5.10: Modeshapes and power exchange between plate and fluid for lowest eigenfrequency of a finite segment of length $L = 60$ with free-clamped conditions at the upstream edge and free-clamped conditions at the downstream edge. Plate parameters: $U = 0.05$, $T = U^2$, $\lambda = 0$ and $\alpha = 2$. Legend same as in figure 5.4.

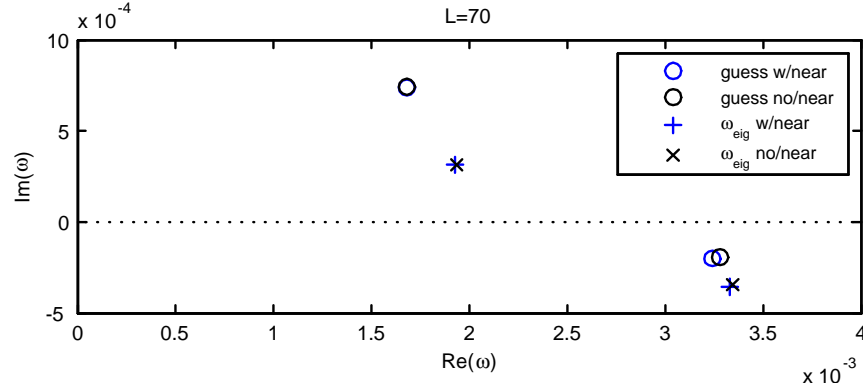


Figure 5.11: Complex eigenfrequencies for a finite segment of length $L = 70$ with free-clamped conditions at the upstream edge and free-clamped conditions at the downstream edge. Plate parameters: $U = 0.05$, $T = U^2$, $\lambda = 0$ and $\alpha = 2$.

L = 70

The eigenfrequencies and mode shapes for a slightly longer segment for the same edge conditions and plate parameters are plotted in figures 5.11 and 5.12. The frequency of the lowest eigenmode is substantially higher for this case and this is reflected in the relatively less pronounced effect of the nearfields.

We note that the pressure diverges at both the upstream and downstream edges for this type of edge condition. All edge conditions that involve a discontinuity in the plate deflection (such as a free edge) have an octupole load component which results in divergent pressures at the discontinuity, as discussed in section 4.3.3. The integral of the product between pressure and plate velocity, however, is finite, as seen in the bottom right plot of figure 5.12.

5.3.3 Clamped Leading Edge, Free Trailing Edge

L = 100

As a final example, we briefly consider the flag-like combination of a clamped-clamped leading edge and free-free trailing edge for $L = 100$. The power normalized reflection coefficients are plotted in figure 5.13. The infinite plate has two-sided fluid flow and enough pre-tension ($T = U^2$) to eliminate convectively unstable waves.

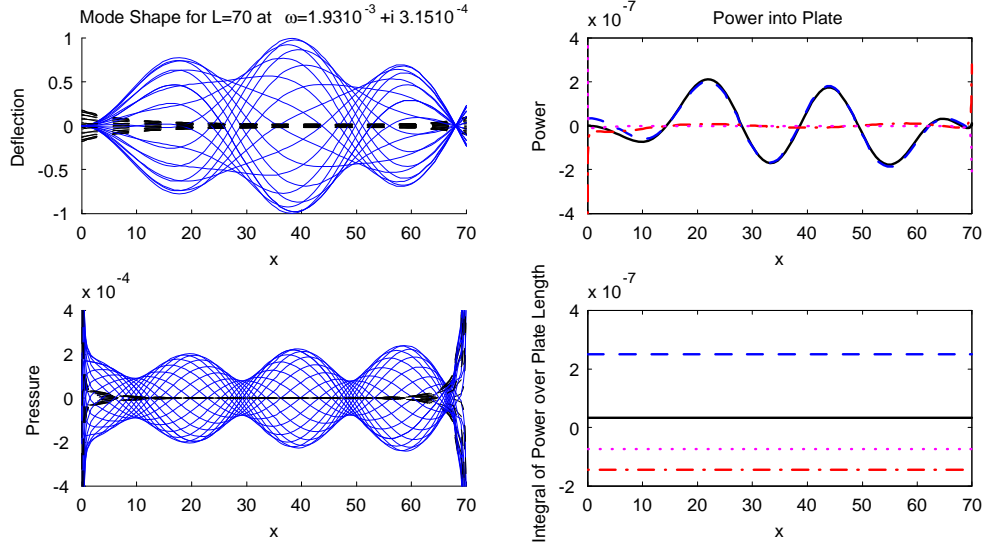


Figure 5.12: Modeshapes and power exchange between plate and fluid for lowest eigenfrequency of a finite segment of length $L = 70$ with free-clamped conditions at the upstream edge and free-clamped conditions at the downstream edge. Plate parameters: $U = 0.05$, $T = U^2$, $\lambda = 0$ and $\alpha = 2$. Legend same as in figure 5.4.

The lowest (single unstable) eigenfrequency is shown in figure 5.14. We observe that the nearfields have a minimal effect (less than 1%) on the value of the complex eigenfrequency.

The deflection and pressure mode shapes corresponding to this eigenfrequency are plotted in figure 5.15. We note that the nearfields are insignificant in determining the displacement mode shape at the free-free trailing edge but that they are a significant component of the total pressure at the same edge.

5.4 Summary

In this chapter we investigated the unstable resonances of quasi-finite plate segments formed by two local constraints or discontinuities. We develop a framework for the inclusion of all nearfields involved in the scattering process (including the mutual interaction between the nearfields emanating from the upstream and downstream edges) and succeed in solving for the complex resonance frequencies of these segments exactly.

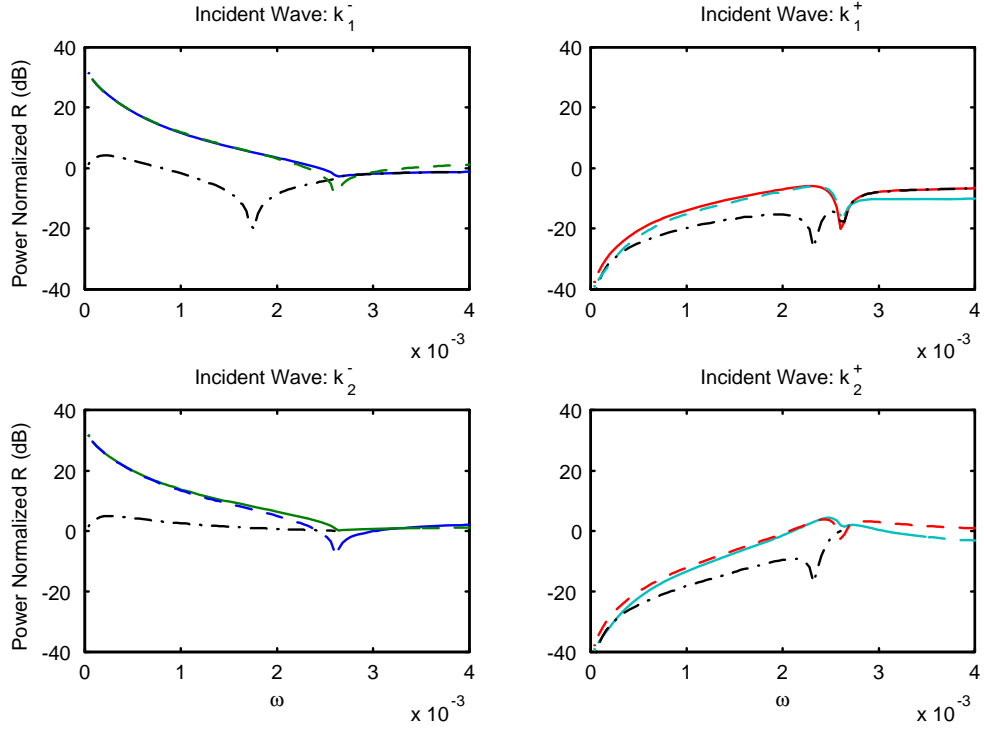


Figure 5.13: Power normalized reflection coefficients for clamped-clamped conditions at the upstream edge and free-free conditions at the downstream edge. Plate parameters: $U = 0.05$, $T = U^2$, $\lambda = 0$ and $\alpha = 2$.

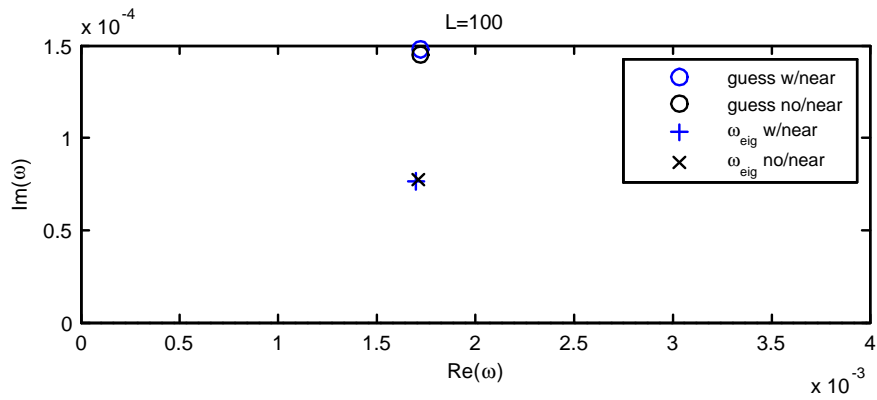


Figure 5.14: Complex eigenfrequencies for a finite segment of length $L = 100$ with clamped-clamped conditions at the upstream edge and free-free at the downstream edge. Plate parameters: $U = 0.05$, $T = U^2$, $\lambda = 0$ and $\alpha = 2$.

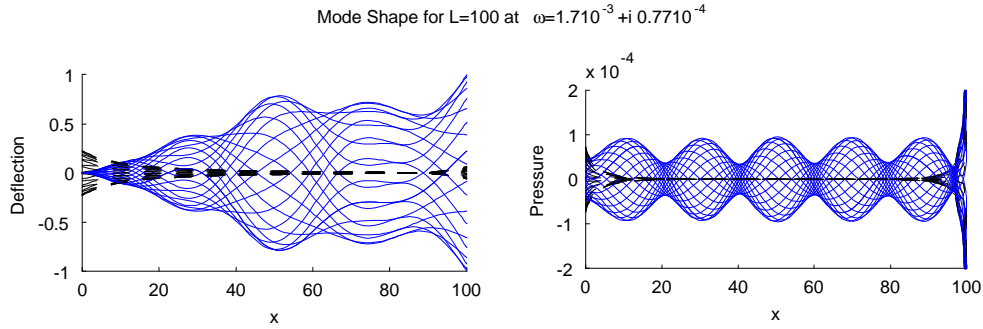


Figure 5.15: Deflection and pressure modes for lowest eigenfrequency of a finite segment of length $L = 100$ with clamped-clamped conditions at the upstream edge and free-free conditions at the downstream edge. Plate parameters: $U = 0.05$, $T = U^2$, $\lambda = 0$ and $\alpha = 2$. Legend same as in figure 5.4.

Our solutions are valid for arbitrarily small segment lengths. We find that the exclusion of the nearfields does not appreciably alter the complex eigenfrequencies even for very short plates, but that it affects the energy balance calculations. We conclude that the nearfields may safely be ignored in most configurations if all that's required are approximate values of the resonance frequencies and temporal growth rates.

Chapter 6

Scattering from Leading Edge

In this chapter we solve for the reflection coefficients for waves scattering from the leading edge of a submerged semi-infinite fluid-loaded plate in mean flow. The scattering problem we wish to solve is shown in figure 6.1. An upstream propagating wave $\eta_{inc} = Ie^{-ik_j^-x}$, with amplitude I and free wavenumber k_j^- , is incident on the leading edge. It is assumed that the excitation or plate discontinuity that excited the incident wave is well in the far field of the leading edge so that there are no near-fields as part of the incident field.

This two-part boundary value problem will be solved using the Wiener-Hopf technique. The structural conditions at the leading edge need not be specified at the outset, since our Wiener-Hopf solution is valid for arbitrary edge conditions. Evaluation of the scattered field, however, requires that we specialize to a given set of edge conditions. This is accomplished for a representative set of edge conditions, including the condition of an externally applied driver at the free edge.

Oswell (1992) has solved the free-edge problem using a Wiener-Hopf based ap-

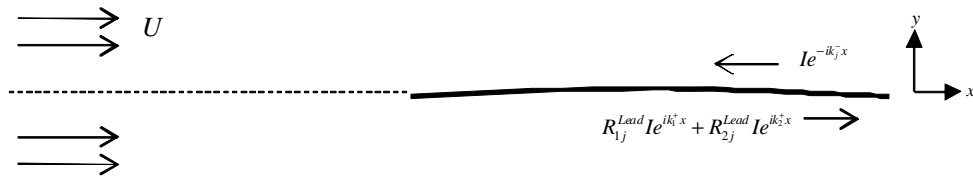


Figure 6.1: Scattering of plate waves from the upstream edge of a semi-infinite plate.

proach and offered solutions that are valid in the asymptotic limit of very low frequencies. The method of solution described in this chapter uses a different Wiener-Hopf equation than that employed by Oswell (1992), and the solution itself has a simpler form compared to the solution achieved by Oswell (1992). Our method follows more closely the approach of Peake (2004), who solved the equivalent edge scattering problem for a clamped plate in an infinite rigid baffle. In particular, we adopt Peake's (2004) approach of numerically splitting the Wiener-Hopf kernel. Our solution is not limited to a free edge and is valid throughout the frequency range where compressibility effects can be neglected.

6.1 System Equations Using Half-Range Transforms

The first step in applying the Wiener-Hopf technique is to express the field quantities in terms of half-range Fourier transforms which are analytic in either the upper or the lower halves of the complex- k plane, or R^+ and R^- . The precise definition of the boundaries of R^+ and R^- depends on the plate parameters T and λ , as well as the relevant frequency range, and is further determined by the requirements of causality (figure 6.2).

For large $\text{Im}\{\omega\}$, the poles and branch points in the complex k -plane are far away from the real k axis and R^+ is defined as the half space extending from $+i\infty$ down to, but not including, the pole with the smallest negative imaginary part in the lower half plane. Likewise, R^- is defined as extending from $-i\infty$ up to but not including the pole closest to the real k axis in the upper half plane. R^+ and R^- therefore span a well established strip of overlap S . As the limit $\text{Im}\{\omega\} \rightarrow 0$ is taken, the overlap strip S shrinks to the causal contour Γ_k defined in Chapter 2 and whose path is deformed to avoid any poles crossing the real k axis according to the Briggs-Bers technique. For $\text{Im}\{\omega\} = 0$, R^+ is therefore defined as the half-space above Γ_k plus the infinitesimally narrow overlap strip S , and R^- is the half-space below Γ_k plus S .

The half-range transforms for the potential, $\Phi^+(k) = F^+(\varphi(x))$ and $\Phi^-(k) =$

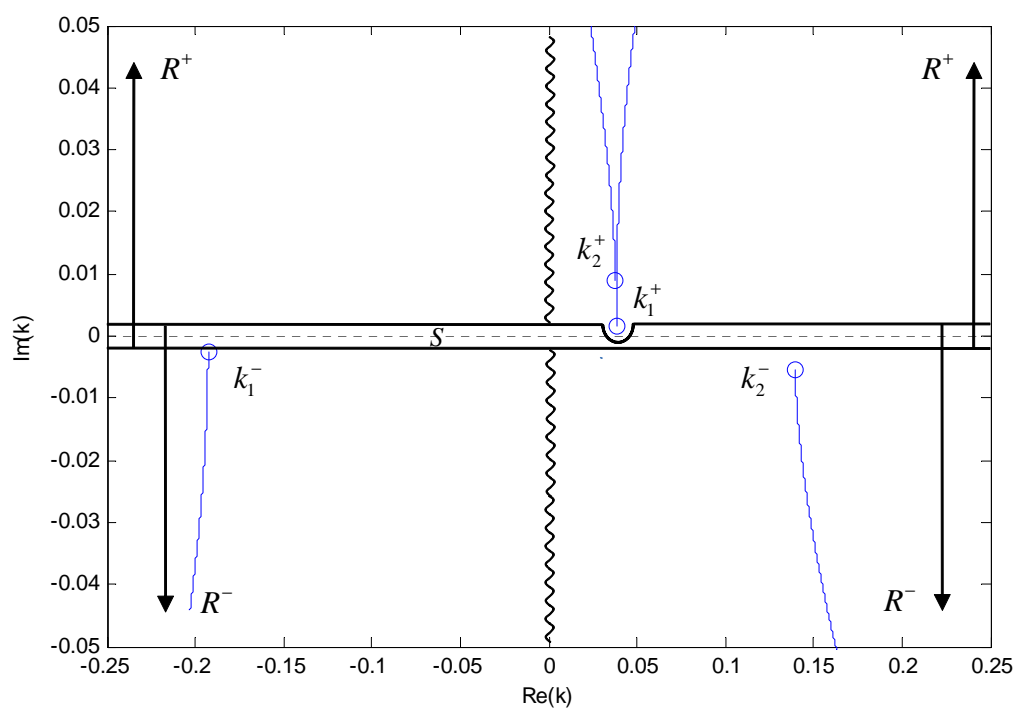


Figure 6.2: The upper and lower halves of the complex- k plane, R^+ & R^- , and the strip of overlap S .

$F^-(\varphi(x))$, are defined as

$$\Phi^+(k) = \int_{-\infty}^0 \varphi(x) e^{-ikx} dx, \quad (6.1)$$

$$\Phi^-(k) = \int_0^{+\infty} \varphi(x) e^{-ikx} dx. \quad (6.2)$$

Here, $\Phi^\pm(k)$ are analytic in the upper and lower half planes, respectively. The inverse transform is obtained by operating on the full range transform of the potential $\Phi(k) = \Phi^+(k) + \Phi^-(k)$ and is given by

$$\varphi(x) = \frac{1}{2\pi} \int_{-\infty}^{+\infty} [\Phi^+(k) + \Phi^-(k)] e^{+ikx} dk. \quad (6.3)$$

The half-range transforms of axial derivatives of the field variables can be obtained by repeatedly applying the chain rule in a straight forward manner. The transform of the n^{th} order derivative of the plate deflection is given by

$$F^-\left(\frac{\partial^n \eta(x)}{\partial x^n}\right) = (ik)^n \tilde{\eta}^-(k) - \sum_{m=1}^n (ik)^{(m-1)} \frac{\partial^{(n-m)} \eta(+0)}{\partial x^{(n-m)}}, \quad (6.4)$$

where $\tilde{\eta}^-(k) \equiv \int_0^{+\infty} \eta(x) e^{-ikx} dx$ is the half-range transform of the plate deflection. The derivatives evaluated at the edge are a by product of taking $x = +0$ as the lower integration limit in (6.2).

In terms of the half-range transforms just defined, the fluid-plate system of equations are expressed as follows. Laplace's equation is satisfied throughout the entire domain and yields, after satisfying the boundedness condition at $|y| \rightarrow \infty$,

$$\begin{aligned} \Phi(k, y) &= \Phi^+(k, y) + \Phi^-(k, y) \\ &= A(k) e^{-\gamma(k)|y|}, \end{aligned} \quad (6.5)$$

where $A(k)$ is an unknown function of the axial wavenumber. Taking the $\partial/\partial y$ of (6.5), we obtain a relation for the vertical component of the fluid velocity that must also hold throughout the entire domain

$$\begin{aligned} \frac{\partial \Phi}{\partial y} &= -\gamma(k) \Phi, \\ \frac{\partial \Phi^+}{\partial y} + \frac{\partial \Phi^-}{\partial y} &= -\gamma(k) (\Phi^+ + \Phi^-). \end{aligned} \quad (6.6)$$

In the spatial half-plane containing the plate (for $x \geq 0$) we obtain the following expressions for the linearized Bernoulli equation, the continuity condition and the plate equation,

$$\tilde{p}^- = i(\omega - Uk) \Phi^- + U\varphi(+0), \quad (6.7a)$$

$$\frac{\partial \Phi^-}{\partial y} = -i(\omega - Uk) \tilde{\eta}^- - U\eta(+0), \quad (6.7b)$$

$$-\alpha \tilde{p}^- = [k^4 + Tk^2 + \lambda - \omega^2] \tilde{\eta}^- - h(k), \quad (6.7c)$$

respectively, where

$$h(k) \equiv \eta'''(+0) + ik\eta''(+0) - (k^2 + T)\eta'(+0) - ik(k^2 + T)\eta(+0) \quad (6.8)$$

is obtained by application of (6.4) to the plate stiffness and tension operators. $h(k)$ has four unknown constants consisting of the edge deflection $\eta(+0)$ and its higher order derivatives. Two of these constants will be specified by the particular choice of edge conditions, and the other two are to be determined as part of the solution.

Symmetry dictates that the total potential is an odd function of y . This implies that, in the absence of a wake or an elastic structure that can create a jump or discontinuity in φ along $y = 0$, the total potential $\varphi_{total} = \varphi + \varphi_{inc}$, defined as the sum of the incident and scattered fields, must be identically zero. We therefore conclude that $\varphi = -\varphi_{inc}$ on $y = 0$. For an incident potential field $\varphi_{inc}(x, y) = (\omega - Uk_j^-) / \gamma(k_j^-) \eta_{inc}(x) e^{-\gamma(k)|y|}$, the scattered potential upstream of the edge is simply

$$\varphi = -i \operatorname{sgn}(y) \frac{I(\omega - Uk_j^-)}{\gamma(k_j^-)} e^{ik_j^- x}, \quad x \leq 0, \quad y = 0. \quad (6.9)$$

We take the half-range transform of φ given above and obtain

$$\Phi^+ = -i \frac{I(\omega - Uk_j^-)}{\gamma(k_j^-) (k - k_j^-)}, \quad k_j^- \in R^-, \quad (6.10)$$

in terms of the incident field quantities alone. Φ^+ is therefore a ‘known’ function, whereas $\partial \Phi^+ / \partial y$, Φ^- and $\partial \Phi^- / \partial y$ are the unknown functions that we would like to solve.

6.2 Wiener-Hopf Equation

Eliminating $\tilde{\eta}^-$ and \tilde{p}^- from (6.7), we obtain an expression relating the plate potential and the transverse fluid velocity

$$\begin{aligned} \alpha (\omega - Uk)^2 \Phi^- = & -\mathcal{P}(k) \frac{\partial \Phi^-}{\partial y} \\ & + i (\omega - Uk) (\alpha U \varphi(+0) - h(k)) - U \eta(+0) \mathcal{P}(k), \end{aligned} \quad (6.11)$$

where

$$\mathcal{P}(k) \equiv k^4 + Tk^2 + \lambda - \omega^2$$

is the plate operator term. $\mathcal{P}(k)$ is a 4th order polynomial in k that can also be written in terms of the *in-vacuo* plate wavenumbers $\mathcal{P}(k) = (k^2 - k_p^2)(k^2 - k_m^2)$, where

$$k_p = \frac{+1}{\sqrt{2}} \left[-T + (T^2 + 4\omega^2 - 4\lambda)^{\frac{1}{2}} \right]^{\frac{1}{2}}, \quad (6.12a)$$

$$k_m = \frac{+i}{\sqrt{2}} \left[+T + (T^2 + 4\omega^2 - 4\lambda)^{\frac{1}{2}} \right]^{\frac{1}{2}}, \quad (6.12b)$$

are the R^+ roots of $k^4 + Tk^2 + \lambda - \omega^2 = 0$. The R^- *in-vacuo* plate roots are simply $-k_p$ and $-k_m$. For $T = \lambda = 0$, k_p and k_m reduce to the R^+ Euler beam roots, $\omega^{1/2}$ and $i\omega^{1/2}$, respectively.

We now combine (6.5) and (6.11) to obtain a single equation relating R^+ and R^- quantities. Start by joining (6.10) with (6.5) to obtain

$$\Phi^- - i \frac{I(\omega - Uk_j^-)}{\gamma(k_j^-)(k - k_j^-)} = -\frac{1}{\gamma(k)} \frac{\partial \Phi^+}{\partial y} - \frac{1}{\gamma(k)} \frac{\partial \Phi^-}{\partial y} \quad (6.13)$$

and use it to eliminate Φ^- from (6.11). This yields an equation relating $\partial \Phi^+ / \partial y$ and $\partial \Phi^- / \partial y$

$$\begin{aligned} & \left\{ \mathcal{P}(k) - \frac{\alpha(\omega - Uk)^2}{\gamma(k)} \right\} \frac{\partial \Phi^-}{\partial y} \\ & = \frac{\alpha(\omega - Uk)^2}{\gamma(k)} \frac{\partial \Phi^+}{\partial y} - i \frac{I(\omega - Uk_j^-) \alpha(\omega - Uk)^2}{\gamma(k_j^-)(k - k_j^-)} \\ & \quad + i (\omega - Uk) (\alpha U \varphi(+0) - h(k)) - U \eta(+0) \mathcal{P}(k). \end{aligned} \quad (6.14)$$

We can proceed with the above equation and recast it into Wiener-Hopf form. In fact, this is the solution path that Oswell (1992) takes. However, a more convenient form of the Wiener-Hopf equation is obtained by instead relating $\partial\Phi^+/\partial y$ and Φ^- . We use (6.13) to eliminate $\partial\Phi^-/\partial y$ in (6.11) and obtain

$$\begin{aligned} & \left\{ \gamma(k) \mathcal{P}(k) - \alpha(\omega - Uk)^2 \right\} \Phi^- \\ &= -\mathcal{P}(k) \frac{\partial\Phi^+}{\partial y} - \gamma(k) \mathcal{P}(k) \frac{I(\omega - Uk_j^-)}{\gamma(k_j^-)(k - k_j^-)} \\ & \quad - i(\omega - Uk)(\alpha U\varphi(+0) - h(k)) + U\eta(+0)\mathcal{P}(k). \end{aligned} \quad (6.15)$$

We define the quantity in the brackets as our Wiener-Hopf kernel

$$K \equiv \gamma(k) \mathcal{P}(k) - \alpha(\omega - Uk)^2, \quad (6.16)$$

and use this definition to replace all explicit occurrences of the branch cut with $\gamma(k) = (K + \alpha(\omega - Uk)^2)/\mathcal{P}(k)$ to obtain

$$\begin{aligned} & K\Phi^- + K \frac{I(\omega - Uk_j^-)}{\gamma(k_j^-)(k - k_j^-)} \\ &= -\mathcal{P}(k) \frac{\partial\Phi^+}{\partial y} - \alpha(\omega - Uk)^2 \frac{I(\omega - Uk_j^-)}{\gamma(k_j^-)(k - k_j^-)} \\ & \quad - i(\omega - Uk)(\alpha U\varphi(+0) - h(k)) + U\eta(+0)\mathcal{P}(k). \end{aligned} \quad (6.17)$$

The key operation in the Wiener-Hopf method is the multiplicative factorization of the kernel into factors that are regular, non-zero and have algebraic behaviour at infinity in R^+ and R^- ,

$$K = K^+ K^-, \quad (6.18)$$

followed by re-organization of (6.17) into an equation with all terms analytic in R^+ pulled to one side of the equality sign and all those analytic in R^- to the other. This

is accomplished in the following equation:

$$\begin{aligned}
& K^- \Phi^- + \frac{I(\omega - Uk_j^-)}{\gamma(k_j^-)(k - k_j^-)} [K^- - K^-(k_j^-)] \\
&= -\frac{[k^4 - k_p^4]}{K^+} \frac{\partial \Phi^+}{\partial y} - \frac{\alpha(\omega - Uk)^2}{K^+} \frac{I(\omega - Uk_j^-)}{\gamma(k_j^-)(k - k_j^-)} \\
&\quad - \frac{i(\omega - Uk)}{K^+} (\alpha U \varphi(+0) - h(k)) + \frac{U\eta(+0)}{K^+} [k^4 - k_p^4] \\
&\quad - \frac{I(\omega - Uk_j^-)}{\gamma(k_j^-)(k - k_j^-)} K^-(k_j^-). \tag{6.19}
\end{aligned}$$

(6.19) is the equation for leading edge scattering in ‘Wiener-Hopf’ form. In addition to dividing through by K^+ , the step from (6.17) to (6.19) involves removing the simple lower half plane pole $k_j^- \in R^-$ from the R^- side of the equation and balancing with the corresponding term on the R^+ side.

The multiplicative factorization of the kernel defined in (6.18) is in general the most challenging step in the procedure. It is not possible to perform this factorization in closed form for our kernel (6.16). Oswell (1992) performs the asymptotic factorization of K for small U and ω , whereas Peake (2004) uses a numerical approach to factorize the kernel. We closely follow the method outlined by Peake (2004) and factorize K numerically. The details are provided in Appendix B. In what follows we shall assume that the kernel K has been successfully factored into K^+ and K^- components, and that the latter are available for numerical evaluation for any input parameter.

6.3 Solution for Arbitrary Edge Conditions

We are now in a position to invoke the main argument of the Wiener-Hopf technique. The Wiener-Hopf equation (6.19) consists of an equality between a left hand side that is analytic in R^- including the overlap region S , and a right hand side that is analytic R^+ also including S . By Liouville’s theorem both sides must therefore be equal to an entire function $E(k)$ which is analytic in all R . $E(k)$ must be a polynomial in k , and to ascertain the order of the polynomial we need to determine the leading order behaviour of (6.19) as $k \rightarrow \infty$.

In Appendix B, we determine that the split kernels vary as $K^\pm \sim k^{5/2}$ for large k . It may appear that the leading order term on the r.h.s. of (6.19) is $U\eta(+0)k^4/K^+ \sim k^{3/2}$. However, it turns out that this term cancels with an identical term contained in the factor $i(\omega - Uk)h(k)/K^+$. The largest term on the r.h.s. is in fact $\partial\Phi^+/\partial y \mathcal{P}(k)/K^+$. Allowing the standard weak singularity in the fluid velocity at the leading edge, i.e., $\partial\varphi/\partial y \sim 1/|x|^{1/2}$ as $x \rightarrow 0$, we deduce from the Abelian theorem that $\partial\Phi^+/\partial y \sim 1/k^{1/2}$ as $k \rightarrow \infty$. The highest order term on the r.h.s. therefore behaves as

$$\frac{\mathcal{P}(k)}{K^+} \frac{\partial\Phi^+}{\partial y} \sim k, \quad k \rightarrow \infty.$$

This suggests that the entire function is at most of order $o(k)$, and so we set

$$E(k) = E_0 + E_1 k, \quad (6.20)$$

where E_0 and E_1 are unknown constants. Each side of equation (6.19) must equal this entire function, generating the following pair of equations (one per half plane):

$$\Phi^- = -\frac{I(\omega - Uk_j^-)}{\gamma(k_j^-)(k - k_j^-)} \left[1 - \frac{K^-(k_j^-)}{K^-} \right] + \frac{E_0}{K^-} + \frac{E_1 k}{K^-}, \quad (6.21)$$

$$\begin{aligned} \mathcal{P}(k) \frac{\partial\Phi^+}{\partial y} &= -\frac{I(\omega - Uk_j^-)}{\gamma(k_j^-)(k - k_j^-)} \left[\alpha(\omega - Uk)^2 + K^+ K^-(k_j^-) \right] \\ &\quad - i(\omega - Uk)(\alpha U\varphi(+0) - h(k)) + U\eta(+0)\mathcal{P}(k) \\ &\quad + E_0 K^+ + E_1 k K^+. \end{aligned} \quad (6.22)$$

Let us examine the number of unknown constants in equations (6.21) and (6.22). In addition to the two unknown constants E_0 and E_1 introduced by the entire function, the factor $h(k)$ contains four edge displacement constants $\eta, \eta', \eta'', \eta'''$ at $x = +0$ given in (6.8). Two of these can be eliminated by application of the structural boundary conditions, leaving two that need to be determined as part of the solution. The edge potential $\varphi(+0)$ can actually be determined independently of the structural boundary conditions. This can be accomplished by two fully equivalent ways.

The first is a physical argument and consists of invoking the continuity of the potential function across $x = 0$, or $\varphi(+0) = \varphi(-0)$, and evaluating $\varphi(-0)$ using (6.9)

at $y = +0$ and $x = -0$ to obtain

$$\varphi(+0) = -i \frac{I(\omega - Uk_j^-)}{\gamma(k_j^-)}. \quad (6.23)$$

Recalling that (6.9) arises from imposing a $\varphi_{total} = 0$ condition on $y = 0$ for $x < 0$, (6.23) is seen to be merely a restatement that $\varphi_{total}(\pm 0) = 0$.

The second way of determining $\varphi(+0)$ is a purely mathematical argument, and consists of asymptotically expanding $\partial\Phi^-(k)/\partial y$ for large k and using Watson's Lemma in reverse fashion to determine $\partial\varphi(x)/\partial y$, and subsequently $\varphi(x)$, for $x \rightarrow +0$. No assumptions about the continuity of the potential at $x = 0$ is made. The derivation is given in full in Appendix B, and the end result is exactly as in (6.23). The mathematical derivation also shows that (6.23) holds for all structural edge conditions.

Either one of equations (6.21) and (6.22) can be used to solve the scattering problem. Equation (6.21) has only two unknown constants and is more compact than equation (6.22) which has four unknowns and a greater number of terms. It would appear then that the best approach is to solve (6.21). It turns out, however, that it is not possible to find two equations to solve for the two unknowns while working with (6.21). Equation (6.22), although more cumbersome, provides us with four equations for the four unknowns through the factor $\mathcal{P}(k)$ multiplying $\partial\Phi^+/\partial y$.

First we ensure that $\partial\Phi^+/\partial y$ is indeed analytic in R^+ . We divide (6.22) through by $\mathcal{P}(k)$ and note that the expression for $\partial\Phi^+/\partial y$ appears to contain two simple poles corresponding to the R^+ *in-vacuo* plate roots. This would violate the condition that $\partial\Phi^+/\partial y$ is analytic in R^+ unless we require that the entire r.h.s. of (6.22) is zero for $k = +|k_p|$ and $k = +i|k_p|$. This gives us two of the four equations we're seeking.

There are two equivalent ways of obtaining the additional pair of equations.

1) We start from (6.21) and use (6.11) to obtain an equation for $\partial\Phi^-/\partial y$

$$\begin{aligned} \mathcal{P}(k) \frac{\partial\Phi^-}{\partial y} &= \alpha(\omega - Uk)^2 \frac{I(\omega - Uk_j^-)}{\gamma(k_j^-)(k - k_j^-)} \left[1 - \frac{K^-(k_j^-)}{K^-} \right] \\ &\quad + i(\omega - Uk)(\alpha U\varphi(+0) - h(k)) - U\eta(+0)\mathcal{P}(k). \end{aligned} \quad (6.24)$$

$\partial\Phi^-/\partial y$ appears in the above equation to have poles at the two *in-vacuo* roots in R^- . This of course violates the analyticity of $\partial\Phi^-/\partial y$ in R^- and we therefore require that

the r.h.s. of (6.24) is zero for $k = -k_p$ and $k = -k_m$, giving us an additional two equations.

2) Alternatively, we can ensure that there are no propagating waves at the *in-vacuo* roots in the far field solution of $\partial\varphi(x \gg 1, 0)/\partial y$, which is obtained by inverse transforming the r.h.s. of (6.22) divided by $\mathcal{P}(k)$. The far field solution is dominated by the residue contributions as we close the contour in the upper half plane and pick up all the poles in R^- . In addition to the pair of poles tied up with the zeros of K^+ which are system roots, there are also the two poles corresponding to the *in-vacuo* plate roots in R^- . The first provide us with a pair of downstream propagating waves that satisfy the fluid-loaded plate equations, whereas the latter are spurious poles thrown up by our method. They are in fact tied up with the nearfields at the edge and cannot propagate to the far field. The r.h.s. of (6.22) must therefore be zero for $k = -k_p$ and $k = -k_m$.

It is fairly straightforward to show that the solution given by the mathematical approach in 1) and that given by the physical argument in 2) are entirely equivalent. One can use the following special identity between the split kernels evaluated at the *in-vacuo* roots k_0 ,

$$K^-(k_0) = -\frac{\alpha(\omega - Uk_0)^2}{K^+(k_0)}, \quad (6.25)$$

to show that the right hand sides of (6.22) and (6.24) are equal to each other at $k_0 = \{-k_p, -k_m\}$, or indeed also at the R^+ roots $k_0 = \{k_p, k_m\}$.

It is convenient to work with one single equation, say (6.22), evaluated at the four *in-vacuo* roots. Consolidating and rearranging terms, our four equations in the four unknown constants become

$$\begin{aligned} & +E_0K^+(k_0) + E_1k_0K^+(k_0) + i(\omega - Uk_0)h(k_0) = \\ & \frac{I(\omega - Uk_j^-)}{\gamma(k_j^-)} \left[\frac{\alpha(\omega - Uk_0)^2}{(k_0 - k_j^-)} + \frac{K^+(k_0)K^-(k_j^-)}{(k_0 - k_j^-)} + \alpha U(\omega - Uk_0) \right], \\ & \text{for } k_0 = \{k_p, k_m, -k_p, -k_m\}. \end{aligned} \quad (6.26)$$

Having determined all the unknown constants in the system, we are ready to solve for the scattered field. We combine (6.21) and (6.10) to obtain the full range transform

of the potential

$$\begin{aligned} \Phi(k) = \Phi^- + \Phi^+ &= \frac{E_0}{K^-(k)} + \frac{E_1 k}{K^-(k)} \\ &- \frac{I(\omega - Uk_j^-)}{\gamma(k_j^-)(k - k_j^-)} \left[1 + i - \frac{K^-(k_j^-)}{K^-(k)} \right]. \end{aligned} \quad (6.27)$$

For solutions downstream from the edge, we inverse transform (6.27) by closing the contour in the upper half plane being careful to pass below any poles that may have crossed over into the 4th quadrant. The far field solution is given by the residue contributions. Since $k_j^- \in R^-$ the only poles that contribute are the zeros of $K^-(k)$. By writing $K^- = K/K^+$, and noting that K^+ is analytic and free of zeros in R^+ , we see that the zeros of $K^-(k)$ are simply the zeros of K in R^+ which are in turn the dispersion roots of the infinite plate because $K = \gamma D$. The scattered far-field potential is therefore

$$\varphi_{far}(x, +0) = \sum_{i=1}^2 \frac{iK^+(k_i^+)}{K_k(k_i^+)} \left[E_0 + E_1 k_i^+ + \frac{I(\omega - Uk_j^-) K^-(k_j^-)}{\gamma(k_j^-)(k_i^+ - k_j^-)} \right] e^{ik_i^+ x}, \quad x \gg 1, \quad (6.28)$$

where k_i^+ are the R^+ roots of the dispersion function $D(k_i^+) = 0$, and K_k is given by

$$K_k \equiv \frac{\partial K}{\partial k} = \frac{5k^5 + 3Tk^3 + (\lambda - \omega^2)k}{\gamma(k)} + 2\alpha U(\omega - Uk). \quad (6.29)$$

In the far field, the deflection and potential for each wave are related through the continuity equation by $\eta(x) = i\varphi(x)\gamma(k)/(\omega - Uk)$. Applying this transformation to each wave component in (6.28) gives the far field deflection

$$\eta_{far}(x) = - \sum_{i=1}^2 \frac{\gamma(k_i^+)}{(\omega - Uk_i^+)} \frac{K^+(k_i^+)}{K_k(k_i^+)} \left[E_0 + E_1 k_i^+ + \frac{I(\omega - Uk_j^-) K^-(k_j^-)}{\gamma(k_j^-)(k_i^+ - k_j^-)} \right] e^{ik_i^+ x}, \quad x \gg 1. \quad (6.30)$$

The reflection coefficients are defined in the usual way as the ratio of the scattered and incident deflection wave amplitudes, and therefore consist of each wave component in (6.30) with $I = 1$, giving

$$R_{ij}^{Lead} = - \frac{\gamma(k_i^+)}{(\omega - Uk_i^+)} \frac{K^+(k_i^+)}{K_k(k_i^+)} \left[E_0 + E_1 k_i^+ + \frac{(\omega - Uk_j^-) K^-(k_j^-)}{\gamma(k_j^-)(k_i^+ - k_j^-)} \right]. \quad (6.31)$$

To obtain the reflected nearfields, one must evaluate the branch cut integral along the $\gamma(k)$ cut in the upper half plane which results in the following integral for the scattered deflection

$$\eta_{near}(x) = -\frac{1}{\pi} \int_0^{+\infty} \frac{K^+(iv)}{D(iv)(\omega - iUv)} \left[E_0 + iE_1v + \frac{I(\omega - Uk_j^-)K^-(k_j^-)}{\gamma(k_j^-)(iv - k_j^-)} \right] e^{-vx} dv. \quad (6.32)$$

The total reflected field is simply $\eta(x) = \eta_{far}(x) + \eta_{near}(x)$.

6.4 Reflection Coefficients for Representative Edge Conditions

There is a three step process for obtaining reflection coefficients for specific edge conditions:

- 1) Apply the structural boundary conditions at the edge to eliminate two of the four unknown plate deflection constants from within $h(k)$ (given in (6.8)).
- 2) Incorporate the reduced $h(k)$ into (6.26) and solve the four equations for the four unknowns. The four constants will now be specific to the edge condition as well as to the incident wave parameters.
- 3) Insert the values of E_0 and E_1 obtained from step 2) above into (6.31) and solve for the reflection coefficients. Note that even though we solve for all four constants, only the two associated with the entire function are needed in the final solution.

6.4.1 Free Edge

The structural boundary conditions for a free edge are given by $\eta''_{total}(0) = 0$ (zero total moment) and $\eta'''_{total}(0) - T\eta'_{total}(0) = 0$ (zero total transverse force). For an incident wave $\eta_{inc} = Ie^{-ik_jx}$, the equivalent scattered quantities are $\eta''(0) = k_j^2 I$ and $\eta'''(0) - T\eta'(0) = ik_j^3 I + iTk_j I$. Substituting these into (6.8), we eliminate two of the four deflection variables to obtain a function $h(k)$ that is specific to a free edge

$$h(k) = -ik(k^2 + T)\eta(0) - k^2\eta'(+0) + (ik_j^3 + iTk_j + k_j^2k)I.$$

The four equations in the four unknown constants E_0 , E_1 , $\eta(0)$ and $\eta'(0)$ are

$$\begin{aligned} E_0 [K^+(k_0)] + E_1 [k_0 K^+(k_0)] + \eta(0) [(\omega - Uk_0) k_0 (k_0^2 + T)] \\ + \eta'(0) [-i(\omega - Uk_0) k_0^2] = (\omega - Uk_0) (k_j^3 + Tk_j + k_j^2 k_0) I + \mathcal{I}(k_0, k_j), \end{aligned} \quad (6.33)$$

for $k_0 = \{k_p, k_m, -k_p, -k_m\}$

where

$$\mathcal{I}(k_0, k_j) \equiv \frac{I(\omega - Uk_j)}{\gamma(k_j)} \left[\frac{\alpha(\omega - Uk_0)^2}{(k_0 - k_j)} + \frac{K^+(k_0) K^-(k_j)}{(k_0 - k_j)} + \alpha U(\omega - Uk_0) \right] \quad (6.34)$$

is a term common to all edge conditions and contains parameters solely related to the incident wave. The magnitude and phase of the reflection coefficient for a free leading edge are given in figure 6.3. The power normalized reflection coefficients are given in figure 6.4. Power normalization consists of weighting the wave amplitudes by the wave impedance and is performed as described previously in equation (4.28). We observe that there is a significant amount of over-reflection at the free edge and that this apparent amplification of the reflected waves is accomplished while conserving power. This is to be expected because a free edge is a conservative scatterer as discussed in Chapter (4). The total power reflected is equal to the incident power as long as the sign of the wave energies is maintained in adding the power of the reflected waves.

As a direct consequence of these power conservation requirements, it can be seen that the mere presence of negative energy waves at the scattering frequency *guarantees* over-reflection. This is in contrast to the power arithmetic in the scattering process from a local plate discontinuity, which allows for the possibility that the incident wave energy is fully transmitted preventing the occurrence of over-reflection.

6.4.2 Clamped Edge

A clamped edge imposes zero total displacement and zero total slope. The scattered deflection and slope at the edge are therefore $\eta(0) = -I$, and $\eta'(0) = -ik_j I$. Eliminating these quantities from $h(k)$, the equations for the four unknown constants E_0 ,

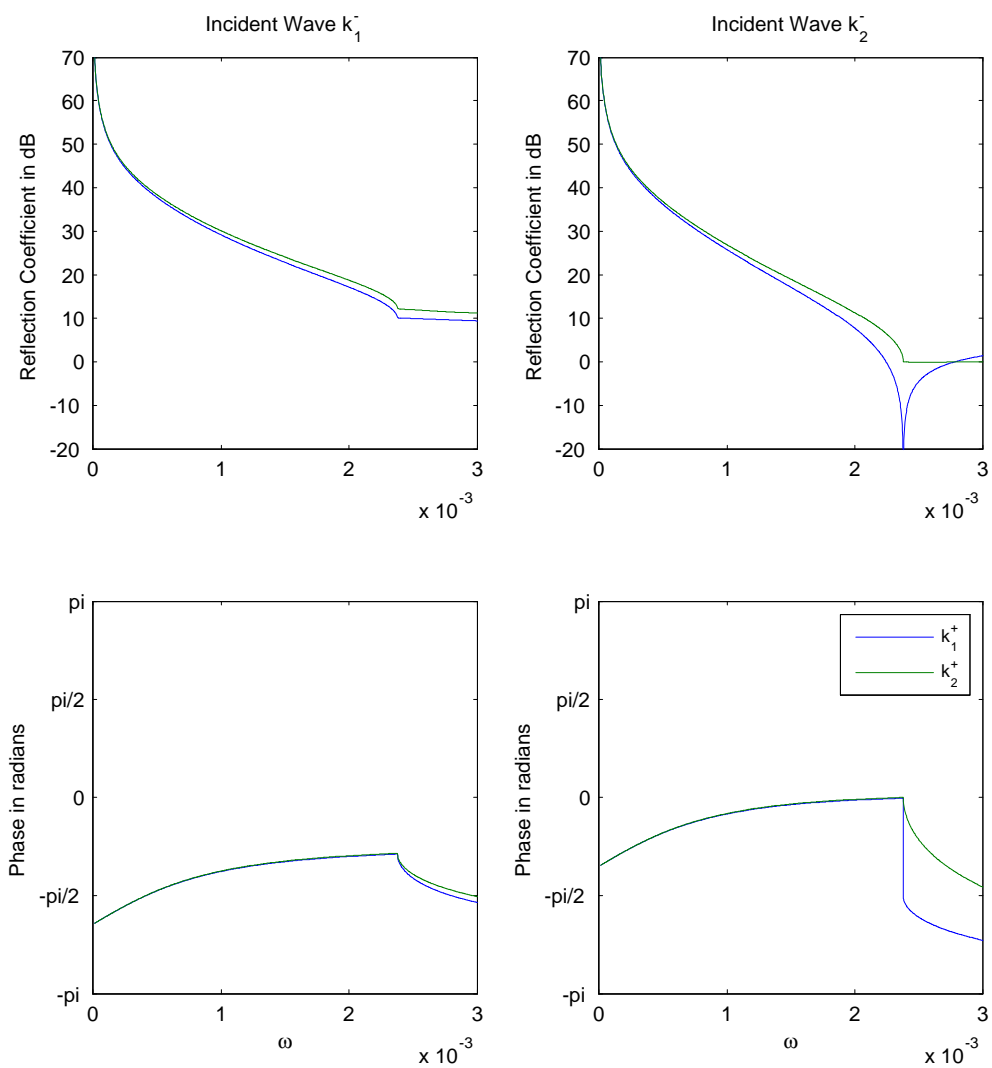


Figure 6.3: Magnitude and phase of the reflection coefficients for a free leading edge for $U = 0.05$, $T = 2U^2$ and $\lambda = 0$.

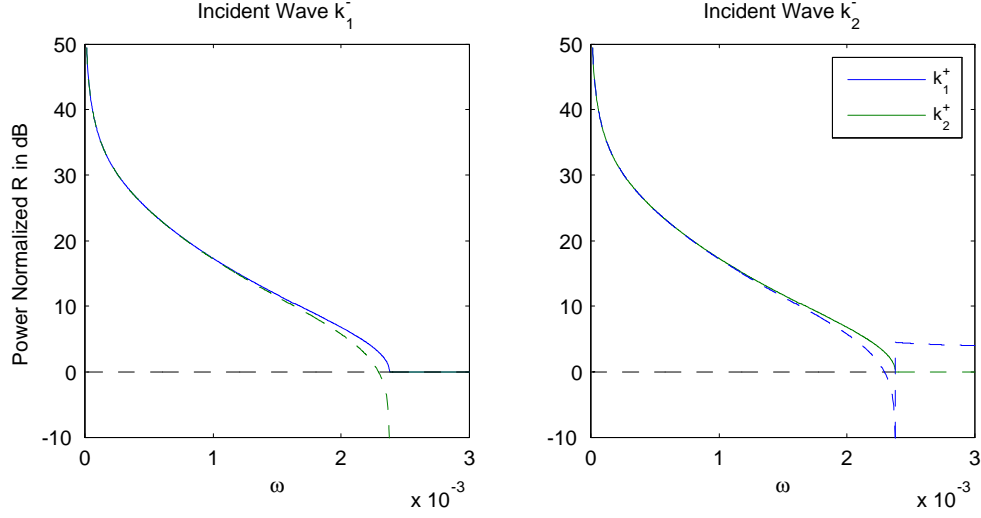


Figure 6.4: Power normalized reflection coefficients for a free leading edge for $U = 0.05$, $T = 2U^2$ and $\lambda = 0$.

E_1 , $\eta''(0)$, and $\eta'''(0)$ become

$$\begin{aligned}
 & E_0 [K^+(k_0)] + E_1 [k_0 K^+(k_0)] + \eta''(0) [-k_0 (\omega - Uk_0)] \\
 & + \eta'''(0) [i(\omega - Uk_0)] = (\omega - Uk_0) (k_j + k_0) (k_0^2 + T) I + \mathcal{I}(k_0, k_j), \\
 & \text{for } k_0 = \{k_p, k_m, -k_p, -k_m\}.
 \end{aligned} \tag{6.35}$$

The magnitude and phase of the raw coefficients are given in figure 6.5 and the power normalized coefficients are given in 6.6. We observe that a clamped leading edge is significantly less over-reflective than the free edge.

6.4.3 Constraint at Edge

Next, we consider a translational constraint such as an attached spring, lumped mass, dashpot or any other point constraint attached to the leading edge that can be described through a local complex impedance Z_c . For the combination of lumped parameters shown in figure (FigZcLead0), the complex impedance is given by

$$Z_c = -i\omega M_c + R_c + \frac{iK_c}{\omega}. \tag{6.36}$$

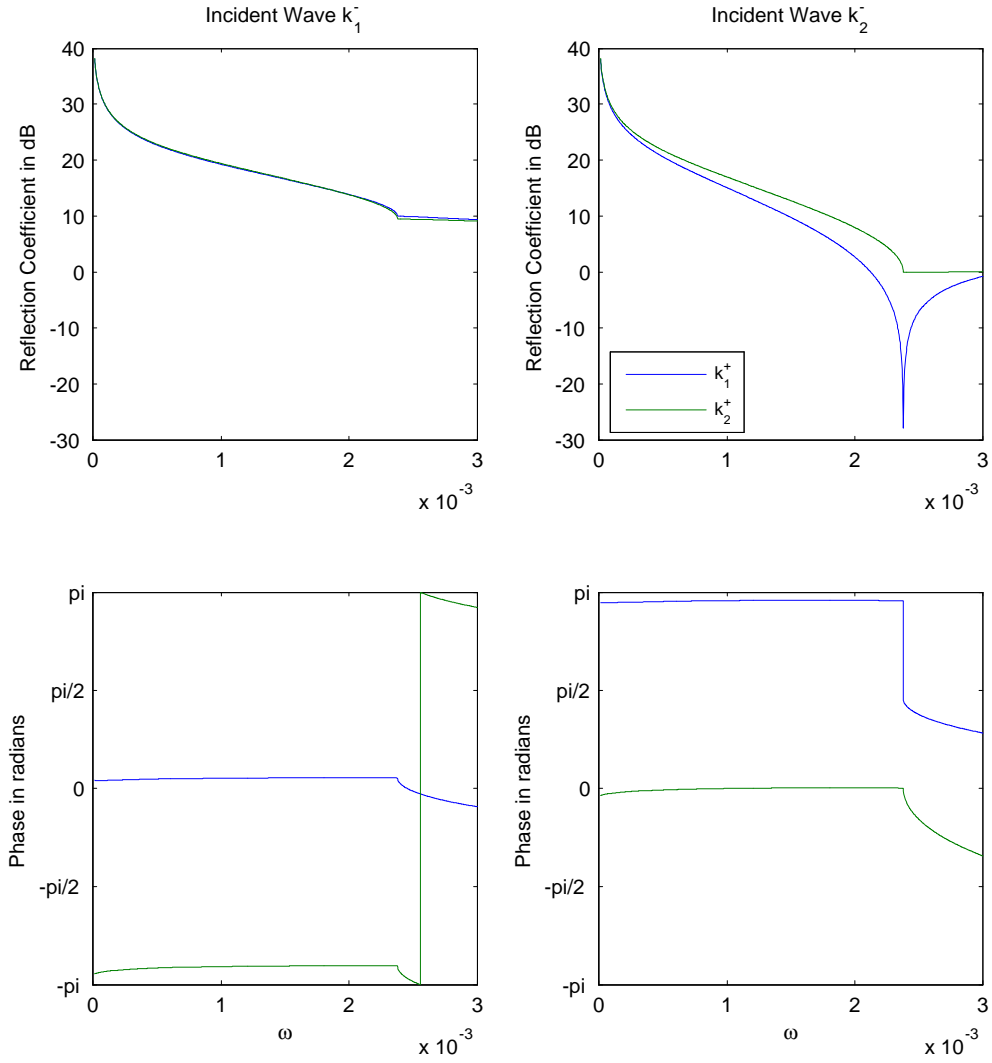


Figure 6.5: Magnitude and phase of the reflection coefficients for a clamped leading edge for $U = 0.05$, $T = 2U^2$ and $\lambda = 0$.

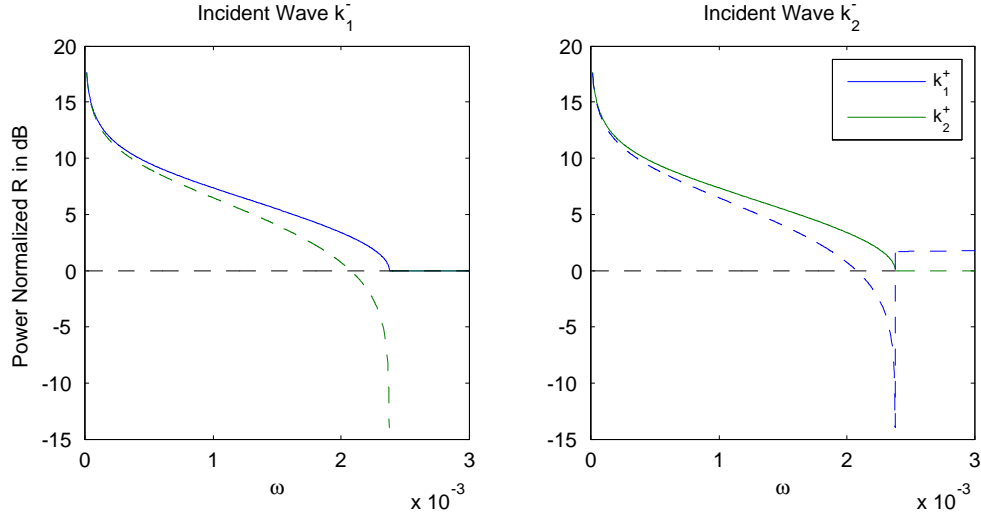


Figure 6.6: Power normalized reflection coefficients for a clamped leading edge for $U = 0.05$, $T = 2U^2$ and $\lambda = 0$.

The vertical reaction force applied to the plate is simply $i\omega\eta_{total}(0)Z_c$ while the moment is zero (by our definition of Z_c as a translational constraint). (We could easily incorporate rotational effects into our analysis but Z_c would then have to be defined through a 2×2 matrix.) The structural boundary conditions in terms of the scattered quantities are therefore $\eta'''(0) - T\eta'(0) - i\omega Z_c\eta(0) = ik_j^3I + iTk_jI + i\omega Z_cI$ and $\eta''(0) = k_j^2I$. We choose to eliminate $\eta'''(0)$ from $h(k)$ and so the equations for the four remaining constants E_0 , E_1 , $\eta(0)$, and $\eta'(0)$ are

$$\begin{aligned} E_0 [K^+(k_0)] + E_1 [k_0 K^+(k_0)] + \eta(0) [(\omega - Uk_0)(k_0(k_0^2 + T) - \omega Z_c)] \\ + \eta'(0) [-i(\omega - Uk_0)k_0^2] = (\omega - Uk_0)(k_j^3 + Tk_j + k_j^2k_0 + \omega Z_c)I + \mathcal{I}(k_0, k_j), \end{aligned} \quad (6.37)$$

for $k_0 = \{k_p, k_m, -k_p, -k_m\}$.

As expected, this is a slightly modified version of the system of the equations for a free edge condition (6.33) which can be recovered by setting $Z_c = 0$ in (6.37).

Figure 6.7 plots the power normalized reflection coefficients for the case where Z_c is a pure dashpot. The dashpot provides a dissipative mechanism by which power is removed from the system. We therefore need to add the power absorbed by the dashpot into our power balance relations. The time averaged power into the dashpot

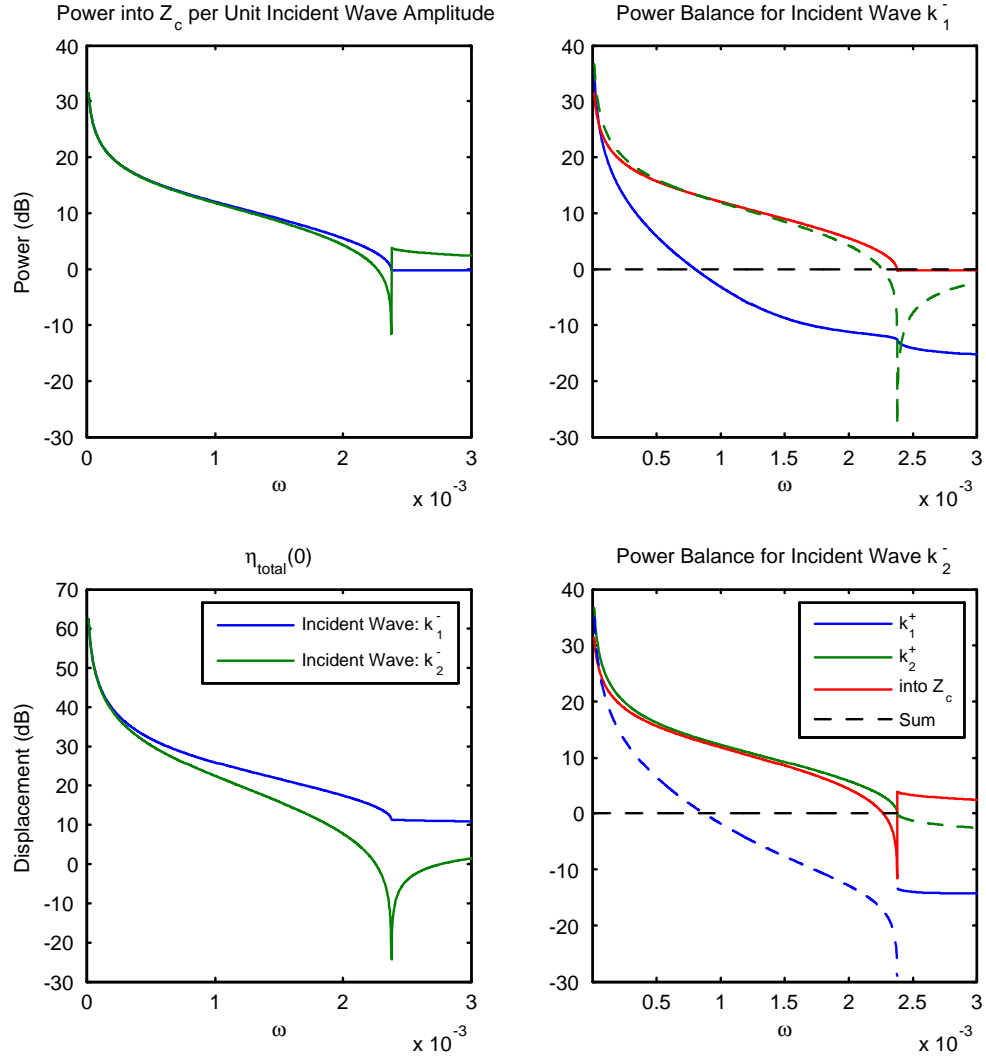


Figure 6.7: Scattering and power absorption at a free leading edge with an attached dashpot $Z_c = R_c$. Power normalized reflection coefficients and normalized power absorbed for $R_c = 0.375$ (dashpot constant), $U = 0.05$, $T = 2U^2$ and $\lambda = 0$.

is given by the product of the force and in phase velocity at the edge, or using the definition of the mechanical impedance, by

$$\begin{aligned}\Pi_c &= \frac{1}{2} \operatorname{Re} \{Z_c\} |\omega \eta_{total}(0)|^2, \\ &= \frac{R_c}{2} |\omega \eta(0) + \omega I|^2,\end{aligned}$$

where $\eta(0)$ is one of the unknowns solved in (6.37). The wave impedance $Z_w(k_j)$ of the incident wave can be used to recast the power extracted from the plate in the form of a power normalized coefficient. The power extracted per unit incident wave power is therefore

$$\frac{\Pi_c}{\Pi_{inc}} = \frac{R_c |\omega \eta(0) + \omega I|^2 / 2}{Z_w(k_j) |\omega I|^2}. \quad (6.38)$$

(Note that the power into the dashpot is a positive energy quantity, and that the sign of the coefficient above is wholly dependent on the wave energy of the incident wave.)

We note that, with the proper normalization of the power absorbed by the dashpot, the total scattered power is once again conserved.

The results in figure 6.7 are for a value of the non-dimensional dashpot constant, $R_c = 0.375$, chosen to maximize the overall power absorbed per unit incident wave power for the k_1^- incident wave.

In the limit $Z_c \rightarrow \infty$, we approach the solution for a hinged edge and the power absorbed into the dashpot tends to 0. In this limit, the boundary condition for the vertical force yields $i\omega Z_c \eta(0) = -i\omega Z_c I$. We would then have to eliminate $\eta(0)$ instead of $\eta'''(0)$ (in addition to $\eta''(0)$) from $h(k)$ and so we end up with a significantly modified system of equations which is given in the next subsection.

6.4.4 Hinged Edge

For a hinged condition, the total displacement and moment are zero, giving $\eta(0) = -I$ and $\eta'(0) = -ik_j I$ and yielding the system of equations

$$\begin{aligned}E_0 [K^+(k_0)] + E_1 [k_0 K^+(k_0)] + \eta'(0) [-i(\omega - Uk_0)(k_0^2 + T)] \\ + \eta'''(0) [i(\omega - Uk_0)] = (\omega - Uk_0) k_0 (k_0^2 + T + k_j^2) I + \mathcal{I}(k_0, k_j),\end{aligned} \quad (6.39)$$

for $k_0 = \{k_p, k_m, -k_p, -k_m\}$.

The magnitude and phase of the raw coefficients are given in figure 6.8 and the power normalized coefficients are given in figure 6.9. We observe that the hinged and clamped reflection coefficients differ mostly in phase and that their magnitudes are almost identical. Closer inspection by means of overlaying the power normalized coefficients shows that the hinged leading edge is slightly more over-reflective than the clamped edge.

6.5 Response for Leading Edge Drive

The same approach as in section 6.4 can be used to solve for the response to a externally applied load at an otherwise free leading edge. We simply set the incident wave amplitude to zero and include the applied loads as part of the structural edge conditions.

For a transverse load F_0 , the equations for the unknown constants resemble those for a translational constraint with $I = 0$ and $i\omega\eta(0) Z_c$ replaced by F_0 ,

$$\begin{aligned} E_0 [K^+(k_0)] + E_1 [k_0 K^+(k_0)] + \eta(0) [(\omega - Uk_0) k_0 (k_0^2 + T)] \\ + \eta'(0) [-i(\omega - Uk_0) k_0^2] = -i(\omega - Uk_0) F_0, \end{aligned} \quad (6.40)$$

for $k_0 = \{k_p, k_m, -k_p, -k_m\}$.

For a prescribed moment M_0 , we just replace F_0 with $ik_0 M_0$ in the above equation. The far field response is obtained by setting $I = 0$ in (6.28),

$$\eta(x) = \sum_{i=1}^2 \frac{-\gamma(k_i^+)}{(\omega - Uk_i^+)} \frac{K^+(k_i^+)}{K_k(k_i^+)} [E_0 + E_1 k_i^+] e^{ik_i^+ x}, \quad x \gg 1. \quad (6.41)$$

Two of the constants solved in equations (6.40) are the drive point deflection $\eta(0)$ and slope $\eta'(0)$. These can be used directly to form the drive point admittances of the semi-infinite plate driven at the leading edge

$$Y_{dp} = \frac{-i\omega\eta(0)}{F_0}, \quad Y_{dp}^{(1)} = \frac{-i\omega\eta'(0)}{M_0}, \quad (6.42)$$

where Y_{dp} is translational velocity per unit force and $Y_{dp}^{(1)}$ is rotational velocity per unit moment. The real parts of these admittances represent the power injected into the semi-infinite plate by a unit amplitude drive.

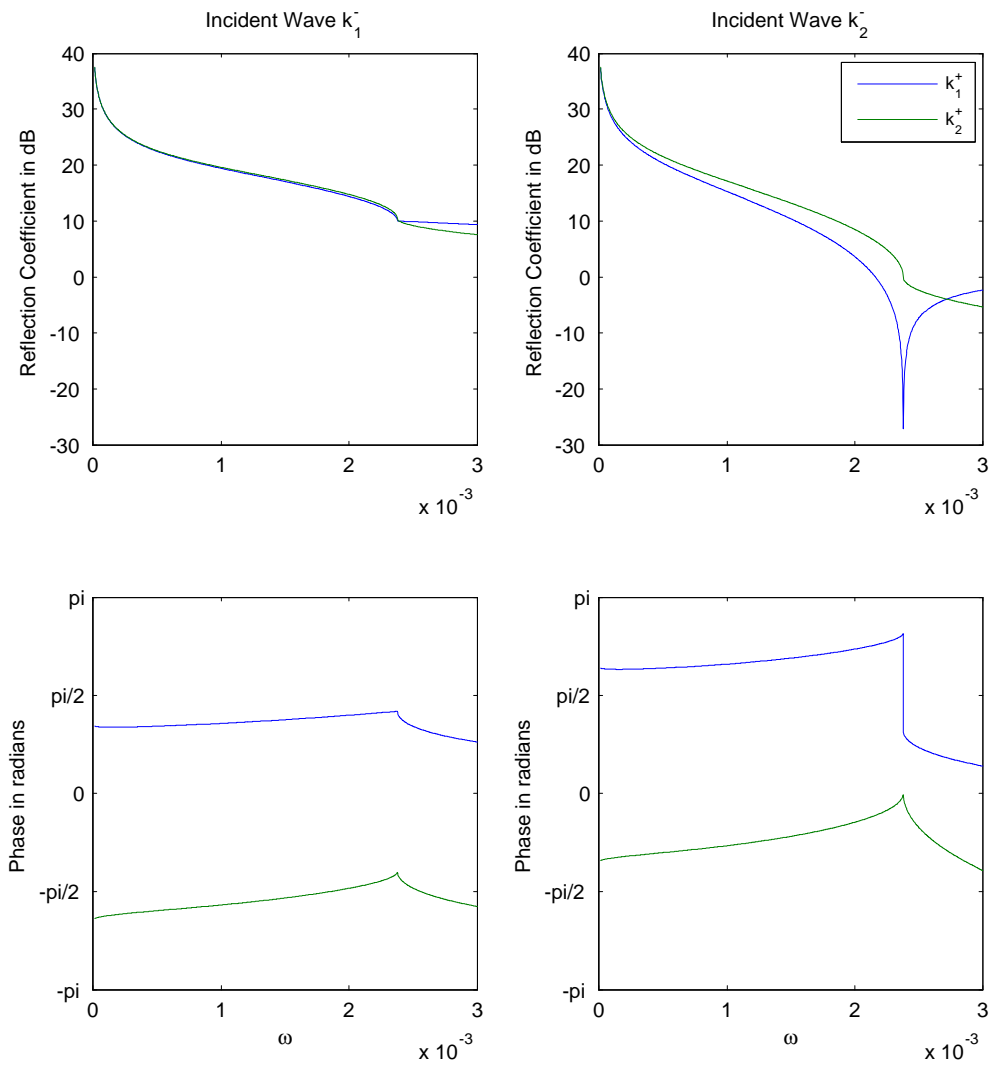


Figure 6.8: Magnitude and phase of the reflection coefficients for a hinged leading edge for $U = 0.05$, $T = 2U^2$ and $\lambda = 0$.

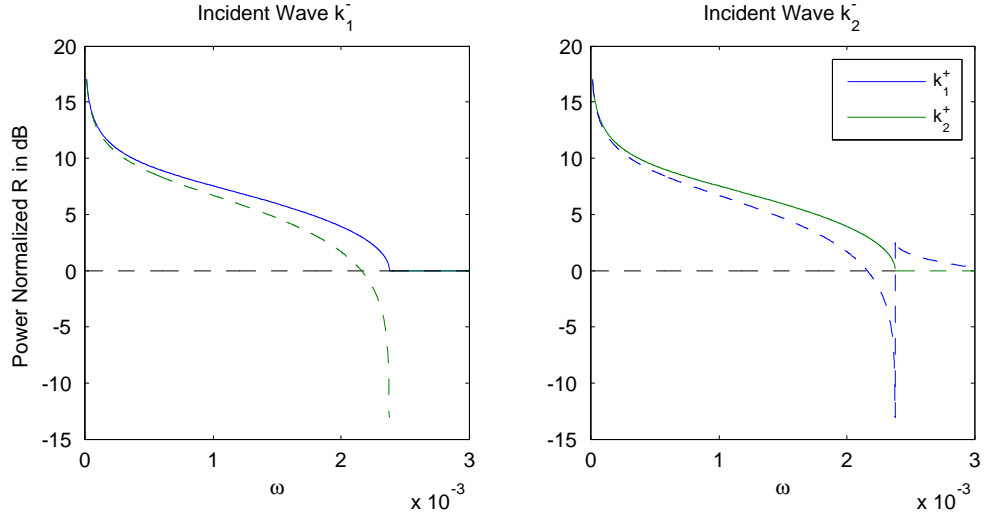


Figure 6.9: Power normalized reflection coefficients for a hinged leading edge for $U = 0.05$, $T = 2U^2$ and $\lambda = 0$.

The results for Y_{dp} are presented in figure 6.10. We observe that the total power transmitted to the far field balances with that injected into the plate. It is worth comparing these results to the more familiar case of a line drive on an infinite plate (top left corner plot in figure 4.4). The most striking difference is that the real part of the admittance is positive throughout the frequency range, including the range $\omega < \omega_p$ where negative energy waves are present indicating that the driver is injecting power *into* the semi-infinite plate. This is in contrast to the infinite plate, where the admittances were negative for $\omega < \omega_p$. Another feature is the absence of any singularities in either the far field or the drive point responses at $\omega = \omega_p$.

The second feature is in fact easier to explain. The singularities in the solution for the line driven infinite plate arose from the coalescence of two roots from separate half planes. In the case of a semi-infinite plate, only two waves travelling in the same direction are generated and the pinch singularity does not arise.

The mathematical explanation for the first phenomenon is also clear. For $\omega < \omega_p$, a semi-infinite plate driven at the leading edge generates two waves, one positive energy and one negative energy. The relative magnitudes (in the power normalized sense)

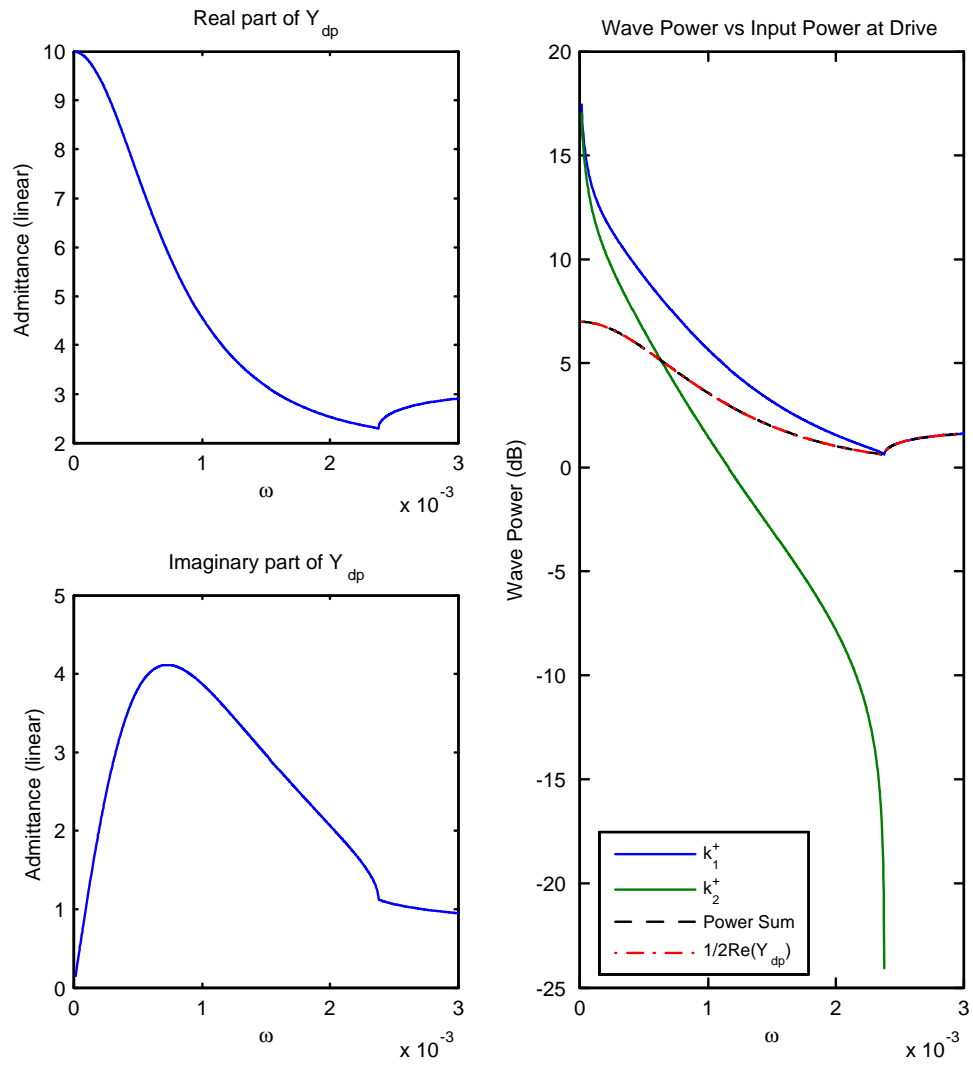


Figure 6.10: Response of semi-infinite plate driven by transverse load at leading edge for $U = 0.05$, $T = 2U^2$ and $\lambda = 0$.

of these two waves determines whether the real part of Y_{dp} is positive or negative. As can be seen from figure 6.10, the positive energy wave has the greater magnitude throughout this range and ends up determining the sign of the real part of Y_{dp} . For the case of the line-driven infinite plate, the wave power associated with the negative energy waves was greater than the power associated with the positive energy waves, resulting in a net negative for $\text{Re}\{Y_{dp}\}$. In the convectively unstable range, energy flux results for the coupling between the exponentially increasing and decreasing waves and the direction of the energy flux is determined by the relative phase between the two waves. For a line driven infinite plate, the two waves are in phase resulting in energy directed towards the drive and a negative $\text{Re}\{Y_{dp}\}$. In contrast, for a semi-infinite plate driven at the leading edge, the two waves are out of phase, resulting in a net energy flux away from the drive and a positive $\text{Re}\{Y_{dp}\}$.

6.6 Summary

In this chapter we used the Wiener-Hopf technique to derive the reflection coefficients for the upstream edge of a semi-infinite plate. We perform the multiplicative factorization of the Wiener-Hopf kernel numerically, and our results for the scattering coefficients are exact. We obtain the scattering matrices for a free edge, a clamped edge and a hinged edge and find that they are all over-reflective for $\omega < \omega_p$. Similarly, we find that a constraint, in the form of a dashpot, absorbs several times the power of an incident wave for $\omega < \omega_p$ when properly tuned. Finally, we solve for the semi-infinite plate drive admittances at the leading edge and find that, in contrast to the line driven infinite plate, $\text{Re}\{Y_{dp}\}$ is positive throughout the frequency range.

Chapter 7

Scattering from Trailing Edge

In this chapter scattering from the trailing edge of a semi-infinite fluid-loaded plate will be solved using the same Wiener-Hopf based approach employed for the leading edge problem. The main difference here is that we will allow a wake to be shed from the trailing edge providing a mechanism by which wave energy may exit the plate

The configuration for the trailing edge scattering problem is shown in figure 7.1. A downstream propagating wave $\eta_{inc} = Ie^{-ik_j^+x}$, with amplitude I and free wavenumber k_j^+ , is incident on the trailing edge of a submerged plate which occupies the half space $-\infty < x < 0$. A wake of amplitude $W = \Delta\varphi/2$, where $\Delta\varphi$ is the jump in potential across $y = 0$, and convective wavenumber ω/U occupies $0 < x < +\infty$.

A Wiener-Hopf based method of solution, valid in the asymptotic limit of small U and ω , was used by Oswell (1992) to solve the problem of a free trailing edge with and without wake. The method described in this chapter uses a different set of Wiener-Hopf equations than those employed by Oswell (1992) to achieve a simpler solution that is valid over all frequencies and flow speeds and for nonzero plate tension and spring support.

7.1 System Equations Using Half-Range Transforms

The half range transforms of the fluid potential are as defined in chapter 6 and are given by equations (6.2) and (6.1). The half-range transform of the plate displacement,

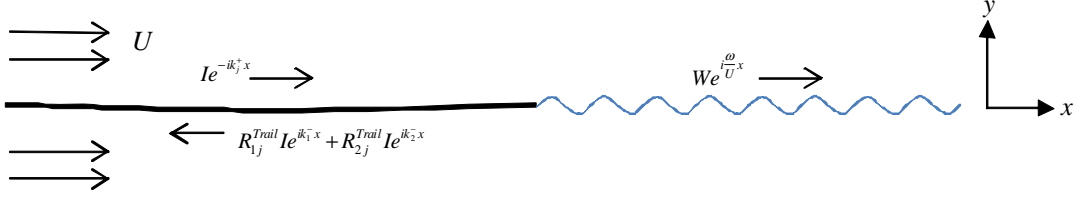


Figure 7.1: Scattering of plate waves from the downstream edge of a semi-infinite plate with wake.

now over $-\infty < x < 0$, is

$$\tilde{\eta}^+(k) \equiv \int_{-\infty}^0 \eta(x) e^{-ikx} dx$$

and the formula for obtaining higher order axial derivatives is now given by

$$F^+ \left(\frac{\partial^n \eta(x)}{\partial x^n} \right) = (ik)^n \tilde{\eta}^+(k) + \sum_{m=1}^n (ik)^{(m-1)} \frac{\partial^{(n-m)} \eta(-0)}{\partial x^{(n-m)}}. \quad (7.1)$$

In terms of the half-range transforms just defined, the system equations for the trailing edge problem are as follows.

The equations relating transformed quantities upstream of the edge, or on the side occupied by the plate, are

$$\tilde{p}^+ = i(\omega - Uk) \Phi^+ - U\varphi(-0), \quad (7.2a)$$

$$\frac{\partial \Phi^+}{\partial y} = -i(\omega - Uk) \tilde{\eta}^+ + U\eta(-0), \quad (7.2b)$$

$$-\alpha \tilde{p}^- = [k^4 + Tk^2 + \lambda - \omega^2] \tilde{\eta}^- + h(k), \quad (7.2c)$$

where

$$h(k) \equiv \eta'''(-0) + ik\eta''(-0) - (k^2 + T)\eta'(-0) - ik(k^2 + T)\eta(-0). \quad (7.3)$$

$h(k)$ is obtained, as before, by applying (7.1) and contains four unknown constants related to the structural edge conditions, two of which can be eliminated using the structural edge conditions and the remaining two determined as part of our solution.

Downstream from the edge, symmetry once again dictates that the total potential is an odd function of y . But now, the presence of a wake creates a finite jump, $\Delta\varphi(x, 0) = \varphi(x, y = +0) - \varphi(x, y = -0)$, in the potential at $y = 0$. If we identify $W = \Delta\varphi(x, 0)/2$

(or in terms of $y = +0$ quantities as $W = \Delta\varphi(x, 0y = +0)$) as the wake amplitude, the total potential must therefore equal the wake potential on $y = 0$, or $\varphi_{total} = \varphi + \varphi_{inc} = We^{i(\omega/U)x}$. The scattered field downstream of the edge is now given by

$$\varphi = We^{i(\omega/U)x} - i \operatorname{sgn}(y) \frac{I(\omega - Uk_j^+)}{\gamma(k_j^+)} e^{ik_j^+ x}, \quad x \geq 0, \quad y = 0, \quad (7.4)$$

and its half range transform is

$$\Phi^-(k, 0) = -i \frac{W}{(k - \omega/U)} - i \frac{I(\omega - Uk_j^+)}{\gamma(k_j^+) (k - k_j^+)}, \quad k_j \in R^+, \quad (7.5)$$

where the pole associated with the convective wavenumber ω/U is also in R^+ . If we set $W = 0$, we recover the case for scattering with no wake which corresponds to $\varphi_{total}(x, 0) = 0$. The latter may better represent the scattering process from a blunt trailing edge.

Finally, the equation relating R^+ and R^- quantities through the transformed potential and its vertical derivative remains unchanged and is given by

$$\frac{\partial \Phi^+}{\partial y} + \frac{\partial \Phi^-}{\partial y} = -\gamma(k) (\Phi^+ + \Phi^-). \quad (7.6)$$

7.2 Wiener-Hopf Equation

Eliminating $\tilde{\eta}^+$ and \tilde{p}^+ from (7.2), we obtain an expression relating the plate-side quantities

$$\begin{aligned} \alpha(\omega - Uk)^2 \Phi^+ &= -\mathcal{P}(k) \frac{\partial \Phi^+}{\partial y} \\ &+ i(\omega - Uk) (\alpha U \varphi(-0) - h(k)) - U \eta(-0) \mathcal{P}(k), \end{aligned} \quad (7.7)$$

where $\mathcal{P}(k) \equiv [k^4 + Tk^2 + \lambda - \omega^2]$ is the augmented plate operator as before. We combine (7.5) and (7.6) to obtain

$$\Phi^+ - i \frac{W}{(k - \omega/U)} - i \frac{I(\omega - Uk_j^+)}{\gamma(k_j^+) (k - k_j^+)} = -\frac{1}{\gamma(k)} \frac{\partial \Phi^+}{\partial y} - \frac{1}{\gamma(k)} \frac{\partial \Phi^-}{\partial y} \quad (7.8)$$

and use it to eliminate Φ^+ from (7.7) to generate an equation relating the vertical fluid velocities on both sides $\partial\Phi^+/\partial y$ and $\partial\Phi^-/\partial y$

$$\begin{aligned} \left\{ \mathcal{P}(k) - \frac{\alpha(\omega - Uk)^2}{\gamma(k)} \right\} \frac{\partial\Phi^+}{\partial y} &= \frac{\alpha(\omega - Uk)^2}{\gamma(k)} \frac{\partial\Phi^-}{\partial y} \\ &\quad - i \frac{\alpha W(\omega - Uk)^2}{(k - \omega/U)} - i \frac{I(\omega - Uk_j^+) \alpha(\omega - Uk)^2}{\gamma(k_j^+) (k - k_j^+)} \quad (7.9) \\ &\quad + i(\omega - Uk)(\alpha U\varphi(-0) - h(k)) - U\eta(-0)\mathcal{P}(k). \end{aligned}$$

Oswell (1992) proceeds to recast this equation in Wiener-Hopf form. However, as we saw for the leading-edge problem, it is more convenient to work with the equation relating $\partial\Phi^-/\partial y$ and Φ^+ . Using (7.8) to eliminate $\partial\Phi^+/\partial y$ in (7.7) and rearranging terms, we obtain

$$\begin{aligned} K\Phi^- + K \frac{I(\omega - Uk_j^+)}{\gamma(k_j^+) (k - k_j^+)} &\quad (7.10) \\ &= -\mathcal{P}(k) \frac{\partial\Phi^+}{\partial y} - \alpha(\omega - Uk)^2 \frac{I(\omega - Uk_j^+)}{\gamma(k_j^+) (k - k_j^+)} \\ &\quad - i(\omega - Uk)(\alpha U\varphi(+0) - h(k)) + U\eta(+0)\mathcal{P}(k), \end{aligned}$$

where $K \equiv \gamma(k)\mathcal{P}(k) - \alpha(\omega - Uk)^2$ is the same Wiener-Hopf kernel defined in chapter 6.

With the multiplicative factorization of the kernel $K = K^+K^-$ as described in Appendix (WH), followed by normalization of the terms containing the two (upper half plane) poles $\omega/U \in R^+$ and $k_j^+ \in R^+$ on the R^- side of the equation, (7.10) can

be recast in Wiener-Hopf form

$$\begin{aligned}
& K^+ \Phi^+ + \frac{W}{(k - \omega/U)} \left[K^+ - K^+ \left(\frac{\omega}{U} \right) \right] + \frac{I \left(\omega - U k_j^+ \right)}{\gamma \left(k_j^+ \right) \left(k - k_j^+ \right)} \left[K^+ - K^+ \left(k_j^+ \right) \right] \\
&= - \frac{\mathcal{P}(k)}{K^-} \frac{\partial \Phi^-}{\partial y} - \frac{\alpha (\omega - U k)^2}{K^-} \frac{I \left(\omega - U k_j^+ \right)}{\gamma \left(k_j^+ \right) \left(k - k_j^+ \right)} \\
&\quad - \frac{i (\omega - U k)}{K^-} (\alpha U \varphi(-0) - h(k)) + \frac{U \eta(-0)}{K^-} \mathcal{P}(k) \\
&\quad - \frac{WU}{(k - \omega/U)} K^+ \left(\frac{\omega}{U} \right) - \frac{I \left(\omega - U k_j \right)}{\gamma \left(k_j^+ \right) \left(k - k_j^+ \right)} K^+ \left(k_j^+ \right). \tag{7.11}
\end{aligned}$$

Once again, setting $W = 0$ in this equation gives the Wiener-Hopf equation for no wake.

7.3 Upstream Solution

We determine the leading order behavior of the r.h.s. of (7.11) as $k \rightarrow \infty$. We find that for the trailing edge problem, the $(\partial \Phi^- / \partial y) \mathcal{P}(k) / K^-$ is again the leading order term. However, the presence of a wake alters its k dependence. By prescribing a wake downstream of the edge we are effectively imposing a Kutta condition which requires that the fluid velocity be finite at the edge. The velocity at the trailing edge is therefore $\partial \varphi / \partial y \sim x^0$ as $x \rightarrow 0$, and its transform $\partial \Phi^- / \partial y \sim 1/k$ as $k \rightarrow \infty$. And with $K^- \sim k^{5/2}$ from Appendix B, we find that the highest order term on the r.h.s. behaves as

$$\frac{\mathcal{P}(k)}{K^-} \frac{\partial \Phi^-}{\partial y} \sim k^{\frac{1}{2}}, \quad k \rightarrow \infty. \tag{7.12}$$

Next, we invoke Louiville's Theorem which states that both sides of the Wiener-Hopf equation (7.11) must be equal to an entire function $E(k)$ which is analytic throughout R . The order of the polynomial $E(k)$ must be chosen to balance with the largest term on the lowest order side of (7.11). We therefore conclude that for $W \neq 0$, the entire function is a constant, or

$$E(k) = E_0. \tag{7.13}$$

Setting each side of (7.11) equal to this entire function, we obtain the pair of

independent equations

$$\begin{aligned} \Phi^+ = & -\frac{I(\omega - Uk_j^+)}{\gamma(k_j^+)(k - k_j^+)} \left[1 - \frac{K^+(k_j^+)}{K^+} \right] \\ & + \frac{E_0}{K^+} - \frac{W}{(k - \omega/U)} \left[1 - \frac{K^+(\omega/U)}{K^+} \right], \end{aligned} \quad (7.14)$$

$$\begin{aligned} \mathcal{P}(k) \frac{\partial \Phi^-}{\partial y} = & -\frac{I(\omega - Uk_j^+)}{\gamma(k_j^+)(k - k_j^+)} \left[\alpha(\omega - Uk)^2 + K^+(k_j^+)K^- \right] \\ & - i(\omega - Uk)(\alpha U \varphi(-0) - h(k)) + U \eta(-0) \mathcal{P}(k) \\ & + E_0 K^- - \frac{iW}{(k - \omega/U)} K^+(\omega/U) K^-. \end{aligned} \quad (7.15)$$

The edge potential $\varphi(-0)$ can once again be determined independently of the edge conditions. We can invoke continuity of the potential function across $x = 0$, $\varphi(-0) = \varphi(+0)$, or pursue the more rigorous derivation almost identical to that outlined for the leading edge in Appendix B to find

$$\varphi(-0) = W - i \frac{I(\omega - Uk_j^+)}{\gamma(k_j^+)}. \quad (7.16)$$

There are four unknown constants in (7.15) that have to be determined before we can write down the final solution. These are the wake amplitude W , the entire function constant E_0 and two plate deflection constants contained in the factor $h(k)$. Two additional unknown constants in $h(k)$ can be eliminated by application of the structural conditions at the edge.

The need to neutralize the *in-vacuo* plate roots associated with the $\mathcal{P}(k)$ factor multiplying $\partial \Phi^- / \partial y$ in (7.15) again provides us with the four equations required to solve for the four unknown constants, and the trailing edge version of equations (6.26) are found to be

$$\begin{aligned} E_0 K^-(k_0) + iW \frac{K^+(\omega/U) K^-(k_0)}{(k - \omega/U)} + i(\omega - Uk_0) h(k_0) = \\ \frac{I(\omega - Uk_j^+)}{\gamma(k_j^+)} \left[\frac{\alpha(\omega - Uk_0)^2}{(k_0 - k_j^+)} + \frac{K^-(k_0) K^+(k_j^+)}{(k_0 - k_j^+)} + \alpha U(\omega - Uk_0) \right], \\ \text{for } k_0 = \{k_p, k_m, -k_p, -k_m\}. \end{aligned}$$

We are now ready to solve for the scattered field. We combine (7.14) and (7.5) to obtain an expression for the full range potential

$$\begin{aligned} \Phi(k) = & \frac{E_0}{K^+(k)} - \frac{W}{(k - \omega/U)} \left[i + 1 - \frac{K^+(\omega/U)}{K^+(k)} \right] \\ & - \frac{I(\omega - Uk_j^+)}{\gamma(k_j^+)(k - k_j^+)} \left[i + 1 - \frac{K^+(k_j^+)}{K^+(k)} \right]. \end{aligned} \quad (7.17)$$

For solutions upstream from the edge, we close the contour in the lower half plane avoiding any poles that may have crossed over from the first quadrant when taking the inverse transform of (7.17). The far field solution is given by the residue contributions. The two poles at k_j^+ and ω/U are both in the upper half plane, hence the only poles that contribute are the zeros of $K^+(k)$, which are just the zeros of $K = K^+K^-$ in R^- (given that K^- is analytic and free of zeros in R^-), and simply correspond to the upstream travelling roots of the dispersion equation.

The scattered far-field potential and deflection upstream of the edge are therefore

$$\begin{aligned} \varphi_{far}(x, +0) = & \sum_{i=1}^2 \frac{iK^-(k_i^-)}{K_k(k_i^-)} \left[E_0 + iW \frac{K^+(\omega/U)}{(k_i^- - \omega/U)} \right. \\ & \left. + \frac{I(\omega - Uk_j^+) K^+(k_j^+)}{\gamma(k_j^+)(k_i^- - k_j^+)} \right] e^{ik_i^- x}, \quad x \ll -1, \end{aligned} \quad (7.18)$$

$$\begin{aligned} \eta_{far}(x) = & - \sum_{i=1}^2 \frac{\gamma(k_i^-)}{(\omega - Uk_i^-)} \frac{K^-(k_i^-)}{K_k(k_i^-)} \left[E_0 + iW \frac{K^+(\omega/U)}{(k_i^- - \omega/U)} \right. \\ & \left. + \frac{I(\omega - Uk_j) K^+(k_j^+)}{\gamma(k_j)(k_i^- - k_j^+)} \right] e^{ik_i^- x}, \quad x \ll -1, \end{aligned} \quad (7.19)$$

where k_i^- are the R^- roots of the dispersion function $D(k_i^-) = 0$ and $K_k \equiv \partial K / \partial k$ is given in (6.29). The reflection coefficients, defined in terms of far field deflection wave amplitudes, are therefore:

$$R_{ij}^{Trail} = - \frac{\gamma(k_i^-)}{(\omega - Uk_i^-)} \frac{K^-(k_i^-)}{K_k(k_i^-)} \left[E_0 + iW \frac{K^+(\omega/U)}{(k_i^- - \omega/U)} + \frac{(\omega - Uk_j^+) K^+(k_j^+)}{\gamma(k_j)(k_i^- - k_j^+)} \right], \quad (7.20)$$

with $I = 1$, in the solution for E_0 and W . The reflected near field is obtained by evaluating the branch cut integral along the $\gamma(k)$ cut (contained in $K(k)$) in the lower half plane and is given by

$$\eta_{near}(x) = -\frac{1}{\pi} \int_0^{+\infty} \frac{K^-(-iv)}{D(-iv)(\omega + iUv)} \left[E_0 - iW \frac{K^+(\omega/U)}{(iv + \omega/U)} - \frac{I(\omega - Uk_j^+) K^-(k_j^+)}{\gamma(k_j^+)(iv + k_j^+)} \right] e^{+vx} dv, \quad x \leq 0. \quad (7.21)$$

The scattered deflection is given by the sum of the pole contributions and the near field contribution, $\eta = \eta_{far} + \eta_{near}$.

In the absence of a wake, a situation that might more accurately model scattering from a blunt trailing edge, the Kutta condition is no longer satisfied and a weak singularity in the fluid velocity is allowed to exist. The behavior of the dominant term (7.12) now becomes $\sim k^1$ for large k and the entire function (7.13) has to be augmented by one order to become $E(k) = E_0 + E_1 k$. This Wiener-Hopf problem is almost identical to the leading edge problem solved in chapter 6 save for a few sign differences and with the roles of the upstream and downstream travelling waves swapped. The derivation follows along identical lines and will not be presented here. The solution consists of replacing all the wake terms in (7.3), (7.18), (7.19) and (7.20) with the additional E_1 term from the entire, or

$$iW \frac{K^+(\omega/U)}{(k_i - \omega/U)} \longleftrightarrow E_1 k. \quad (7.22)$$

7.4 Downstream Solution

The solution downstream from the trailing edge is obtained by closing the contour in the upper half plane when inverting (7.17). There are two pole contributions, ω/U and k_j^+ , corresponding respectively to the wake propagating at the convective wavenumber and a term that cancels exactly with the incident wave. The solution is

$$\varphi(x) = W e^{i(\omega/U)x} - i \frac{I(\omega - Uk_j)}{\gamma(k_j)} e^{ik_j^+ x}, \quad x \geq 0,$$

which corresponds exactly to (7.4), as expected. We note that the range of x over which the downstream solution is valid extends all the way down to $x = 0$. This is

because the function (7.17) is meromorphic, or free of branch cuts, in R^+ and hence does not have a nearfield for $x \geq 0$.

7.4.1 The Wake Impedance

In order to account for the total power scattered at the trailing edge, we need to solve for the wave power carried by a wake of amplitude W . We pursue the approach of chapter 3 that led to the identification of the wave flux for plate waves. Figure (W1) has the configuration for a wake of infinite extent, displaced from the horizontal by η and propagating at the convective wavenumber ω/U . The potential field carried by a wake of amplitude W is

$$\varphi(x, y, t) = \text{sgn}(y) W e^{i(\omega/U)x} e^{-(\omega/U)|y|} e^{-i\omega t}. \quad (7.23)$$

The pressure field induced by this wake is identically zero everywhere by Bernoulli's equation. The displacement of the wake from the horizontal is given by $\eta = d e^{i(\omega/U)x} e^{-i\omega t}$ where d does not necessarily have a simple relationship with the wake amplitude W and will be assumed by us to be prescribed separately.

With reference to the analysis of section 3.1 of chapter 3, the time averaged fluid flux as given by (3.19) becomes

$$\begin{aligned} \langle J_f \rangle &= \alpha \int_0^{+\infty} \langle p \varphi_x + U \varphi_x^2 \rangle dy \\ &= \frac{\alpha}{2} \int_0^{+\infty} \text{Re} \{ U \varphi_x \overline{\varphi_x} \} dy \\ &= \frac{1}{4} \alpha \omega |W|^2. \end{aligned} \quad (7.24)$$

The interface flux, given in (3.20), arises from an interface with non-zero vorticity being displaced from the horizontal and is given by

$$\begin{aligned} \langle J_i \rangle &= \alpha U \langle \varphi_t \eta \rangle \\ &= -\frac{1}{2} \text{Re} \{ i \alpha \omega U W \overline{d} \}. \end{aligned} \quad (7.25)$$

In contrast to an elastic plate, all structural inertia and restoring forces are zero for the wake together with any fluxes associated with them. Therefore the total wake flux

is simply the sum of the fluid and interface fluxes

$$\langle J_{wake} \rangle = \frac{1}{4} \alpha \omega |W|^2 - \frac{1}{2} \operatorname{Re} \{ i \alpha \omega U W \bar{d} \}. \quad (7.26)$$

The maximum contribution from J_i comes when the wake amplitude and displacement are exactly out of phase, and there is no contribution when they are in phase.

7.5 Reflection Coefficients for Representative Edge Conditions

The same three step process for obtaining reflection coefficients introduced in chapter 6 also applies to the trailing edge.

1) Apply the structural boundary conditions at the edge to eliminate two of the four unknown plate deflection constants from within $h(k)$ (given in (7.3)).

2) Incorporate the reduced $h(k)$ into (7.3) and solve the four equations for the four unknowns. The four constants will now be specific to the edge condition as well as to the incident wave parameters.

3) Insert the values of E_0 and W (wake) or E_1 (no wake) obtained from step 2) above into (7.20) and solve for the reflection coefficients.

7.5.1 Free Edge with Wake

Application of the zero total moment and zero total transverse force edge conditions in the presence of an incident wave $\eta_{inc} = I e^{-ik_j x}$, yields the scattered quantities $\eta''(0) = k_j^2 I$ and $\eta'''(0) - T\eta'(0) = ik_j^3 I + iTk_j I$ at $x = -0$. Substituting these into $h(k)$ (7.3) we eliminate two of the four deflection variables to obtain the four equations in the four unknown constants E_0 , W , $\eta(0)$ and $\eta'(0)$ for a free trailing edge with wake

$$\begin{aligned} E_0 [K^-(k_0)] + iW \left[\frac{K^+(\omega/U) K^-(k_0)}{(k_0 - \omega/U)} \right] + \eta(0) [(\omega - Uk_0) k_0 (k_0^2 + T)] \\ + \eta'(0) [-i(\omega - Uk_0) k_0^2] = (\omega - Uk_0) (k_j^3 + Tk_j + k_j^2 k_0) I + \mathcal{I}(k_0, k_j), \\ \text{for } k_0 = \{k_p, k_m, -k_p, -k_m\}. \end{aligned} \quad (7.27)$$

Here, $\mathcal{I}(k_0, k_j)$ is the same factor common to all edge conditions given in (6.34).

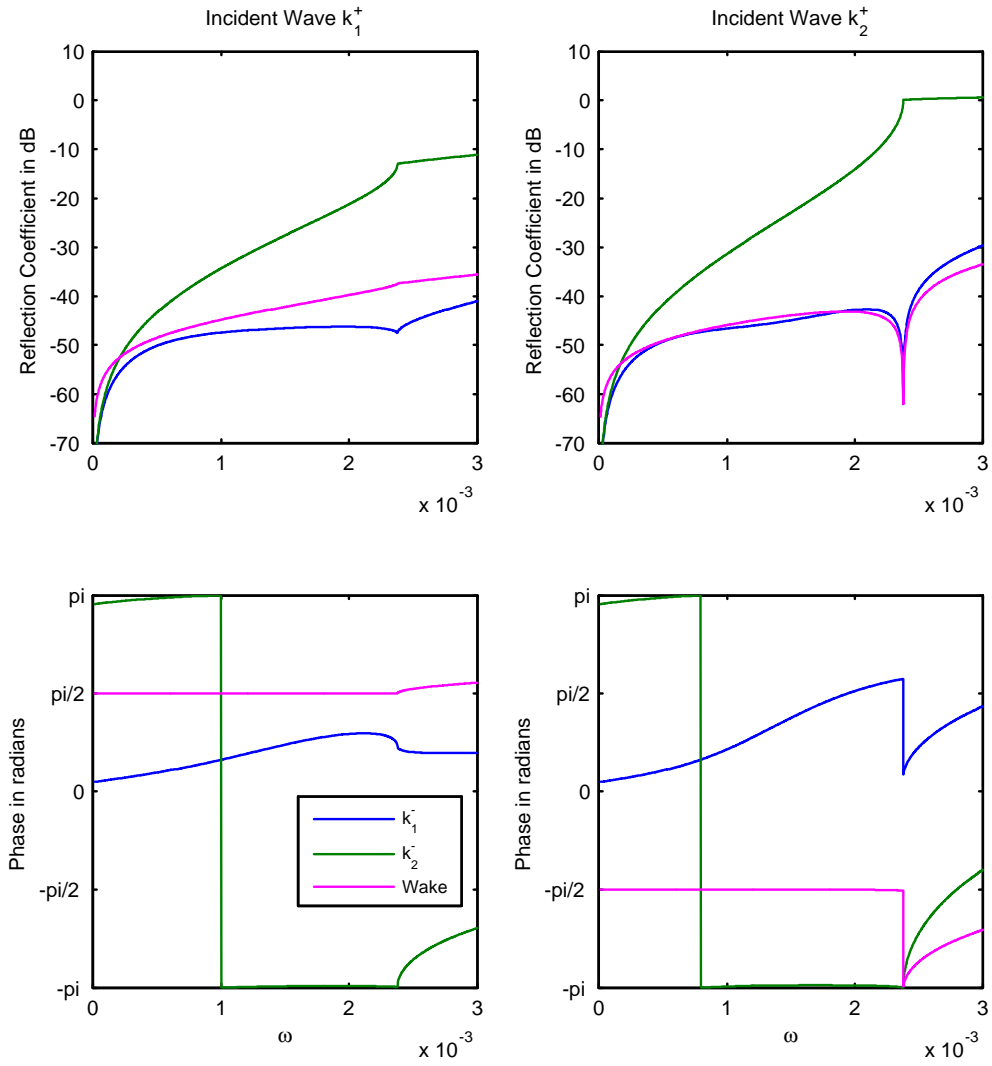


Figure 7.2: Magnitude and phase of reflection coefficients and wake amplitude for a free trailing edge with wake for $U = 0.05$, $T = 2U^2$ and $\lambda = 0$.

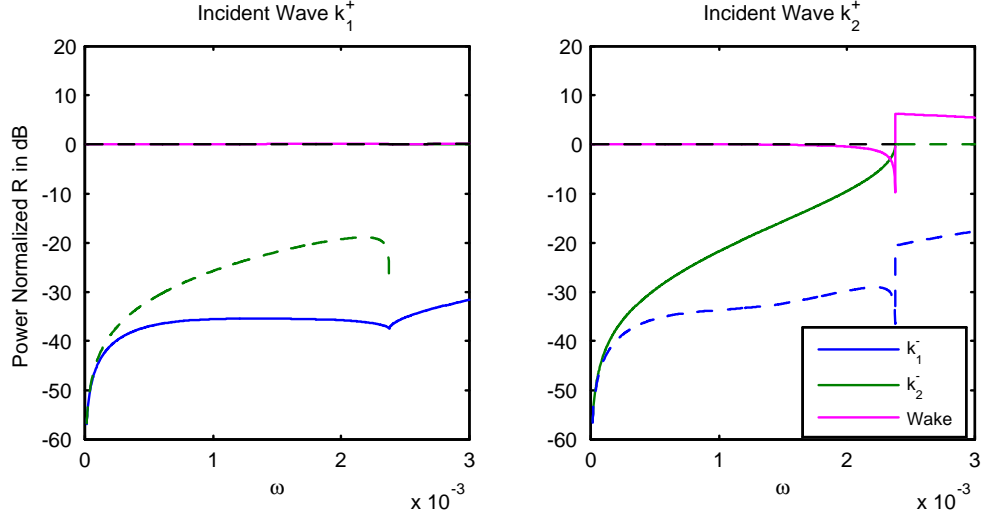


Figure 7.3: Power normalized reflection coefficients and wake amplitude for a free trailing edge with wake for $U = 0.05$, $T = 2U^2$ and $\lambda = 0$.

The magnitude and phase of the reflection coefficients, together with the wake amplitude W for a unit incident wave, are given in figure 7.2. The power normalized reflection coefficients and wake amplitude are given in figure 7.3. The reflected wave amplitudes are power normalized in the usual way (as described previously in equation (4.28)), whereas the wake amplitude is power normalized using the expression for the wake flux given in (7.26) by setting $d = \eta(0)$ for the deflection amplitude of the wake, where $\eta(0)$ is the deflection at the free edge solved in (7.27).

We observe that the incident wave energy is almost entirely absorbed in the wake, especially at very low frequencies, where the power normalized reflection coefficients tend to zero. This can clearly be seen in each of the three sub-plots of figure 7.4 which show the spatial response to an incident propagating wave k_1^+ at the fixed frequency $\omega = 1.5 \times 10^{-3}$ for three sets of plate parameters.

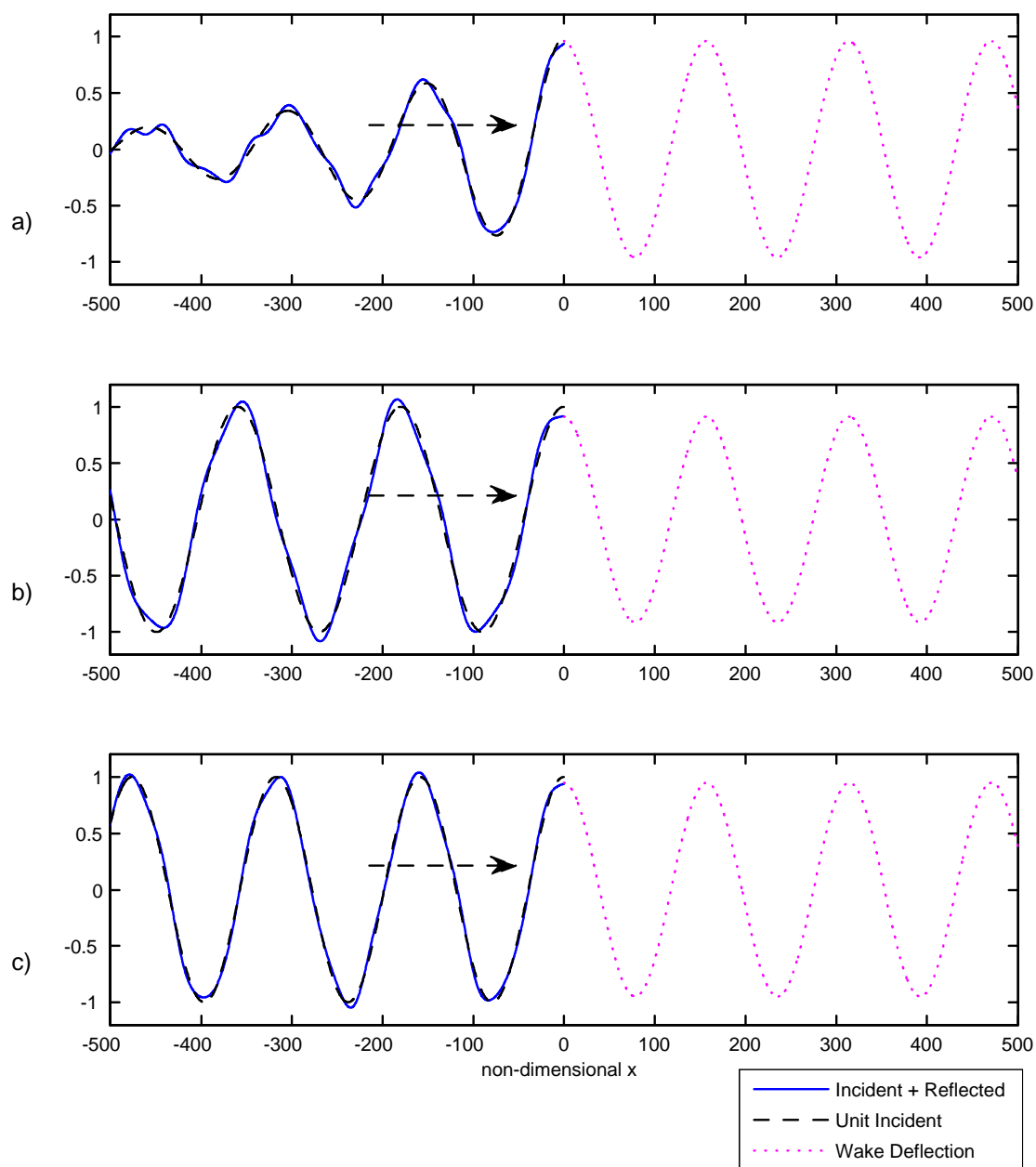


Figure 7.4: Spatial response for trailing edge with wake to unit incident wave k_1^+ at $\omega = 1.5 \times 10^{-3}$ and for plate parameters: $U = 0.05$; a) $T = 0, \lambda = 0$; b) $T = 2U^2, \lambda = 0$; c) $T = 0, \lambda = 5U^5$.

7.5.2 Free Edge without Wake

For the corresponding condition of a free trailing edge without wake, we set $W = 0$ and solve for the four unknown constants E_0 , E_1 , $\eta(0)$ and $\eta'(0)$ in

$$\begin{aligned} E_0 [K^-(k_0)] + E_1 [k_0 K^-(k_0)] + \eta(0) [(\omega - Uk_0) k_0 (k_0^2 + T)] \\ + \eta'(0) [-i(\omega - Uk_0) k_0^2] = (\omega - Uk_0) (k_j^3 + Tk_j + k_j^2 k_0) I + \mathcal{I}(k_0, k_j), \end{aligned} \quad (7.28)$$

for $k_0 = \{k_p, k_m, -k_p, -k_m\}$.

The magnitude and phase of the reflection coefficients are given in figure 7.5. The power normalized reflection coefficients are given in 7.6, and show a sizeable over-reflection process much like the one observed for a free leading edge.

7.5.3 Constraint at Edge without Wake

Next, we consider a translational constraint described through a local complex impedance Z_c attached to a blunt trailing edge with no wake. The vertical reaction force applied to the plate is $i\omega\eta_{total}(0)Z_c$ while the moment is zero. With these edge conditions, the equations for the four remaining constants E_0 , E_1 , $\eta(0)$, and $\eta'(0)$ are

$$\begin{aligned} E_0 [K^-(k_0)] + E_1 [k_0 K^-(k_0)] + \eta(0) [(\omega - Uk_0) (k_0 (k_0^2 + T) - \omega Z_c)] \\ + \eta'(0) [-i(\omega - Uk_0) k_0^2] = (\omega - Uk_0) (k_j^3 + Tk_j + k_j^2 k_0 + \omega Z_c) I + \mathcal{I}(k_0, k_j), \end{aligned} \quad (7.29)$$

for $k_0 = \{k_p, k_m, -k_p, -k_m\}$.

We again specialize to the case where the constraint is a pure dashpot, $Z_c = R_c$, where R_c is the dashpot constant. Figure 7.7 is the counterpart of 6.7 for the leading edge dashpot and plots the power normalized reflection coefficients for the a dashpot constant that achieves the maximum amount of incident wave power absorbed for the k_1^+ incident wave. The extracted power is expressed in the form of a power normalized coefficient using (6.38) and we see from the the dashed black line at 0dB that the total power scattered and absorbed is once again equal to the incident wave power. We note that the maximum power absorption is achieved with a comparable value of the dashpot constant but that the amount of power harvested as a proportion of the

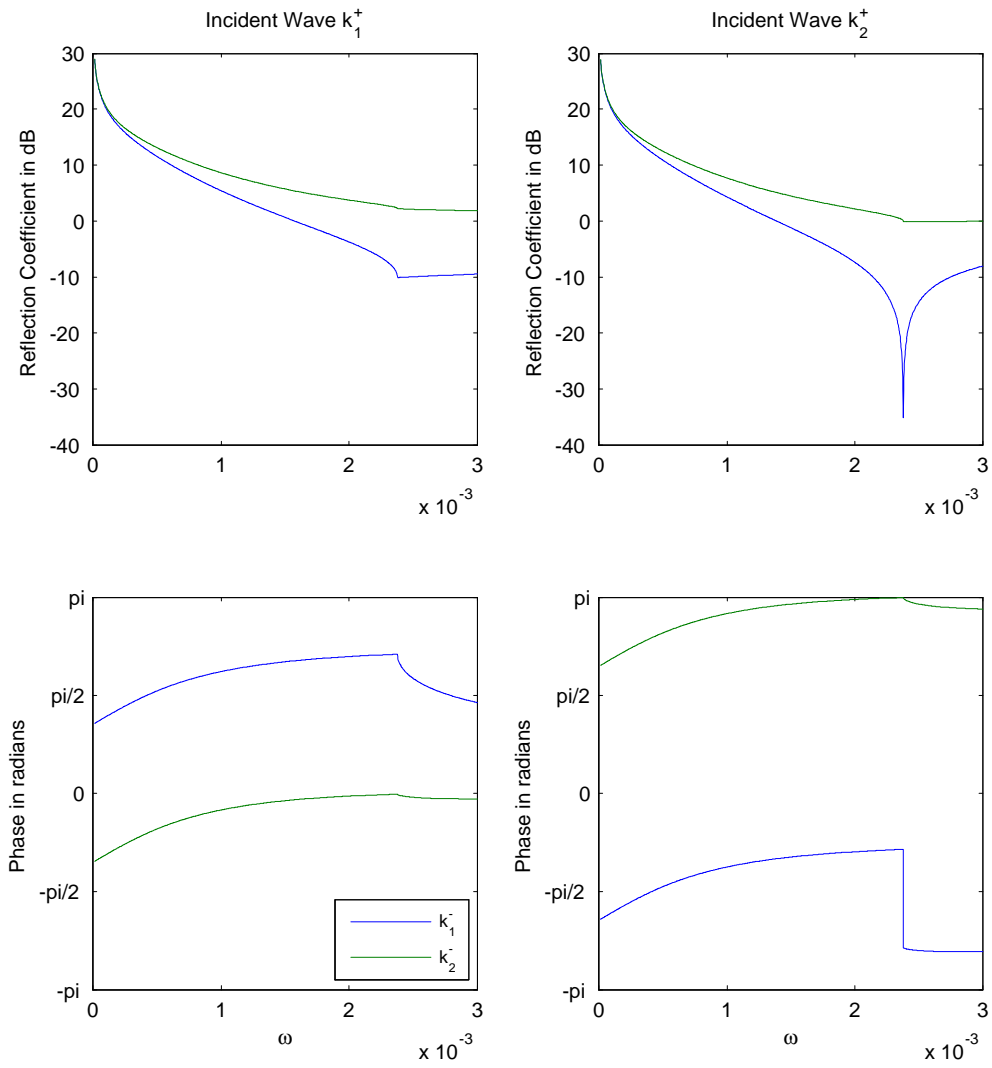


Figure 7.5: Magnitude and phase of reflection coefficients for a free trailing edge without wake for $U = 0.05$, $T = 2U^2$ and $\lambda = 0$.

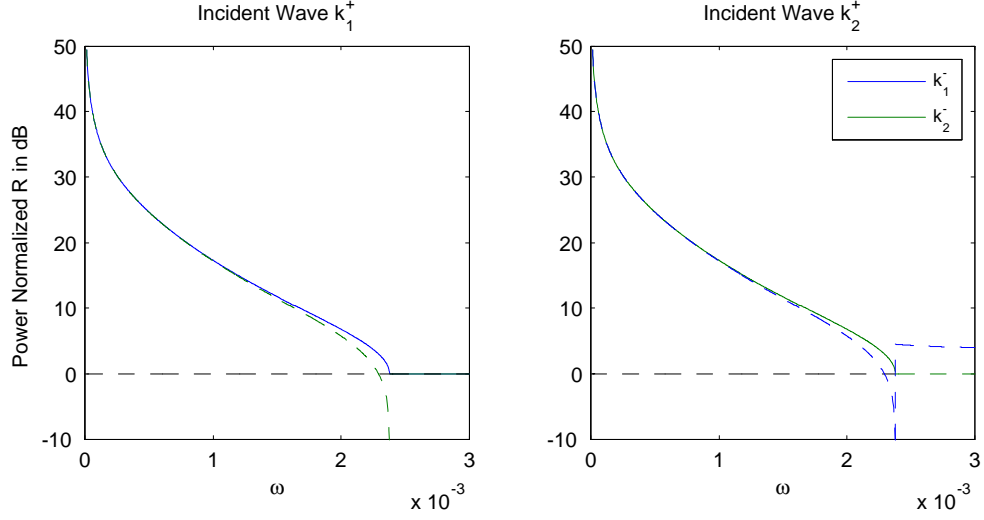


Figure 7.6: Power normalized reflection coefficients and power balance for a free trailing edge without wake for $U = 0.05$, $T = 2U^2$ and $\lambda = 0$.

incident wave power is significantly less than that achieved by a well-tuned dashpot at the leading edge.

7.5.4 Hinged Edge without Wake

For completion, we also include the results for a hinged trailing edge without wake

$$\begin{aligned}
 E_0 [K^-(k_0)] + E_1 [k_0 K^-(k_0)] + \eta'(0) [-i(\omega - Uk_0)(k_0^2 + T)] \\
 + \eta'''(0) [i(\omega - Uk_0)] = (\omega - Uk_0) k_0 (k_0^2 + T + k_j^2) I + \mathcal{I}(k_0, k_j), \\
 \text{for } k_0 = \{k_p, k_m, -k_p, -k_m\}.
 \end{aligned} \tag{7.30}$$

The magnitude and phase of the reflection coefficients are given in figure 7.8 and the power normalized reflection coefficients are given in 7.9. We note that, even though the raw reflection coefficients have much smaller magnitudes than the coefficients for a hinged leading edge, the power normalized coefficients are almost identical indicating that a hinged edge is equally over-reflective at either end.

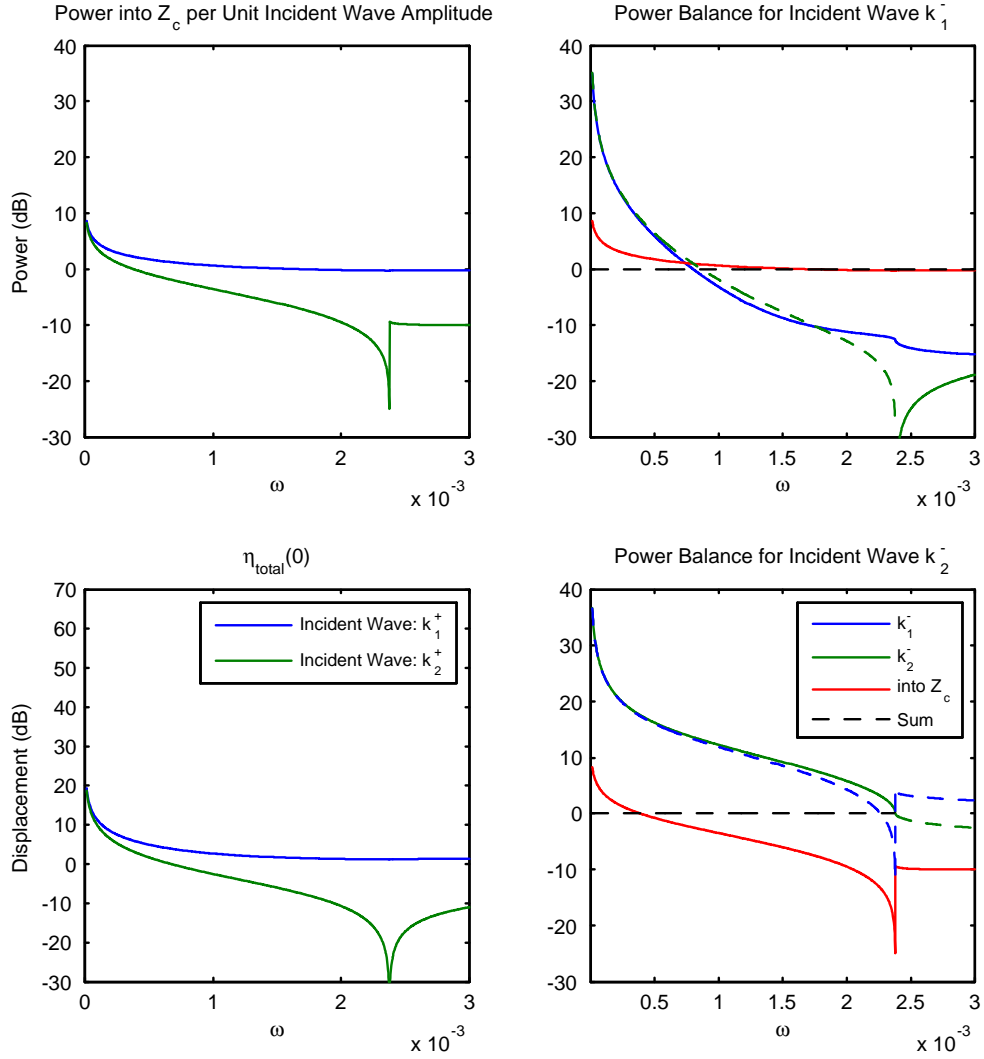


Figure 7.7: Scattering and power absorption at a free trailing edge (no wake) with an attached dashpot $Z_c = R_c$. Power normalized reflection coefficients and normalized power absorbed for $R_c = 0.335$ (dashpot constant), $U = 0.05$, $T = 2U^2$ and $\lambda = 0$.

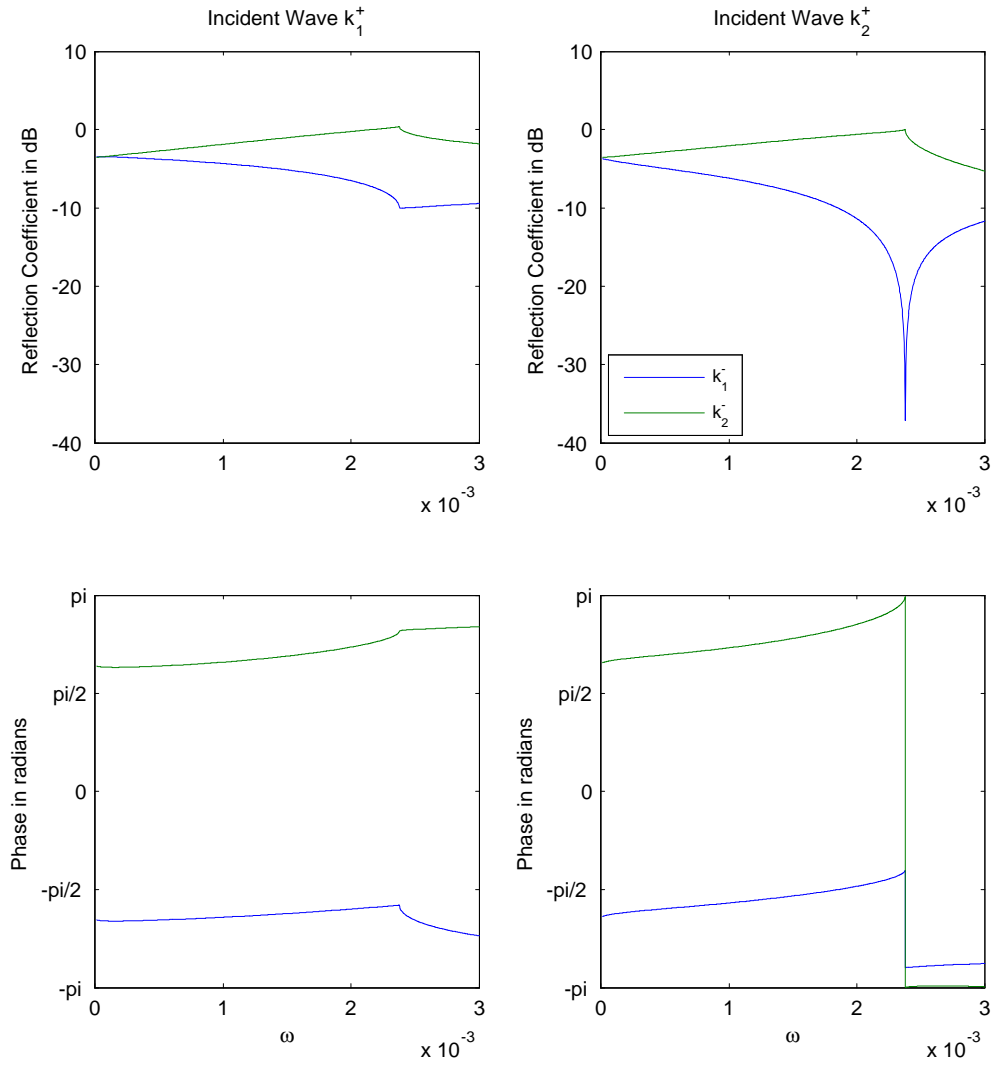


Figure 7.8: Magnitude and phase of reflection coefficients for a hinged trailing edge without wake for $U = 0.05$, $T = 2U^2$ and $\lambda = 0$.

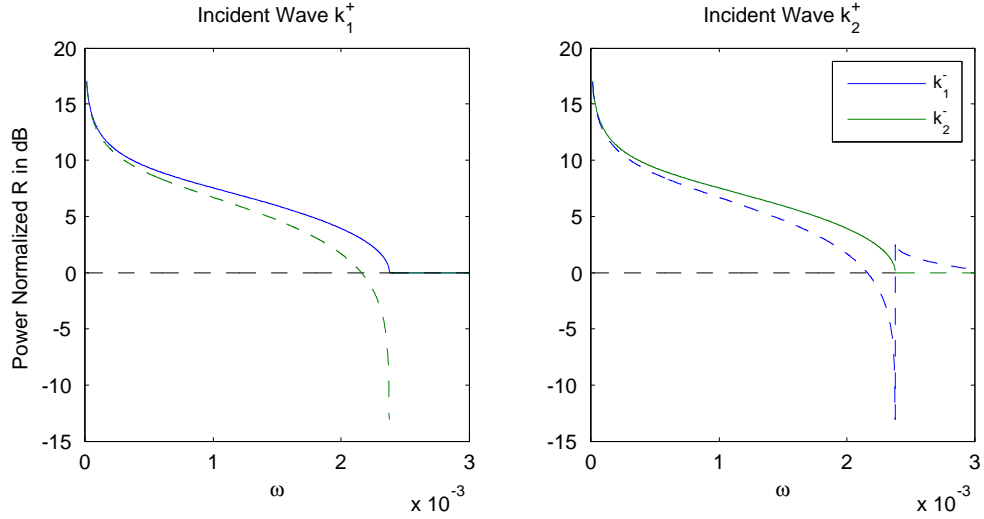


Figure 7.9: Power normalized reflection coefficients for a hinged trailing edge without wake for $U = 0.05$, $T = 2U^2$ and $\lambda = 0$.

7.6 Response for Trailing Edge Drive

7.6.1 Without Wake

For the response to an externally applied load at a free and wakeless trailing edge, we set the incident wave amplitude to zero and incorporate the applied loads through the structural edge conditions.

For a transverse load F_0 , the equations for the unknown constants with no wake present are

$$\begin{aligned}
 E_0 [K^-(k_0)] + E_1 [k_0 K^-(k_0)] + \eta(0) [(\omega - Uk_0) k_0 (k_0^2 + T)] \\
 + \eta'(0) [-i(\omega - Uk_0) k_0^2] = -i(\omega - Uk_0) F_0, \\
 \text{for } k_0 = \{k_p, k_m, -k_p, -k_m\}.
 \end{aligned} \tag{7.31}$$

The response to a prescribed moment M_0 can be obtained by making the substitution $F_0 \rightarrow ik_0 M_0$ in equations (7.31) above. The far field response is obtained by making the substitution (7.22) and setting $I = 0$ in (7.19)

$$\eta_{far}(x) = \sum_{i=1}^2 \frac{-\gamma(k_i^-)}{(\omega - Uk_i^-)} \frac{K^-(k_i^-)}{K_k(k_i^-)} [E_0 + E_1 k_i^-] e^{ik_i^- x}, \quad x \ll -1. \tag{7.32}$$

The drive point deflection $\eta(0)$ and slope $\eta'(0)$ obtained from solving equations (7.31) are used to form the drive point admittances

$$Y_{dp} = \frac{-i\omega\eta(0)}{F_0}, \quad Y_{dp}^{(1)} = \frac{-i\omega\eta'(0)}{M_0}, \quad (7.33)$$

where Y_{dp} is translational velocity per unit force and $Y_{dp}^{(1)}$ is rotational velocity per unit moment. The power injected into the semi-infinite plate at the trailing edge by a unit amplitude drive is given by the real parts of these admittances.

The results for Y_{dp} are plotted in figure 7.10. We observe that the total power transmitted to the far field balances with that injected into the plate. Comparing these results with the equivalent results for a leading edge drive given in figure 6.10 we find that, remarkably, the real and imaginary parts of Y_{dp} are equal. Although the trailing edge driver imparts more power than the leading edge driver to the individual waves it generates, the total power imparted is the same whether the driver is at the upstream or downstream edge (the latter is implied by the equality between the real parts of Y_{dp}).

We also note that Y_{dp} becomes purely resistive as $\omega \rightarrow 0$ for the choice of plate parameters used in figure 7.10. This is in fact a feature of the response only for $T \neq 0$ when, at low enough frequencies, the tension restoring forces dominate the bending forces and the plate acts much like a string in tension which is purely resistive at the drive instead of as a bending beam which has both resistive and reactive components at the drive.

7.6.2 With Wake

If we further assume that, together with an applied external load, the Kutta condition is satisfied at the trailing edge the results above need to be modified as follows.

A wake of (potential) amplitude $We^{i(\omega/U)x}$ now occupies the space $x > 0$. The equations for the unknown constants for an applied transverse load F_0 become

$$\begin{aligned} E_0 [K^-(k_0)] + W \left[\frac{iK^+(\omega/U)}{(k_0 - \omega/U)} K^-(k_0) \right] + \eta(0) [(\omega - Uk_0) k_0 (k_0^2 + T)] \\ + \eta'(0) [-i(\omega - Uk_0) k_0^2] = -i(\omega - Uk_0) F_0, \end{aligned} \quad (7.34)$$

for $k_0 = \{k_p, k_m, -k_p, -k_m\}$.

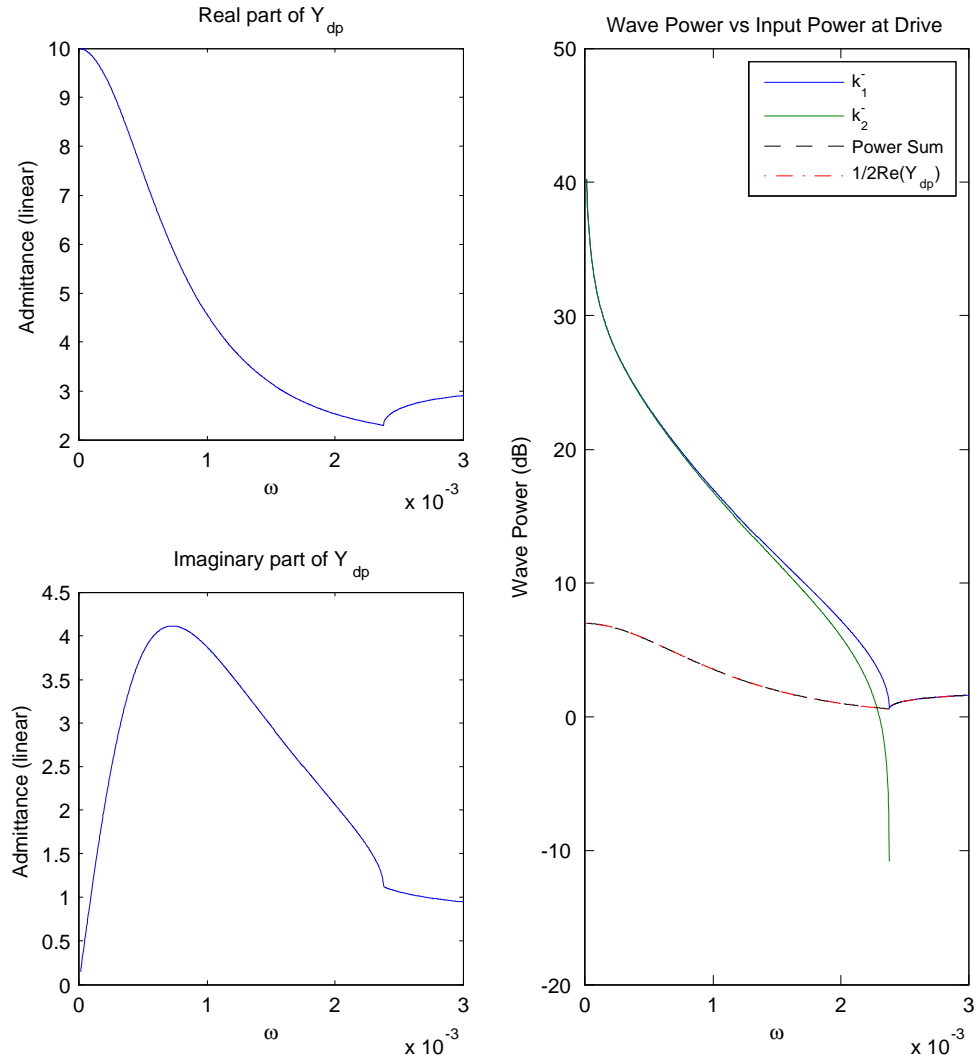


Figure 7.10: Response of semi-infinite plate driven by transverse load at trailing edge without wake for $U = 0.05$, $T = 2U^2$ and $\lambda = 0$.

The far field response is now given by setting $I = 0$ in (7.19) and substituting in W and E_0 from (7.34) above. The drive point admittances are still given by (7.33) with deflection $\eta(0)$ and slope $\eta'(0)$ provided by (7.34).

The problem of the trailing edge drive with wake has now been solved. However, we need one additional piece of information to be able to evaluate the power entrained in the wake. That is the deflection of the wake vortex sheet from the horizontal given by $de^{i(\omega/U)x}$. The natural choice is to take $d = \eta(0)$ where $\eta(0)$ is a solution of (7.34). The power entrained in the wake can then be calculate using the expression for wake flux given in (7.26).

Figure 7.11 plots the drive point and far field responses for a driver at the trailing edge with wake. The choice of wake displacement amplitude discussed above is only needed to power normalize the wake coefficient. The wave amplitudes are of course power normalized independently of this choice. The drive point Y_{dp} also does not depend on this choice.

7.7 Summary

In this chapter we used the Weiner-Hopf technique to derive the reflection coefficients for the downstream edge of a semi-infinite plate. As for the leading edge, the multiplicative factorization of the Weiner-Hopf kernel is evaluated numerically and exactly, and so our results for the scattering coefficients are exact. We obtain the scattering matrices for a free edge, a clamped edge and a hinged edge and find that they are all over-reflective for $\omega < \omega_p$. The exception is the free trailing edge with wake which, incredibly, is found to absorb almost all of the incident wave energy. We also discover that in order to properly account for the power in the wake, a term proportional to the wake deflection amplitude must be included. Finally, we solve for the semi-infinite drive admittances at the trailing edge and find that when there is no wake, $\text{Re}\{Y_{dp}\}$ is positive throughout the frequency range just like at the leading edge. When a trailing edge wake is present, $\text{Re}\{Y_{dp}\}$ is significantly smaller in magnitude and negative throughout $\omega < \omega_p$.

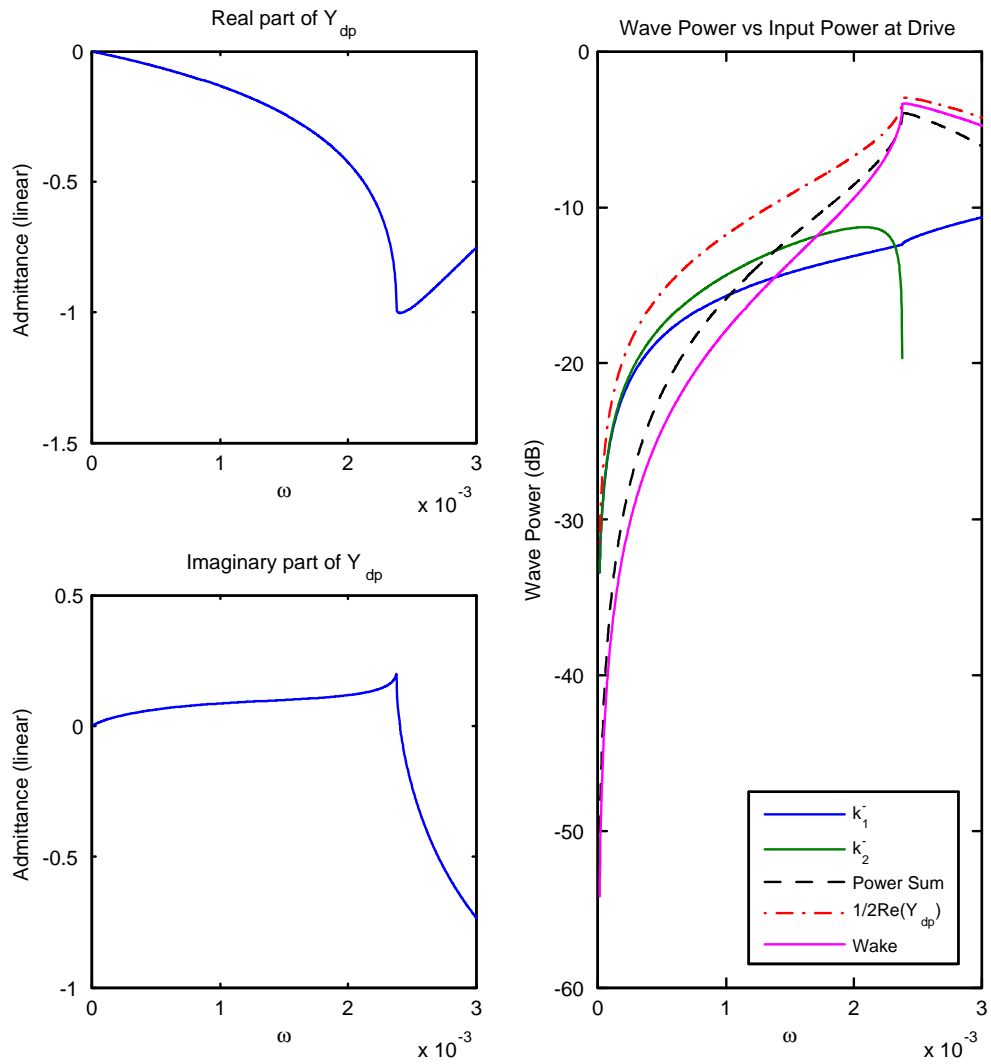


Figure 7.11: Response of semi-infinite plate driven by transverse load at trailing edge with wake for $U = 0.05$, $T = 2U^2$ and $\lambda = 0$.

Chapter 8

Global Modes of Long, Finite Plates

In this chapter we study the self-sustaining, unstable resonances of plates immersed in a moving fluid. We will use the reflection coefficients derived by the Weiner-Hopf method in chapters 6 and 7 to solve for the global modes of a finite plate. We limit our analysis to ‘long plates’ out of necessity; our Weiner-Hopf based reflection coefficients are for incident propagating waves only and do not account for reflections from incident nearfields. Our analysis is therefore valid for plates whose edges are far enough, for the longest wavelength and lowest frequency of interest, such that the nearfield from one edge does not significantly effect the other edge.

8.1 Global Modes for Large L

We consider a ‘long’ plate of length L with 2×2 reflection matrices R^L and R^T at the leading and trailing edges respectively. The derivation of the condition for resonance is identical to that presented in section 5.1.1 and will not be repeated here. We will only restate the main result: the eigenfrequencies are complex roots of the system determinant $\det(I - \mathcal{G}) = 0$ (5.7), where I is the identity matrix, and \mathcal{G} is the 2×2 ‘propagating waves only’ gain matrix defined in (5.8) and whose terms are given in (5.9).

The results for the global modes of specific finite plates presented in this chapter are all obtained by numerically sweeping the complex- ω and L planes for zeros of the system determinant. The procedure adopted here is described in great detail in Peake (2004) and entails evaluating all components comprising the gain matrix for complex ω . These include the exponential propagation factors as well as the Weiner-Hopf obtained reflection coefficients.

The need to evaluate the reflection coefficients for complex frequencies has a clear physical rationale. At resonance, all waves incident on a plate edge are vibrating at the same frequency. If the system is unstable, the incident waves will in addition be accompanied by a temporal growth rate embodied by the (positive) imaginary part of the eigenfrequency. For a given edge condition, the reflection coefficient for an incident wave which is growing in time differs by a small but important amount from the reflection coefficient for an incident wave with real frequency. The difference in magnitude and phase between the two scattering processes is captured precisely by evaluating the reflection coefficient at the complex eigenfrequency in question.

8.1.1 Estimates of Maximum Growth Rate

In general, the unstable resonance growth in a finite plate is due to a combination of over-reflection at the edges and amplification during propagation caused by convectively unstable waves. Doaré & de Langre (2006) have proposed a method for separating the respective contributions to unstable growth due to the reflections and the propagation path. It is based on the inequality

$$\|\mathcal{G}^+\| \leq \|R^L\| \|\Phi^-\| \|R^T\| \|\Phi^+\|, \quad (8.1)$$

where $\|M\|$ is the 2-norm of matrix M which is found by computing the square root of the largest eigenvalue of $M^\dagger M$. Since $|\lambda_{\max}| \leq \|\mathcal{G}\|$, where λ_{\max} is the largest eigenvalue of \mathcal{G} , the product of the four scalar terms on the right hand side of (8.1) provides an upper bound on the gain of the finite system. The upper bound on the contribution from the reflections alone is given by the product of the two scalar quantities $\mathcal{R}_{2norm} = \|R^L\| \|R^T\|$ and that for the propagation alone is given by $\mathcal{P} = \|\Phi^-\| \|\Phi^+\|$. Since Φ^- and Φ^+ are diagonal matrices, the upper bound on the propagation gain is

simply the product of the magnitudes of the most amplified upstream and downstream travelling waves. Using the naming scheme for waves that we've adopted, the upper bound for propagation is simply

$$\mathcal{P} = \left| e^{ik_1^+ L} \right| \left| e^{ik_1^- L} \right|. \quad (8.2)$$

As mentioned in section 5.1.1, the terms $R_{ij}^T R_{ji}^L$ that appear along the diagonal of the gain matrix are power normalized quantities. They consist of products of reflection coefficients for the same pair of upstream and downstream travelling waves and have the property that

$$\begin{aligned} R_{ij}^T R_{ji}^L &= \left(\frac{Z_w^{\frac{1}{2}}(k_i^-)}{Z_w^{\frac{1}{2}}(k_j^+)} R_{ij}^T \right) \left(\frac{Z_w^{\frac{1}{2}}(k_j^+)}{Z_w^{\frac{1}{2}}(k_i^-)} R_{ji}^L \right) \\ &\equiv \sqrt{P_{ij}^T P_{ji}^L}, \end{aligned}$$

where P are the power normalized reflection coefficients defined in (4.28). Each term $R_{ij}^T R_{ji}^L$ therefore represents the total power exchanged at the edges between a given pair of upstream and downstream propagating waves (in our example k_i^- and k_j^+). Retaining the phase of R_{ij}^T and R_{ji}^L while evaluating their complex product implicitly limits us to the power exchanged for the specific case of $L = 0$.

If we instead strip the phase out of each coefficient and evaluate the products of their magnitudes, one can argue that we have captured the upper bound of this power exchange for all separation distances L . Summing the contributions from all four such combinations of upstream and downstream travelling waves must therefore provide an upper bound on the net power scattered at the edges. This quantity is simply the trace of the product between the 'phase-less' upstream and downstream reflection matrices, or

$$\mathcal{R}_{trace} = |R_{11}^T| |R_{11}^L| + |R_{12}^T| |R_{21}^L| + |R_{21}^T| |R_{12}^L| + |R_{22}^T| |R_{22}^L|. \quad (8.3)$$

We will see shortly that \mathcal{R}_{trace} provides a lower and tighter estimate than \mathcal{R}_{2norm} on the upper bound of the reflection gain.

If the individual terms of \mathcal{R}_{trace} , or the products of reflection coefficient given in (8.3), are to represent power exchange at a plate edge then we need to discard all

terms involving the two structural evanescent waves k_2^- and k_2^+ for $\omega > \omega_p$. Although these waves do not carry power to the far field (the real parts of their wave impedances are zero), the terms containing reflection coefficients associated with these waves in (8.3) do not yield zero. This is because for very short plate lengths, the two structural evanescent fields can interact to generate a net flux of energy much like in the phenomenon of optical tunneling. However, this can only happen when the upstream and downstream edges are so close that they are in each other's nearfields, which is of course in contradiction with our 'long plate' assumption. We therefore need to omit these terms from (8.3) for $\omega > \omega_p$ if our understanding of \mathcal{R}_{trace} as the net exchange of energy at the edges of a long plate is to remain consistent over all frequencies, giving

$$\mathcal{R}_{trace} = |R_{11}^T| |R_{11}^L|, \quad \omega > \omega_p. \quad (8.4)$$

We note here that in the convectively unstable regime, there also exists a pair of downstream travelling waves, k_1^+ and k_2^+ , that do not carry any flux when taken individually. However, as discussed by Crighton & Oswell (1991), a net non-zero flux does arise from their interaction, and the magnitude of this flux is independent of the separation distance between the plate ends because both waves emanate from the same upstream edge. Therefore, the terms involving reflection coefficients associated with these waves must be retained in (8.3).

Finally, we note that the predictions for maximum growth involved in both \mathcal{R}_{2norm} and \mathcal{R}_{trace} are necessarily made for real ω and do not capture the small differences in the magnitude of the reflection coefficient that result from introducing small positive imaginary parts into ω to account for the non-zero temporal growth rates. Fortunately, these appear to generally reduce the magnitude of R and hence do not alter the upper limit of our estimates.

8.1.2 From Maximum Gain to Temporal Growth Rate

We will be using the local maxima of $\text{Re}\{\lambda_{\max}\}$ (evaluated for real ω) to obtain an initial estimate for the complex resonance frequencies. This will serve as the initial guess for our root solver, which solves for the actual complex eigenfrequencies by sweeping the entire complex ω plane for the zeros of the system determinant $\det(I - \mathcal{G})$

(5.7). To convert from gain to temporal growth rates we set

$$\text{Im}\{\omega\} \approx \frac{\ln(\text{Re}\{\lambda_{\max}\})}{T_{rt}}, \quad (8.5)$$

where T_{rt} is the fastest round trip time across the plate. Our estimate for the shortest round trip time is based on the largest group velocities for downstream and upstream travelling waves and is given by

$$T_{rt} \approx \frac{L}{\text{Re}\{v_g(k_1^+)\}} - \frac{L}{v_g(k_1^-)}. \quad (8.6)$$

It is necessary to take the real part of $v_g(k_1^+)$ over the range of frequencies where convective instabilities exist and the minus sign in (8.6) is necessary because $v_g(k_1^-)$ is negative.

8.1.3 The Kulikovskii Condition

There is one additional bound on the temporal growth rate that we must introduce. The Kulikovskii criterion determines the limiting value of $\text{Im}\{\omega\}$ when the plate length tends to infinity, and is given by

$$\min_{\substack{i=1,2 \\ j=1,2}} \left(\text{Im}\{k_i^+ - k_j^-\} \right) = 0, \quad (8.7)$$

where the minimum of $\text{Im}\{\omega\}$ over the four combination of waves must be chosen.

The criterion was first introduced by Kulikovskii in 1966 in the context of electron beam instability and cited in Volume 10 of the Course for Theoretical Physics, Physical Kinetics, pg 283, by Lifshitz and Pitaevskii's (1981). More recently, it has been used in the context fluid-elastic instabilities by Doare & de Langre (2002) and Peake (2004). It represents a balance between the most amplified wave travelling downstream and the least attenuated wave travelling upstream. In our context, the two waves in question are always k_1^+ and k_1^- , therefore the condition in (8.7) can be written more succinctly as

$$\text{Im}\{k_1^+ - k_1^-\} = 0. \quad (8.8)$$

For the frequency range where convectively unstable waves are present, this balance is achieved for finite positive values of $\text{Im}\{\omega\}$. Outside this frequency range, only $\text{Im}\{\omega\} = 0$ satisfies equation (8.8).

8.1.4 An Explicit Kulikovskii Condition?

If we substitute our upper bound on gain from (8.3) into (8.5), we obtain

$$\begin{aligned}\operatorname{Im}\{\omega\} &\approx \frac{\ln(\mathcal{R}_{trace})}{T_{rt}} + \frac{\ln(\mathcal{P})}{T_{rt}} \\ &= \left(\frac{\ln(\mathcal{R}_{trace})}{L} + \frac{\ln(\mathcal{P})}{L} \right) v_g^{\parallel},\end{aligned}\tag{8.9}$$

where T_{rt} is the shortest round trip time given by (8.6) and

$$v_g^{\parallel} \equiv \left(\frac{1}{\operatorname{Re}\{v_g(k_1^+)\}} - \frac{1}{v_g(k_1^-)} \right)^{-1}\tag{8.10}$$

is the parallel sum of the fastest upstream and downstream going group velocities involved in the expression for T_{rt} .

The term involving the propagation factors yields

$$\begin{aligned}\frac{\ln(\mathcal{P})}{L} &= \frac{\ln\left(\left|e^{ik_1^+L}\right|\right) + \ln\left(\left|e^{ik_1^-L}\right|\right)}{L} \\ &= \frac{-\operatorname{Im}\{k_1^+\}L + \operatorname{Im}\{k_1^-\}L}{L} \\ &= -\operatorname{Im}\{k_1^+\} + \operatorname{Im}\{k_1^-\}.\end{aligned}$$

As we take the limit $L \rightarrow \infty$, the term involving the reflection coefficients in (8.9) goes to zero because \mathcal{R}_{trace} is independent of plate length, giving

$$\operatorname{Im}\{\omega\} \approx [-\operatorname{Im}\{k_1^+\} + \operatorname{Im}\{k_1^-\}] v_g^{\parallel}, \quad L \rightarrow \infty.\tag{8.11}$$

This is an approximate version of the Kulikovskii condition, in which the $\operatorname{Im}\{\omega\}$ is now given explicitly. The approximation again comes from evaluating the imaginary part of the wavenumbers k_1^+ and k_1^- for $\operatorname{Re}\{\omega\}$, whereas the implicit solution involved in (8.8) inherently incorporates the temporal growth rate.

8.2 Finite Flag Configurations

8.2.1 Clamped Leading Edge, Free Trailing Edge (No Wake)

$$\mathbf{T} = \mathbf{U}^2$$

We will first consider a clamped-free plate which has just enough tension ($T = U^2$) to eliminate convectively unstable waves, but retains a wide enough frequency range for

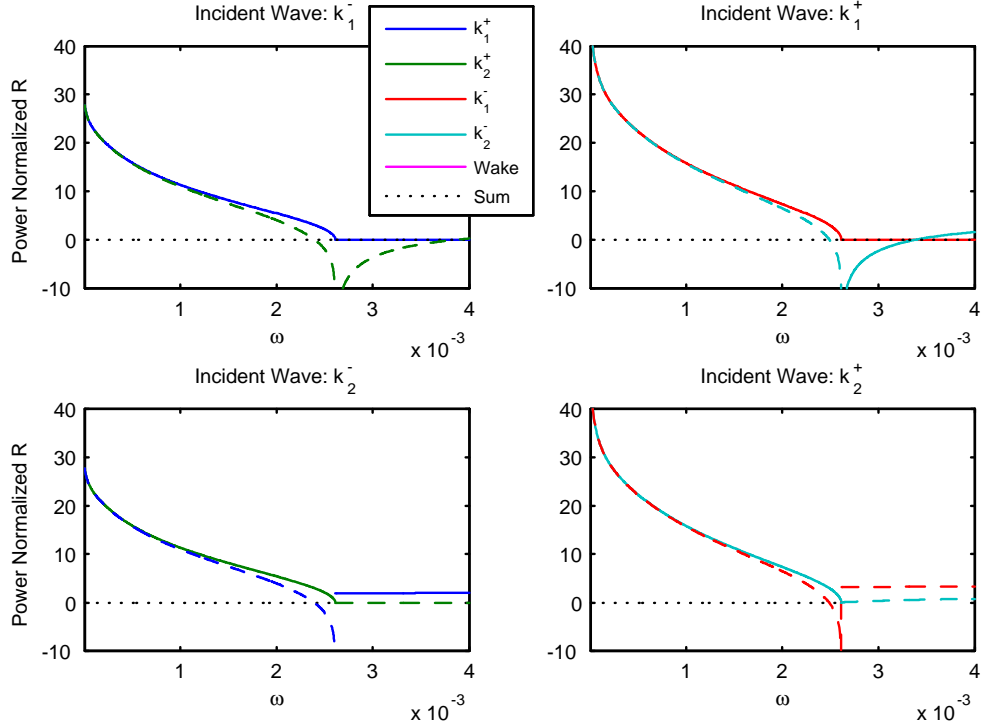


Figure 8.1: Power normalized reflection coefficients for a clamped upstream edge (figures in left column) and a free trailing edge with no wake (figures on right) for plate parameters $U = 0.05$, $T = U^2$ and $\lambda = 0$.

which negative energy waves exist to enable over-scattering at the edges (dispersion plot of figure 2.4c). The power normalized reflection coefficients for both edges are plotted in a single figure (figure 8.1) with the left column representing scattering at the upstream edge and the right column, scattering at the downstream edge.

Both edges are clearly over-reflective for $\omega < \omega_p$ and upper bounds on the gain due to the reflection process alone are given by the two estimates \mathcal{R}_{2norm} and \mathcal{R}_{trace} discussed in the previous section. Those two quantities are plotted in figure 8.2 and show that \mathcal{R}_{trace} provides a consistently lower bound than \mathcal{R}_{2norm} , with $\mathcal{R} = 1$ (i.e., a gain of unity) comprising the boundary between stable and unstable resonance. The difference between the two estimates is particularly striking for frequencies $\omega > \omega_p$, where \mathcal{R}_{2norm} appears to predict the possibility of gains around 8. This is purely a result of our having omitted the structural evanescent waves from the R matrices when

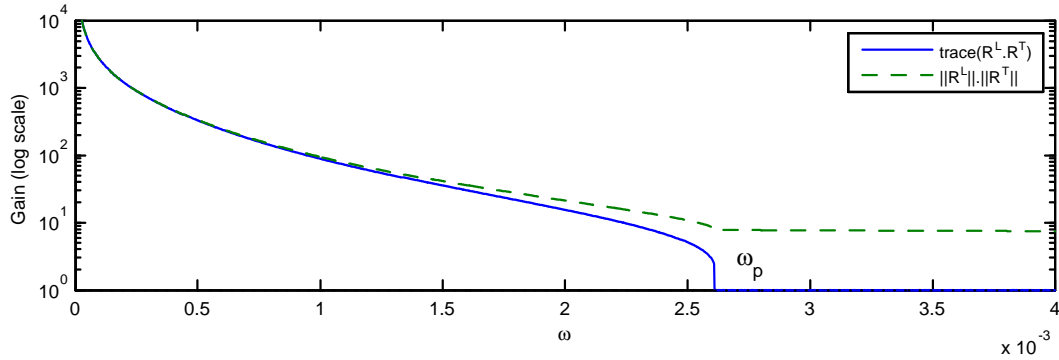


Figure 8.2: Estimates for upper bounds on gain due to the reflection processes alone for a plate clamped at the upstream edge and free (with no wake) at the downstream edge. Plate parameters: $U = 0.05$, $T = U^2$ and $\lambda = 0$ (dispersion plot of figure 2.4c).

computing \mathcal{R}_{trace} . The same large- L arguments can be used to omit those same terms prior to evaluating the 2-norm of the reflection matrices (now reduced to two scalars). In that case, \mathcal{R}_{2norm} collapses to the lower line given by \mathcal{R}_{trace} in our figure. However, we have retained all terms of R when evaluating \mathcal{R}_{2norm} primarily to highlight this contrast.

The two estimates, however, provide comparable values for the gain for frequencies $\omega < \omega_p$ and predict that the lower resonance frequencies will experience the largest gains. This is of course due entirely to all eight individual power normalized reflection coefficients tending to ∞ as $\omega \rightarrow 0$.

The maximum eigenvalue of the gain matrix (evaluated for real ω) is plotted in figure 8.3 for four representative plate lengths. The local maxima of the real part of the maximum eigenvalue (which also coincide with the frequencies at which the imaginary part crosses zero) provide us with an initial estimate of the resonance frequencies and temporal growth rates of the finite system. Overlaid on top of the maximum eigenvalue are our estimates for the upper bound on the gain given by $\mathcal{P}\mathcal{R}_{trace}$. In our case, the propagation path does not provide a contribution to the gain (for real ω) due to the total absence of convectively unstable waves. Therefore, $\mathcal{P} = 1$ and an upper bound on the gain is provided solely by \mathcal{R}_{trace} which is independent of plate length. The upper bound is therefore the same in all four sub-figures. We observe that in no instance does λ_{max} cross this upper bound and that $\mathcal{P}\mathcal{R}_{trace}$ provides a particularly tight bound for

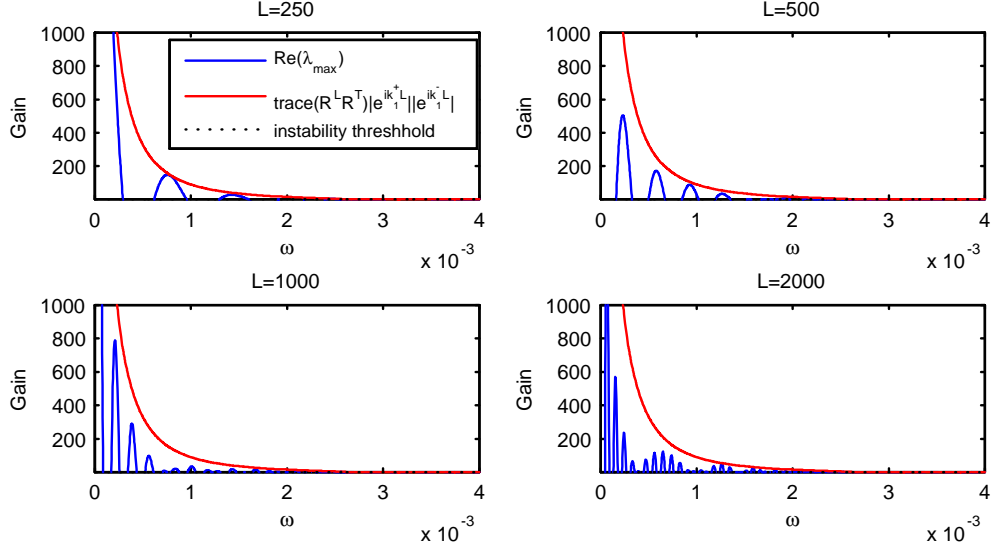


Figure 8.3: Real part of the maximum eigenvalue of the gain matrix, $\text{Re}\{\lambda_{\max}\}$, vs. estimates for the upper bounds on gain, $\mathcal{PR}_{\text{trace}}$, for a plate clamped at the upstream edge and free (with no wake) at the downstream edge. Plate parameters: $U = 0.05$, $T = U^2$ and $\lambda = 0$.

small L .

As described in section 8.1.2, the maxima of $\text{Re}\{\lambda_{\max}\}$ are converted into temporal growth rates $\text{Im}\{\omega\}$ through the transformation formula given in (8.5) and used as an initial guess in our exact root solver for (5.7). These initial guesses, together with the exact complex eigenvalues, are plotted in figure 8.4. Also overlaid are the upper bounds on the gain from figure 8.3 transformed into temporal growth rates again using (8.5). Given that the round trip time is a function of plate length, the estimates for the upper bound of $\text{Im}\{\omega\}$ now vary with L even though they are based on contributions from the over-reflecting edges only.

We observe that there are generally fewer actual eigenfrequencies than initial guesses. This is because not all local maxima of $\text{Re}\{\lambda_{\max}\}$ are able to achieve the resonance condition, $\text{Re}\{\lambda\} = 1$ and $\text{Im}\{\lambda\} = 0$, as the imaginary part of frequency is increased (or decreased) from 0. We also observe that the initial guesses appear to almost always overestimate the temporal growth rate. This is reassuring because our estimates for the upper bound are also based on the $\text{Re}\{\omega\}$ evaluation of the reflec-

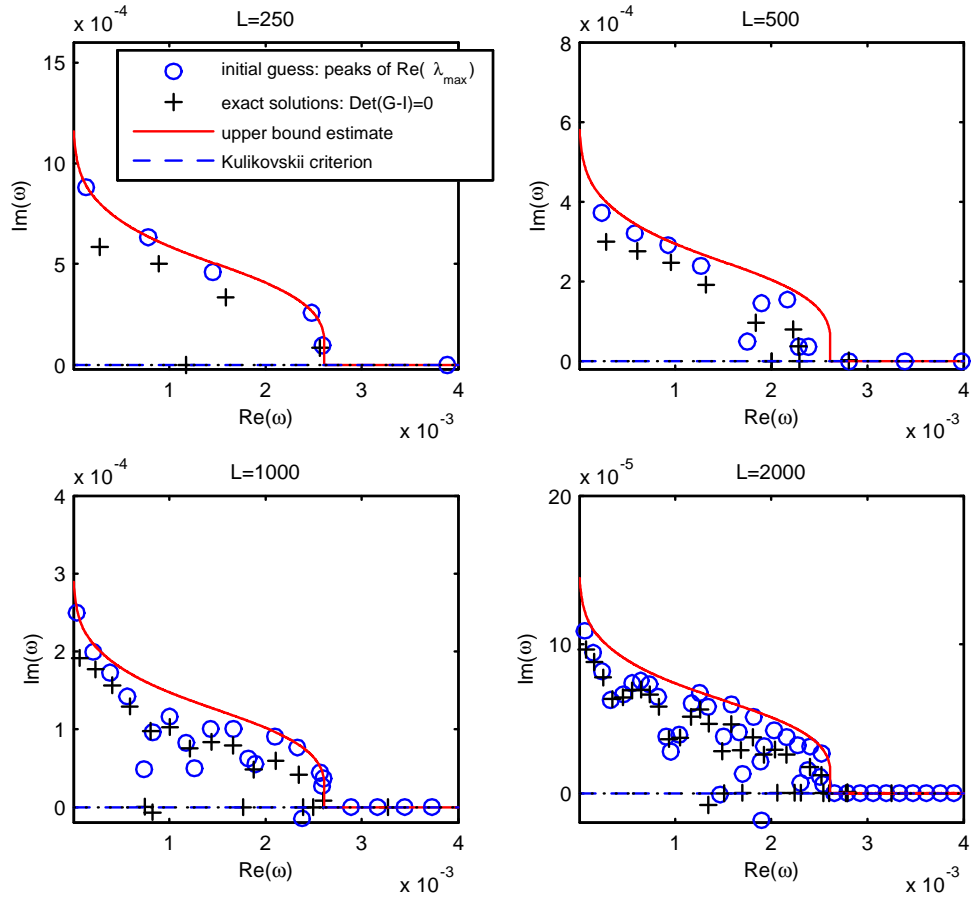


Figure 8.4: Real and imaginary parts of eigenfrequencies, and bounds for temporal growth rates, for a plate clamped at the upstream edge and free (with no wake) at the downstream edge. Plate parameters: $U = 0.05$, $T = U^2$ and $\lambda = 0$.

tion coefficients. The reason for this is probably due to the fact (observed numerically but not proved) that the magnitudes of reflection coefficients tend to decrease with increasing, positive $\text{Im}\{\omega\}$.

We note that the Kulikovskii condition for the set of plate parameters chosen in this example is $\text{Im}\{\omega\} = 0$. We therefore expect the imaginary parts of the finite plate eigenfrequencies to tend to 0 as $L \rightarrow \infty$. This trend is clearly seen in figure 8.4. In fact, it is easy to show that our own upper bound also tends to 0 in this limit. As we've seen, the upper bound for the gain is independent of plate length whereas the round trip time grows linearly with L , giving $\text{Im}\{\omega\} = \ln(\mathcal{PR}_{trace})/T_{rt} \rightarrow 0$ for $L \rightarrow \infty$.

Figure 8.5 plots slices through the $\text{Re}\{\omega\}$ and L planes of the system determinant $\det(I - \mathcal{G})$ for four, fixed, values of the $\text{Im}\{\omega\}$. The zero of the determinant (or in this case the minima of the log magnitude) show up as deep blue dots. The presence of these dark patches indicates that the unique combination of $\text{Re}\{\omega\}$, $\text{Im}\{\omega\}$ and L is very close to a global mode of the finite plate. The dark ridges in the figure for $\text{Im}\{\omega\} = 0$, for instance, trace out the neutral or stable resonances of the system. And the absence of dark hues in the upper right hand of the figure for $\text{Im}\{\omega\} = 0.0045$, indicates that the resonances with the largest unstable growth rates are limited to low frequencies consistent with our analysis above.

T = 0

We conclude this subsection with a short discussion of results for a clamped-free plate with no pre-tension ($T = 0$) so that convectively unstable waves exist on the equivalent infinite plate over the lower range of frequencies $0 < \omega < \omega_s$ (dispersion plot of figure 2.4a). The gain \mathcal{R} due to the reflection coefficients alone, shown in figure 8.6, is somewhat larger but has the same qualitative behavior. The fundamental difference, however, is that the propagation gain is now greater than unity and given by $\mathcal{P} = |e^{ik_1^+ L}|$. This does not affect the maximum temporal growth rates of the system for small L but dominates the upper limit for large L as shown in figure 8.7. The Kulikovskii condition is now non-zero over $0 < \omega < \omega_s$ and acts as a lower limit on the unstable growth rates preventing them from tending to zero as $L \rightarrow \infty$.

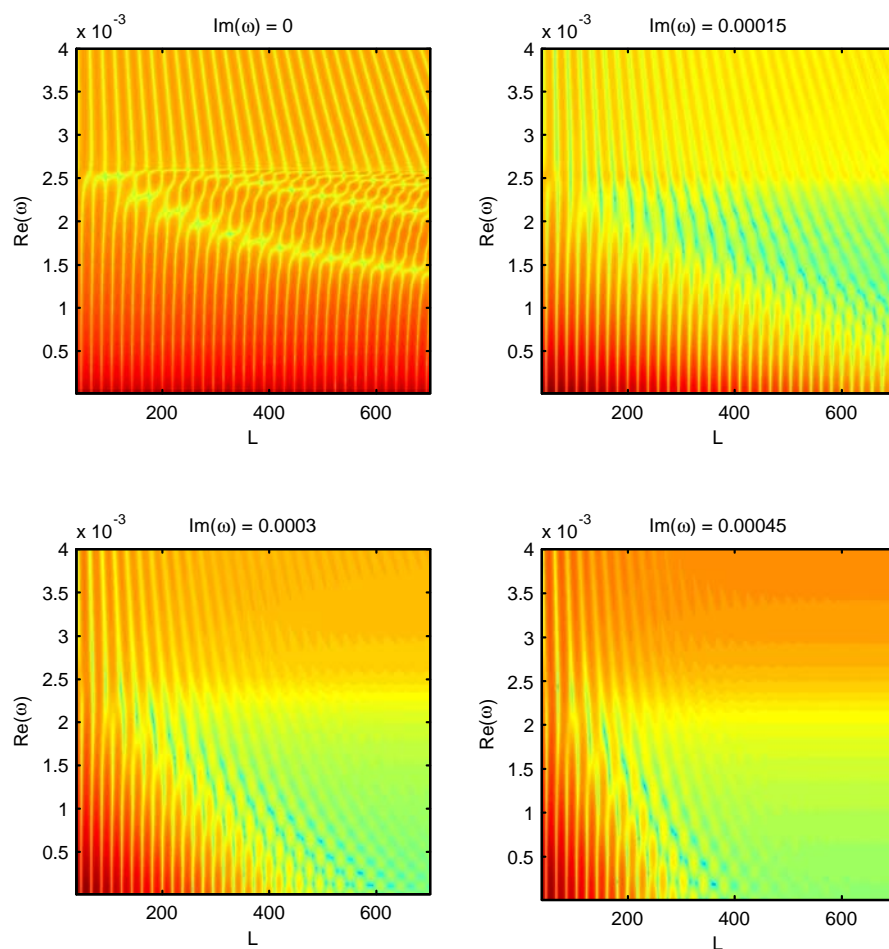


Figure 8.5: The system determinant $\det(I - \mathcal{G})$ at fixed values of $\text{Im}\{\omega\}$. The deep blue dots represent minima of the absolute value of the determinant, or the global modes of the finite plate at the given temporal growth rate.

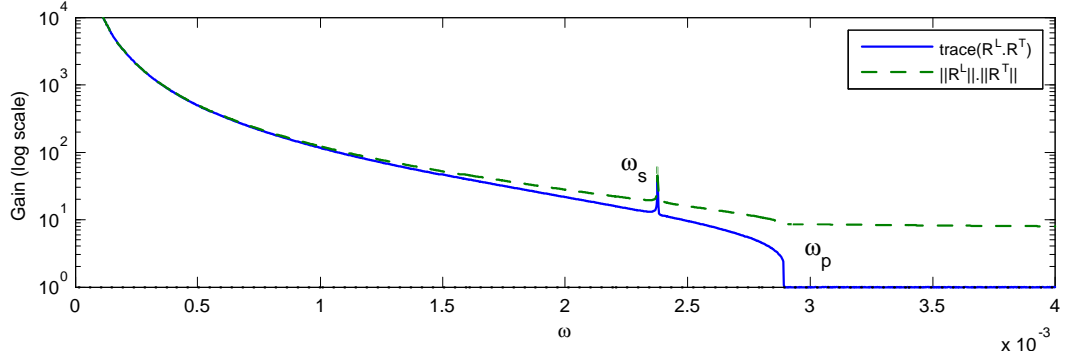


Figure 8.6: Upper bounds on gain due to the reflection processes alone for a clamped-free plate with $U = 0.05$, $T = 0$ and $\lambda = 0$ (dispersion plot of figure 2.4a).

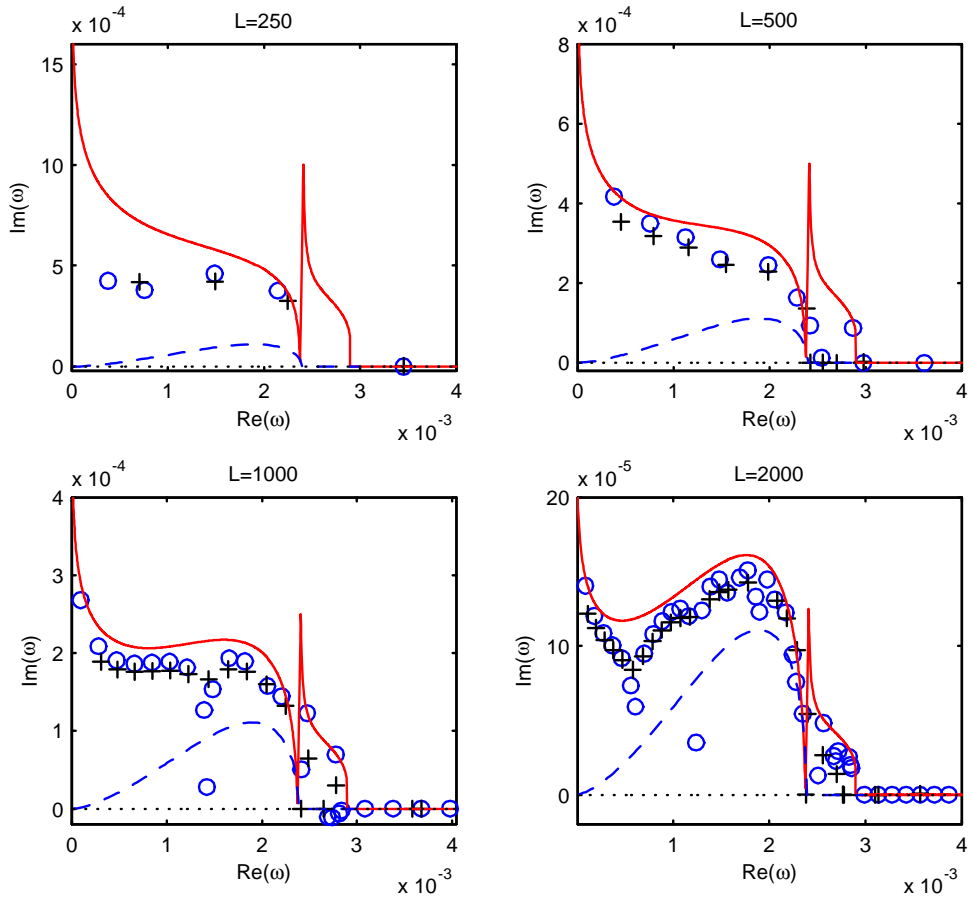


Figure 8.7: Complex eigenfrequencies, and bounds for temporal growth rates, for a clamped-free plate for $U = 0.05$, $T = 0$ and $\lambda = 0$. Legend as for figure 8.4

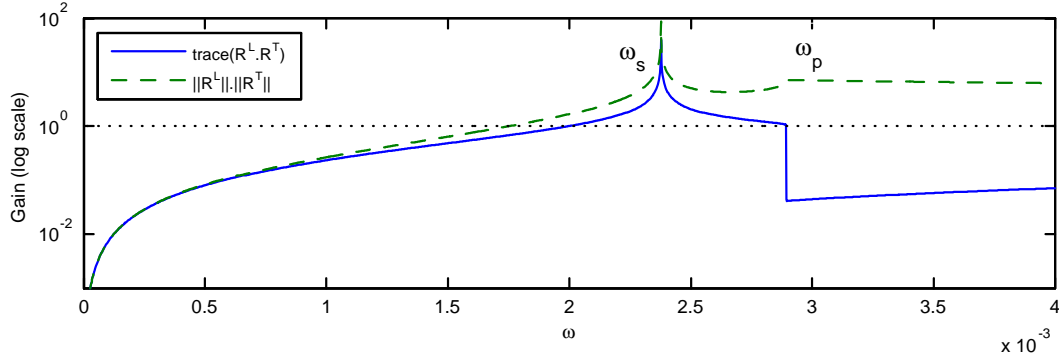


Figure 8.8: Net gain through reflection alone for a clamped-free plate with trailing edge wake and $U = 0.05$, $T = 0$ and $\lambda = 0$ (dispersion plot of figure 2.4a).

8.2.2 Clamped Leading Edge, Free Trailing Edge (With Wake)

T = 0

The upper bound on the net power reflected at the boundaries of a clamped-free plate with trailing edge wake is given in figure 8.8 (dispersion plot of figure 2.4a). The amount of over-reflection at the upstream edge is not enough to compensate for the power lost to the wake at the trailing edge, creating a net power deficit at low frequencies. There is only a narrow range of frequencies around $\omega = \omega_s$ that can sustain unstable resonance growth through the scattering process alone. This flag-like configuration is therefore one where the propagation path, and hence the plate length, plays a crucial role in determining system global stability. For $T = 0$, the frequency range $0 < \omega < \omega_s$ sustains convectively unstable waves. We can therefore expect that the propagation gain will compensate for the power loss through the edges for very long plates.

Figure 8.9 plots the temporal growth rates and global eigenmodes for four different plate lengths. We observe that the most unstable eigenmodes are found around $\omega = 0.002$ where $\text{Im}\{k_1^+\}$ has a maximum. In the limit of very long plate lengths, the upper bound on the temporal growth rate approaches the Kulikovskii condition *from below*.

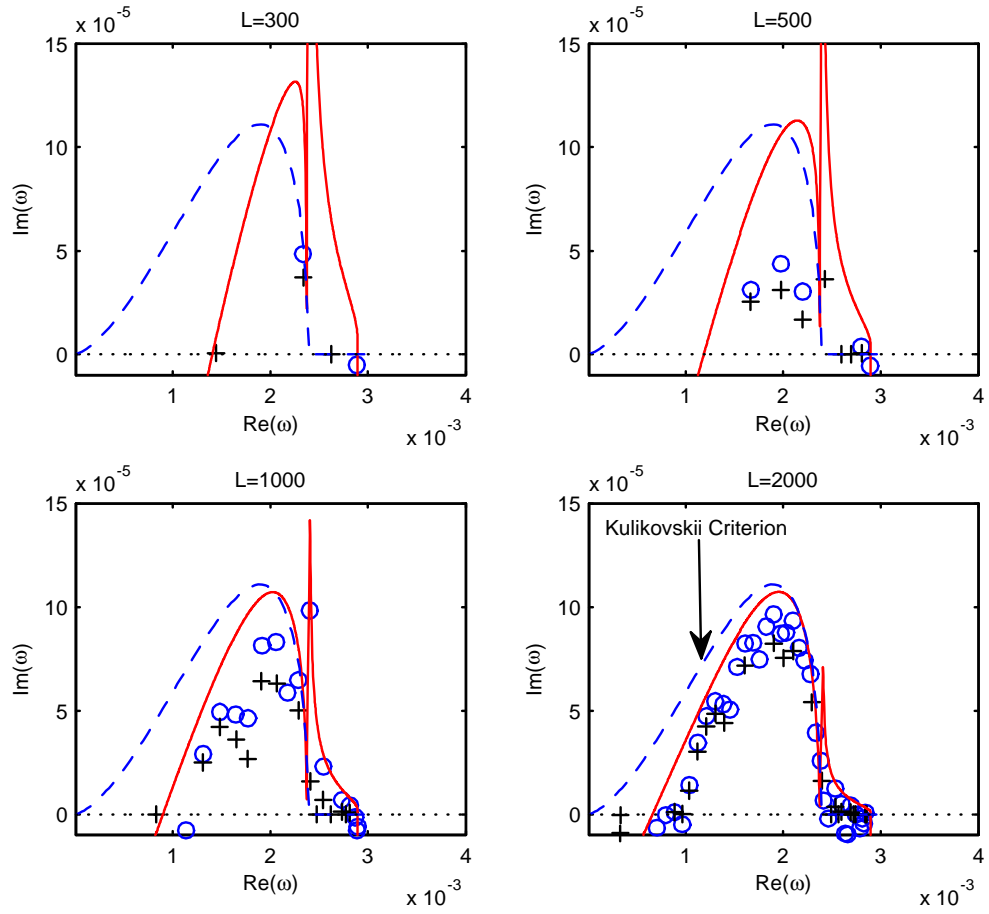


Figure 8.9: Complex eigenfrequencies and upper bounds on temporal growth rates for a clamped-free plate with trailing edge wake for $U = 0.05$, $T = 0$ and $\lambda = 0$. Caption as in figure 8.4.

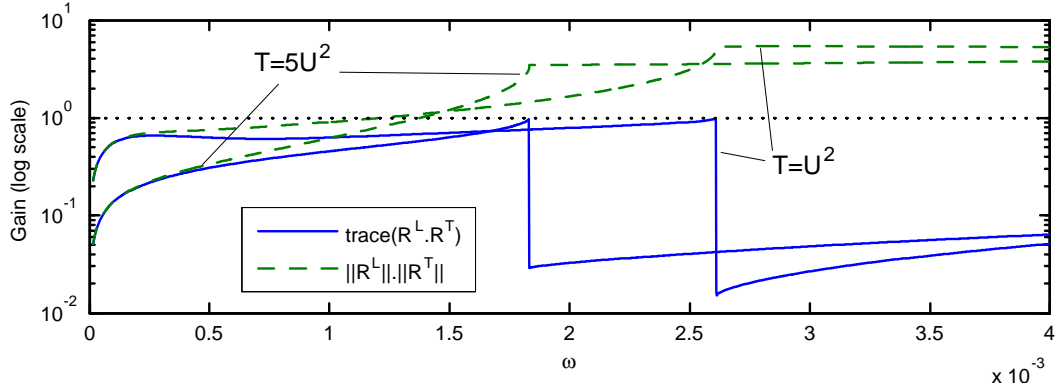


Figure 8.10: Upper bounds on gain through reflection alone for a clamped-free plate with trailing edge wake for two values of the pretension, $T = U^2$ and $T = 5U^2$, for $U = 0.05$, $\lambda = 0$.

$$\mathbf{T} \geq \mathbf{U}^2$$

For large enough values of pre-tension, the convective instabilities are eliminated and the propagation path no longer contributes to plate instability. Figure 8.10 plots the reflection only upper bounds on gain for two values of the pre-tension $T \geq U^2$. It can be seen that the net reflected power, as predicted by the tighter upper bound \mathcal{R}_{trace} , is less than unity over all frequencies. Therefore, the clamped-free flag with trailing edge wake is globally and locally stable for $T \geq U^2$.

We note that the \mathcal{R}_{2norm} based upper bound does not rule out the presence of global instabilities at higher frequencies for $T \geq U^2$. Here is a case where the choice of estimate, \mathcal{R}_{trace} vs. \mathcal{R}_{2norm} , makes a significant qualitative difference in our overall evaluation of the global stability of a given finite plate configuration. The accuracy of the \mathcal{R}_{trace} as a tighter, more representative, upper bound is again demonstrated in figures 8.11 and 8.12 which confirm that there are no unstable global modes for this flag configuration.

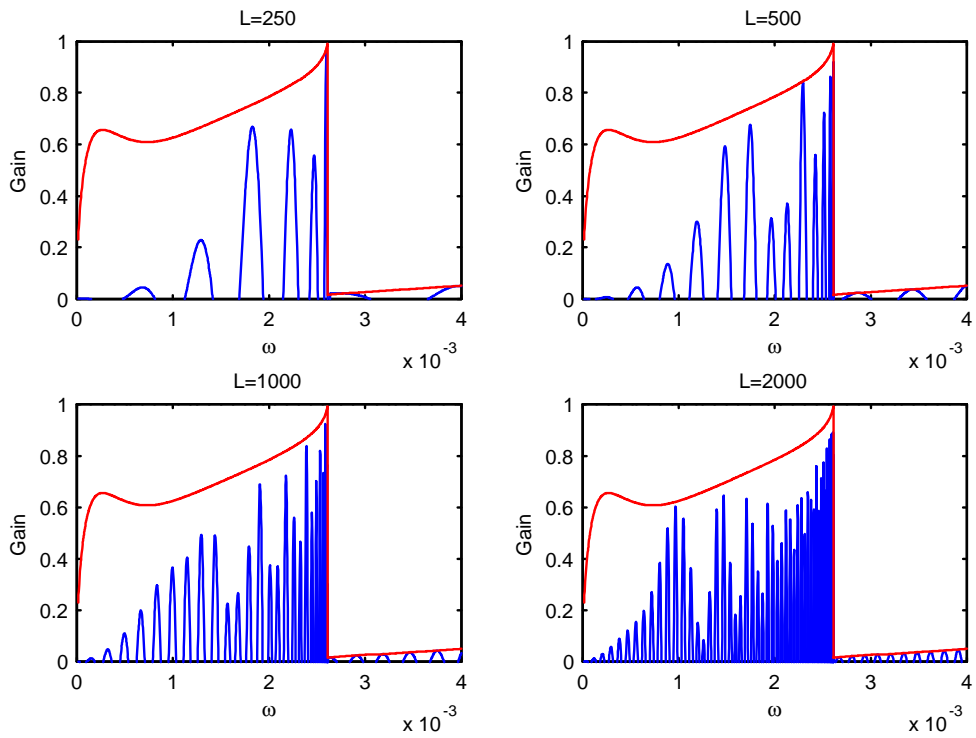


Figure 8.11: Real parts of the maximum eigenvalue of gain matrix for a clamped-free plate with trailing edge wake for $U = 0.05$, $T = U^2$ and $\lambda = 0$. Caption as in figure 8.3.

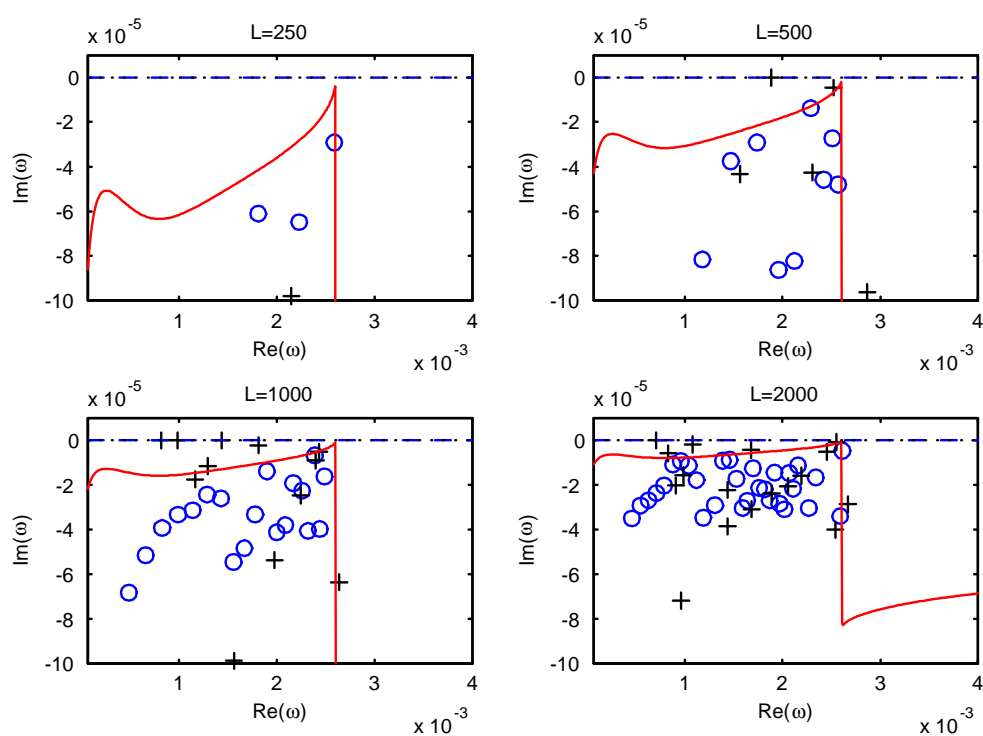


Figure 8.12: Complex eigenfrequencies and upper bounds on temporal growth rates for a clamped-free plate with trailing edge wake for $U = 0.05$, $T = U^2$ and $\lambda = 0$. Caption as in figure 8.4.

8.2.3 Free Leading Edge, Free Trailing Edge (With Wake)

$$\mathbf{T} = \mathbf{U}^2$$

Estimates for the upper bound on the net power reflected at the edges of a free-free plate with trailing edge wake are given in figure 8.13, and predict unstable global modes at low frequencies (dispersion plot given in figure 2.4c). The results are for $T = U^2$ which provides just enough pre-tension to eliminate all convectively unstable waves and as a result, the propagation path does not contribute to the unstable gain. It is instructive to compare this case with the identical configuration of a flag with clamped instead of a free leading edge just discussed in section 8.2.2. There, we concluded that the flag with a clamped leading edge is stable for all lengths. We discovered in chapter 6 that a free leading edge is more over-reflective than a clamped leading edge. Evidently, a flag with a free leading edge provides enough amplification through over-reflection to counteract the significant loss of wave energy into the wake at the trailing edge thereby creating a system that is globally unstable at low frequencies.

This is another case where the two estimates for maximum gain give qualitatively different predictions. Although they provide identical results for $\omega \rightarrow 0$, they diverge quite substantially for ω close to ω_p . The estimate based on \mathcal{R}_{trace} predicts that the unstable growth rates diminish to zero as $\omega \rightarrow \omega_p$, whereas \mathcal{R}_{2norm} predicts that they somewhat increase in the same limit. Overlays of the \mathcal{R}_{trace} prediction over the $\text{Re}\{\lambda_{\max}\}$ for four different plate lengths in figure 8.14 clearly show that \mathcal{R}_{trace} indeed provides a tighter and more accurate bound on the greatest possible gain. We note that the upper bound is particularly tight for $\omega > \omega_p$ where \mathcal{R}_{trace} just skirts the maxima of $\text{Re}\{\lambda_{\max}\}$.

This flag configuration provides another instance where the differences between \mathcal{R}_{trace} and \mathcal{R}_{2norm} are not merely academic; they provide different insights into the nature of the unstable global modes. \mathcal{R}_{2norm} suggests that the unstable modes would be fairly evenly distributed through $\omega < \omega_p$, whereas \mathcal{R}_{trace} suggests that the most unstable eigenmodes are concentrated at the very low frequency end of the spectrum. The growth rates of the actual complex eigenfrequencies are plotted in figure 8.15 and confirm the story-line advanced by the \mathcal{R}_{trace} prediction.

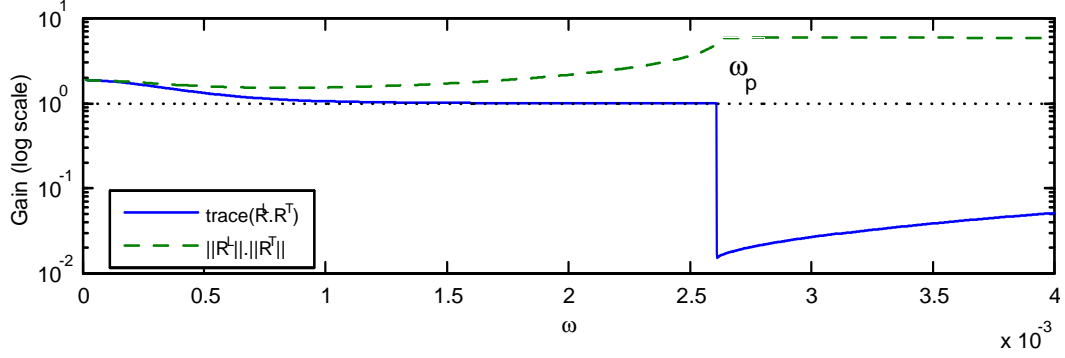


Figure 8.13: Upper bounds on gain through reflection alone for a free-free plate with trailing edge wake for $U = 0.05$, $T = U^2$ and $\lambda = 0$ (dispersion plot of figure 2.4c).

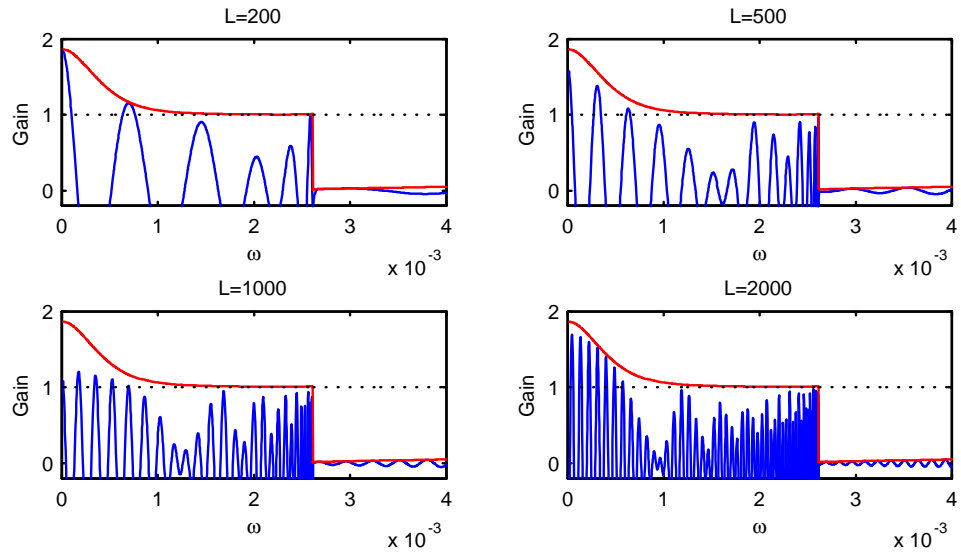


Figure 8.14: Real parts of the maximum eigenvalue of gain matrix for a free-free plate with trailing edge wake for $U = 0.05$, $T = U^2$ and $\lambda = 0$. Caption as in figure 8.3.

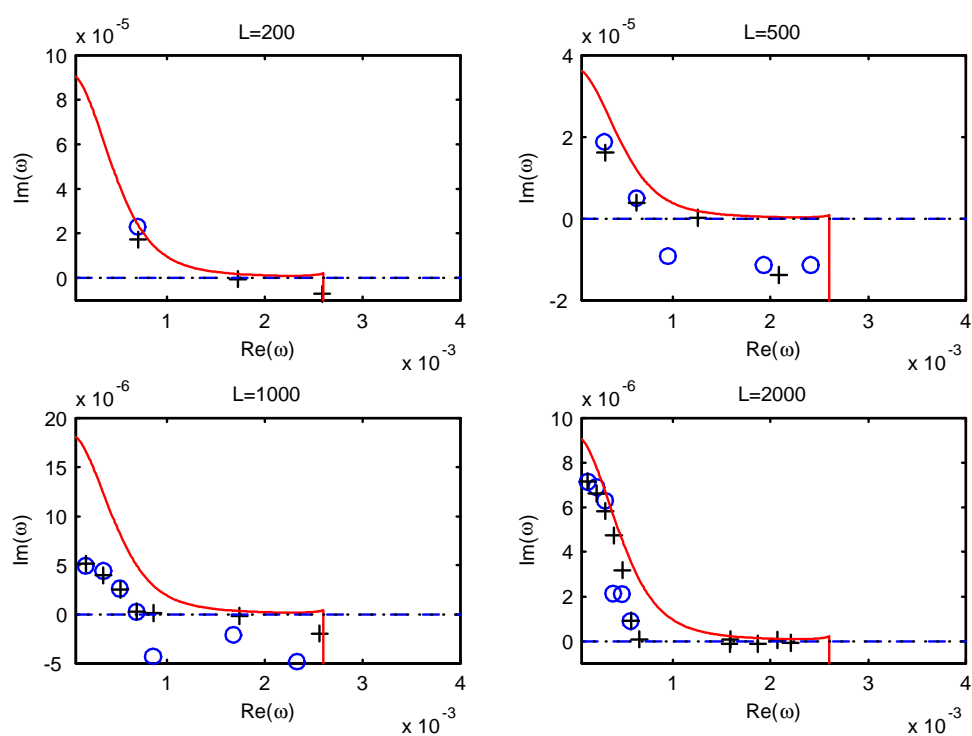


Figure 8.15: Complex eigenfrequencies and upper bounds on temporal growth rates for a free-free plate with trailing edge wake for $U = 0.05$, $T = U^2$ and $\lambda = 0$. Caption as in figure 8.4.

8.3 Summary

In this chapter we solved for the complex resonance frequencies of long, finite plates immersed in mean flow for combinations of upstream and downstream edge conditions derived in the previous two chapters. We derived upper and lower bounds on the unstable growth rates of finite plates with given edge conditions. We found that a flag-like configuration of a clamped leading edge and a free trailing edge with wake is destabilized for $U < U_c$ only by the presence of convective unstable waves and for large L . The net loss of power through the edges must be compensated by the growth of downstream propagating disturbances to achieve global instability at sub-critical speeds. We therefore conclude that, with enough restoring force (e.g., through plate tension or spring support), a flag clamped at the leading edge is globally stable for all $U < U_c$. In contrast, a flag with a free leading edge undergoes enough net amplification at the edges that it is globally unstable for all U .

Chapter 9

Computational Results for Finite Plate

In this chapter we solve for the response of an impulsively started fluid-loaded plate through a direct numerical evaluation of the system of differential equations (2.3a-2.3d). A primary aim is to see *if* and *when* the features predicted by the infinite and ‘very long’ plate theories developed in earlier chapters manifest themselves on the actual plate. The particular plate configuration we have chosen to study is perhaps the simplest to model computationally: a baffled plate with clamped edges and one-sided flow.

There have been numerous computational studies of fluid-loaded panels or baffled plates. However, only Lucey (1998) has performed a direct numerical study of a linear plate in the parameter regime that we are interested in and with the explicit aim of testing the predictions of the Crighton & Oswell (1991) theory.

9.1 Computational Model

The discretization scheme for our computational studies consists of fourth order finite differences in space for the plate, constant Boundary Elements for the fluid, and an explicit ‘leapfrog’ time-stepping scheme. We analytically evaluate the convective derivative terms by ‘transferring’ the differentials from the response functions to the

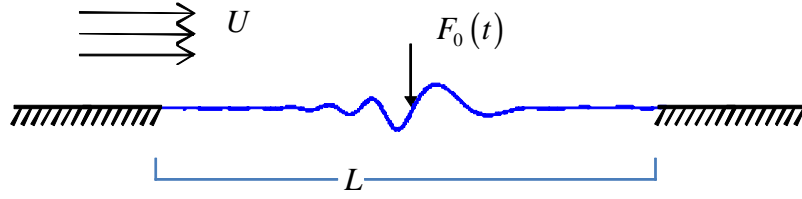


Figure 9.1: A baffled plate of length L clamped at the edges with one-sided flow.

source function. In addition, we evaluate the singular panels analytically and to a high order of accuracy. The outcome is a computational model that appears to provide minimal amounts of numerical dissipation, phase distortion and group speed delay. This is attested by the extremely good correlation with analytical predictions documented in section 9.3 below. Full details of the computational model are given in Appendix C.

9.2 Results for a Baffled Plate Clamped at Both Edges

We consider a baffled plate of length $L = 500$ with a zero deflection and zero slope structural edge condition imposed at both ends, with one sided fluid loading ($\alpha = 1$) and with $U = 0.05$. The plate has no pretension or spring support ($T = \lambda = 0$). We apply an impulse, consisting of a half-sine wave with frequency $\omega = \omega_p = 2.36 \times 10^{-3}$, at the midpoint $x = 0$ of the plate (figure 9.1).

A sample computational input-output plot is given in figure 9.2. Figure 9.2b plots the input forcing as a function of time, figure 9.2c plots the trajectory of the maximum deflection point on the plate and figure 9.2d is the velocity of that point compared with the mean flow speed. Figure 9.2a is a snapshot of the plate response at the maximum time mark of figures 9.2c and 9.2d. The evolution of the plate response can be further observed in figure 9.3 where five snapshots of the plate response are presented. We observe the following time-domain response features:

- Downstream travelling disturbances grow in amplitude as they propagate and are convected at just below the flow speed U (see figure 9.2d). In contrast, upstream travelling disturbances are slower and are highly dispersive.

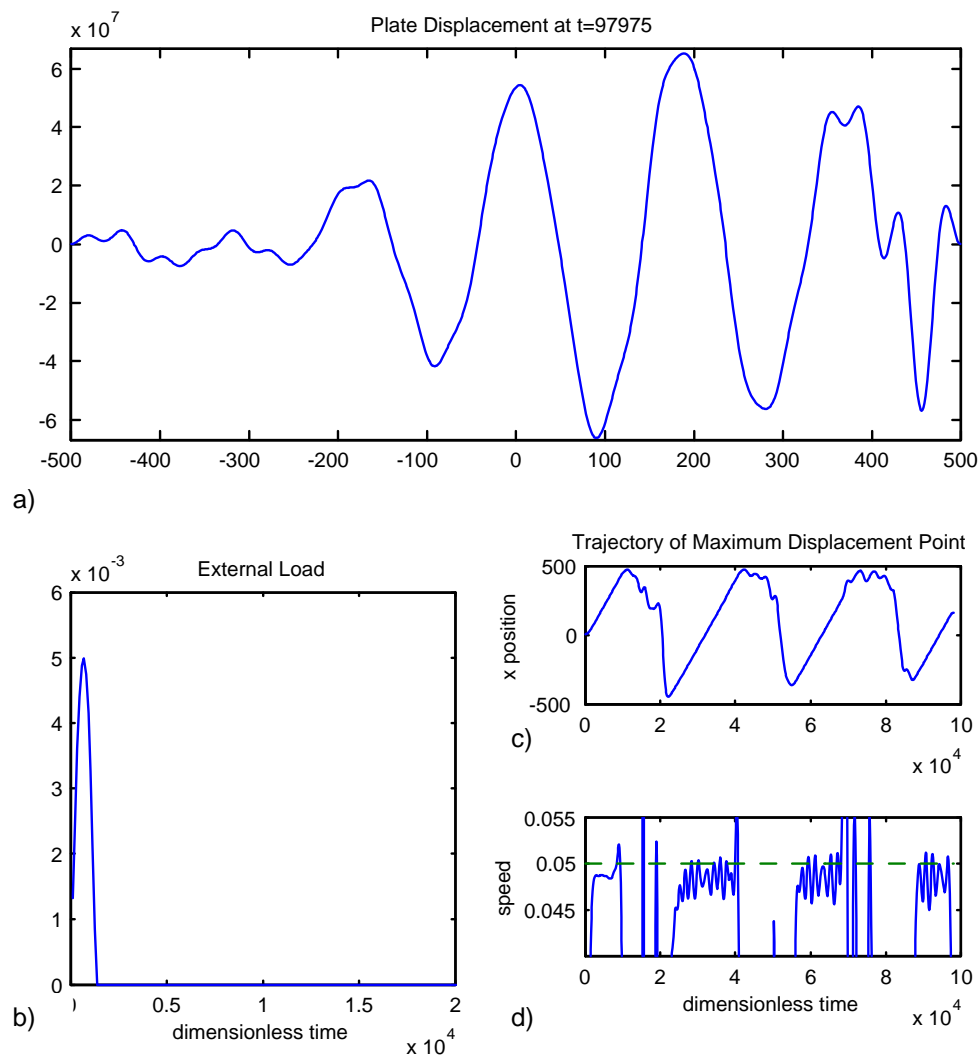


Figure 9.2: Sample computational input-output plots for a baffled, clamped plate, for $U = 0.05$, $T = \lambda = 0$, $\alpha = 1$ and $L = 500$.

- The upstream edge reflects incident disturbances with greatly increased amplitudes, whereas the amplitude of reflected waves from the downstream edge appear to be of the same order as the incident waves.
- For large time, the initial impulse becomes highly dispersed and the plate response resembles a standing wave with growing amplitude in the downstream direction.

9.2.1 Spectral Content

The transition from transient to steady state behavior can be observed in the wavenumber spectrogram of figure 9.4b. It consists of a plot of the magnitude of the spatial Fourier transform of the plate displacement at discrete time steps. The wavenumber spectrum at each time step has been normalized by its maximum value at that time step. The discrete spots in wavenumber at early time represent the scattering of the initial impulse at the plate boundaries. After about fifteen round-trips, the initial disturbances have sufficiently dispersed to allow for a more continuous, or steady state, wavenumber signature to emerge.

Immediately following the initial excitation, the disturbances travelling back and forth on the plate carry a range of wavenumbers and frequencies. However, each wavenumber-frequency pair falls on the dispersion curve for the equivalent infinite plate as shown in figure 9.4a. The discrete data points in figure 9.4a correspond to peaks in the spatial and temporal Fourier transforms of the plate displacement field taken over the entire plate length and over successive time intervals corresponding to a single round-trip travel time of the pulse.

Each set of three circles of the same color represents the spectral content of the response over the same interval. For instance, the three data points in red correspond to the plate response taken over an interval of time corresponding to the first round trip performed by the impulse (i.e., for $0 < t < 1.6 \times 10^4$), the set of points in blue correspond to the second round trip, and so forth, culminating in the data points in magenta which correspond to an interval of response taken around the $t = 3 \times 10^5$ time mark.

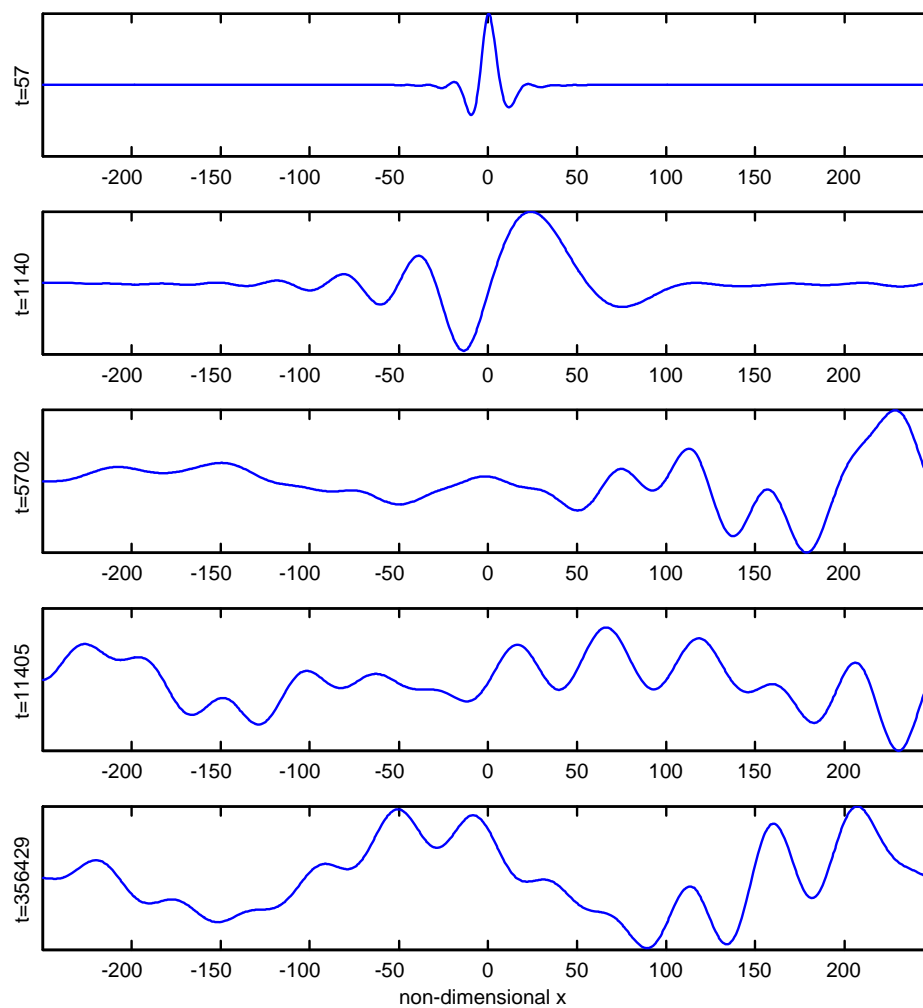


Figure 9.3: Snapshots of plate deflection for $U = 0.05$, $T = \lambda = 0$, $\alpha = 1$ and $L = 500$. Deflection amplitude has been rescaled with time.

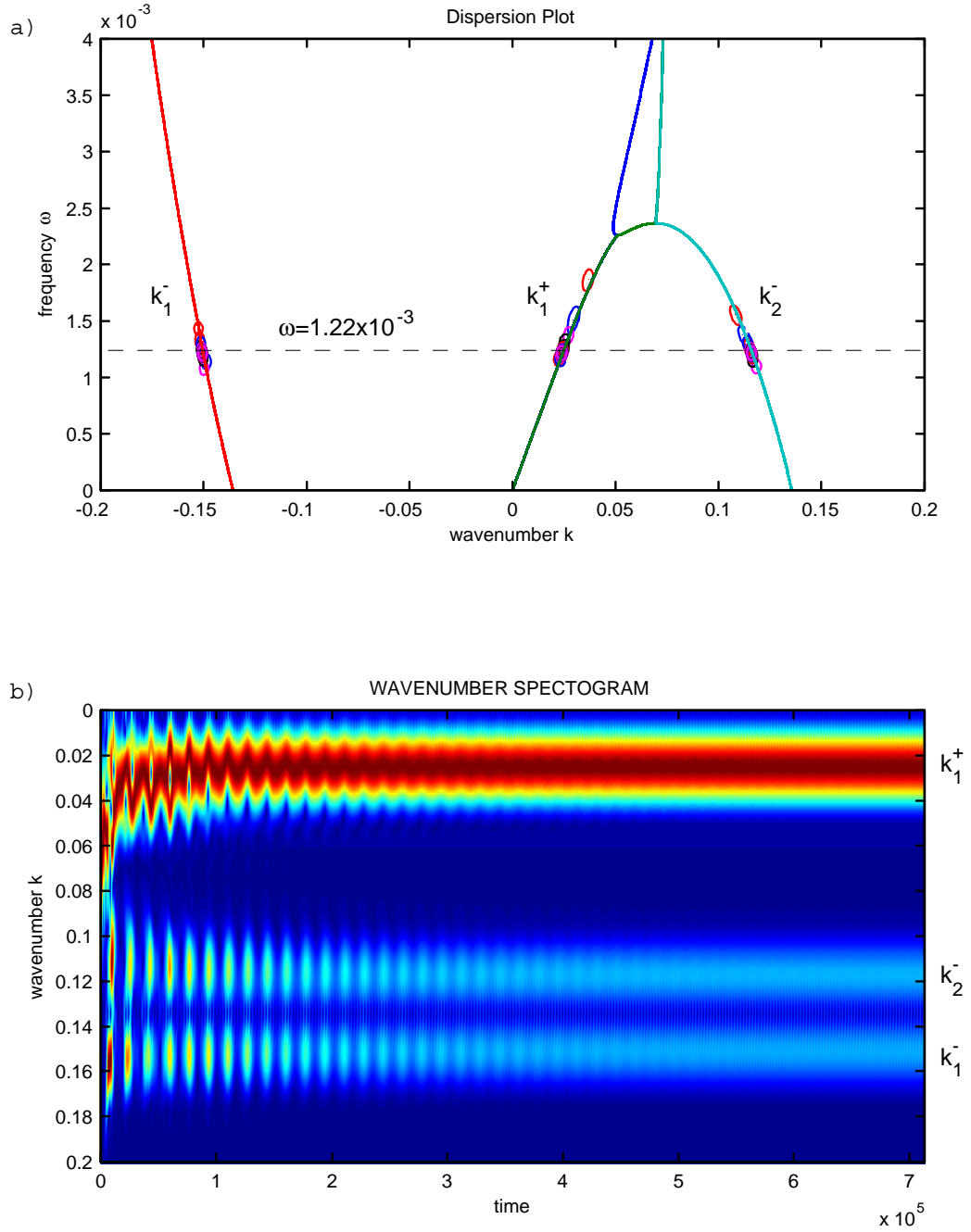


Figure 9.4: Comparison between finite plate computational results and the infinite plate theory for $U = 0.05$, $T = \lambda = 0$, $\alpha = 1$ and $L = 500$. a) Infinite plate dispersion plot overlaid with the frequency-wavenumber content of finite plate response at discrete time intervals. b) Normalized wavenumber spectrogram of finite plate response as a function of time. Darker hues represent higher spectral content.

Within three to four round trips, the linear response asymptotes to a single frequency and single temporal growth rate for all waves. Spatially, this ‘steady state’ resembles a standing wave pattern formed by the k_1^+ , k_1^- and k_2^- waves.

9.2.2 Growth Rate

The linear growth rate is computed by fitting an envelope to the time domain signal at any fixed point (away from the edges) on the plate. The envelope is constructed by identifying and joining the positive peaks of the time domain response followed by a ‘smoothing’ of the peaks by taking a running average over the output. It was found, however, that the large exponential growth rates in the raw signal greatly degraded the quality of the envelope, especially during the final ‘smoothing’ step. Therefore, an iterative process was implemented whereby the raw signal was first normalized by an exponential at the estimated growth rate and then fitted with an envelope. An initial guess at the growth rate is made by taking $\omega_i = \ln(\eta(t_0))/t_0$ of the largest peak in the original signal. Subsequent adjustments to the growth rate are made while operating on the normalized signal and requiring that the envelope is ‘flat’ for large time, as shown in figure 9.5a. Although this final judgment is made visually (by examining plots such as figure 9.5a) and the adjustment to the growth rate is entered manually in the code, we were able to achieve an accuracy of at least three significant digits.

Figure 9.5b compares the final estimate of ω_i with the growth rate obtained by applying $\omega_i = \ln(\eta(t))/t$ to the un-normalized version of the envelope shown in figure 9.5a. It can be seen that the constant temporal growth rates reported here are in fact asymptotic limits that the plate reaches for large time. At any finite time, the maximum growth rate recorded on the plate would be slightly less than this maximum.

9.2.3 A Word on Convergence

The left column of figure 9.6 overlays the plate deflection for the numerical simulation run at three different spatial discretization levels with the ratio $\Delta t/\Delta x^2$ (the Courant number for an *in-vacuo* Euler beam) held fixed. The snapshots are provided at five time marks, as indicated on the figure, and expressed in terms of cycles of the dominant

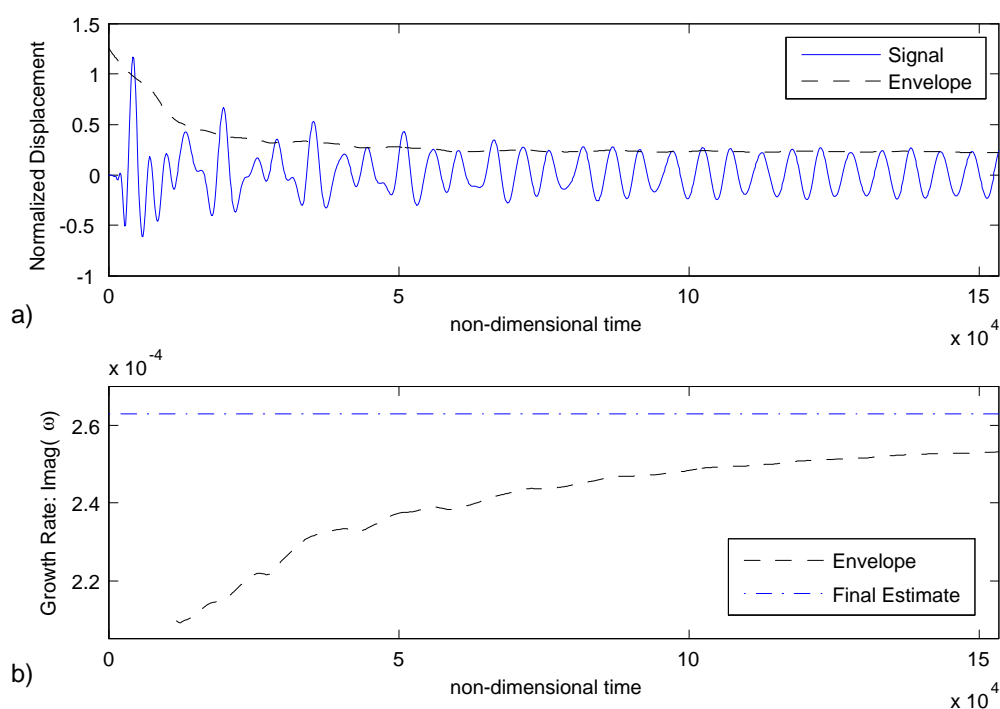


Figure 9.5: Computing the temporal growth rate for a clamped, baffled plate with $U = 0.05$, $T = \lambda = 0$, $\alpha = 1$, $L = 500$ and mesh size of $M = 2000$. a) An envelope is fitted after normalizing the raw deflection signal by an exponential with constant growth rate shown in figure 9.5b. b) The smoothed, time dependent envelope of the unnormalized deflection signal in figure 9.5a, compared with the final estimate of the constant growth rate.

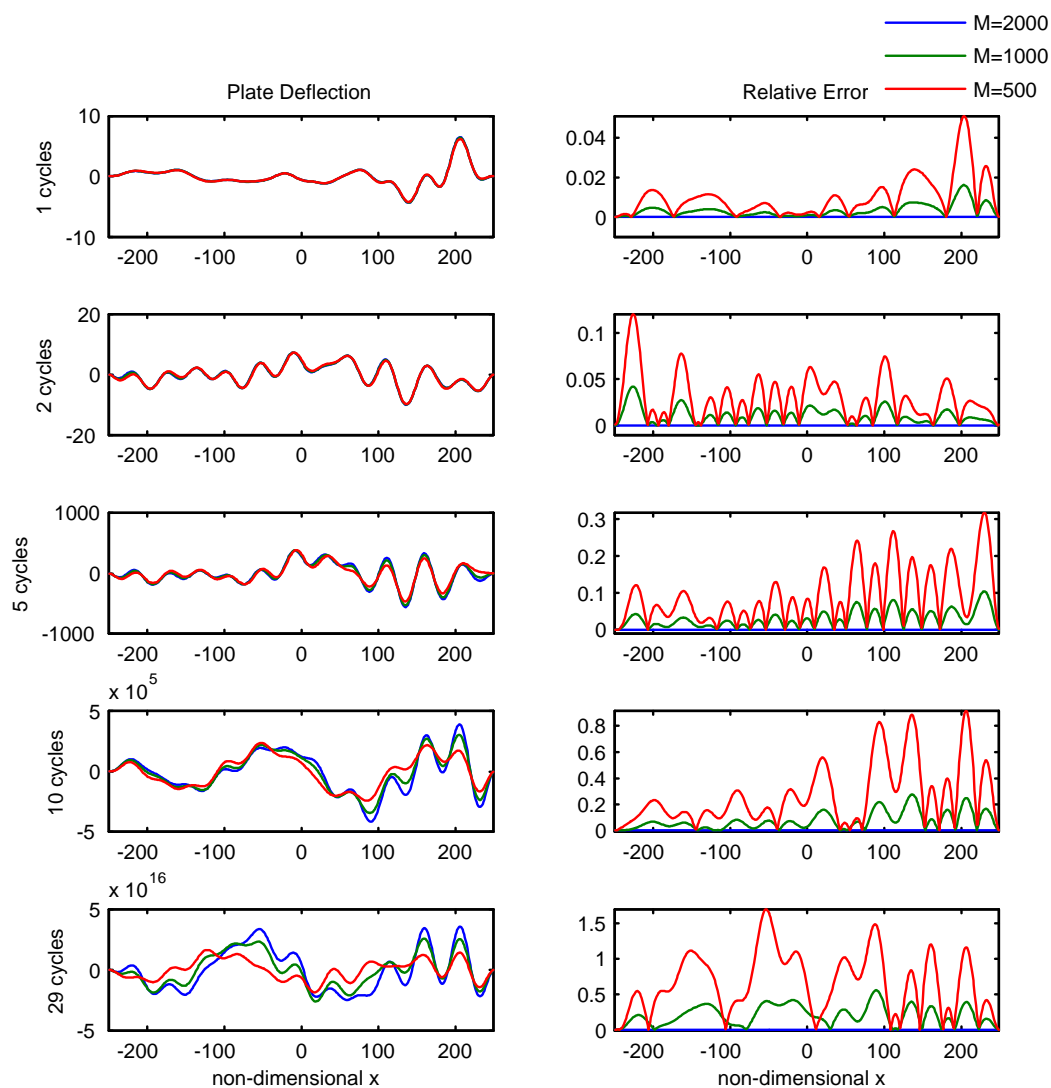


Figure 9.6: Convergence error for three different mesh sizes: $M = 500$, $M = 1000$ and $M = 2000$.

	M = 500	M = 1000	M = 2000
$\text{Re}\{\omega_{res}\}$	1.22×10^{-3}	1.22×10^{-3}	1.22×10^{-3}
$\text{Im}\{\omega_{res}\}$	2.59×10^{-4}	2.62×10^{-4}	2.63×10^{-4}
$k_1^+(\omega_{res})$	0.0239	0.0238	0.0238
$k_1^-(\omega_{res})$	0.1511	0.1508	0.1507
$k_2^-(\omega_{res})$	0.1165	0.1156	0.1155

Table 9.1: Convergence of resonance frequencies and wavenumbers as a function of mesh size M .

frequency on the plate for large time ($\omega = 1.22 \times 10^{-3}$ in this case). The right column of figure 9.6 plots the corresponding relative error, defined as the ratio of plate deflections magnitudes, at each time mark with the most densely discretized plate (i.e., $M = 2000$) used as benchmark. The results indicate that by the 5th cycle, the plate deflections have begun to diverge (from 8% for $M = 1000$ to 25% for $M = 500$) and that doubling the mesh size can only be expected to improve the error by a factor of 3.

Divergence in deflection is to be expected in wave propagation models run over several cycles. What we are most interested in, however, are other metrics of the response such as its frequency and wavenumber content as well as the temporal growth rates for large time. Table 9.1 shows that convergence for these quantities is achieved even for the case with the coarsest mesh.

Finally, a few words on the implication of the relative error values in figure 9.6. We have used 4th order accurate finite difference formulae to evaluate the spatial derivatives in our scheme. Our expectation is that the error would decrease at least as Δx^4 . Instead, halving Δx appears to reduce the relative error by only a factor of 3, which is not even a reduction of order Δx^2 ! The discrepancy may be explained by our use of constant boundary elements, a low order method, to perform the fluid panel integrations. One might expect that the use of linear or quadratic boundary elements would improve convergence.

9.3 Comparison with Analytical Predictions

In this section we apply the method of chapter 8 to analytically predict the resonance frequencies and maximum growth rate of the baffled plate configuration used in our

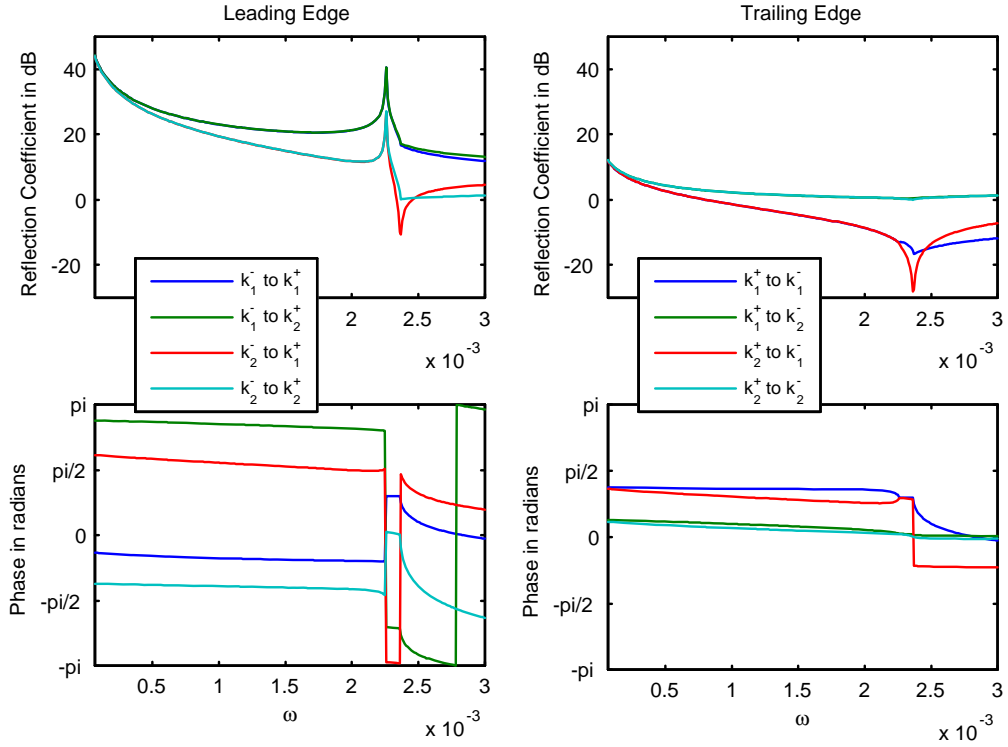


Figure 9.7: Magnitude and phase of the leading and trailing edge reflection coefficients for a baffled plate, clamped at the edges. For $U = 0.05$, $T = \lambda = 0$, and $\alpha = 1$.

computational study. A plate length of $L = 500$ certainly qualifies as a ‘long plate’ in the context of the long plate asymptotics of chapter 8, and we can therefore safely ignore the nearfields associated with the plate edges, with the exception of very low frequencies.

9.3.1 Reflection Coefficients for a Clamped, Baffled Plate

Peake (2004) uses the Wiener-Hopf technique to solve for the reflection coefficients from the leading and trailing edges of a clamped plate in a rigid baffle. These coefficients (equation (4.8) & (4.13) in Peake 2004) are reproduced below using the notation and

Wiener-Hopf kernels adopted in this thesis:

$$R_{ij}^{Lead} = \frac{K^+(k_i^+) \gamma^-(k_i^+) K^-(k_j^-)}{K_k(k_i^+) \gamma^-(k_j^-) (k_i^+ - k_j^-)}, \quad (9.1a)$$

$$R_{ij}^{Trail} = \frac{K^-(k_i^-) \gamma^+(k_i^-) K^+(k_j^+)}{K_k(k_i^-) \gamma^+(k_j^+) (k_i^- - k_j^+)}. \quad (9.1b)$$

Here, $\gamma^+(k)$ and $\gamma^-(k)$ are the multiplicatively factorized branch cut factors defined by $\gamma^+(k) \gamma^-(k) \equiv \gamma(k) = \sqrt{k^2}$, analytic in R^+ and R^- , respectively. The magnitude and phase of these coefficients are plotted in figure 9.7.

We note that in the frequency range over which most of the disturbances on the plate model were found to exist, i.e., $1 \times 10^{-3} < \omega < 2 \times 10^{-3}$, these reflection coefficients are qualitatively consistent with edge scattering processes that were observed; the leading edge reflection coefficients are on the order of $20dB$ whereas the trailing edge coefficients are on the order of $0dB$. It may appear from these observations that the upstream edge is ‘over-reflective’ whereas the downstream edge is not. However, one must remember that these observations of the plate response, as well as the related reflection coefficients, are based on ratios of wave deflection amplitude and do not necessarily represent ratios of scattered power.

It in fact turns out that both sets of edges are strongly over-reflective, as can be seen from the power normalized reflection coefficients plotted in figure 9.8. We find that the plate over-reflects at both the leading and trailing edges for all frequencies $\omega < \omega_p = 2.36 \times 10^{-3}$ over which negative energy waves exist. This is in keeping with the general rule, dictated by energy conservation, discussed in section 6.4. Namely, that the existence of negative energy waves is a necessary and sufficient condition for over-reflection from an important class of plate scatterers, those with zero transmission or absorption coefficients, such as the clamped condition studied here.

9.3.2 Global Modes for Long Plate

The reflection matrices given in equations (9.1), combined with the round trip propagation matrices of the plate, yield an equation for the linear response of the finite plate. The condition for resonance follows directly from the roots of the related eigenvalue

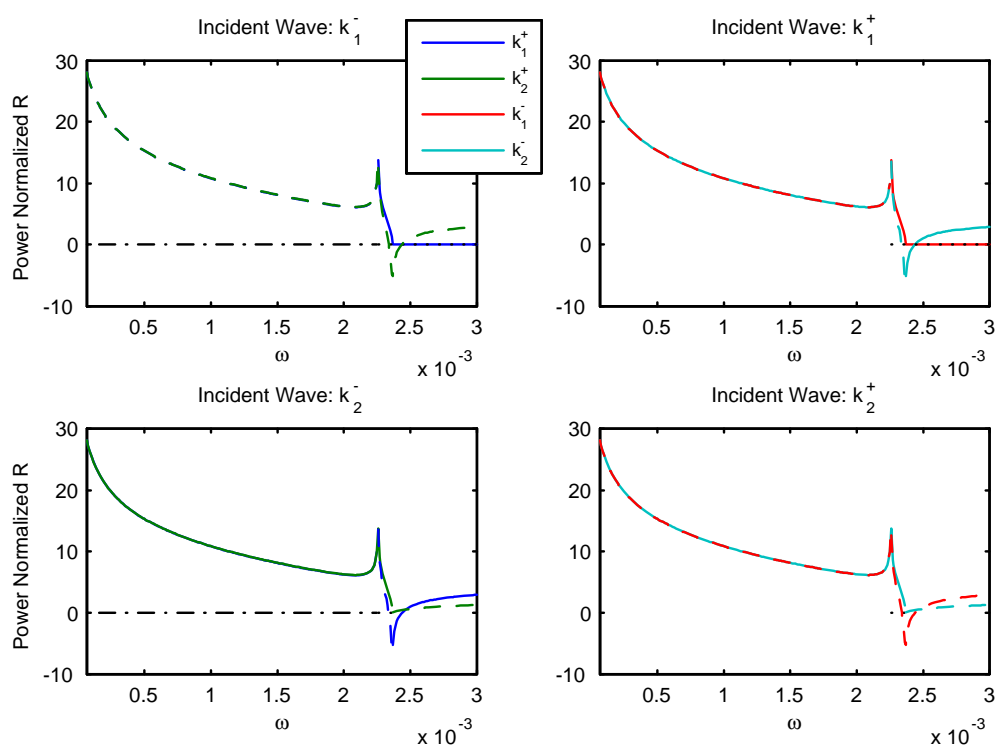


Figure 9.8: Power normalized reflection coefficients for a baffled plate, clamped at the edges. For $U = 0.05$, $T = \lambda = 0$, $\alpha = 1$.

equation. The latter is equivalent to solving for the zeros of the determinant of the system equation,

$$\det \left(\mathbf{I} - \mathbf{R}^{Lead} \begin{bmatrix} e^{-ik_1^- L} & 0 \\ 0 & e^{-ik_2^- L} \end{bmatrix} \mathbf{R}^{Trail} \begin{bmatrix} e^{ik_1^+ L} & 0 \\ 0 & e^{ik_2^+ L} \end{bmatrix} \right) = 0, \quad (9.2)$$

where, \mathbf{R}^{Lead} and \mathbf{R}^{Trail} are the 2×2 reflection matrices and \mathbf{I} is the identity matrix.

The roots of the above equation are found numerically by sweeping the complex- ω and (real) L planes for values that minimize the determinant. The approach is described in great detail in chapter 8 and will not be repeated here. The image in figure 9.9 is that of the determinant given in (9.2) as a function of real frequency and plate length evaluated at a single value of the imaginary frequency, $\omega_i = 2.64 \times 10^{-4}$, chosen to correspond with the maximum growth rate observed on the plate. The determinant is plotted in decibels and the dark hews correspond to minima of the magnitude and hence to the locus of the unstable resonances of the finite plate with growth rates close to $\omega_i = 2.64 \times 10^{-4}$.

For a given plate length, there are a discrete set of complex frequencies that have positive imaginary parts. We find that for our plate length of $L = 500$, there are seven resonance frequencies with positive imaginary parts that result in temporally unstable resonance. These complex resonance frequencies are marked on figure 9.9 and listed in table 9.2. The resonance frequency with the largest positive imaginary part (D), $\omega_{res} = 1.22 \times 10^{-3} + i2.64 \times 10^{-4}$, is expected to dominate the response of the finite plate for large time. It agrees exceedingly well with our computationally obtained steady state resonance frequency and growth rate given in the right-hand most column of table 9.1.

9.4 Conclusion

The near perfect agreement between our analytical predictions based on long plate asymptotics and the output of our computational model serves as a validation for both approaches. In particular, we have found that the infinite plate waves predicted by Crighton & Oswell (1991) manifest themselves on the finite plate almost immediately following an initial impulse and dominate the linear response thereafter.

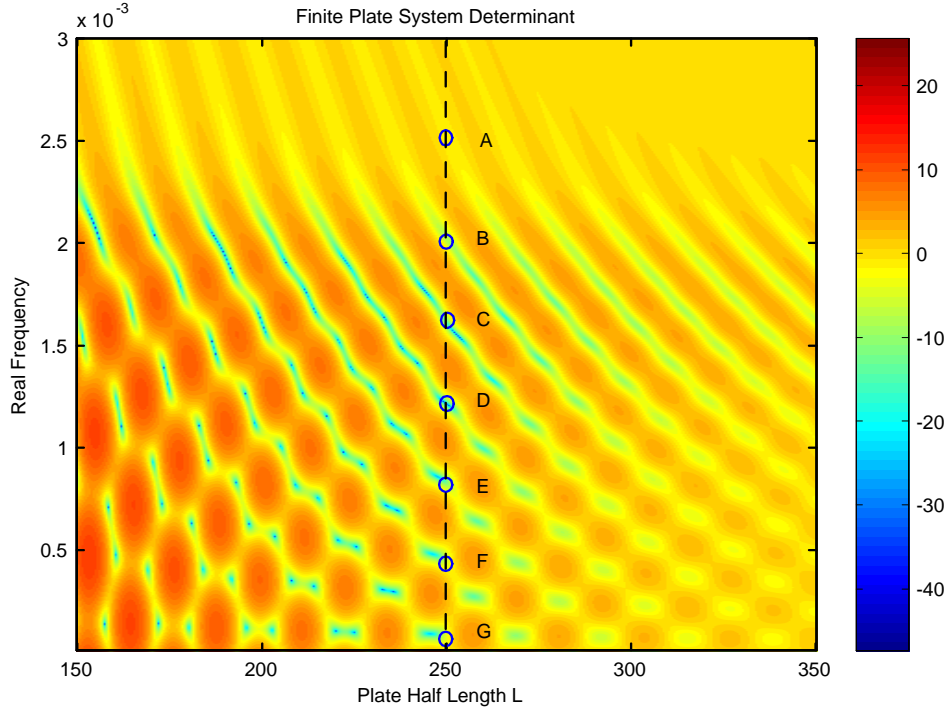


Figure 9.9: Finite plate system determinant for a fixed value of the imaginary frequency $\omega_i = 2.64 \times 10^{-4}$. The deep blue dots represent minima of the absolute value of the determinant, or the global modes of the finite plate at the given temporal growth rate.

	$\text{Re}(\omega_{res})$	$\text{Im}(\omega_{res})$
A	2.3648×10^{-3}	0.02976×10^{-4}
B	2.0239×10^{-3}	2.33872×10^{-4}
C	1.60898×10^{-3}	2.52036×10^{-4}
D	1.21697×10^{-3}	2.64460×10^{-4}
E	0.83951×10^{-3}	2.46439×10^{-4}
F	0.46395×10^{-3}	2.19361×10^{-4}
G	0.09226×10^{-3}	2.01178×10^{-4}

Table 9.2: Analytical complex resonance frequencies for a baffled plate of length $L=500$, clamped at both edges. The computational predictions, from Table 9.1, is that $\text{Re}(\omega_{res}) = 1.22 \times 10^{-3}$, $\text{Im}(\omega_{res}) = 2.64 \times 10^{-4}$.

We have also effectively validated the entire approach, first applied by Peake (2004), whereby semi-infinite plate scattering theory based on the Wiener-Hopf technique is used to derive reflection coefficients at the plate edges, and use these in combination with the infinite plate waves to construct the resonance response of a long, finite plate. The fact that we are able to so accurately predict the real and imaginary parts of the dominant resonance frequency attests to the accuracy (in both magnitude and phase) of the scattering coefficients derived using our approach and also to the validity of the method used to solve for the complex eigenvalues of a finite plate.

Finally, the fact that wave energy on the vibrating plate falls so neatly on the theoretical dispersion curve confirms the accuracy of the spatial discretization and panel integration approach described in Appendix C.

Chapter 10

Conclusions

The primary objective of this dissertation has been to use a wave-based approach to solve for the response of finite length flow-loaded structures. . Informed and inspired by the work of Howe (1994), Peake (2004) and Doare & de Langre (2006), we undertook a systematic study of the scattering properties of waves from local plate discontinuities and from the edges of long plates. We derived bounds on the unstable growth rates of finite plates and solved for the complex eigenfrequencies as a function of plate length and edge conditions. Finally, we developed a computational model for the direct integration of the fluid-loaded plate equations and favorably compared our analytical predictions to the latter.

10.1 Summary of Results

In chapter 2 we extended the ‘infinite plate’ results of Crighton & Oswell (1991) to include the influence of double sided flow and the effects of plate pretension. Most notably, we derived approximate expressions for the effect of plate tension on the onset of absolute instability (AI). In chapter 3 we derived the energy balance relations for the fluid-loaded extended plate (i.e., for a plate with two sided flow, spring foundation and plate pretension). We defined a generalized wave impedance, Z_w , valid for both positive energy waves (PEW) and negative energy waves (NEW). We showed that, unlike for the case of increasing the spring support λ , increasing T does not entirely

eliminate NEWs but severely limits the ω - k range over which they can exist.

In chapter 4 we solve the problem of scattering from local discontinuities using a multipole source approach. Our solutions are exact and include the deflection, pressure and potential nearfields due to fluid-loading effects. We introduce the concept of power normalized scattering coefficients, and show that overall power is indeed conserved during the scattering process if the sign of the wave energy is preserved. We argue that this property, combined with the presence of NEWs on the plate, is responsible for the phenomenon of over-scattering.

In chapter 5 we investigate the unstable resonances of quasi-finite plate segments formed by two local constraints or discontinuities. We develop a framework for the inclusion of all nearfields involved in the scattering process (including the mutual interaction between the nearfields emanating from the upstream and downstream edges) and succeed in solving for the complex resonance frequencies of these segments exactly. Our solutions are valid for arbitrarily small segment lengths. We find that the exclusion of the nearfields does not appreciably alter the eigenfrequencies even for very short plates and that they may potentially be ignored.

In chapters 6 and 7 we use the Weiner-Hopf technique to derive the reflection coefficients of semi-infinite plates for a variety of upstream and downstream edge conditions, including the case of a free trailing edge with wake. We find that the edges are over-reflective in the frequency range where NEWs are present. The exception is a free trailing edge with wake which, remarkably, is found to absorb almost all of the incident wave energy. We also discover that in order to properly account for the power in the wake, a term proportional to the wake deflection amplitude must be included. We find that a properly tuned dashpot, attached at the leading or trailing edges (with no wake), is capable of absorbing several times the power of an incident wave for $\omega < \omega_p$. Finally, we solve for the semi-infinite plate drive admittances at the leading edge and trailing edges (no wake) and find that, in contrast to the line driven infinite plate, $\text{Re}\{Y_{dp}\}$ is positive for both throughout the frequency range.

In chapter 8 we solve for the complex resonance frequencies of long, finite plates immersed in mean flow for combinations of upstream and downstream edge conditions

derived in chapters 6 and 7. We derive upper and lower bounds on the unstable growth rates of finite plates with given edge conditions. We find that a flag-like configuration of a clamped leading edge and a free trailing edge with wake is destabilized for $U < U_c$ only by the presence of convective unstable waves and for large L . The net loss of power through the edges must be compensated by the growth of downstream propagating disturbances to achieve global instability at sub-critical speeds. We therefore conclude that, with enough restoring force (e.g., through plate tension or spring support), a flag clamped at the leading edge is globally stable for all $U < U_c$. In contrast, a flag with a free leading edge undergoes enough net amplification at the edges that it is globally unstable for all U .

In chapter 9 we formulate a computational model of a plate in an infinitely long rigid baffle. We solve for the time domain response to a point impulsive load and examine the spectral content of disturbances on the plate and find that, although they initially contain a range of frequencies and wavenumbers, they all fall on the dispersion curve of the corresponding infinite plate. For large time, the response asymptotes to a single frequency and temporal growth rate. We find that this complex frequency coincides almost exactly with the dominant complex eigenfrequency obtained by the global mode analysis of chapter 8.

10.2 Outline for Future Work

We have examined the stability of a number of representative finite flag configurations but have by no means carried out an exhaustive analysis of every possible configuration, or the rich behavior that results from the interplay between the plate parameters L , T and λ . Instead, we have developed a number of rigorous analytical and numerical tools for the analysis of the global stability of fluid-loaded plates that can be used for a comprehensive analysis of a wide range of such systems. In this section, we present a list of items for future research. Some consist of direct application of the tools developed in this dissertation while others require an extension of these tools.

10.2.1 Further Work on Local Scatterers

The results of chapter 4 would benefit from a time domain analysis of the impulse response from a local scatterer. This would consist of evaluating the inverse Fourier transforms of the scattering coefficients. Combining the deflection and pressure impulse responses may provide greater insight into the process by which energy is exchanged between the plate and the fluid at the scatterer than the frequency domain analysis alone.

The work of chapter 5 would be complemented with an examination of the flux interactions between two or more local scatterers. Preliminary numerical results indicate that the nearfields from two adjacent scatterers interact to produce a net flux, even though the flux associated with each individual nearfield disturbance is zero. This constitutes a mechanism by which energy can enter or exit the finite segment formed by two scatterers and may have some important implications in terms of stability.

Studying the propagation of wave energy outside the quasi-finite segments at resonance is also of some value. Does the structural flux outside $[-L/2, L/2]$ increase with ω_i ? Is the total flux still conserved? Finally, we need to determine if the interaction between two structural evanescent waves (i.e., k_2^+ and k_2^-) emanating from the upstream and downstream edges of very short segments for $\omega > \omega_p$ creates the possibility of unstable growth, as predicted by the $G > 1$ values observed in the R_{2norm} term encountered in chapter 8? Given that one would also have to include the net power flux due to the nearfields, it would make more sense to carry out this analysis within the framework of the quasi-finite segments of chapter 5 where one has access to the complete scattered field.

10.2.2 Refining the Edge Coefficients

Our results for the reflection matrices (propagating waves only) from the upstream and downstream edges of immersed plates obtained in chapters 6 and 7 are exact. However, we were not able to express the coefficient in closed form primarily because the factorization of the Wiener Hopf kernel $K(\omega, k)$ was performed numerically. We could follow Oswell's (1992) lead and attempt an analytical factorization of the ker-

nel for asymptotically small ω . This, combined with asymptotic expressions for the dispersion roots k_j^\pm (that we've already solved for), will give us the leading order dependence of the reflection coefficients on the drive frequency, ω , as well as on the physical parameters T , λ , α and U .

A significantly more challenging task would be to attempt a Wiener-Hopf type solution of the edge scattering problem for an incident nearfield. If successful, this would enable us to extend the analysis of finite plates carried out in chapter 8 to comparatively short plates. This may entail decomposing the algebraically decaying incident nearfield disturbance into the equivalent of a multipole expansion over an infinite number of terms, retaining the first few terms in the expansion, and solving the Wiener-Hopf problem for each term.

10.2.3 A More Complete Wake Model

In chapter 7 the deflection amplitude, d , of the trailing edge wake was assumed to equal the plate deflection at the edge, $\eta(0)$. The wake deflection, $\eta_{wake} = d e^{i(\omega/U)x} e^{-i\omega t}$, is needed to properly account for the power carried by the wake. And our estimate for the latter was found to be inaccurate for instances where there are non-zero loads at the edge. A more precise way of determining η_{wake} is therefore needed, together with a robust explanation of the physical significance of the additional terms, $\frac{1}{2} \text{Re} \{i\alpha\omega U W \bar{d}\}$, in the expression for the wake flux (7.26).

10.2.4 Improving the Finite Flag Analytical Model

It would be instructive to compare the analytical predictions for the complex eigenvalues obtained in chapter 8 with those obtained by a Galerkin type solution of the same finite plate configurations. To this end, we would need to generate U vs. L graphs for the stability boundaries using our approach. Our expectation is that the Galerkin solution based on the superposition of a finite number of *in-vacuo* modes would do best for very 'short' plates and that our approach would give a more accurate and efficient solution for 'long' plates.

If it has proved possible to include the *nearfield* to *nearfield* terms in the system

determinant, then an investigation of the shortest possible plate lengths achievable by our method should be undertaken. One can once again use the computational model of chapter 9 as the ultimate benchmark. If it has not proved possible to fully account for all the nearfields in the reflection matrix, it would still be worthwhile to include the *propagating to nearfield* scattering terms based on equations (6.32) and (7.21) into our formulation. This will also enable one to solve for the approximate mode shapes (deflection and pressure) for very long plates and examine the net exchange of energy between the plate and the flow near the edges.

We have argued that R_{trace} provides a tighter and more accurate upper bound for the maximum growth rate of finite plates compared to R_{2norm} . However, unlike for the predictions based on R_{2norm} , there is no rigorous proof of this. Proving that R_{trace} does indeed provide an upper bound for the gain matrix (5.9) should probably be at the top of any future to do list.

10.2.5 Further Computational Studies

In this thesis we have focused almost exclusively on the subcritical flow regime, $U < U_c$. The phenomenon of absolute instability in finite domains is perhaps best studied computationally at first. Therefore, running the existing computational model for $U > U_c$ ought to be our first computational task in any future work. Does plate length control the absolute instability? Do the propagating modes appear and where do they fall on the dispersion plot? Do the non-AI instabilities described in this dissertation dominate for large time?

It should also be straightforward to reformulate our computational model so that it can handle finite plates immersed in fluid (i.e., in free field). This will allow us to directly examine the analytical predictions of the many examples given in chapter 8. Adding a trailing edge wake would probably be the most challenging task. Panel methods have successfully been used to model vortex wakes and that would be the sensible way to proceed in our case.

Effect of dissipation. Abrahams & Wickham (2001) have shown that the net effect of even small amounts of structural dissipation is to render the flow-loaded plate

absolutely unstable at all speeds. However, the temporal growth rates associated with typical values of the plate structural loss factors are exceedingly small and it is likely that the instability mechanisms described in this thesis will dominate for large time. The exception is the flag configuration (with a clamped leading edge, a free trailing edge with wake and sufficient plate restoring forces) that we predict to be stable. It would therefore be worthwhile to use this finite plate configuration to computationally investigate the effects of structural damping.

The ultimate computational task would be to include non-linear terms in the plate/fluid system and to solve for the fully non-linear response. The ability to turn certain non-linear effects ‘on’ and ‘off’ would help determine which non-linear effects are primarily responsible for amplitude saturation and which can be neglected in any future analytical studies. Peake (2004) has found that non-linear tension is the key saturating mechanism for baffled plates clamped at the edges. In fact, enabling a non-linear tension term in our baffled plate model would be very straightforward and we would be looking for the non-linear attractor behavior predicted by Peake. It is not clear, however, what the comparable saturating mechanism would be for flag-like configurations where one or more free edges exist. Another key question to be answered by a non-linear computational model: which, if any, of the linear response features survive during large amplitude motions?

10.2.6 Validation with Other Published Results

Validation of the theory advanced in this dissertation with published experimental studies on flapping flags should be undertaken. Initial studies ought to focus on flags in water –as opposed to flags in air– primarily because the phenomena we describe in this thesis all occur in the heavy fluid loading regime as described by Crighton (1989). Two notable experiments documented in the literature are 1) the filament in a soap film experiments of Zhang et. al. (2000) and 2) the mylar in water experiments of Vandenberg & Shelley (2005). Preliminary studies reveal that both experiments fall within the parameter regime analyzed in this thesis. The non-dimensional flow speeds are close to or below to the critical flow speed and the frequency-wavenumber

pairs measured are smaller than the pinch ω - k and therefore within the range where convectively unstable and negative energy waves may exist.

Once the flags in water experiments have been satisfactorily explained, we may wish to move on to published experiments of flapping flags in air. Notable experimental studies include: aluminum foil in air of Huang's (1995), thin aluminum sheets in air of Tang & Dowell (2003), ribbon in air of Lemaitre et al (2005) and most recently, mylar sheets in air of Eloy et al (2007). It is entirely possible, however, that the instabilities observed in flags immersed in air flows are due to physical mechanism not captured by our theory. In fact, a preliminary look suggests that the non-dimensional flow speeds involved in these experiments are significantly higher than U_c and the ω - k 's measured are greater than the pinch ω - k .

It would also be valuable to undertake a comparison with published computational simulations of flapping flags. Notable computational studies conducted at high or infinitely large Reynolds Numbers include the fully non-linear models of Michelin & Llewlynn-Smith (2008), Alben & Shelley (2008) and Connell and Yue (2007).

Chapter 11

References

Abrahams, I. D. 1981 Scattering of sound by a heavily loaded finite elastic plate. *Proc. R. Soc. Lond. A* **378**, 89–117.

Abrahams, I. D. 1983 Scattering of sound by an elastic plate with flow. *J. Sound Vib.* **89**, 213–231.

Abrahams, I. D. & Wickham, G. R. 2001 On transient oscillations of plates in moving fluids. *Wave Motion* **33**, 7–23.

Alben, S. & Shelley, M.J. 2008 Flapping states of a flag in an inviscid fluid: Bistability and the transition to chaos. *Phys. Rev. Lett.* **100**, 074301.

Arzoumanian, S., Peake, N. 2010 Fluid-structure interaction with mean flow: over-scattering and unstable resonance growth, *Proceedings of ASME 2010 3rd Joint US-European Fluids Engineering Summer Meeting and 8th International Conference on Nanochannels, Microchannels, and Minichannels, FEDSM2010-ICNMM2010, August 1-5, 2010, Montreal, Canada*.

Benjamin, T. B. 1960 Effects of a flexible boundary on hydrodynamic stability, *J. Fluid Mech.* **9**, 513–532.

Benjamin, T. B. 1963 The threefold classification of unstable disturbances in flexible surfaces bounding inviscid flows. *J. Fluid Mech.* **16**, 436–450.

Bers, A. 1983 Space-time evolution of plasma instabilities – absolute and convective. In *Handbook of Plasma Physics* (ed. M. N. Rosenbluth & R. Z. Sagdeev), vol.

1, pp. 451–517. North-Holland.

Brazier-Smith, P. R. & Scott, J. F. 1984 Stability of fluid flow in the presence of a compliant surface. *Wave Motion* **6**, 547–560.

Brebbia, C.A. & Dominguez, J. 1998 *Boundary Elements An Introductory Course*. Wit Press.

Briggs, R. J. 1964 *Electron-stream Interaction with Plasmas*. MIT Press.

Cairns, R. A. 1979 The role of negative energy waves in some instabilities of parallel flows. *J. Fluid Mech.* **92**, 1–14.

Carpenter, P. W. & Garrad, A. D. 1985 The hydrodynamic stability of flow over Kramer-type compliant surfaces. Part 1. Tollmien–Schlichting instabilities. *J. Fluid Mech.* **155**, 465–510.

Carpenter, P. W. & Garrad, A. D. 1986 The hydrodynamic stability of flow over Kramertype compliant surfaces. Part 2. Flow-induced surface instabilities. *J. Fluid Mech.* **170**, 199–232.

Connell, B. & Yue, D. 2007 Flapping dynamics of a flag in a uniform stream. *J. Fluid Mech.* **581**, 33–67.

Crighton, D. G. & Innes, D. 1984 The modes, resonances and forced response of elastic structures under heavy fluid loading. *Phil. Trans. R. Soc. Lond. A* **312**, 295–341.

Crighton, D. G. 1989 The 1988 Rayleigh Medal Lecture—fluid loading—the interaction between sound and vibration. *J. Sound Vib.* **133**, 1–27.

Crighton, D. G. & Oswell, J. E. 1991 Fluid loading with mean flow. I. Response of an elastic plate to localized excitation. *Phil. Trans. R. Soc. Lond. A* **335**, 557–592.

Doare, O. & de Langre, E. 2002 Local and global instability of fluid-conveying pipes on elastic foundations. *J. Fluids Struct.* **16**, 1–14.

Dowell, E. H. 1975 *Aeroelasticity of Plates and Shells*. Noordhoff.

Drazin, P. G. & Reid, W. H. 1981 *Hydrodynamic Stability*. Cambridge University Press.

Ellen, C. H. 1973 The stability of simply supported rectangular surfaces in uniform subsonic flow. *Trans. ASME: J. Appl. Mech.* **40**, 68–72.

- Eloy, C., Souilliez, C. & Schouveiler, L. 2007 Flutter of a rectangular plate. *J. Fluids Struct.* **23**, 904-919.
- Howe, M.S. 1994 Scattering of Bending Waves by Open and Closed Cracks and Joints in a Fluid-loaded Elastic Plate, *Proc. R. Soc. Lond. A*, **444**, pp. 555-571.
- Howe, M.S. 1998 *Acoustics of fluid-structure interactions*. Cambridge University Press.
- Huang, L. 1995 Flutter of cantilevered plates in axial flow. *J. Fluids Struct.* **9**, 127-147.
- Huerre, P. & Monkewitz, P. A. 1990 Local and global instabilities in spatially developing flow. *J. Fluid Mech.* **159**, 151-168.
- Junger, M. C. & Feit, D. 1986 *Sound, Structures, and Their Interaction*. MIT Press.
- Kelbert, M. & Sazonov, I. 1996 *Pulses and Other Processes in Fluids*. Kluwer.
- Kornecki, A. 1974 Static and dynamic instability of panels and cylindrical shells in subsonic potential flow. *J. Sound Vib.* **32**, 251-263.
- Kornecki, A. 1978 Aeroelastic instabilities of infinitely long plates. I, *Solid Mech. Arch.* **3**, 281-440.
- Kramer, M. O. 1960 Boundary layer stabilisation by distributed damping. *J. Am. Soc. Nav. Engrs.* **72**, 25-33.
- Landahl, M. T. 1962 On the stability of a laminar incompressible boundary layer over a flexible surface. *J. Fluid Mech.* **13**, 609-632.
- Lemaitre, C., Hemon, P. & de Langre, E. 2005 Instability of a long ribbon hanging in axial air flow. *J. Fluids Struct.* **20** (7), 913-925.
- Lifshitz, E. M. & Pitaevskiĭ, L.P. 1981 *Physical Kinetics (Course of Theoretical Physics, Vol 10)*. Butterworth-Heinemann.
- de Langre, E. 2002 Absolutely unstable waves in inviscid hydroelastic systems *J. Sound Vib.* **256**, 299-317.
- Lighthill, M. J. 1958 *An Introduction to Fourier Analysis and Generalised Functions*. Cambridge University Press.
- Lucey, A. D. 1998 The excitation of waves on a flexible panel in a uniform flow.

Phil. Trans. R. Soc. Lond. **356**, 2999–3039.

Lucey, A. D. & Carpenter, P. W. 1992 A numerical simulation of the interaction of a compliant wall with inviscid flow. *J. Fluid Mech.* **234**, 121–146.

Lucey, A. D. & Carpenter, P. W. 1993 On the difference between the hydroelastic instability of infinite and very long compliant panels. *J. Sound Vib.* **163**, 176–181.

Michelin, S., Llewellyn Smith, S.G. & Glover, B.J. 2008 Vortex shedding model of a flapping flag. *J. Fluid Mech.* **617**, 1–10.

Noble, B. 1988 *Methods Based on the Wiener-Hopf Technique*. 2nd Ed. Chelsea.

Oswell, J. E. 1992 Fluid loading with mean flow. *PhD Thesis*, Cambridge University, UK.

Païdoussis, M.P. 2005 *Fluid-structure Interactions, Slender Structures and AxialFlow, Vol.2*. AcademicPress.

Peake, N. 1997 On the behaviour of a fluid-loaded cylindrical shell with mean flow, *J. Fluid Mech.* **338**, pp. 387-410

Peake, N. 2001 Nonlinear stability of a fluid-loaded elastic plate with mean flow. *J. Fluid Mech.* **434**, 101–118.

Peake, N. 2004 On the Unsteady Motion of a Long Fluid-loaded Elastic Plate with Mean Flow, *J. Fluid Mech.* **507**, pp. 335-366.

Pitman, M.W., Lucey, A.D., 2009 On the Direct Determination of the Eigenmodes of Finite Flow-Structure Systems, *Proc. R. Soc. Lond. A*, **465**, pp. 257-281.

Tang, D. M., Yamamoto, H. & Dowell, E. H. 2003 Flutter and limit cycle oscillations of two-dimensional panels in three-dimensional axial flow. *J. Fluids Struct.* **17**, 225-242.

Schmid, P. J. & Henningson, D. S. 2001 *Stability and transition in shear flows*. Springer.

Stokes, A., Conti, M., Corrado, C., Arzoumanian, S., 2001 A transmission line approach to the acoustic analysis of piping systems, *Proceedings of 2001 ASME International Mechanical Engineering Congress and Exposition, November 11-16, 2001, New York, NY*.

Appendix A

Derivation of Jump Matrix

$$\partial^n G_+^{(m)} - \partial^n G_-^{(m)}$$

In this Appendix we derive the components of the ‘jump’ matrix of (4.16). From the equations for the multipole loads given in (4.3) and from the definition of the Green’s Function as the response to a unit amplitude load, we can write down the following identities:

$$\Delta f_0 = \Delta \left[\partial^3 G^{(m)} - T \partial G^{(m)} \right] = \begin{cases} +1 & m = 0 \\ 0 & m = 1, 2, 3 \end{cases} \quad (\text{A.1a})$$

$$\Delta f_1 = \Delta \left[\partial^2 G^{(m)} - T G^{(m)} \right] = \begin{cases} -1 & m = 1 \\ 0 & m = 0, 2, 3 \end{cases} \quad (\text{A.1b})$$

$$\Delta f_2 = \Delta \left[\partial G^{(m)} \right] = \begin{cases} +1 & m = 2 \\ 0 & m = 0, 1, 3 \end{cases} \quad (\text{A.1c})$$

$$\Delta f_3 = \Delta \left[G^{(m)} \right] = \begin{cases} -1 & m = 3 \\ 0 & m = 0, 1, 2 \end{cases} \quad (\text{A.1d})$$

where $\Delta [G] \equiv G_+ (0) - G_- (0)$ is the ‘jump’ in the value of G at $x = 0$.

The -1 signs in equations (A.1) come from operating on an odd numbered derivative of the delta function (Lighthill 1958)

$$\int_{-\infty}^{+\infty} f(x) \delta^{(m)}(x) dx = (-1)^m \frac{\partial^m}{\partial x^m} f(x).$$

The zeros on the second line of each of the equations in (A.1) follow from (4.3) and by construction. For instance, the identities of equation (A.1a) imply that the monopole

($m = 0$) strength of a response due to a dipole ($m = 1$) load, or a quadrupole ($m = 2$) load, or indeed any pure multipole load other than a monopole, is zero.

Every equation in (A.1) imposes a condition along a row of the jump matrix. Starting from the bottom, equation (A.1d) implies that all terms across the first row (i.e., $n = 0$) are zero, except for the term in the final column ($m = 3$) which is -1 , i.e.,

$$\Delta \left[G^{(0)} \right] = 0, \quad (\text{A.2a})$$

$$\Delta \left[G^{(1)} \right] = 0, \quad (\text{A.2b})$$

$$\Delta \left[G^{(2)} \right] = 0, \quad (\text{A.2c})$$

$$\Delta \left[G^{(3)} \right] = -1. \quad (\text{A.2d})$$

Similarly, equation (A.1c) implies that all terms across the second row (i.e., $n = 1$) are zero, except for the term in the third column ($m = 2$) which is $+1$, i.e.,

$$\Delta \left[\partial G^{(0)} \right] = 0, \quad (\text{A.3a})$$

$$\Delta \left[\partial G^{(1)} \right] = 0, \quad (\text{A.3b})$$

$$\Delta \left[\partial G^{(2)} \right] = +1, \quad (\text{A.3c})$$

$$\Delta \left[\partial G^{(3)} \right] = 0. \quad (\text{A.3d})$$

Along the third row (i.e., $n = 2$), equation (A.1b) along with the results of (A.2) imply that

$$\Delta \left[\partial^2 G^{(0)} - T G^{(0)} \right] = 0 \Rightarrow \Delta \left[\partial^2 G^{(0)} \right] = 0, \quad (\text{A.4a})$$

$$\Delta \left[\partial^2 G^{(1)} - T G^{(1)} \right] = -1 \Rightarrow \Delta \left[\partial^2 G^{(1)} \right] = -1, \quad (\text{A.4b})$$

$$\Delta \left[\partial^2 G^{(2)} - T G^{(2)} \right] = 0 \Rightarrow \Delta \left[\partial^2 G^{(2)} \right] = 0, \quad (\text{A.4c})$$

$$\Delta \left[\partial^2 G^{(3)} - T G^{(3)} \right] = 0 \Rightarrow \Delta \left[\partial^2 G^{(3)} \right] = -T. \quad (\text{A.4d})$$

Finally, along the fourth row (i.e., $n = 3$), equation (A.1a) along with the results of

(A.3) give

$$\Delta \left[\partial^3 G^{(0)} - T \partial G^{(0)} \right] = +1 \Rightarrow \Delta \left[\partial^3 G^{(0)} \right] = +1, \quad (\text{A.5a})$$

$$\Delta \left[\partial^3 G^{(1)} - T \partial G^{(1)} \right] = 0 \Rightarrow \Delta \left[\partial^3 G^{(1)} \right] = 0, \quad (\text{A.5b})$$

$$\Delta \left[\partial^3 G^{(2)} - T \partial G^{(2)} \right] = 0 \Rightarrow \Delta \left[\partial^3 G^{(2)} \right] = +T, \quad (\text{A.5c})$$

$$\Delta \left[\partial^3 G^{(3)} - T \partial G^{(3)} \right] = 0 \Rightarrow \Delta \left[\partial^3 G^{(3)} \right] = 0. \quad (\text{A.5d})$$

Collecting the results of equations (A.2-A.5), we obtain the jump matrix given in (4.16):

$$\Delta \left[\partial^n G_+^{(m)} \right] = \begin{bmatrix} 0 & 0 & 0 & -1 \\ 0 & 0 & +1 & 0 \\ 0 & -1 & 0 & -T \\ +1 & 0 & +T & 0 \end{bmatrix}. \quad (\text{A.6})$$

Appendix B

Wiener-Hopf Solution Details

In this Appendix we undertake the exact, numerical factorization of the Wiener-Hopf kernel and determine the edge potential used in chapters 6 & 7.

B.1 Exact Factorization of Kernel $K(k, \omega)$

We use the method outlined in Peake (2004) to numerically (and exactly) factorize our Wiener-Hopf kernel $K(k, \omega)$. Peake factorizes the closely related kernel $\mathcal{D}(k, \omega) = -K(k, \omega) / \gamma(k)$.

First, we define an inner kernel $E(k)$ which is non-zero along the k -plane integration contour and approaches 1 as $k \rightarrow \pm\infty$ along the real axis so that its logarithm tends to zero at infinity

$$E(k) \equiv \frac{K(k, \omega)}{\sqrt{k^2 + N^2} \prod_{n=1}^4 (k - k_n)} \quad (\text{B.1})$$

$$= \frac{\gamma(k) \mathcal{P}(k) - \alpha(\omega - Uk)^2}{\sqrt{k^2 + N^2} \prod_{n=1}^4 (k - k_n)}, \quad (\text{B.2})$$

where, k_n are the roots of the dispersion function (2.6). The factor $\sqrt{k^2 + N^2}$ (with N an arbitrary constant of order 1) was included to give $E(k)$ the correct behaviour at $k \rightarrow \infty$.

We then factorize $E(k)$ into a product of functions $E^+(k)$ and $E^-(k)$ that are analytic and non-zero in the upper and lower half planes R^+ and R^- , respectively,

using the Cauchy-integral formula (Noble, 1988)

$$E^{\pm}(k) = \exp \left[\frac{\pm 1}{2\pi i} \int \frac{\ln(E(\xi))}{\xi - k} d\xi \right]. \quad (\text{B.3})$$

The integration contour in (B.3) must lie in the strip of overlap S (see section 6.1) and is taken as the real axis, indented above or below any poles $\xi - k = 0$ according to the requirements of causality, as discussed in chapter 2. The integrals in (B.3) are evaluated numerically using standard integration routines. For details, the reader is referred to the excellent description of the numerical integration process –implemented to the letter in this thesis– given in Appendix A of Peake (2004).

As a final step, the terms in the denominator of (B.1) are factorized by inspection (and exactly) to give

$$K^{\pm}(k, \omega) = E^{\pm}(k) \sqrt{k \pm iN} \prod_{n=1}^2 (k - k_n^{\mp}), \quad (\text{B.4})$$

where the branch cuts $\sqrt{k \mp iN}$ originate from $\pm iN$ and run along the imaginary axis through R^+ and R^- respectively. From the form of equation (B.4), and recalling that $E^{\pm}(k) \sim O(1)$ as $k \rightarrow \infty$, we deduce the following asymptotic behaviour for the split kernels

$$K^{\pm}(k) \sim k^{\frac{5}{2}}, \quad k \rightarrow \infty. \quad (\text{B.5})$$

B.2 Determining the Edge Potential $\varphi(+0)$

We determine the leading edge potential $\varphi(+0)$ by following an approach similar to that undertaken by Oswell (1992). We expand $\partial\Phi^-(k)/\partial y$ for large k then deduce the behavior of its transform $\partial\varphi(x)/\partial y$, and subsequently $\varphi(x)$, for $x \rightarrow +0$. Our derivation differs from Oswell's in so far as we use a different Wiener-Hopf kernel and we include the effects of plate pre-tension and spring support.

Start from equation (6.24), expand and reorder terms in decreasing powers of k to find the large k approximation to

$$\begin{aligned} \frac{\partial\Phi^-}{\partial y} = & \frac{1}{\mathcal{P}(k)} \left\{ \alpha(\omega - Uk)^2 \frac{I(\omega - Uk_j^-)}{\gamma(k_j^-)(k - k_j^-)} \left[1 - \frac{K^-(k_j^-)}{K^-(k)} \right] \right. \\ & \left. + i(\omega - Uk)(\alpha U\varphi(+0) - h(k)) - U\eta(+0)\mathcal{P}(k) \right\}. \end{aligned} \quad (\text{B.6})$$

First, combine and simplify the terms involving the structural edge conditions eliminating the k^4 order terms to obtain

$$\begin{aligned}
& -i(\omega - Uk)h(k) - U\eta(+0)\mathcal{P}(k) \\
& = -i(\omega - Uk)\eta'''(+0) + (\omega k - Uk^2)\eta''(+0) \\
& + i(\omega T - UTk + \omega k^2 - Uk^3)\eta'(+0) \\
& + (U\omega^2 - U\lambda - \omega Tk - \omega k^3)\eta(+0). \tag{B.7}
\end{aligned}$$

This step does not involve an approximation. Next, expand the term involving the *in-vacuo* plate operator

$$\begin{aligned}
\frac{1}{\mathcal{P}(k)} &= \frac{1}{k^4 \left(1 + \frac{T}{k^2} + \frac{\lambda - \omega^2}{k^4}\right)} \\
&\approx \frac{1}{k^4} - \frac{T}{k^6} - \frac{\lambda - \omega^2}{k^8} + O(k^{-10}), \quad k \rightarrow \infty.
\end{aligned}$$

Recalling that the Wiener-Hopf split kernel behaves as $K^-(k) \sim k^{5/2}$ as $k \rightarrow \infty$, obtain the leading order terms for the factor involving the incident wave

$$\begin{aligned}
& \alpha(\omega - Uk)^2 \frac{I(\omega - Uk_j^-)}{\gamma(k_j^-)(k - k_j^-)} \left[1 - \frac{K^-(k_j^-)}{K^-(k)}\right] \\
& \approx \frac{I(\omega - Uk_j^-)}{\gamma(k_j^-)} \left(\alpha U^2 k + (\alpha U^2 k_j^- - 2\alpha\omega U) + O(k^{-1})\right), \quad k \rightarrow \infty.
\end{aligned}$$

Substituting all this into (B.6), and ordering terms in decreasing orders of k , we find that the first three leading order terms are

$$\frac{\partial \Phi^-}{\partial y} \approx \frac{A_3}{k} + \frac{A_2}{k^2} + \frac{A_1 - TA_3}{k^3} + \dots, \quad k \rightarrow \infty,$$

where,

$$\begin{aligned}
A_1 &= \alpha U^2 \frac{I(\omega - Uk_j^-)}{\gamma(k_j^-)} - i\alpha U^2 \varphi(+0) - \omega T \eta(+0) \\
&\quad - iUT \eta'(+0) + \omega \eta''(+0) + iU \eta'''(+0), \\
A_2 &= i\omega \eta'(+0) - U \eta''(+0), \\
A_3 &= -\omega \eta(+0) - iU \eta'(+0).
\end{aligned}$$

The terms involving the pre-tension T cancel out, leaving

$$\begin{aligned} \frac{\partial \Phi^-}{\partial y} &\approx \frac{-\omega \eta(+0) - iU \eta'(+0)}{k} + \frac{i\omega \eta'(+0) - U \eta''(+0)}{k^2} \\ &+ \frac{\alpha U^2 \frac{I(\omega - Uk_j^-)}{\gamma(k_j^-)} - i\alpha U^2 \varphi(+0) + \omega \eta''(+0) + iU \eta'''(+0)}{k^3} + \dots, \quad k \rightarrow \infty. \end{aligned} \quad (\text{B.8})$$

We note that the Wiener-Hopf split kernel does not appear at this order.

Watson's Lemma imposes the following relationship between terms asymptotic in k and x

$$\frac{1}{(ik)^n} \rightarrow \frac{x^{n-1}}{(n-1)!}, \quad k \rightarrow \infty, \quad x \rightarrow 0.$$

We use this to obtain the asymptotic behavior of the transform of (B.8) as $x \rightarrow 0$

$$\begin{aligned} \frac{\partial \varphi(x, y=0)}{\partial y} &\approx [U \eta'(+0) - i\omega \eta(+0)] + [U \eta''(+0) - i\omega \eta'(+0)] x \\ &+ \left[-i\alpha U^2 \frac{I(\omega - Uk_j^-)}{\gamma(k_j^-)} - \alpha U^2 \varphi(+0) - i\omega \eta''(+0) + U \eta'''(+0) \right] \frac{x^2}{2!} + O(x^3). \end{aligned} \quad (\text{B.9})$$

Next, we expand the convective derivative of the plate displacement in a Taylor series about $x = 0$

$$\begin{aligned} \frac{\partial \eta(x)}{\partial t} + U \frac{\partial \eta(x)}{\partial x} &\approx -i\omega \eta(0) + U \eta'(0) \\ &+ [-i\omega \eta'(+0) + U \eta''(+0)] x + [i\omega \eta''(+0) + U \eta'''(+0)] \frac{x^2}{2!} + O(x^3). \end{aligned} \quad (\text{B.10})$$

Finally, we invoke the continuity condition and equate equations (B.9) and (B.10) term by term. We find that this identity is satisfied identically for orders x^0 and x^1 , and that at order x^2 we must satisfy

$$\begin{aligned} -i\alpha U^2 \frac{I(\omega - Uk_j^-)}{\gamma(k_j^-)} - \alpha U^2 \varphi(+0) - i\omega \eta''(+0) + U \eta'''(+0) \\ \equiv i\omega \eta''(+0) + U \eta'''(+0). \end{aligned}$$

Solving this yields the following expression for the unknown edge potential

$$\varphi(+0) = -i \frac{I(\omega - Uk_j^-)}{\gamma(k_j^-)}, \quad (\text{B.11})$$

which is identical to (6.23).

We note that the structural edge conditions contained in $\eta(+0)$ and its higher order spatial derivatives fall out of this expression. As a result, the edge potential given in (B.11) is universal and valid for all structural conditions at the edge. As discussed in chapter 6, (B.11) is simply a statement of continuity of potential at the edge.

Appendix C

Computational Model of Baffled Plate

In this Appendix we describe the computational model used to directly solve the system of differential equations for a fluid loaded plate in mean flow embedded in an infinite, rigid baffle.

C.1 Computational model

The linear, non-dimensional equations for a one dimensional (1-D) thin plate of length L in a rigid baffle with vacuum on one side and bounded by a two dimensional (2-D) half plane of (incompressible, inviscid, irrotational) fluid on the other are

$$\nabla^2 \phi(x, y, t) = 0 \quad (\text{C.1})$$

$$p(x, y, t) = - \left(\frac{\partial}{\partial t} \phi(x, y, t) + U \frac{\partial}{\partial x} \phi(x, y, t) \right) \quad (\text{C.2})$$

$$\left. \frac{\partial \phi(x, y, t)}{\partial \hat{n}} \right|_{y=\eta} = \left(\frac{\partial}{\partial t} \eta(x, t) + U \frac{\partial}{\partial x} \eta(x, t) \right) \cdot \hat{n} \quad (\text{C.3})$$

$$\frac{\partial^4}{\partial x^4} \eta(x, t) + T \frac{\partial^2}{\partial x^2} \eta(x, t) + \lambda \eta(x, t) + \frac{\partial^2}{\partial t^2} \eta(x, t) = -p(x, \eta, t) + f(x, t) \quad (\text{C.4})$$

with the additional boundary condition of zero normal velocity on the rigid baffle

$$\frac{\partial \eta}{\partial t} = 0 \quad \& \quad \left. \frac{\partial \phi}{\partial \hat{n}} \right|_{y=\eta} = 0, \quad |x| > \frac{L}{2}. \quad (\text{C.5})$$

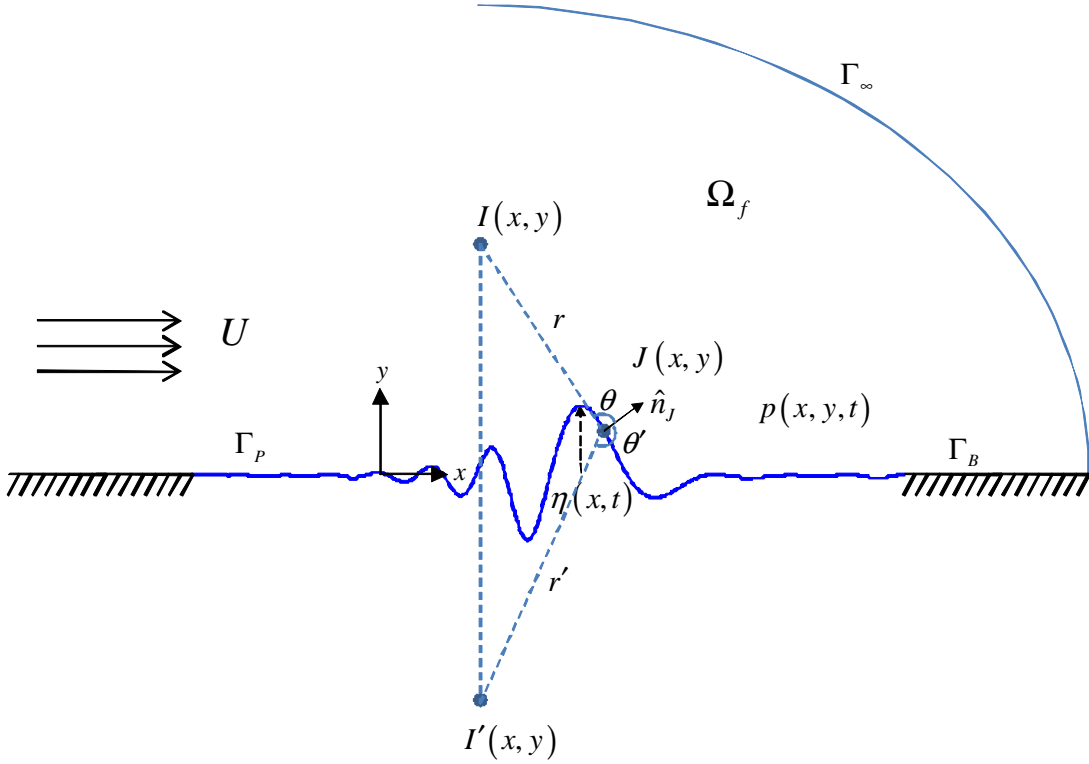


Figure C.1: Baffled plate configuration.

Here, ϕ is the fluid potential, p the fluid pressure, η the plate displacement, \hat{n} the normal to the plate surface pointing into the fluid, and f the force per unit length acting on the plate (figure C.1). The above equations have been linearized for both the structure and the fluid. However, we shall initially carry out the derivations by allowing for geometric nonlinearities at the interface between the two. This is accomplished by evaluating the interface at $y = \eta$. The fully linear case consists of evaluating this interface at $y = 0$.

We begin by solving Laplace's equation (C.1) in the half plane subject to Neumann boundary conditions at $y = \eta$ through a direct boundary integral formulation. The starting point is Green's symmetric identity in 2-D

$$\int_{\Omega_f} (\phi \nabla^2 \psi - \psi \nabla^2 \phi) d\Omega = \int_{\Gamma_B} \phi \frac{\partial \psi}{\partial \hat{n}_B} d\Gamma - \int_{\Gamma_B} \psi \frac{\partial \phi}{\partial \hat{n}_B} d\Gamma, \quad (\text{C.6})$$

where Ω_f is the fluid half plane, Γ_B is the boundary enclosing the half plane including the plate surface, \hat{n}_B is the unit normal to Γ_B pointing into the fluid and ψ is the

fundamental solution defined by the following equations (i.e., the Green's function for Laplace's equation in the half plane bounded by a rigid baffle):

$$\nabla^2 \psi(\mathbf{x}) = -\delta(\mathbf{x} - \mathbf{x}_{\mathbf{I}}) \quad \& \quad \left. \frac{\partial \psi(\mathbf{x}; \mathbf{x}_{\mathbf{I}})}{\partial y} \right|_{y=0} = 0. \quad (\text{C.7})$$

Since we are interested in the value of the fluid potential at the surface of the plate $\Gamma_{\mathbf{J}}$, we consider the source function point in (C.7) to be positioned on the surface $\Gamma_{\mathbf{J}}$. Here, and in what follows, the vectors $\mathbf{I} \equiv (x_{\mathbf{I}}, y_{\mathbf{I}})$ and $\mathbf{J} \equiv (x_{\mathbf{J}}, y_{\mathbf{J}})$ represent the *continuous* coordinates of the source and receiver, respectively. Noting that both $\partial \psi / \partial \hat{n}_B = 0$ and $\partial \phi / \partial \hat{n}_B = 0$ on the baffle beyond the plate domain, and given that the solution $\phi(r)$ decays at least as $1/r$ in the far field so that all surface integrals at infinity amount to zero, equation (C.6) reduces to

$$\frac{1}{2} \phi(\mathbf{I}) + \int_{\Gamma_{\mathbf{J}}} \phi(\mathbf{J}) \frac{\partial \psi(\mathbf{I}, \mathbf{J})}{\partial \hat{n}_{\Gamma_{\mathbf{J}}}} d\Gamma_{\mathbf{J}} = \int_{\Gamma_{\mathbf{J}}} \psi(\mathbf{I}, \mathbf{J}) \frac{\partial \phi(\mathbf{J})}{\partial \hat{n}_{\Gamma_{\mathbf{J}}}} d\Gamma_{\mathbf{J}}, \quad (\text{C.8})$$

where all integrations have been reduced to line integrals restricted to the plate domain $\Gamma_{\mathbf{J}}$. Note that the factor $\frac{1}{2}$ above results from evaluating the surface integral in (C.6) with ϕ at the boundary of the plate. This factor would be 1 for all points away from the boundaries, located at the interior of the fluid domain (Brebbia & Dominguez, 1998).

C.2 Implementation Including Geometric Nonlinearities

The transition from a boundary integral formulation, (C.8), to a boundary element (BEM) formulation (see for example, Brebbia & Dominguez, 1998) is achieved by discretizing the plate surface into M uniformly spaced boundary elements. We assume that ϕ and $\partial \phi / \partial \hat{n}$ are constant inside each element. The continuous boundary integrals of (C.8) now become discrete summations over the elements subdividing the boundary

$$\frac{1}{2} \phi_i + \sum_{j=1}^M H_{ij} \phi_j = \sum_{j=1}^M G_{ij} \left(\frac{\partial \phi}{\partial \hat{n}} \right)_j. \quad (\text{C.9})$$

Here,

$$H_{ij} = \int_{\Gamma_j} \frac{\partial \psi(\mathbf{x}_i, \mathbf{J})}{\partial \hat{n}_{\Gamma_{\mathbf{J}}}} d\Gamma_{\mathbf{J}} \quad (\text{C.10})$$

and

$$G_{ij} = \int_{\Gamma_j} \psi(\mathbf{x}_i, \mathbf{J}) d\Gamma_{\mathbf{J}} \quad (\text{C.11})$$

are $M \times M$ influence matrices evaluated using the Green's function ψ for the half plane. The Addendum (section C.4) contains derivations of these fundamental solutions for the general case of an arbitrarily displaced plate, $y = \eta$, in an infinite baffle.

The off-diagonal elements of H_{ij} and G_{ij} can be evaluated using any numerical integration procedure, such as four-point Gauss quadrature formula. The diagonal elements consist of integrals containing the source singularities and are evaluated analytically. This is a straightforward procedure for constant boundary elements (see Brebbia & Dominguez, 1998).

Once the matrices H_{ij} and G_{ij} have been derived for a particular deformation of the plate surface, the potentials and their normal derivatives at the surface can be related through the matrix equation (summation over repeated indices implied from here on)

$$\bar{H}_{ij}\phi_j = G_{ij} \left(\frac{\partial \phi}{\partial \hat{n}} \right)_j. \quad (\text{C.12})$$

Here, $\bar{H}_{ij} \equiv \frac{1}{2}I_{ij} + H_{ij}$, where I_{ij} is the identity matrix, combines the two terms on the left hand side of (C.9).

In order to evaluate the $\partial\phi/\partial x$ terms introduced by a non-zero mean flow, we require another set of matrix equations. We take $\partial/\partial x_{\mathbf{I}}$ of both sides of (C.8) to obtain

$$\frac{1}{2} \frac{\partial}{\partial x_{\mathbf{I}}} \phi(\mathbf{I}) + \int_{\Gamma_{\mathbf{J}}} \phi(\mathbf{J}) \frac{\partial}{\partial x_{\mathbf{I}}} \frac{\partial \psi(\mathbf{I}, \mathbf{J})}{\partial \hat{n}_{\Gamma_{\mathbf{J}}}} d\Gamma_{\mathbf{J}} = \int_{\Gamma_{\mathbf{J}}} \frac{\partial}{\partial x_{\mathbf{I}}} \psi(\mathbf{I}, \mathbf{J}) \frac{\partial \phi(\mathbf{J})}{\partial \hat{n}_{\Gamma_{\mathbf{J}}}} d\Gamma_{\mathbf{J}}. \quad (\text{C.13})$$

Discretizing (C.13) as above gives

$$\frac{1}{2} \left(\frac{\partial \phi}{\partial x} \right)_i + H_{ij}^x \phi_j = G_{ij}^x \left(\frac{\partial \phi}{\partial \hat{n}} \right)_j, \quad (\text{C.14})$$

where

$$H_{ij}^x = \int_{\Gamma_j} \frac{\partial}{\partial x_i} \left(\frac{\partial \psi(\mathbf{x}_i, \mathbf{J})}{\partial \hat{n}_{\Gamma_{\mathbf{J}}}} \right) d\Gamma_{\mathbf{J}} \quad (\text{C.15})$$

and

$$G_{ij}^x = \int_{\Gamma_j} \frac{\partial}{\partial x_i} (\psi(\mathbf{x}_i, \mathbf{J})) d\Gamma_{\mathbf{J}} \quad (\text{C.16})$$

are the x differentials of H_{ij} and G_{ij} . The partial derivatives in (C.13) are carried out on the source functions ψ and $\partial\psi/\partial\hat{n}$, since we are only computing the variation in x around the source point \mathbf{x}_i . The integrands in (C.15) and (C.16) are derived in the Addendum (section C.4). The off-diagonal terms can once again be computed using Gauss quadrature, whereas the diagonal terms can be evaluated analytically.

Again, once the matrices H_{ij}^x and G_{ij}^x have been obtained, the BEM formulation gives us the relation

$$\frac{1}{2} \left(\frac{\partial\phi}{\partial x} \right)_i = G_{ij}^x \left(\frac{\partial\phi}{\partial\hat{n}} \right)_j - H_{ij}^x \phi_j, \quad (\text{C.17})$$

which can be expressed in terms of the normal derivatives only using (C.12)

$$\begin{aligned} \left(\frac{\partial\phi}{\partial x} \right)_i &= 2G_{ij}^x \left(\frac{\partial\phi}{\partial\hat{n}} \right)_j - 2H_{im}^x \bar{H}_{nk}^{-1} G_{lj} \left(\frac{\partial\phi}{\partial\hat{n}} \right)_j \\ &= K_{ij}^x \left(\frac{\partial\phi}{\partial\hat{n}} \right)_j, \end{aligned} \quad (\text{C.18})$$

where we have defined $K_{ij}^x \equiv 2G_{ij}^x - 2H_{im}^x \bar{H}_{nk}^{-1} G_{lj}$.

We proceed to the spatial discretization of the plate equation (C.4). We use an M point mesh identical to the one used for the boundary elements. The nodes are the mid-points of the boundary elements. We approximate the spatial derivatives through finite differences. Combining the plate equation with the discretized version of the unsteady Bernoulli equation (C.2) evaluated at the plate interface $y = \eta$, we obtain

$$\frac{1}{(\Delta x)^4} \delta^4 [\eta_i] + \frac{\partial^2}{\partial t^2} \eta_i = \frac{\partial}{\partial t} \phi_i + U \left(\frac{\partial\phi}{\partial x} \right)_i + f_i, \quad (\text{C.19})$$

which after substituting in (C.12) and (C.18) becomes

$$\frac{1}{(\Delta x)^4} \delta^4 [\eta_i] + \frac{\partial^2}{\partial t^2} \eta_i = \frac{\partial}{\partial t} \bar{H}_{ij}^{-1} G_{ij} \left(\frac{\partial\phi}{\partial\hat{n}} \Big|_{y=\eta} \right)_j + U K_{ij}^x \left(\frac{\partial\phi}{\partial\hat{n}} \Big|_{y=\eta} \right)_j + f_i. \quad (\text{C.20})$$

We can eliminate the potential terms from the above equation by substituting the discretized continuity equation (C.3)

$$\left(\frac{\partial\phi}{\partial\hat{n}} \Big|_{y=\eta} \right)_j = \frac{\partial}{\partial t} \eta_j \cdot \hat{n}_j + \frac{U}{\Delta x} \delta^1 [\eta_j \cdot \hat{n}_j] \quad (\text{C.21})$$

into (C.20). The finite difference operators, δ^1 and δ^4 , can be the central differences to fourth order in Δx given in (C.34) and (C.36) below. The coupled fluid-plate equation

can now be expressed in terms of the plate deflection alone:

$$\begin{aligned}
\frac{1}{(\Delta x)^4} \delta^4 [\eta_i] + \frac{\partial^2}{\partial t^2} \eta_i &= \frac{\partial}{\partial t} \left\{ \bar{H}_{ij}^{-1} G_{ij} \left(\frac{\partial}{\partial t} (\eta_j \cdot \hat{n}_j) + \frac{U}{\Delta x} \delta^1 [\eta_j \cdot \hat{n}_j] \right) \right\} \\
&\quad + U K_{ij}^x \left(\frac{\partial}{\partial t} (\eta_j \cdot \hat{n}_j) + \frac{U}{\Delta x} \delta^1 [\eta_j \cdot \hat{n}_j] \right) + f_i. \\
&= \frac{\partial}{\partial t} \left\{ \bar{H}_{ij}^{-1} G_{ij} \frac{\partial}{\partial t} (\eta_j \cdot \hat{n}_j) \right\} + \frac{U}{\Delta x} \frac{\partial}{\partial t} \left\{ \bar{H}_{ij}^{-1} G_{ij} \delta^1 [\eta_j \cdot \hat{n}_j] \right\} \\
&\quad + U K_{ij}^x \frac{\partial}{\partial t} (\eta_j \cdot \hat{n}_j) + \frac{U^2}{\Delta x} K_{ij}^x \delta^1 [\eta_j \cdot \hat{n}_j] + f_i. \tag{C.22}
\end{aligned}$$

For the case where the plate surface is taken at $y = \eta$, no further simplifications are possible. The influence matrices \bar{H}_{ij}^{-1} , G_{ij} and K_{ij}^x must be rederived for every new deflection distribution η_i of the plate. In addition, care must be taken in evaluating the time derivatives of the bracketed expressions as both the influence matrices and the displacements are now functions of time. The final step involves discretizing in time. One can for example use a second order centered difference scheme described in the context of the fully linear case in section C.3.5 below.

Only a fully linear computational scheme is implemented in this thesis. We will therefore not pursue the scheme involving geometric nonlinearities further and proceed directly to the full implementation of the linear scheme.

C.3 Fully Linear Implementation

For the fully linear case where the plate surface is taken at $y = 0$, the fundamental solution, now evaluated directly on the rigid baffle, becomes

$$\psi(\mathbf{I}, \mathbf{J}) = -\frac{1}{\pi} \ln R(\mathbf{I}, \mathbf{J}), \tag{C.23}$$

$$\frac{\partial \psi(\mathbf{I}, \mathbf{J})}{\partial \hat{n}_{\Gamma_{\mathbf{J}}}} = 0, \tag{C.24}$$

where $R(\mathbf{I}, \mathbf{J}) = \sqrt{(x_{\mathbf{I}} - x_{\mathbf{J}})^2}$ is the distance between the source and receiver points along $y = 0$. The boundary integral formula of (C.8) reduces to

$$\frac{1}{2} \phi(\mathbf{I}) = \int_{\Gamma_{\mathbf{J}}} \psi(\mathbf{I}, \mathbf{J}) \frac{\partial \phi(\mathbf{J})}{\partial \hat{n}_{\Gamma_{\mathbf{J}}}} d\Gamma_{\mathbf{J}}, \tag{C.25}$$

and the unsteady Bernoulli equation (C.2) can now be written as

$$-p(\mathbf{I}) = \frac{\partial}{\partial t} \int_{\Gamma_{\mathbf{J}}} 2\psi(\mathbf{I}, \mathbf{J}) \frac{\partial \phi(\mathbf{J})}{\partial \hat{n}_{\Gamma_{\mathbf{J}}}} d\Gamma_{\mathbf{J}} + U \frac{\partial}{\partial x} \int_{\Gamma_{\mathbf{J}}} 2\psi(\mathbf{I}, \mathbf{J}) \frac{\partial \phi(\mathbf{J})}{\partial \hat{n}_{\Gamma_{\mathbf{J}}}} d\Gamma_{\mathbf{J}}. \quad (\text{C.26})$$

Combining this with the linearized version of the continuity equation (C.3),

$$\left. \frac{\partial \phi}{\partial \hat{n}} \right|_{y=0} = \frac{\partial}{\partial t} \eta + U \frac{\partial}{\partial x} \eta, \quad (\text{C.27})$$

we can write down an equation for the pressure in terms of plate deflection alone

$$\begin{aligned} -p(\mathbf{I}) &= \frac{\partial}{\partial t} \int_{\Gamma_{\mathbf{J}}} 2\psi(\mathbf{I}, \mathbf{J}) \frac{\partial}{\partial t} \eta(\mathbf{J}) d\Gamma_{\mathbf{J}} + U \frac{\partial}{\partial t} \int_{\Gamma_{\mathbf{J}}} 2\psi(\mathbf{I}, \mathbf{J}) \frac{\partial}{\partial x_{\mathbf{J}}} \eta(\mathbf{J}) d\Gamma_{\mathbf{J}} \\ &+ U \frac{\partial}{\partial x_{\mathbf{I}}} \int_{\Gamma_{\mathbf{J}}} 2\psi(\mathbf{I}, \mathbf{J}) \frac{\partial}{\partial t} \eta(\mathbf{J}) d\Gamma_{\mathbf{J}} + U^2 \frac{\partial}{\partial x_{\mathbf{I}}} \int_{\Gamma_{\mathbf{J}}} 2\psi(\mathbf{I}, \mathbf{J}) \frac{\partial}{\partial x_{\mathbf{J}}} \eta(\mathbf{J}) d\Gamma_{\mathbf{J}}. \end{aligned} \quad (\text{C.28})$$

We evaluate the first and third integrals by first bringing the differentials under the integral sign, as shown below

$$\frac{\partial}{\partial t} \int_{\Gamma_{\mathbf{J}}} 2\psi(\mathbf{I}, \mathbf{J}) \frac{\partial}{\partial t} \eta(\mathbf{J}) d\Gamma_{\mathbf{J}} = \int_{\Gamma_{\mathbf{J}}} 2\psi(\mathbf{I}, \mathbf{J}) \frac{\partial^2}{\partial t^2} \eta(\mathbf{J}) d\Gamma_{\mathbf{J}}, \quad (\text{C.29})$$

$$U \frac{\partial}{\partial x_{\mathbf{I}}} \int_{\Gamma_{\mathbf{J}}} 2\psi(\mathbf{I}, \mathbf{J}) \frac{\partial}{\partial t} \eta(\mathbf{J}) d\Gamma_{\mathbf{J}} = U \int_{\Gamma_{\mathbf{J}}} 2 \frac{\partial}{\partial x_{\mathbf{I}}} \psi(\mathbf{I}, \mathbf{J}) \frac{\partial}{\partial t} \eta(\mathbf{J}) d\Gamma_{\mathbf{J}}. \quad (\text{C.30})$$

The same operations are performed on the second and fourth integrals. However, the latter contain spatial differentials of the plate deflection, making these integrals more challenging to evaluate numerically. We therefore apply integration by parts to ‘transfer’ these spatial differentials from the receiver terms to the source terms, as shown below

$$\begin{aligned} U \frac{\partial}{\partial t} \int_{\Gamma_{\mathbf{J}}} 2\psi(\mathbf{I}, \mathbf{J}) \frac{\partial}{\partial x_{\mathbf{J}}} \eta(\mathbf{J}) d\Gamma_{\mathbf{J}} &= (-1)(-1) U \int_{\Gamma_{\mathbf{J}}} 2 \frac{\partial}{\partial x_{\mathbf{I}}} \psi(\mathbf{I}, \mathbf{J}) \frac{\partial}{\partial t} \eta(\mathbf{J}) d\Gamma_{\mathbf{J}} \\ &+ 2U \psi(\mathbf{I}, \mathbf{J}) \frac{\partial}{\partial t} \eta(\mathbf{J}) \Big|_{\mathbf{J}=-\frac{L}{2}}^{\mathbf{J}=\frac{L}{2}}, \end{aligned} \quad (\text{C.31})$$

$$\begin{aligned} U^2 \frac{\partial}{\partial x_{\mathbf{I}}} \int_{\Gamma_{\mathbf{J}}} 2\psi(\mathbf{I}, \mathbf{J}) \frac{\partial}{\partial x_{\mathbf{J}}} \eta(\mathbf{J}) d\Gamma_{\mathbf{J}} &= (-1)(-1) U^2 \int_{\Gamma_{\mathbf{J}}} 2 \frac{\partial^2}{\partial x_{\mathbf{I}}^2} \psi(\mathbf{I}, \mathbf{J}) \eta(\mathbf{J}) d\Gamma_{\mathbf{J}} \\ &+ 2U^2 \frac{\partial}{\partial x_{\mathbf{I}}} \psi(\mathbf{I}, \mathbf{J}) \eta(\mathbf{J}) \Big|_{\mathbf{J}=-\frac{L}{2}}^{\mathbf{J}=\frac{L}{2}}. \end{aligned} \quad (\text{C.32})$$

Here, a (-1) comes from the integration by parts, and another (-1) from the symmetry property of the fundamental solution, $\partial\psi(\mathbf{I}, \mathbf{J})/\partial x_{\mathbf{J}} = -\partial\psi(\mathbf{I}, \mathbf{J})/\partial x_{\mathbf{I}}$. The benefit comes from transferring the spatial differentials from an unknown quantity, η , to a known quantity, ψ , thereby allowing for an analytical, and therefore exact, evaluation of these derivatives. We note that the terms evaluated at the plate end points, $\mathbf{J} = \pm \frac{L}{2}$, are identically zero for a plate clamped at both ends. We also note that the expressions for the second and third integrals, (C.30) and (C.31), are now equal up to the terms associated with the plate end points.

C.3.1 Singular Panels

All four integrals given in (C.29) through (C.32) contain singularities at the source location, $\mathbf{J} = \mathbf{I}$. Therefore, the region around the source will have to be evaluated separately and with special care.

We expand the term multiplying the source function—call this term $f(x)$, where $f(x)$ is some function of the plate displacement—in terms of a Taylor series about the source point and evaluate the principal value integral of each term. For an integral of the form of equation (C.29), we obtain

$$\begin{aligned}
 \int_{-\Delta x/2}^{\Delta x/2} \psi(x) f(x) dx &\approx \int_{-\Delta x/2}^{\Delta x/2} \ln(|x|) \left[f(0) + x \frac{\partial}{\partial x} f(0) + \frac{x^2}{2!} \frac{\partial^2}{\partial x^2} f(0) + \cdots \right] dx \\
 &= \int_{-\Delta x/2}^{\Delta x/2} \ln(|x|) f(0) dx + \int_{-\Delta x/2}^{\Delta x/2} \ln(|x|) \frac{x^2}{2!} \frac{\partial^2}{\partial x^2} f(0) dx + \cdots \\
 &\approx \Delta x f(0) (1 - \ln(\Delta x/2)),
 \end{aligned}$$

where terms containing odd powers of x have yielded zero and we have only kept the leading order term in the solution. For integrals of the form of equation (C.30), the principal value of the leading order term (as well as all other terms containing even

power of x) is zero and we therefore retain the second order term to obtain

$$\begin{aligned}
 \int_{-\Delta x/2}^{\Delta x/2} \frac{\partial}{\partial x} \psi(x) f(x) dx &\approx - \int_{-\Delta x/2}^{\Delta x/2} \frac{1}{x} \left[f(0) + x \frac{\partial}{\partial x} f(0) + \frac{x^2}{2!} \frac{\partial^2}{\partial x^2} f(0) + \dots \right] dx \\
 &= \int_{-\Delta x/2}^{\Delta x/2} \frac{\partial}{\partial x} f(0) dx + \int_{-\Delta x/2}^{\Delta x/2} \frac{x^2}{3!} \frac{\partial^3}{\partial x^3} f(0) dx + \dots \\
 &\approx \Delta x \frac{\partial}{\partial x} f(0). \tag{C.33}
 \end{aligned}$$

Applying the same approach to integrals of the form of (C.32) yields a leading order term of the form $f(0)/\Delta x$, which is divergent for $\Delta x \rightarrow 0$ and is a clear indication that the integral itself is hyper-singular and hence non-integrable.

This suggests that we recast the integral in (C.32) in a form that does not involve the second derivative of the source function in the immediate vicinity of the source point. We define a narrow integration domain Γ_0 of length Δx around the source and exclude from this domain the integration by parts operation, by which the spatial derivative is transferred from receiver to source, to obtain

$$\begin{aligned}
 U^2 \frac{\partial}{\partial x_{\mathbf{I}}} \int_{\Gamma_{\mathbf{J}}} 2\psi(\mathbf{I}, \mathbf{J}) \frac{\partial}{\partial x_{\mathbf{J}}} \eta(\mathbf{J}) d\Gamma_{\mathbf{J}} &= U^2 \int_{\Gamma_{\mathbf{J}} - \Gamma_0} 2 \frac{\partial^2}{\partial x_{\mathbf{I}}^2} \psi(\mathbf{I}, \mathbf{J}) \eta(\mathbf{J}) d\Gamma_{\mathbf{J}} \\
 &+ U^2 \int_{\Gamma_0} 2 \frac{\partial}{\partial x_{\mathbf{I}}} \psi(\mathbf{I}, \mathbf{J}) \frac{\partial}{\partial x_{\mathbf{J}}} \eta(\mathbf{J}) d\Gamma_{\mathbf{J}} + 2U^2 \frac{\partial}{\partial x_{\mathbf{I}}} \psi(\mathbf{I}, \mathbf{J}) \eta(\mathbf{J}) \Big|_{\mathbf{J}=-\frac{L}{2}}^{\mathbf{J}=\mathbf{I}-\frac{\Delta x}{2}} \\
 &+ 2U^2 \frac{\partial}{\partial x_{\mathbf{I}}} \psi(\mathbf{I}, \mathbf{J}) \eta(\mathbf{J}) \Big|_{\mathbf{J}=\mathbf{I}+\frac{\Delta x}{2}}^{\mathbf{J}=\frac{L}{2}}.
 \end{aligned}$$

The integral containing $\partial^2 \psi / \partial x^2$ can be evaluated numerically as before whereas the singular integral now contains a source term of the form $\partial \psi / \partial x$ and is evaluated in the manner of (C.33) to yield

$$\int_{-\Delta x/2}^{\Delta x/2} \frac{\partial}{\partial x} \psi(x) \frac{\partial}{\partial x} f(x) dx \approx \Delta x \frac{\partial^2}{\partial x^2} f(0).$$

C.3.2 Spatial Discretization

As described in section C.2 above, we discretize the plate surface into M uniformly spaced elements and assume that ϕ and $\partial\phi/\partial\hat{n}$ are constant inside each element. The structural nodes are therefore the mid-points of the boundary elements. We approximate the spatial derivatives through the following fourth order finite central differences:

$$\frac{\partial}{\partial x}\eta(\mathbf{I}) \approx \frac{\delta^1[\eta_i]}{\Delta x} = \frac{1}{12\Delta x} (\eta_{i-2} - 8\eta_{i-1} + 8\eta_{i+1} - \eta_{i+2}) + O(\Delta x^6), \quad (\text{C.34})$$

$$\frac{\partial^2}{\partial x^2}\eta(\mathbf{I}) \approx \frac{\delta^2[\eta_i]}{\Delta x^2} = \frac{1}{12\Delta x^2} (-\eta_{i-2} + 16\eta_{i-1} - 30\eta_i + 16\eta_{i+1} - \eta_{i+2}) + O(\Delta x^6), \quad (\text{C.35})$$

$$\begin{aligned} \frac{\partial^4}{\partial x^4}\eta(\mathbf{I}) &\approx \frac{\delta^4[\eta_i]}{\Delta x^4} \\ &= \frac{1}{6\Delta x^4} (-\eta_{i-3} + 12\eta_{i-2} - 39\eta_{i-1} + 56\eta_i - 39\eta_{i+1} + 12\eta_{i+2} - \eta_{i+3}) + O(\Delta x^6). \end{aligned} \quad (\text{C.36})$$

The clamped structural edge conditions are satisfied by imposing a zero displacement and zero slope condition at the outermost edges of the end panels. This is accomplished by defining three ‘phantom’ points beyond each edge and imposing the zero displacement and zero slope condition at the mid-point between the final plate node and the first ‘phantom’ node. Approximate expressions for the plate displacement and slope at the halfway point between two nodes are obtained by expanding in a Taylor series about the nodal point

$$\eta\left(\mathbf{I} \pm \frac{\Delta x}{2}\right) \approx \eta(\mathbf{I}) \pm \frac{\Delta x}{2} \frac{\partial\eta(\mathbf{I})}{\partial x} \pm \frac{1}{2!} \left(\frac{\Delta x}{2}\right)^2 \frac{\partial^2\eta(\mathbf{I})}{\partial x^2} \pm \frac{1}{3!} \left(\frac{\Delta x}{2}\right)^3 \frac{\partial^3\eta(\mathbf{I})}{\partial x^3} + \dots$$

and expressing the differentials in terms of finite differences at the full nodal points to obtain the following fourth order finite difference formulae:

$$\eta_{i+\frac{1}{2}} \approx \frac{1}{128} (3\eta_{i-2} - 20\eta_{i-1} + 90\eta_i + 60\eta_{i+1} - 5\eta_{i+2}) + O(\Delta x^6), \quad (\text{C.37a})$$

$$\eta_{i-\frac{1}{2}} \approx \frac{1}{128} (-5\eta_{i-2} + 60\eta_{i-1} + 90\eta_i - 20\eta_{i+1} + 3\eta_{i+2}) + O(\Delta x^6). \quad (\text{C.37b})$$

A similar approach can be used to obtain finite difference formulae for the slope at a halfway point

$$\begin{aligned} \frac{\partial}{\partial x} \eta \left(\mathbf{I} \pm \frac{\Delta x}{2} \right) &\approx \frac{\delta^1 \left[\eta_{i \pm \frac{1}{2}} \right]}{\Delta x} = \\ &\frac{1}{1920} (\mp 3\eta_{i-2} \pm 95\eta_{i-1} \mp 2190\eta_i \mp 95\eta_{i+1} \pm 3\eta_{i+2}) + O(\Delta x^6). \end{aligned} \quad (\text{C.38})$$

Equations (C.37a) and (C.37b) can be added to give an expression for the sum of equally weighted displacements at the edge of the same panel

$$\begin{aligned} \eta \left(\mathbf{I} - \frac{\Delta x}{2} \right) + \eta \left(\mathbf{I} + \frac{\Delta x}{2} \right) &\approx \eta_{i-\frac{1}{2}} + \eta_{i+\frac{1}{2}} = \\ -\frac{1}{64}\eta_{i-2} + \frac{5}{16}\eta_{i-1} + \frac{45}{32}\eta_i + \frac{5}{16}\eta_{i+1} - \frac{1}{64}\eta_{i+2} &+ O(\Delta x^6). \end{aligned} \quad (\text{C.39})$$

This formula will be used in section C.3.3 below.

C.3.3 Evaluation of Spatial Integrals

With this choice of spatial discretization, the influence coefficients contained in the boundary integral equation (C.28) become matrices with the following constant elements:

$$G_{ij} = \int_{\Gamma_j} \psi(i, \mathbf{J}) d\Gamma_{\mathbf{J}} = - \int_{\Gamma_j} \frac{\ln R_{i\mathbf{J}}}{\pi} d\Gamma_{\mathbf{J}}, \quad (\text{C.40})$$

$$G_{ij}^x = \int_{\Gamma_j} \frac{\partial}{\partial x_i} (\psi(i, \mathbf{J})) d\Gamma_{\mathbf{J}} = \int_{\Gamma_j} \frac{(x_i - x_{\mathbf{J}})}{\pi R_{i\mathbf{J}}^2} d\Gamma_{\mathbf{J}}, \quad (\text{C.41})$$

$$G_{ij}^{xx} = \int_{\Gamma_j} \frac{\partial^2}{\partial x_i^2} (\psi(i, \mathbf{J})) d\Gamma_{\mathbf{J}} = - \int_{\Gamma_j} \frac{1}{\pi R_{i\mathbf{J}}^2} d\Gamma_{\mathbf{J}}, \quad (\text{C.42})$$

where, $R_{i\mathbf{J}} = \sqrt{(x_i - x_{\mathbf{J}})^2}$. These off-diagonal coefficients, $j \neq i$, are evaluated numerically using four point Guassian quadrature. The surface integrals, excluding the source panels, can now be expressed as

$$\begin{aligned} -p_i &= 2G_{ij} \frac{\partial^2}{\partial t^2} \eta_j + 4UG_{ij}^x \frac{\partial}{\partial t} \eta_j + 2U^2 G_{ij}^{xx} \eta_j \\ &+ 2UG_{ij} \frac{\partial}{\partial t} \eta_j \Big|_{j=1}^{j=M} + 2U^2 G_{ij}^{xx} \frac{\partial}{\partial t} \eta_j \Big|_{j=1}^{j=M} + p_i^{source}, \quad j \neq i. \end{aligned} \quad (\text{C.43})$$

The contributions from the source panels are straightforward to compute for the integrals containing the source terms ψ and $\partial\psi/\partial x$. They are

$$\frac{(1 - \ln(\Delta x/2)) \Delta x}{\pi} \frac{\partial^2}{\partial t^2} \eta_i \quad (\text{C.44})$$

and

$$\frac{1}{12\pi} \frac{\partial}{\partial t} (\eta_{i-2} - 8\eta_{i-1} + 8\eta_{i+1} - \eta_{i+2}), \quad (\text{C.45})$$

respectively. The contribution from the U^2 integral contains terms that need to be evaluated at the edges of the source panel and therefore require special care.

First, we use finite differences at halfway points to evaluate the term involving the second order spatial derivative of the plate displacement. We combine these with the term to be evaluated at the panel edges, also involving the halfway points. Finally, we transform the halfway points into full nodal points using the formula derived in (C.39) to obtain the final expression of (C.46), as shown below:

$$\begin{aligned} & U^2 \int_{\Gamma_0} 2 \frac{\partial}{\partial x_{\mathbf{I}}} \psi(\mathbf{I}, \mathbf{J}) \frac{\partial}{\partial x_{\mathbf{J}}} \eta(\mathbf{J}) d\Gamma_{\mathbf{J}} + 2U^2 \frac{\partial}{\partial x_{\mathbf{I}}} \psi(\mathbf{I}, \mathbf{J}) \eta(\mathbf{J}) \Big|_{\mathbf{J}=\mathbf{I}-\frac{\Delta x}{2}}^{\mathbf{J}=\mathbf{I}+\frac{\Delta x}{2}} \\ & \approx -\frac{U^2}{3\pi\Delta x} \left(-\eta_{i-1} + 16\eta_{i-\frac{1}{2}} - 30\eta_i + 16\eta_{i+\frac{1}{2}} - \eta_{i+1} \right) + \frac{U^2}{\pi} \frac{2}{\Delta x} \left(\eta_{i-\frac{1}{2}} + \eta_{i+\frac{1}{2}} \right) \\ & \approx \frac{U^2}{\pi\Delta x} \left(\frac{5}{96}\eta_{i-2} - \frac{7}{24}\eta_{i-1} + \frac{85}{16}\eta_i - \frac{7}{24}\eta_{i+1} + \frac{5}{96}\eta_{i+2} \right). \end{aligned} \quad (\text{C.46})$$

We add the results of (C.44), (C.45) and (C.46) to obtain the total contribution from the source panel integrals

$$\begin{aligned} p_i^{source} & \approx \frac{(1 - \ln(\Delta x/2)) \Delta x}{\pi} \frac{\partial^2}{\partial t^2} \eta_i + \frac{1}{12\pi} \frac{\partial}{\partial t} (\eta_{i-2} - 8\eta_{i-1} + 8\eta_{i+1} - \eta_{i+2}) \\ & + \frac{U^2}{\pi\Delta x} \left(\frac{5}{96}\eta_{i-2} - \frac{7}{24}\eta_{i-1} + \frac{85}{16}\eta_i - \frac{7}{24}\eta_{i+1} + \frac{5}{96}\eta_{i+2} \right). \end{aligned} \quad (\text{C.47})$$

C.3.4 Combined Plate Equation

The fully linearized fluid-plate equation expressed in terms of plate deflection alone now becomes

$$\begin{aligned}
& \frac{1}{\Delta x^4} \delta^4 [\eta_i] + \frac{T}{\Delta x^2} \delta^2 [\eta_i] + \lambda \eta_i + \frac{\partial^2}{\partial t^2} \eta_i = \\
& 2G_{ij} \frac{\partial^2}{\partial t^2} \eta_j + 4UG_{ij}^x \frac{\partial}{\partial t} \eta_j + 2U^2 G_{ij}^{xx} \eta_j + f_i \\
& + \frac{\Delta x (1 - \ln(\Delta x/2))}{\pi} \frac{\partial^2}{\partial t^2} \eta_i + \frac{1}{12\pi} \frac{\partial}{\partial t} (\eta_{i-2} - 8\eta_{i-1} + 8\eta_{i+1} - \eta_{i+2}) \\
& + \frac{U^2}{\pi \Delta x} \left(\frac{5}{96} \eta_{i-2} - \frac{7}{24} \eta_{i-1} + \frac{85}{16} \eta_i - \frac{7}{24} \eta_{i+1} + \frac{5}{96} \eta_{i+2} \right) \\
& + 2UG_{ij} \frac{\partial}{\partial t} \eta_j \Big|_{j=1}^{j=M} + 2U^2 G_{ij}^{xx} \frac{\partial}{\partial t} \eta_j \Big|_{j=1}^{j=M},
\end{aligned} \tag{C.48}$$

where $\delta^2 [\eta_i]$ and $\delta^4 [\eta_i]$ are the fourth order finite differences given in (C.35) and (C.36).

C.3.5 Time Stepping

The final step in our computational scheme consists of discretizing in time. We use a second order central difference scheme, also known as the ‘leapfrog method,’ to write

$$\frac{\partial}{\partial t} \eta_i^n \approx \frac{1}{2\Delta t} (\eta_i^{n+1} - \eta_i^{n-1}) \tag{C.49}$$

$$\frac{\partial^2}{\partial t^2} \eta_i^n \approx \frac{1}{(\Delta t)^2} (\eta_i^{n+1} - 2\eta_i^n + \eta_i^{n-1}). \tag{C.50}$$

By applying this differencing procedure to (C.48) and collecting all $n+1$ terms on the left hand side, we obtain

$$\begin{aligned}
& - \left[\frac{2}{\Delta t^2} G_{ij} + \frac{2U}{\Delta t} G_{ij}^x \right] \eta_j^{n+1} + \left(\frac{1}{\Delta t^2} - \frac{(1 - \ln(\Delta x/2)) \Delta x}{\pi \Delta t^2} \right) \eta_i^{n+1} \\
& - \frac{1}{24\pi \Delta t} (\eta_{i-2}^{n+1} - 8\eta_{i-1}^{n+1} + 8\eta_{i+1}^{n+1} - \eta_{i+2}^{n+1}) + \frac{U}{\Delta t} G_{i1} (\eta_1^{n+1} - \eta_M^{n+1}) + \frac{U^2}{\Delta t} G_{i1}^{xx} (\eta_1^{n+1} - \eta_M^{n+1}) \\
& = - \frac{2}{\Delta t^2} G_{ij} \eta_j^n + 2U^2 G_{ij}^{xx} \eta_j^n - \frac{(1 - \ln(\Delta x/2)) \Delta x}{\pi \Delta t^2} \eta_i^n - \frac{1}{\Delta x^4} I_{ij} \delta^4 [\eta_j^n] - \frac{T}{\Delta x^2} \delta^2 [\eta_i^n] - \lambda \eta_i^n + f_i \\
& + \frac{U^2}{\pi \Delta x} \left(\frac{5}{96} \eta_{i-2}^n - \frac{7}{24} \eta_{i-1}^n + \frac{85}{16} \eta_i^n - \frac{7}{24} \eta_{i+1}^n + \frac{5}{96} \eta_{i+2}^n \right) \\
& - \left[\frac{2}{\Delta t^2} G_{ij} + \frac{2U}{\Delta t} G_{ij}^x \right] \eta_j^{n-1} + \left(\frac{1}{\Delta t^2} - \frac{(1 - \ln(\Delta x/2)) \Delta x}{\pi \Delta t^2} \right) \eta_i^{n-1} \\
& - \frac{1}{24\pi \Delta t} (\eta_{i-2}^{n-1} - 8\eta_{i-1}^{n-1} + 8\eta_{i+1}^{n-1} - \eta_{i+2}^{n-1}) + \frac{U}{\Delta t} G_{i1} (\eta_1^{n-1} - \eta_M^{n-1}) + \frac{U^2}{\Delta t} G_{i1}^{xx} (\eta_1^{n-1} - \eta_M^{n-1})
\end{aligned} \tag{C.51}$$

The time stepping procedure using (C.51) consists of solving for the displacements at time $n + 1$ with prior knowledge of the displacements for times n and $n - 1$. The left hand side of (C.51) can be organized in the form of an $M \times M$ matrix (call it C) multiplying an $M \times 1$ vector of unknown displacements. Since all η_i^n and η_i^{n-1} are known from previous time steps, the right hand side reduces to an $M \times 1$ vector (call it V). The result is a system of M equations in M unknowns given through the matrix representation

$$C_{ij} [\eta_j^{n+1}] = V_i (\eta^n, \eta^{n-1}). \quad (\text{C.52})$$

The solution consists of inverting the matrix \mathbf{C} once, and using this inverted matrix to operate on the right hand side vector at each time step to obtain the new deflections

$$\boldsymbol{\eta}^{n+1} = \mathbf{C}^{-1} \mathbf{V}. \quad (\text{C.53})$$

C.4 Addendum: Derivation of Non-Linear Influence Coefficients

C.4.1 Fundamental Solutions

The solution of the fundamental equation in the half-plane for a source at point \mathbf{I} can be represented as the superposition of the free space Green's functions at the real source \mathbf{I} and its mirror image across the baffle \mathbf{I}' ,

$$\psi(\mathbf{I}, \mathbf{J}) = \frac{1}{2\pi} \ln \left(\frac{1}{r(\mathbf{I}, \mathbf{J})} \right) + \frac{1}{2\pi} \ln \left(\frac{1}{r'(\mathbf{I}', \mathbf{J})} \right). \quad (\text{C.54})$$

Here, \mathbf{J} is the receiver, $r(\mathbf{I}, \mathbf{J})$ is the distance $\sqrt{(x_I - x_J)^2 + (y_I - y_J)^2}$ between source and receiver and all primed variables correspond to contributions from the virtual source at $\mathbf{I}' \equiv (x_{I'}, y_{I'}) = (x_I, -y_I)$. The surface fluxes, normal to Γ at the receiver point \mathbf{J} , are given by

$$\begin{aligned} \frac{\partial \psi}{\partial \hat{n}_\Gamma} &= \frac{\partial \psi}{\partial x_J} \hat{n}_x + \frac{\partial \psi}{\partial y_J} \hat{n}_y \\ &= \frac{\partial \psi}{\partial r} \cdot \hat{\mathbf{r}} \cdot \hat{\mathbf{n}}_\Gamma \\ &= \frac{\cos \theta}{2\pi r} + \frac{\cos \theta'}{2\pi r'} \end{aligned} \quad (\text{C.55})$$

where $\cos \theta = \hat{r}_x \cdot \hat{n}_x + \hat{r}_y \cdot \hat{n}_y$ is a function of the angle between the normal to the plate surface and the line connecting the source and receiver. The unit vectors corresponding to the latter are defined as

$$\hat{r}_x = \frac{(x_I - x_J)}{\sqrt{(x_I - x_J)^2 + (y_I - y_J)^2}}, \quad (\text{C.56})$$

$$\hat{r}_y = \frac{(y_I - y_J)}{\sqrt{(y_I - y_J)^2 + (y_I - y_J)^2}}. \quad (\text{C.57})$$

Hence, they point from the receiver towards the source.

The x -directional fluxes of the fundamental solutions given above are

$$\begin{aligned} \frac{\partial}{\partial x_I} \psi &= \frac{1}{2\pi r} \hat{r}_x + \frac{1}{2\pi r'} \hat{r}'_x \\ &= -(x_I - x_J) \left(\frac{1}{2\pi r^2} + \frac{1}{2\pi r'^2} \right) \end{aligned} \quad (\text{C.58})$$

and

$$\begin{aligned} \frac{\partial}{\partial x_I} \frac{\partial \psi}{\partial \hat{n}_\Gamma} &= \frac{\partial}{\partial x_I} \left(\frac{\hat{r}_x \cdot \hat{n}_x + \hat{r}_y \cdot \hat{n}_y}{2\pi r} \right) + \frac{\partial}{\partial x_I} \left(\frac{\hat{r}'_x \cdot \hat{n}_x + \hat{r}'_y \cdot \hat{n}_y}{2\pi r'} \right) \\ &= -\frac{1}{\pi} \frac{(x_I - x_J)}{r^4} ((x_I - x_J) \cdot \hat{n}_x + (y_I - y_J) \cdot \hat{n}_y) + \frac{1}{2\pi} \frac{\hat{n}_x}{r^2} \\ &\quad - \frac{1}{\pi} \frac{(x_I - x_J)}{r'^4} ((x_I - x_J) \cdot \hat{n}_x + (y_I + y_J) \cdot \hat{n}_y) + \frac{1}{2\pi} \frac{\hat{n}_x}{r'^2}. \end{aligned} \quad (\text{C.59})$$

C.4.2 Evaluation of Integrals

The components of G_{ij} , H_{ij} , G_{ij}^x and H_{ij}^x consist of integrals of the above four fundamental solutions, equations (C.54), (C.55), (C.58) and (C.59) respectively, over individual boundary elements. All off-diagonal components $i \neq j$ are evaluated numerically using four point Gaussian quadrature. The formulae given in these four equations can be readily used for this purpose with the additional expressions for the surface normals at a boundary element given by

$$(\hat{n}_x)_j = \left(\frac{-(y_r - y_l)}{\sqrt{(x_r - x_l)^2 + (y_r - y_l)^2}} \right)_j \quad (\text{C.60})$$

and

$$(\hat{n}_y)_j = \left(\frac{(x_r - x_l)}{\sqrt{(x_r - x_l)^2 + (y_r - y_l)^2}} \right)_j. \quad (\text{C.61})$$

Here, $(x_r, y_r)_j$ and $(x_l, y_l)_j$ are the right end and left end coordinates of boundary element j . ‘Right’ and ‘left’ are determined with respect to the normal pointing out of an element into the fluid domain.